




ADVERTIMENT. L'accés als continguts d'aquesta tesi queda condicionat a l'acceptació de les condicions d'ús establertes per la següent llicència Creative Commons:  http://cat.creativecommons.org/?page_id=184

ADVERTENCIA. El acceso a los contenidos de esta tesis queda condicionado a la aceptación de las condiciones de uso establecidas por la siguiente licencia Creative Commons:  <http://es.creativecommons.org/blog/licencias/>

WARNING. The access to the contents of this doctoral thesis it is limited to the acceptance of the use conditions set by the following Creative Commons license:  <https://creativecommons.org/licenses/?lang=en>

TOWARDS TRANSLATIONAL NANOBIOTECHNOLOGY: BIOMEDICAL APPLICATIONS OF NOBLE METAL NANOPARTICLES

MURIEL FREIXANET GUSTÀ

DOCTORAL THESIS

Memòria presentada per optar al grau de Doctor per la
Universitat Autònoma de Barcelona

Programa de doctorat en Bioquímica, Biologia Molecular i
Biomedicina

Director

Prof. Victor F. Puntes

Tutora

Dra. Julia Lorenzo Rivera

Barcelona, Setembre 2022

Table of Contents

<i>Table of Contents</i>	<i>i</i>
<i>List of Abbreviations</i>	<i>v</i>
Thesis Overview	1
Chapter 1: General Introduction	3
1.1 Nanoparticles and Nanotechnology	5
1.1.1 Plenty of room at the bottom	5
1.1.2 A route to monodispersity	6
1.2 Optical Properties of Plasmonic Nanoparticles	8
1.3 The Nano-Bio Interface	12
1.3.1 Nanoparticle's Biomedical <i>Historicum</i>	12
1.3.2 Biomedical Applications	13
1.3.3 Interactions at the nanoscale	20
1.4 Health Impact and Regulation	24
1.5 References	27
Chapter 2: Cationic Gold Nanoparticles Mediated mRNA Delivery for Production of CAR-T lymphocytes for Chronic Lymphoid Leukaemia Immunotherapy	41
2.1 Introduction	43
2.1.1 CAR T-Cell Therapy	44
2.1.2 The unmet medical need	46
2.1.3 The nanotechnology dimension	47

2.1.4	Scientific relevance of the selected materials	49
2.2	Scope of the study	52
2.3	Results and Discussion	53
2.3.1	Development and Characterization of nanovectors	53
2.3.2	Uptake and Delivery Mechanistic Aspects	76
2.3.3	Transfection of mRNA with Nanovectors	88
2.3.4	Cytotoxicity and Risk Assessment of Nanovectors	95
2.4	References	99

Chapter 3: Confocal Imaging of Unlabelled Nanoparticles in Cells and Biological Tissues

107

3.1	Introduction	109
3.2	Scope of the study	111
3.3	Results and Discussion	112
3.3.1	Principles of Au NP Scattering	112
3.3.2	Single Particle Imaging	113
3.3.3	Au NP Size Resolution Limit	116
3.3.4	Confocal Imaging of Au NPs in Biological Systems	119
3.3.5	Other Materials	130
3.4	References	133

Chapter 4: Size Effects on Ag NP - Antibiotic Synergy

137

4.1	Introduction	139
4.2	Scope of the study	145
4.3	Results and Discussion	146
4.3.1	Synthesis of Silver Nanoparticles	146
4.3.2	Size-dependent corrosion of Silver Nanoparticles in biological media	149

4.3.3	Biocidal Effects of Silver Nanoparticles	155
4.3.4	Nanoparticle-Bacteria Interaction	159
4.3.5	Modelled Ag NPs Dissolution and Ag ⁺ Consumption	161
4.4	References	163

Chapter 5: Experimental Section: Chemicals, Materials, Methods and Techniques **167**

5.1	Chapter 2. Cationic Gold nanoparticles mediated mRNA delivery for production of CAR-T lymphocytes for Chronic Lymphoid Leukaemia Immunotherapy	169
5.1.1	Chemicals	169
5.1.2	Synthesis of Nanoparticles	170
5.1.3	Functionalization of Nanoparticles	172
5.1.4	Loading of Nanoparticles with oligonucleotides	173
5.1.5	Uptake and Delivery Mechanistic Aspects	174
5.1.6	Transfection of mRNA with nanovectors	176
5.1.7	Cytotoxicity and Risk Assessment of nanovectors	178
5.2	Chapter 3. Confocal Imaging of Unlabelled Nanoparticles in Cells and Biological Tissues	180
5.2.1	Chemicals	180
5.2.2	Synthesis of Nanoparticles	180
5.2.3	Simulations	182
5.2.4	Confocal Laser Scanning Microscopy (CSLM)	183
5.2.5	Nanoparticles on Biological Systems	184
5.3	Chapter 4. Size Effects on Ag NP - Antibiotic Synergy	186
5.3.1	Chemicals	186
5.3.2	Synthesis of Silver Nanoparticles	186
5.3.3	Size-dependent corrosion of Silver Nanoparticles in biological media	188

5.3.4	Biocidal effects of Silver	188
5.3.5	Nanoparticle-Bacteria interaction	189
5.3.6	Simulations	190
5.4	Nanoparticle's Characterization Techniques	192
5.4.1	Transmission Electron Microscopy (TEM)	192
5.4.2	Dynamic Light Scattering (DLS)	192
5.4.3	Zeta-Potential (Z-Pot; ζ)	193
5.4.4	UV-Vis Spectroscopy	193
5.5	References	195

Chapter 6: General Conclusions **197**

6.1	Cationic Gold nanoparticles mediated mRNA delivery for production of CAR-T lymphocytes for Chronic Lymphoid Leukaemia Immunotherapy	200
6.2	Confocal Imaging of Unlabelled Nanoparticles in Cells and Biological Tissues	201
6.3	Size Effects on Ag NP - Antibiotic Synergy	202

List of Abbreviations

Abs	Absorption
ADME	Administration, Distribution, Metabolism and Excretion
AP	Aggregation Parameter
AUT	11-Amino-1-Undecanethiol
BSA	Bovine Serum Albumin
CAR	Chimeric Antigen Receptor
CAR T	Chimeric Antigen Receptor T-cell
cCCM	completed Cell Culture Media
CLL	Chronic Lymphocytic Leukaemia
CLSM	Confocal Laser Scanning Microscopy
DLS	Dynamic Light Scattering
DMEM	Dulbecco's Modified Eagle Medium
Em	Emission
Ex	Excitation
Ext	Extinction
FIC	Fractional Inhibitory Concentration
FITC	Fluorescein-5-Isothiocyanate
GFP	Green Fluorescence Protein
LSPR	Localized Surface Plasmon Resonance
MBC	Minimal Biocidal Concentration
MDR	Multidrug Resistant
MES	2-(N-morpholino)ethanesulfonic acid
MIC	Minimal Inhibitory Concentration
mRNA	messenger RNA
NP	Nanoparticle
PB	Phosphate Buffer
PC	Protein Corona
PEI	Polyethyleneimine

PI	Propidium Iodide
PVP	Polyvinylpyrrolidone
ROS	Reactive Oxygen Species
SC	Sodium Citrate
Sca	Scattering
SEM	Scanning Electron Microscopy
SPR	Surface Plasmon Resonance
ssDNA	single stranded DNA
TA	Tannic Acid
TEM	Transmission Electron Microscopy
TSB	Trypticase Soy Broth
UV-Vis	Ultraviolet-Visible Spectroscopy
Z-Pot	Zeta Potential

Thesis Overview

This thesis aims to contribute to this emerging field, in which the biomedical and synthetic worlds combine into a new interdisciplinary science concerned with the safe and efficient use of nanomaterials for biological applications. The merging of this two quite different fields poses a challenge for its success. In the past few decades nanotechnology has experienced an exponential growth, and consequently their potential applications in the medical field. However, despite very promising results, expectations have not been matched towards their translation into the market, mostly due to lack of expertise and knowledge gaps between both areas. In the recent years it has become evident that proper understanding and communication between biology and nanoscience, along with extensive characterization studies of the nanomaterials, is essential to unleash nanomedicine to its full potential and improve patient quality and expectation of life.

This work was focused on the rational application of inorganic nanoparticles in the biomedical field. Three very different approaches were taken, from using nanoparticles as delivery scaffolds or active principles to their imaging in biological systems. Although many concepts are introduced in the dissertation in order to cover the basic concepts of the wide science fields it touches, it is only a little sample illustrating the huge extend of the nanomedicine potential.

CHAPTER 1 offers an introduction to the basic notions of inorganic nanoparticles, mainly focused on plasmonic nanoparticles, Au and Ag. It is aimed to provide the fundamental concepts to understand the properties and behaviour of nanoparticles, and the critical issues to bear in mind for their safe and rational use in biology. Some examples of their possible applications are presented, as well as, a brief discussion on their potential health risk and regulation.

CHAPTER 2 proposes to bind mRNA to gold nanoparticles (NP) functionalized with amine terminated molecules as a safer way to target the cytosol via endocytosis, aiming to produce CAR T-Cells for the treatment of Chronic Lymphocytic Leukaemia. Gold

nanoparticles are of special interest for genetic material delivery due to their biocompatibility, tuneable surface chemistry where a combination of therapeutic and targeting moieties can be loaded, and their special optical and electronic properties allow fine monitoring of the evolution, distribution and modifications of their chemical environment. More importantly, this strategy overcomes the main limitations of standard gene therapy approaches based on viral vectors, while inducing a slow release of the mRNA inside the cell extending the mRNA half-life and protein expression, compared to current non-viral methods.

CHAPTER 3 is probably the most interdisciplinary work of this thesis, bridging nanoparticle synthesis and their optical properties with the microscopy and biology fields. Here, it is reported the imaging of several unlabelled inorganic nanoparticles, relevant in the biomedical field, in the laser scanning confocal microscopy. Theoretical simulations of their optical properties are coupled to their experimental observation in the microscope, thus providing a user-friendly methodology applicable to many other cases. The relevance of this work relies on the possibility of studying NP-cell interactions at high resolution and/or in real-time without the need of expensive and specialized equipment.

CHAPTER 4 is an extended study of the synergistic effect of the combination of antibiotics with silver nanoparticles on different strains of drug resistant bacteria. It emphasizes the importance of the quality of the nanomaterials, correlating the dependency of the nanoparticle's size with the observed biological effects. Thus, a broad characterization of the synthesized nanoparticles in the biological medias used is performed, studying observed chemical transformations of the nanoparticles.

CHAPTER 5 covers all the materials and methods used con Chapter 2, Chapter 3 and Chapter 4 for their development. It is divided according to the specific methodology of each chapter. It also includes a section regarding common nanoparticle's characterization techniques.

CHAPTER 1

GENERAL INTRODUCTION

General Introduction

1.1 Nanoparticles and Nanotechnology

1.1.1 Plenty of room at the bottom

Inorganic nanoparticles (NPs) are a wide class of materials that include particulate substances with size at the nanometric scale, which present properties that differ from the bulk material. A bulk material usually exhibits constant physical properties regardless of its size. Oppositely, at the nanoscale, the physicochemical properties of the material can change depending on the number of atoms and the percentage of those atoms at the surface of the nanomaterial, namely the surface-to-volume ratio. Some of these size-dependent properties include melting point or colour of the material, chemical reactivity, quantum confinement in semiconductor NPs, surface plasmon resonance in some metallic NPs, superparamagnetism in magnetic materials. The limit size at which materials start displaying size-related properties with respect to the bulk material is material-dependent and has been proposed to be 100 nm. [1,2] Obviously, this definition is quite generic and there is no strict boundary. Consequently, nanotechnology covers the science of the manipulation of matter at the nanometric scale to form functional structures.

NPs display physicochemical characteristics that induce unique electrical, mechanical, optical and imaging properties that are extremely looked-for in certain applications within the medical, electronic and environmental sectors. The potential benefits of nanotechnology have been documented by many manufacturers at high and low levels and marketable products are already being mass-produced such as microelectronics, aerospace and pharmaceutical industries. [3–6]

Size effects, that extend over a wide variety of NP and applications, have opened a new and exciting possibility to tune the chemical and physical properties of a material, without the need to search for new material compositions. Consequently, advanced synthesis routes that offer not only control over the composition, as typically required for traditional bulk synthesis, but also control of particle size, shape and surface chemistry have become essential in the way to study and apply the dimension-dependent properties of nanomaterials, with remarkable interest in noble metal, Au and Ag, NPs.

1.1.2 A route to monodispersity

The technological revolution of characterization tools played a key role in the emergence and advances in the field of nanotechnology, as well as, the availability of new methods of synthesizing nanomaterials. Nano-sized objects or structures have always been present in nature, such as those made of noble metals, semiconductors, and oxides. [7–9] However, their characterization and control over their morphology came in recent times. Engineered NPs differ from naturally occurring NPs because they display extended colloidal stability, and because they can achieve high degree of structural and morphological monodispersity. NPs hold great promise for advances in a large number of fields due to their novel material properties, from catalysis to diagnosis and disease treatment. But success in their application to its full potential critically depends on the understanding and control over their production and stability, along with the ultimate physicochemical transformations and interactions with biological systems.

In order to distinguish NPs from general particulate matter, monodispersity becomes crucial. Among the number of ways to define monodispersity, some of them are based on the value of the standard deviation with respect to the value of the mean size of a NP solution. Traditionally, NPs can be defined as monodispersed when a predominately homogeneous NP population with >90% uniformity can be detected.

Among the different methods of preparing NPs, the chemical synthesis in a solution is probably the most employed route, which has the intrinsic advantages of producing more uniform and stable samples at high concentration, compared to other synthetic approaches. [10] Although Faraday described the first synthesis of a pure gold colloid in 1857, [11] it was not until the 1940s that LaMer first introduced the concept of the formation of monodisperse colloidal NPs. [12] In 1951, Turkevich et al. performed the first structural studies of Au NPs by electron microscopy, [13–15] and further work developed by Frens

showed the possibility to tune the size of spherical Au NPs. [16] These studies became the foundation of a large amount of posterior colloidal synthetic methods developed for obtaining NPs with defined size, shape and surface chemistry. [17–24] Murphy [25] and Liz-Marzan [26] accomplished remarkable improvements by reporting the synthesis of monodisperse Au NPs of up to ~180 nm in diameter using ascorbic acid as a reducing agent and cetyl-trimethylammonium bromide (CTAB) as a cationic surfactant. Although CTAB-based methods allow the control of Au NP size and morphology, the use of molecules that strongly bind to the Au surface restricts the possibility of further functionalization because their replacement is difficult to achieve. [27] This condition is especially important in biomedicine, where the ability to render a biological functionality to inorganic nanostructures is one of the cornerstones of this emerging field. In this context, citrate-stabilized Au NPs are unique candidates because the loosely bound capping layer provided by the citrate ions can easily be exchanged with other molecules. In this way, Au NPs derived with proteins, peptides, antibodies, and DNA have been used in promising applications in the fields of diagnosis, therapy, drug delivery, and sensing, among others. [28–30] Control over size is a key point in the use of NPs, especially in the biomedical field, since it influences important biological properties such as interaction with proteins, biodistribution and clearance rate. Populations within a sample of NPs with low monodispersity can greatly differ in their intrinsic properties, displaying huge differences in their physicochemical transformations (as aggregation, corrosion or dissolution rates) and interactions at the bio-interface. Consequently, the use of polydisperse NPs, that don't behave homogeneously, introduces high case-to-case variability with low results reproducibility.

Reduced size comes at a price, and NPs are thermodynamically unstable which causes them to rapidly transform to reduce their surface energy. Large surface area and low atom coordination at the NP surface determine the high energy potential of NPs and consequently their behaviour and reactivity profiles. [31] Excess of surface energy is dissipated through chemical reactions and physical alterations, either via aggregation or dissolution processes, or by passivating their surfaces with adsorbed molecules. Due to their great instability, at useful concentrations, naked NPs are not stable in water and they need to be stabilized after their synthesis. In order to prevent NPs aggregation, it is generally required to provide the NP with the repulsion forces, which can be done either by electrostatic repulsion, for example designing a double electrical layer of inorganic ions around the NP surface, or by steric repulsion, by conjugation of larger highly soluble organic or biological molecules.

Despite the crucial role of this stabilization layer, most studies merely focus on the inorganic core of the nanostructure, overlooking the surface stabilization shell. Even though the core of the NPs determines its physicochemical properties, the surface chemistry dictates the interactions with the surrounding medium. This is particularly important in biological scenarios, where surface interactions ultimately determine the formation of the protein corona, the intracellular uptake and localization of the NPs, and in turn, their biological functions. [32,33] By controlling the surface chemistry, conjugation can also be used as an interface for functionalization, providing chemical and biological moieties to tune the behaviour and fate of NPs. Still, in too many cases the loss of colloidal stability is behind the lack or unexpected biological behaviours, as size-dependent properties are lost when NPs aggregate. Under controlled environments surface stability is easily reached, but biological fluids (as cell culture media or biological fluids) are complex mixtures of salts, proteins and other small organic molecules that may promote destabilization of NPs. Knowledge and understanding of NP interactions and fate on those environments is critical to preserve colloidal stability all along the process. [34]

1.2 Optical Properties of Plasmonic Nanoparticles

The optical and electronic properties of NPs are interdependent to a greater extent. For instance, noble metal NPs have size-dependent optical properties and exhibit a strong UV–visible extinction band that is not present in the spectrum of the bulk metal. It is known as the localized surface plasma resonance (LSPR), and it arises from the coherent oscillation of the NP's electrons of the conduction band in resonance with the incident electromagnetic field (**Figure 1.1**). It is well established that the peak wavelength of the LSPR spectrum is dependent upon the size, shape and inter-particle spacing of the NPs, as well as its own dielectric properties and those of its local environment including the substrate, solvents and surfactants. [35–39]

The contribution of the different parameters to the total extinction of small spherical metal nanoparticles is described by the Mie theory. [40,41] Mie solved Maxwell's equation for electromagnetic light interacting with a small metallic sphere. With the appropriate boundary conditions for a spherical object, his calculations gave a series of multipole oscillations (dipole, quadrupole...) for the extinction cross-section of the particles as a function of the particle radius.

The term “extinction” means the loss of light from a directly transmitted beam and allows to study the ability of NPs to interact resonantly with light. It is usually expressed as extinction efficiency (Q_{ext}), which is a theoretically and dimensionless parameter. It is the sum of two different contributing mechanisms: absorption and scattering. The absorption of electromagnetic radiation (light) is the process by which the energy of a photon is taken up by matter, while scattering takes account of the light that is diverged from a straight trajectory. Moreover, when working with colloidal dispersions of NPs the empirical value of extinction, also called absorbance when referred to experimental results, is commonly used.

$$\sigma_{ext} = \sigma_{abs} + \sigma_{sca}$$

For NP much smaller than the wavelength (<25 nm) of the interacting visible light, all electrons in the entire particle experiences a roughly uniform electric field leading to the excitation of the dipolar plasmon resonance, which is the only contributing significantly to the extinction cross-section. [42]

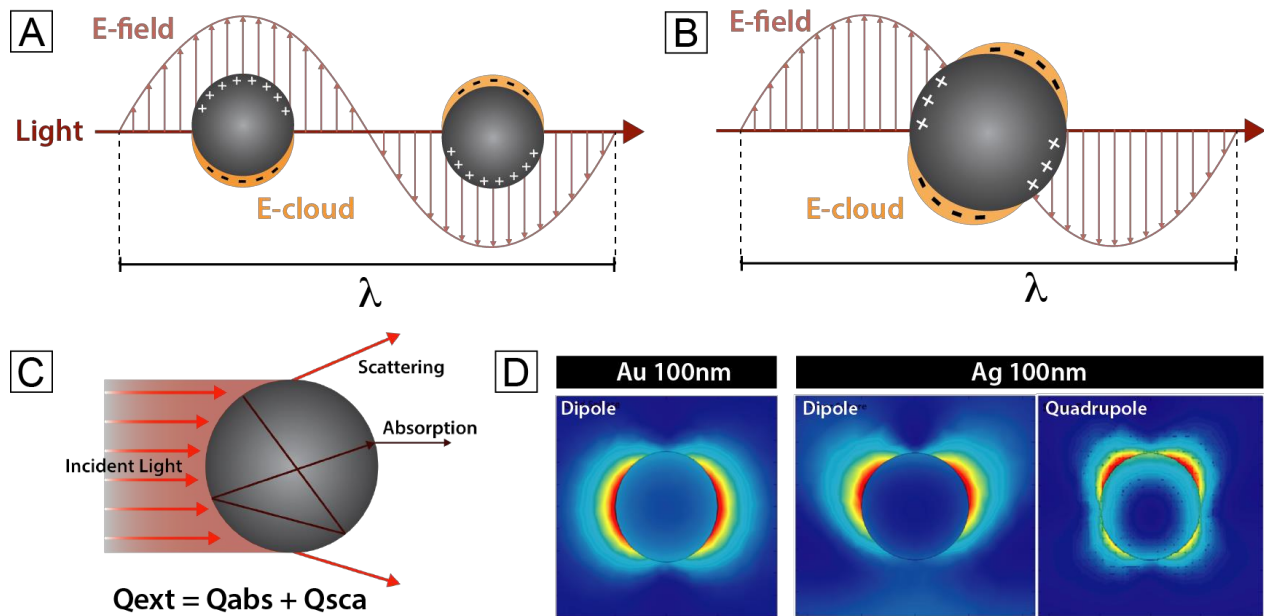


Figure 1.1. Surface Plasmon Resonance of NPs. Scheme of electron oscillations in a metal sphere under the influence of an electric field induced by an incident light radiation. **(A)** The sphere responds to a spatially constant electric field when its size is much smaller than the light wavelength, resulting in a coherent dipolar oscillation of the conduction electrons. **(B)** The electric field is no longer homogeneous along the sphere when its size is comparable to the light wavelength, leading to multipole oscillations. **(C)** Schematic representation of the Mie theory. The NP interaction with the incident light will result into a partial light scattering and absorption, and their sum is the total extinction. **(D)** E-field profile for gold dipole, as well as silver dipole and quadrupole peaks for 100 nm diameter nanoparticles (adapted from ref [43]).

For large particles (>25 nm), the extinction spectrum is then composed of the sum of absorption and scattering modes, each of which has a contribution that depends on the particle size. As NP's size increases, light cannot polarize homogeneously and the field is no longer uniform throughout the NP, which results in phase retardation effects. As a consequence, the appearance of higher-order modes is observed in larger particles, which become more dominant with increasing particle size, causing plasmon dipolar absorption band to red-shift while the bandwidth increases. This also results in the appearance of quadrupole resonances and octupole peaks for very large particles at shorter wavelengths. As a result of these unique optical properties, NPs of different sizes exhibit different colours and different degrees of absorption and scattering of light. [35]

To illustrate this phenomenon, the optical properties of solid Au and Ag spheres have been calculated based on Mie theory, using Mie Plot software. [44,45] **Figure 1.2** shows the calculated spectra of the efficiency of absorption (Q_{abs}), scattering (Q_{sca}), and extinction (Q_{ext}) for Au and Ag spherical NPs of different sizes (10, 50, 100 and 200 nm). The optical absorption and scattering properties of these NPs can be tuned by changing their size and shape. The increase in the ratio of scattering to absorption with NPs volume provides a tool for NPs selection. For instance, larger NPs are more suitable for light-scattering-based imaging applications while NPs with a high absorption cross-section, facilitates selective photothermal therapy. [46–48]

The recognition that the LSPR is sensitive to changes in several parameters has resulted in intense research and development of noble metal nanostructures for their application in many areas including chemical and biological sensing, imaging, optoelectronics, energy harvesting and conversion, and medicine. [49] Intrinsic properties of NPs can be tailored by controlling their morphology (e.g., size and shape), [50] composition (e.g., monocomponent vs alloys), [51] structure (e.g., solid vs hollow), [52] surface chemistry [53,54] and the refractive index of the local environment. [55] Among the three metals that display plasmon resonances in the visible spectrum (Ag, Au, Cu), Ag exhibits the highest efficiency of plasmon excitation, and it is the only material whose plasmon resonance can be tuned to any wavelength in the visible and near-infrared (NIR) range by modifying Ag NP's morphology. [35,56]

In addition to technological implications, the optical signature of NPs is also useful as a characterization tool. This is interesting because optical techniques are non-destructive and may enable measurements in situ and in real time of the state of the NPs. An important

requisite for the implementation of NPs is the control of their interaction with the surrounding environment, which is usually achieved by its functionalization with the appropriate molecules. In the case of plasmonic NPs, these molecules act as transducers that, after binding to the NPs, convert small increases in the local refractive index into spectral red shifts. Bastus et al. performed an extensive study, coupling theoretical simulations and experimental data, where they investigated the effect of composition, size, and surface coating on the sensitivity of localized multipolar surface plasmon resonances in colloidal solutions of Ag and Au NPs. Results show a higher relative sensitivity of (i) Ag than Au NPs, (ii) larger NPs, (iii) longer molecules, (iv) SH anchor groups, and (v) dipolar modes. [35] Further, optical properties can also be used to monitor and identify chemical transformation processes, as aggregation, dissolution and oxidation. Understanding NP's transformations is critical, not only to better interpret the biological effect of the NPs but also to better able to design NPs for a specific purpose. In this regard, Piella et al. modelled and study the time-dependent optical properties of Au and Ag NPs after different physicochemical transformation processes, thus proposing as a qualitative guide to identify the evolution of Au and Ag NPs in biological environments. [42]

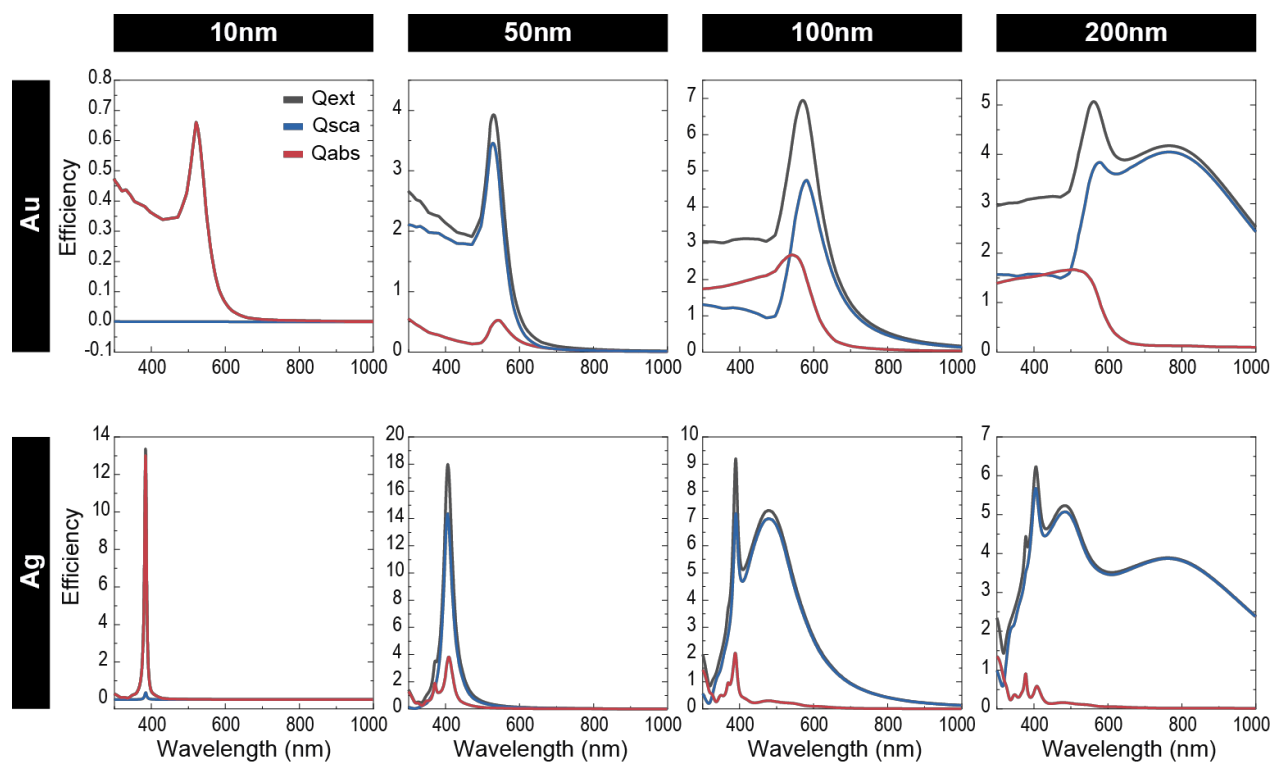


Figure 1.2. Optical properties of Au and Ag NPs. Mie theory absorption (blue), scattering (red) and extinction (black) spectra of Au and Ag NPs of diameter 10 nm, 50 nm, 100 nm and 200 nm. Spectra are shown in terms of efficiency, which is the ratio of the calculated optical cross-section of a NP to its actual geometrical cross-section.

1.3 The Nano-Bio Interface

1.3.1 Nanoparticle's Biomedical *Historicum*

Exploiting novel physicochemical and biological properties exhibited by nanoscale materials to improve human health is perhaps the fundamental element of nanomedicine. In recent years, nanomedicine has provided a useful set of research tools and medical devices for researchers and clinicians, and more will come in the near future. However, the therapeutic use of inorganic nanoparticles in humans is not entirely new. Traditionally, colloidal gold (*Aurum Potabile* – form the latin “potable gold”) was administered for its supposed therapeutic benefits since the antiquity, initially in old China and then through the silk road up to Switzerland where was described by Paracelsus in the 16th century. In the same way, the use of silver nanoparticles (colloidal silver) as a disinfecting agent had already been used since ancient times and was then approved by the Food and Drug Administration (FDA) more than 130 years ago. [57]

Already in modern times, we continued with the medical use of gold salts for the treatment of Rheumatoid arthritis (Auranofin, Ridaura®), which when enter inside the body are reduced spontaneously into nanoparticles smaller than 5 nm and expelled by urine. Another example of uses of sub-nanometric inorganic material is Alum (Aluminum Sulfate), [58] the most widespread adjuvant for vaccines.

More recently, new engineered NPs have been developed for therapeutic use. Amorphous porous silicon dioxide (SiO₂) NPs were designed as drug delivery platforms, [59,60] where its degradation generates silicic acid, a promoter of osteogenesis and proposed to treat osteoporosis – recently considered as Generally Regarded As Safe (GRAS) by the FDA. [61] On the other hand, magnetic iron oxide (Fe₃O₄) NPs, were developed with numerous medical applications: as contrast agents for MRI (Resovist®), [62] as hyperthermia agents for the treatment of cerebral neuroblastoma and glioblastoma (MagForce®), [63] or as an injectable anti-anaemic drug in patients with fragile kidney (Feromuxytol®). [64] The list goes on, with many others that are still in clinical trials.

In this context, it is not surprising that nanomedicine has been the focus of strong support as in the case of the European Technology Nanomedicine Platform (ETNP) or the United States Nanotechnology Characterization Laboratory (NCL) acknowledging the future importance of nanomedicine. [65] Similarly, in recent declarations, the 2016 Noble Prize

on Chemistry Bernard Feringa was describing his achievements as “Such molecular machines can be developed in smart medicines that seek out disease or damage and deliver drugs to fight or fix it, and in smart materials, which can adapt in response to external triggers such as changes in light or temperature”, underlying the potentially huge impact nanomedicine will have in the coming future. [66]

1.3.2 Biomedical Applications

New drugs or active principles discovered from nature seem to have been exhausted, and the newly designed drugs – immune therapy, stem cell therapy or genetic therapy – are not yet fully working. In this regard, nanomedicine has emerged as a “disruptive technology”, with great potential to contribute to improving treatments of different diseases by the generation of new diagnostic and therapeutic products, and by assisting other existing technologies.

Depending on their mechanism of action, NPs can be designed as scaffolds or actuators, or even a combination of both. In the first case, the NP is at the service of the drug/active principle (e.g.: to transport it) whereas in the other case, NPs are active by themselves where the coating is at the service of the NP (e.g. for stabilization or targeting). The outcome is a complex NP which is understood as a toolbox for monitoring and manipulating biological states. In these platforms, different drugs, ligands and biomolecules can be combined (by absorption, loading, coordination bonding, entrapment, etc) [32,51,67,68] and different tasks (delivery, heat, irradiate) can be performed. [69,70] For that, NPs are unique to bring therapeutic and imaging agents to diseased tissue. So, NPs are ideal scaffolds to combine therapeutic and diagnostic agents, enabling thus theranostic approaches (simultaneous concerted diagnosis and therapy). Further, in the diagnosis field, optical methods are widely used in the current analytical technologies, where many NP's properties as optical signatures (e.g. LSPR) and surface chemistry can and have been used for sensor development with remarkable efforts in Au NPs. Below, some examples of the rational use of inorganic NPs in the biomedical field are exposed. The biological applications of inorganic NPs are summarized in **Figure 1.3**.

1.3.2.1 NPs as scaffolds

Nanoscale drug delivery agents have been developed and exploited to enhance the delivery of drugs in the treatment of several diseases showing potential benefits in terms of

pharmaceutical flexibility, selectivity, dose reduction and minimization of adverse effects. [71] Many conventional therapies can be improved through the use of drug delivery systems (DDS). DDS are designed to modify the pharmacokinetics and biodistribution of small and macro-molecular drugs, to protect them from degradation extending their half-life, and also improve the delivery of poorly water-soluble drugs. Clearly, once a molecule is associated with a NP, its fate and biodistribution are determined by the NP physicochemical features rather than the drug. Thus, nanocarriers can strongly contribute to modifications of pharmacokinetics and biodistribution of numerous active principles, by driving them through different pathways, depending on the morphological, surface state and physicochemical properties of the nanocarrier. In fact, the strategy of adding other chemical moieties to the drug, has been a traditional way to alter drug pharmacokinetics in both ways, their biodistribution and their in-body metabolization, what determines dosing (concentration and time) parameters in the different organs. [72]

This is of special importance in the case of anticancer therapies in which a widespread distribution of small molecular chemotherapeutic drugs is often limiting treatments due to severe side effects that make impossible to reach the full benefits of the therapy. In the work of Comenge et. al, they reported the use of Au NPs to detoxify the anti-tumoural agent cisplatin, linked to the NP via a pH-sensitive coordination bond for endosomal release. [66] They showed that cisplatin-induced toxicity was clearly reduced without affecting its therapeutic benefits in mice models. Furthermore, the transport of the drug with the proper coating of the NP and/or using hollow nanostructures may limit not only systemic degradation of the drugs but also the ejection of drugs from the cells before they act (drug efflux) and other drug-detoxifying. [73–75] All these combinatory effects can overwhelm and override the resistance mechanisms of tumoural cells, improving anti-cancer conventional treatments. For instance, in the work of Meng et al. (2010), mesoporous silica NPs were used as a platform to deliver both doxorubicin and siRNA in a drug-resistant cancer cell line (KB-V1 cells). As the used siRNA knocks down gene expression of a drug exporter used to improve drug sensitivity to chemotherapeutic agents, this dual delivery was capable of increasing drug concentration intracellularly and in the nucleus to levels exceeding that of free doxorubicin or the drug being delivered in the absence of siRNA.

The possibility of the rational control of the functionalization of inorganic NPs with biomolecules is particularly important for cancer immunotherapy: the training of the immune system to attack the tumour, [76,77], especially in the case of therapeutic vaccines. Three critical elements are considered to be essential in the composition of an effective

vaccine: an antigen to trigger a specific immune response, an adjuvant able to stimulate the innate immunity, and a delivery system to ensure optimal delivery. [78] To obtain the full activation of antigen-presenting cells (APCs), the simultaneous action of antigens and adjuvants is critical. In this regard, inorganic NPs can help to develop (a) safe and powerful adjuvants to stimulate the immune system in a non-specific way [28,29] that induces an inflammatory state able to detect the otherwise evading tumours; [76,79] and (b) as antigen-presenter platforms, [80] by conjugating them to tumour-associated antigens to develop the adaptive immune response against it (by boosting the immune response through the aggregation and repetition of these antigens on the NP surface). Another immune-based cancer therapy approach is the use of antibodies for blocking signalling pathways. [81] In these particular cases, the instability of the exogenous antibodies and their low efficiency calls for nano-conjugation. [73,82] Thus, by condensing the antibodies on top of a NP surface, they are protected from systemic degradation [83] and their pharmacokinetic profile is altered allowing for improved targeting. [84] Additionally, the use of NP-antibody conjugates has shown a prolonged antibody therapy effect by avoiding receptor recycling as well as decreasing the needed antibody dose in the case of Cetuximab-Au NPs conjugates targeting the epidermal growth factor receptor (EGFR) of A431 tumoural cells. In this work, the coverage density and orientation of antibodies were strictly controlled to properly evaluate their effect. Results showed EGFR blocking, along with their altered trafficking signalling effects. The blocking effects of Cetuximab were increased and sustained for a longer time when associated with the Au NPs. [73]

The use of nanocarriers for gene therapy has also been extensively reported in the literature due to the current limitations of approved strategies. Despite their high efficiency and common usage in gene delivery, viral vectors inherit fundamental drawbacks (immunological problems, insertional mutagenesis and limitations in the size of the carried therapeutic genes) that need to be addressed. [85] Functional inorganic nanomaterials recently emerged as robust and versatile nano-scaffolds for effective gene delivery applications. [86,87] Significantly, without the limitations associated with viral vectors, inorganic nanomaterials further offer an appealing set of properties for practical applications, including scalability in synthesis, facile functionalization, chemical and thermal stability and optical signatures that allow its precise detection. These properties are important for sterilization, low inherent toxicity (especially for gold, iron oxide and silica nanoparticles), availability in a wide range of sizes and shapes, and the possibility of real-time tracking by various spectroscopic techniques. [88] Single-stranded DNA

functionalized gold nanoparticles developed by Mirkin et al. demonstrated excellent gene delivery efficiency. [89] These nanoparticles demonstrated greater knockdown of gene expression, higher binding affinity for target DNA, higher immunity to nuclease, and lower cell toxicity than antisense DNA delivered by either Lipofectamine® or Cytofectin®. Moreover, as alternative strategies to deliver nucleic acids to tumours, a controlled-release system responding to the unique environments of tissues and external stimuli has been investigated recently. Gold nanorods have strong absorption bands in the near-infrared region, and the absorbed light energy is then converted into heat, the so-called “photothermal effect”. Because the near-infrared light can penetrate deeply into tissues, the surface of the gold nanorod could be modified with double-stranded DNA for controlled release. [90] When the dsDNA-modified gold nanorods were irradiated by near-infrared light, single-stranded DNA was released due to thermo-denaturation induced by the photothermal effect. The amount of released ssDNA was dependent upon the power and exposure time of light irradiation. The release of ssDNA after light irradiation was also observed in Colon-26 tumours grown in mice when the dsDNA-modified gold nanorods were directly injected into the tumours. [91]

1.3.2.2 NPs as actuators

Some inorganic NPs are active principles based on their composition. Few examples have been explained previously, such as the case of SiO₂ used for the treatment of osteoporosis, or Fe₃O₄ for anaemia treatment. Another interesting example is CeO₂, which has been reported to display anti-inflammatory and radio-protection properties. CeO₂ NPs in the size range of 3–50 nm have recently received increased attention for their participation in biochemical redox reactions, providing sites for free radical scavenging and reducing inflammation. [92–94] Most therapeutic CeO₂ NPs applications are proposed based on their ability to reduce ROS levels and consequently, the levels of most pro-inflammatory mediators, such as inducible nitric oxide synthase, nuclear factor $\kappa\beta$, tumour necrosis factor- α , and interleukins. [95–98] Indeed, CeO₂ NPs were recently found to have multi-enzyme mimetic properties, including those related to superoxide dismutase (SOD), catalase, and oxidase. [99] In this context, CeO₂ NPs have potential applications in many different medical fields, as (i) cardiology reducing the myocardial oxidative stress in cardiomyopathy, [100] (ii) oncology protecting cells from radiation-induced damage, [101] and (iii) hepatology where they have been reported to display hepatoprotective effects

against non-alcoholic steatosis. [102] On the other hand, the antibacterial properties of Ag and its mechanisms of action will be deeply discussed on Chapter 4.

Inorganic NPs can also be used as imaging and radiation contrast agents. Despite that the current knowledge on the subject is still scattered and too heterogeneous to deliver useful tools for society, many recent discoveries and advances preclude the inevitable success of nanomedicine, as far as the right strategies and methodologies are pursued. Thanks to their high electronic density, inorganic NPs can act as antennas that absorb photons of determined wavelengths, to which we are transparent. Thus, radiotherapy effects can be enhanced in such a way that employed doses can be decreased where only the NPs allow the toxic effect, improving localized radiotherapy. Inorganic materials can absorb strongly X-rays and selectively enhance the damage inflicted on tumoural tissue in radiotherapy treatments. This is mediated by the fact that these materials absorb strongly the primary radiation beam, especially high Z number atoms. Subsequently, this generates a cascade of secondary low-energy electrons (LEEs) highly toxic within a very short range around the NP, [103] which is the main source of energy deposition and radiation-induced damage in biological tissue. [104] Additionally, the irradiated metallic NP can be activated producing catalytically free radicals as hydroxyl radicals $\text{OH}\cdot$ and hydrogen peroxide H_2O_2 among others, [105] which can initiate further reactions and induce oxidative stress and cellular damage. [105,106] Recent works studying the effects of Au NPs in combination with radiation in various cell lines found a damage enhancement factor between 1.5 and 3.4 times depending on the size of the NPs, [107] incident energy, [108] and cell type. [109,110]

Inorganic NPs can be also used in combination with near-infrared (NIR) photons ($\lambda 800\text{--}1100\text{ nm}$) both for molecular imaging and selective photothermal therapy. [111] Here, some Au NPs such as Au nanorods [112,113] or hollow Au NPs [114] present a suitable strong surface plasmon resonance light absorption in the NIR. This is a region of the light spectrum where there is a window of transparency for biological tissues (known as the therapeutic window) from the overlapping light absorption of water, haemoglobin, and melanin. Thus, the possibility to excite in the NIR region allows for both, minimization of photo damage of biological specimens and maximization of the penetration depth into the tissue of the excitation light.

In addition, superparamagnetic NPs offer attractive possibilities to treat cancer by inducing hyperthermia. [115] Magnetic NPs can be manipulated by external magnetic fields, which show intrinsic high penetrability into human tissue. [116,117] When these NPs are exposed

to an alternating magnetic field of sufficient strength and frequency, there is a conversion of magnetic energy into thermal energy. The heat generated is then transferred to the cells surrounding the NPs, which can result in cancer cell death by apoptosis once the local temperature exceeds 40 °C and proteins denature. [118,119] Several groups have shown significant tumour inhibition during hyperthermia therapy by employing Fe_3O_4 NPs. [120] Indeed, this technology is already applied in the clinic in Germany, and soon in Spain. As mentioned before, the same NPs can also be used as highly biocompatible contrast agents in magnetic resonance imaging (MRI). [121]

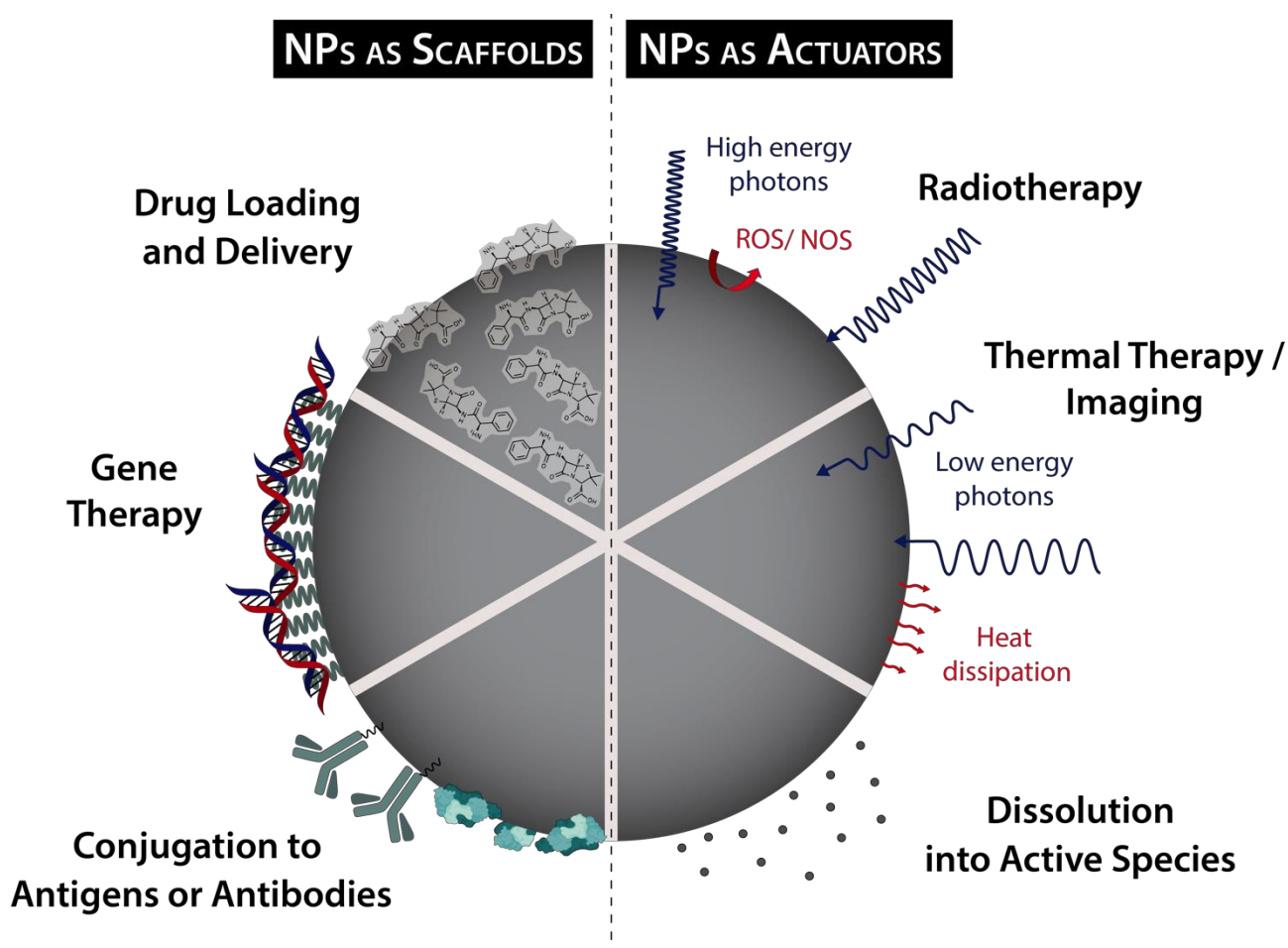


Figure 1.3. Schematic representation of the applications of inorganic NPs. NPs can act as scaffolds when the core is at the service of the coating, which include their use as drug delivery systems, or in gene therapy. NP conjugated with antigens or antibodies can also be used as adjuvants, for blocking signalling pathways, or for antigen targeting. Alternatively, NPs can act as actuators when the properties of core can be used for treatment or imaging, as in radiotherapy or MRI imaging. Also, NP can also be used as a reservoir of ions, which are the actual active principles released by dissolution from the NP surface.

1.3.2.3 NPs as biosensors

Plasmonic NPs absorb and scatter light intensely at their surface plasmon resonance (SPR) wavelength region and such properties make them some of the most valuable optical probes for sensing applications. [36,38,39,51,122–125] The SPR wavelength of Au and Ag NP can be tuned from the visible to the near IR region by changing their size and shape. The strong light extinction coefficient of noble metal NPs at the visible light region makes them easily observable by the naked eye or detectable by inexpensive instruments. The possibility of tuning the LSPR band of NPs (including nanorods, shells, stars, and other shapes) to the near IR region makes them promising materials for *in vivo* imaging and analysis. As explained in the previous section, the optical properties of NPs are highly dependent on the surface chemistry and the inter-particle interactions too. In fact, the vast majority of techniques developed so far involving NPs as optical probes are based on changes in the optical signature of NPs induced by the analyte targeting, with outstanding relevance of Au NPs due to their inertness.

A typical Au NP contains two structural components: the metal core and the surface coating. Since NPs have a high surface-to-volume ratio, and their surface chemistry is easily tuneable, specific surface coating of NPs provides an ideal platform for detection and sensing. Upon target analyte binding, the surface plasmon resonance of the Au NPs will change due to the surface chemistry change, or inter-particle interactions. The LSPR change of Au NPs can be then detected either by light absorption or light scattering techniques, as the antigen binding is used as the transducer signal. [49]

Depending on the origin of the LSPR change, a distinction between two types of LSPR sensors can be made. The first one is based on the aggregation of the colloid which results in an apparent colour change from red to blue due to inter-particle coupling, where metallic nanoparticles approach each other closer than their particle diameter. [124,126] A well-known application of this technology is the development of a pregnancy test. In this sensor technology, Au NPs and micro-latex beads were used, both coated with specific antibodies against the b-hCG hormone that is produced by pregnant women in high amounts. Upon mixing these particles with urine containing the hormone, pink aggregates could be clearly observed. [127]

The other sensor type is based on the sensitivity of the LSPR to changes in the dielectric constant of the surrounding medium or surfactants. When molecules bind to an Au NP, the refractive index will change inducing a shift of the LSPR, whose sensitivity is analyte

distance dependent. To increase the performance and assay sensitivity of this sensor platform, other materials and nanostructured patterns on transparent surfaces have been developed. For example, the plasmon wavelength of silver nanotriangles, [128] AuAg nanoshells, [129–131] nanorings, [132] nanocrosses, [133] showed an enhanced sensitivity for refractive index changes and proved potential in monitoring biomolecular interactions.

Apart from LSPR-based methods, other sensing techniques exist based on NP-ligand interactions: surface-enhanced Raman scattering (SERS), metal-enhanced fluorescence (MEF), and metal-induced fluorescence quenching. In SERS, the scattered light is detected from the Raman active dye molecules located on the surface of Au NPs, which is enhanced several orders of magnitude by the metal core. [129] On the other hand, fluorescence-based methods can be designed according to the interaction of the target with the gold core. When a fluorophore is attached to a metal nanoparticle, the fluorescence of the fluorophore can be enhanced or quenched, largely depending on the distance from the fluorophore to the nanoparticle core. Competitive assays are often designed using the metal-induced fluorescence quenching phenomenon, while direct assays are conducted based on the MEF effect. [49]

Last but not least, Au NPs have also been used in many point-of-care devices due to their versatility and storage stability. One, if not the most, application of Au NPs is on the basis of lateral flow assays. The user friendliness, low cost, and easy operation are the most attractive advantages of the LFA, with broad applications to food safety, environmental monitoring, clinical diagnosis, and so forth. In current LFAs, the recognition element involves both biomolecules and NPs. High-affinity biomolecules (e.g. antibodies, aptamers) are used to identify the target in complex sample matrices, and NPs are used to translate the invisible chemical reactions into detectable signals. The signal amplification strategies supported by NPs also greatly enhance the sensitivity and performance of LFAs, such as the enhancement of gold NPs tags by silver NPs. [131]. Widely known examples are the paper strip pregnancy test or the rapid antigen test for Covid-19. [134,135]

1.3.3 Interactions at the nanoscale

A key feature of molecular structures or biological entities in the body is their systematic organization at the nanoscale. Research and development in nanotechnology has allowed us to put man-made nanoscale objects into living cells. [136]

Interfacing the as-synthesized NPs with biological media is not always straightforward. The chemical environment desirable for inorganic NPs and the one desirable for cells and biomolecules may be quite different and certainly, in many approaches, obviously incompatible. Due to their higher percentage of surface atoms and their colloidal nature, once brought into contact with a physiological medium, NPs experience processes that transform them towards more stable thermodynamic states. [137,138] Thus, the NP surface has to be modified in order to be inserted efficiently into the biological machinery. The requirements are (i) controlled colloidal stability, (ii) controlled interaction with proteins in plasma, (iii) controlled (no) immunogenicity, (iv) controlled chemical reactivity and (v) controlled integrity of the material for its expulsion or destruction after use. As said, once being brought into contact with a medium, NPs experience modifications due to interactions between them and components from that biological medium, including aggregation, corrosion, oxidation, dissolution and interaction with media proteins. More than one of these processes can happen at the same time and there might also be competition between them, being aggregation between NPs or of NPs to proteins the most common leading cases. [31,139]

1.3.3.1 Aggregation, Dissolution, and Oxidation

It is well-known that some NPs can dissolve in certain dispersing media. [140–142] The extent of their dissolution depends not only on their intrinsic properties such as size and shape, but also on characteristics of the surroundings, including pH and ionic strength, as well as the presence of organic matter, mainly proteins. [143,144] This has strong consequences, not only on the metabolization and expulsion of NPs from the body, but also on their regulation, since if they are permanent, they may be regulated as a device (like an implant) while if they are metabolized and/or expelled, they may be regulated as a drug.

Regarding aggregation, the loss of colloidal stability has a dramatic effect since NP lose their size-dependent properties. There are several factors that cause the aggregation of colloidal NPs, for instance, the initial concentration of NPs and ionic strength of the medium, which is well described in the DLVO theory for colloidal stability. [145,146] In these cases, NP aggregation is due to the charge screening effect of salts present in biological media which causes a compression of the electrolytic double layer and loss of inter-particle electrostatic repulsion. [147] Therefore, unless steric repulsion is provided to the NP surface, it has been observed that NPs tend to agglomerate/aggregate after relatively short incubation times in different buffers and biological media. It has to be noticed that no

aggregation occurs in media with high protein concentration like serum, despite the high saline concentration. Here, the stability of NPs is maintained thanks to the formation of a Protein Corona and corresponding steric repulsion. In this case, the stabilizing mechanism changes from electrostatic to steric, and then the charge screening becomes irrelevant. The competition between aggregation induced by high ionic concentration and stabilization by protein absorption is well correlated to the relative amounts of both – ions and proteins – in the media and can be controlled by the addition sequence. [148] The extracellular agglomeration of NPs, or the agglomeration occurring prior or during exposure to *in vitro* or *in vivo* models has a significant impact on the observed biological effects and conclusions about their size-dependent (immuno)toxicity. [149,150]

1.3.3.2 Protein Corona Formation

Biological fluids are complex aqueous media composed of electrolytes, proteins, lipids, and carbohydrates, able to adsorb (by electrostatic, hydrophobic, van der Waals, and dispersive forces) onto the surfaces of the NPs, especially proteins, forming a protein-dense coating known as Protein Corona (PC). [151–155] The PC shields the original surface properties of the NPs acting as a surfactant and alters their size and composition providing the NPs with a new biological identity. [154,156,157] Indeed, once the corona is formed, [159] it is what actually the cell “sees”. [155] The composition, structure, and kinetics of the PC formation depend on (i) the specific characteristics of the biological environments in which NPs are dispersed, especially protein composition [158] and their relative concentration, [159,160] (ii) the physicochemical features of the dispersed material – such as NP chemical composition, [161] morphology, [151,162,163] surface charge and exposed functional groups, [148,159] 16,27 and hydrophobicity [151,164] – and (iii) exposure time, which directly correlates with the relative abundance of proteins and the different protein-NP binding affinities (Vroman’s effect). [148,161,165]

When the NP and the protein solutions are mixed, two different kinetic processes are competing at the same time: (i) the destabilization and further aggregation of the NPs between themselves (homo-aggregation) promoted by the high ionic strength of the media in which they are dispersed, and (ii) the stabilization of the NP surface against aggregation via protein adsorption (hetero-aggregation). In a later study performed by Piella et al. aiming to investigate the size-dependency of NP-protein interaction, they found out that in excess of free proteins, the aggregation of the particles is not exclusively determined by the probability of collisions of two individual particles but it may be affected by additional

parameters. [166] Interestingly, small particles appear to be slightly more stable than large ones. This could be related to faster protein coating or a faster dispersion of the NP due to increased Brownian motion as size decreases. Consequently, stability conditions depend on both the characteristics of the NPs, and the ratio between the NPs and protein concentration in the media. The formation of a PC on top of the NP surface has been observed to control biodistribution, uptake and biological response, transforming them from innocuous to toxic, or reverse. As discussed before, surface properties of NPs play a very significant role in determining the NP's behaviour with proteins in different environments.

The kinetics of these separate, but often co-existing, processes are strongly influenced by the respective concentrations of the causing chemical agents. These coupled processes are mediated by the different interactions between the NPs and components of the biological medium in which they are exposed, and ultimately determine the nature of the nano-bio interface.

1.3.3.3 Protein Corona: from the biomolecule perspective

Regarding biological and medical applications, it is important not only the adsorption of proteins themselves but also the implications that this adsorption entails for the protein, especially the maintenance of its tertiary (or quaternary) structure, since biological function depends largely on it. Size is known to be an important issue in nano-bio interactions and has a significant impact on determining NP's surface properties, which critically modulate its interaction with proteins. [167] An increasing surface curvature of a NP affects the surface chemistry by altering its surface charge increasing the isoelectric point, even to close to zero values (increasing its hydrophobicity) or altering the acidity of the coating molecules lowering their pK_a . [168–170] Certainly, these properties modulate how NP interact with proteins and the strength of such interaction. In some cases, proteins retain their structure and functionality, and even also have synergistic or cooperative effects. However, other situations may lead to perturbation of the protein structure with harmful consequences such as the loss of its functionality, or the exposure of non-native cryptic epitopes that may trigger all sorts of biological responses as well as induce protein aggregation processes (e.g. fibrillation or prion formation). [171] However, biomolecules may also promote NP aggregation. This phenomenon is mediated by protein-protein interaction, which may occur at a high protein concentration on the NP surface. In some cases, protein molecules form bridges between NPs, mainly due to structural perturbations in protein molecules but they also may occur without structural perturbation and may be

entirely determined by electrostatic interaction between protein molecules. [172,173] In light of these considerations, understanding the mechanisms and factors of NP-protein interactions is necessary for prospective diagnostic and therapeutic applications of NPs. Various techniques should be used to accurately and carefully modify NP properties, which is crucial in terms of the structures and functions of the adsorbed proteins and, hence, the NP toxicity mediated by the alterations of these proteins. [174–177]

1.4 Health Impact and Regulation

The fact that inorganic NPs are similar in size to biological matter, allows them to specifically interact with molecular and cellular structures, and to manipulate biological states, structures and functions in a radically new way, which makes them extremely attractive for biomedical applications. [49,178–181] As discussed in the previous sections, nanoscale agents have been under intense research and exploited to enhance the delivery of drugs in the treatment of several diseases showing potential benefits in terms of pharmaceutical flexibility, selectivity, dose reduction, and minimization of adverse effects. At the same time, and for the same reasons, NPs can, either intentionally or unintentionally, enter the body and/or the environment. Consequently, concerns have been risen regarding NP potential human and environmental hazards. Thus, the same properties that offer great promise to provide scientific and technological breakthroughs may also lead to unexpected biological effects not anticipated from materials of the same composition in the bulk form. [31] Further, the subtle alteration of the NP state after their exposure to biological fluids may have critical consequences on NP behaviour and performance not anticipated if the nanomaterial has not been properly characterized. [168,182] Therefore, in recent years, it has become evident that it is necessary to systematically and accurately define particle characteristics not only in order to understand their potential effects on biological systems but also to ensure that results are reproducible.

Despite the tremendous potential of nanomedicine and hundreds of millions (if not billions) poured from funding institutions, it could be acknowledged that little progress has been made towards matching expectations. Only 50 nano-formulations have reached the market, and only a few encapsulation systems have been approved by regulatory agencies for therapeutic use. [70] These difficulties at any developmental stage are mainly owed to the lack of a clear and absolute international regulatory definition of these materials, their

toxicity levels, and how they should be approached and explored, which delays their clinical translation. Hence, many nano-formulations fail to achieve success in preclinical trials, and as a consequence, there are only a few trials in clinical research, mostly facing numerous regulatory challenges. This uncertainty, created by the lack of consistency across the board, can ultimately hurt funding, research, and development, thus destroying public acceptance and perception of nano-based products. [183]

Nanomaterials and nanotechnology are areas of innovation that have developed faster than regulatory frameworks. [184] Nano-based systems are still currently regulated by existing regulatory frameworks for drugs and medical devices, but there is no specific regulatory structure for them. [185] Global regulatory trends for nanomedicines lack essential data on the manufacturing process, pharmacokinetics, pharmacodynamics, and immunotoxicity that demonstrates the product's safety. [186] This lack of regulatory harmonization specific to NPs has delayed their clinical use, [30,31] despite the fact that NPs properties are transforming the medical research. [183,187]

Efforts to overcome the challenges in the development of nanomedicines have led academia, industry, and regulatory agencies to maintain an open dialogue through forums, seminars, and talks. [188] In 2010, the first international scientific workshop on nanomedicines was held, with the participation of 27 countries. [189] Since then, the symposia have continued to review existing and emerging nanomedicines, analysing aspects such as characterization, biodistribution, and interaction with biological systems to prepare for evaluating these products in the future and identifying development parameters with gaps in knowledge. [190] To date, regulatory agencies recommend a case-by-case analysis, introducing specific trial modifications for each, however, using the same regulatory process as applied for conventional drugs. [191] In 2017, the FDA provided a guidance document, not legally binding, for the nanotechnology-based products for industry. [192] They propose a list of risk factors to address for the safety assessment of a nanomaterial:

- Adequacy of characterization of the material structure and its function. Complexity of the material structure.
- Understanding of the mechanism by which the physicochemical properties of the material impact its biological effects (e.g., effect of particle size on pharmacokinetic parameters).

- Understanding the *in vivo* release mechanism based on the material physicochemical properties.
- Predictability of *in vivo* release based upon established *in vitro* release methods.
- Physical and chemical stability.
- Maturity of the nanotechnology (including manufacturing and analytical methods).
- Potential impact of manufacturing changes, including in-process controls and the robustness of the control strategy on critical quality attributes of the drug product.
- Physical state of the material upon administration. Route of administration.
- Dissolution, bioavailability, distribution, biodegradation, accumulation and their predictability based on physicochemical parameters and animal studies.

It is worth noting that, all along this guidance, an evident emphasis on the adequate and extensive characterization of the nanomaterial on all stages is essential, as well as the understanding of a nanomaterial's intended use and application. This puts in the open that given the natural instability of colloidal and biological systems, it is needed to develop “good practices” in the characterization of such materials where multiple aspects of the sample are analysed as a function of time. Unlike the development of other therapeutic products, the evaluation of the toxicity potential of NPs in biological systems begins with the complete physicochemical characterization, which contributes to the principles of quality, safety, and efficacy. [192,193] To make a product effective in the clinical setting, it is necessary to employ appropriate characterization techniques that efficiently correlate effect with biological consequences, and may predict toxicological or therapeutic outcomes at the early stage of product development. [194]

Therefore, the following aspects of nano-pharmacokinetics (ADME studies but adapted to NP characteristics): what does the body do to the NP rather than what does the NP do to the body, and the consequences that this entails for the body and the NP are a key enabling-knowledge. It is accepted that NPs may suffer transformations when travelling through different parts of the body, which completely change their biological identity and behaviour. Thus, the understanding of the precise evolution of NPs inside the human body (or biological systems) is a pressing need *sine qua non* to develop nanomedicine. Otherwise, we may face another decade where promising results with NPs are observed in the lab but never translated into the clinic to improve patient quality and expectation of life. [70]

1.5 References

- [1] Casals, E., Gonzalez, E., & Puentes, V. F. Reactivity of inorganic nanoparticles in biological environments: insights into nanotoxicity mechanisms. *Journal of Physics D: Applied Physics* 45, 443001 (2012)
- [2] Casals, E., Vázquez-Campos, S., Bastús, N. G., & Puentes, V. Distribution and potential toxicity of engineered inorganic nanoparticles and carbon nanostructures in biological systems. *TrAC - Trends in Analytical Chemistry* 27, 672–683 (2008)
- [3] Weiss, J., Takhistov, P., & McClements, D. J. Functional Materials in Food Nanotechnology. *Journal of Food Science* 71, R107–R116 (2006)
- [4] Dong, H., Wen, B., & Melnik, R. Relative importance of grain boundaries and size effects in thermal conductivity of nanocrystalline materials. *Scientific Reports* 4, 7037 (2014)
- [5] Ma, E. Nanocrystalline materials: Controlling plastic instability. *Nature Materials* vol. 2 7–8 (2003)
- [6] Todescato, F., Fortunati, I., Minotto, A., Signorini, R., Jasieniak, J., & Bozio, R. Engineering of Semiconductor Nanocrystals for Light Emitting Applications. *Materials* 9, 672 (2016)
- [7] Dominika Dybowska, A., Luciene Maltoni, K., Piella, J., Najorka, J., Puentes, V., & Valsami-Jones, E. *Naturally occurring clay nanoparticles in Latosols of Brazil central region: detection and characterization. Geophysical Research Abstracts* vol. 17 (2015)
- [8] Akaighe, N., MacCuspie, R. I., Navarro, D. A., Aga, D. S., Banerjee, S., Sohn, M., & Sharma, V. K. Humic acid-induced silver nanoparticle formation under environmentally relevant conditions. *Environmental Science and Technology* 45, 3895–3901 (2011)
- [9] Heiligt, F. J. & Niederberger, M. The fascinating world of nanoparticle research. *Materials Today* vol. 16 262–271 (2013)
- [10] Park, J., Joo, J., Soon, G. K., Jang, Y., & Hyeon, T. Synthesis of monodisperse spherical nanocrystals. *Angewandte Chemie - International Edition* vol. 46 4630–4660 (2007)
- [11] X. The Bakerian Lecture. —Experimental relations of gold (and other metals) to light. *Philosophical Transactions of the Royal Society of London* 147, 145–181 (1857)
- [12] Lamer, V. K. & Dinegar, R. H. Theory, Production and Mechanism of Formation of Monodispersed Hydrosols. *Journal of the American Chemical Society* 72, 4847–4854 (1950)
- [13] Turkevich, J., Garton, G., & Stevenson, P. C. The color of colloidal gold. *Journal of Colloid Science* 9, 26–35 (1954)
- [14] Turkevich, J., Stevenson, P. C., & Hillier, J. The formation of colloidal gold. *Journal of Physical Chemistry* 57, 670–673 (1953)

- [15] Turkevich, J., Stevenson, P. C., & Hillier, J. A study of the nucleation and growth processes in the synthesis of colloidal gold. *Discussions of the Faraday Society* vol. 11 55–75 (1951)
- [16] Frens, G. Controlled Nucleation for the Regulation of the Particle Size in Monodisperse Gold Suspensions. *Nature Physical Science* 241, 20–22 (1973)
- [17] Piella, J., Bastús, N. G., & Puentes, V. Size-Controlled Synthesis of Sub-10-nanometer Citrate-Stabilized Gold Nanoparticles and Related Optical Properties. *Chemistry of Materials* 28, 1066–1075 (2016)
- [18] Bastús, N. G., Comenge, J., & Puentes, V. Kinetically controlled seeded growth synthesis of citrate-stabilized gold nanoparticles of up to 200 nm: Size focusing versus ostwald ripening. *Langmuir* 27, 11098–11105 (2011)
- [19] Bastús, N. G., Merkoçi, F., Piella, J., & Puentes, V. Synthesis of Highly Monodisperse Citrate-Stabilized Silver Nanoparticles of up to 200 nm: Kinetic Control and Catalytic Properties. *Chemistry of Materials* 26, 2836–2846 (2014)
- [20] Puentes, V. F., Krishnan, K. M., & Alivisatos, A. P. Colloidal Nanocrystal Shape and Size Control: The Case of Cobalt. *Science* 291, 2115–2117 (2001)
- [21] Peng, X., Manna, L., Yang, W., Wickham, J., Scher, E., Kadavanich, A., & Alivisatos, A. P. Shape control of CdSe nanocrystals. *Nature* 404, 59–61 (2000)
- [22] Brust, M., Walker, M., Bethell, D., Schiffrin, D. J., & Whyman, R. Synthesis of thiol-derivatised gold nanoparticles in a two-phase liquid-liquid system. *Journal of the Chemical Society, Chemical Communications* 801–802 (1994)
- [23] Ahmadi, T. S., Wang, Z. L., Green, T. C., Henglein, A., & El-Sayed, M. A. Shape-Controlled Synthesis of Colloidal Platinum Nanoparticles. *Science* 272, 1924–1926 (1996)
- [24] Murray, C. B., Norris, D. J., & Bawendi, M. G. Synthesis and Characterization of Nearly Monodisperse CdE (E = S, Se, Te) Semiconductor Nanocrystallites. *Journal of the American Chemical Society* 115, 8706–8715 (1993)
- [25] Jana, N. R., Gearheart, L., & Murphy, C. J. Seeding growth for size control of 5–40 nm diameter gold nanoparticles. *Langmuir* 17, 6782–6786 (2001)
- [26] Rodríguez-Fernández, J., Pérez-Juste, J., García De Abajo, F. J., & Liz-Marzán, L. M. Seeded growth of submicron Au colloids with quadrupole plasmon resonance modes. *Langmuir* 22, 7007–7010 (2006)
- [27] Leonov, A. P., Zheng, J., Clogston, J. D., Stern, S. T., Patri, A. K., & Wei, A. Detoxification of gold nanorods by treatment with polystyrenesulfonate. *ACS Nano* 2, 2481–2488 (2008)
- [28] Bastús, N. G., Sánchez-Tilló, E., Pujals, S., Farrera, C., López, C., Giralt, E., Celada, A., Lloberas, J., & Puentes, V. Homogeneous conjugation of peptides onto gold nanoparticles enhances macrophage response. *ACS Nano* 3, 1335–1344 (2009)
- [29] Pujals, S., Bastús, N. G., Pereiro, E., López-Iglesias, C., Puentes, V. F., Kogan, M. J., & Giralt, E. Shuttling Gold Nanoparticles into Tumoral Cells with an Amphipathic Proline-Rich Peptide. *ChemBioChem* 10, 1025–1031 (2009)
- [30] Sperling, R. A., Gil, P. R., Zhang, F., Zanella, M., & Parak, W. J. Biological

- applications of gold nanoparticles. *Chemical Society Reviews* 37, 1896–1908 (2008)
- [31] Barbero, F., Russo, L., Vitali, M., Piella, J., Salvo, I., Borrajo, M. L., Busquets-Fité, M., Grandori, R., Bastús, N. G., Casals, E., & Puentes, V. Formation of the Protein Corona: The Interface between Nanoparticles and the Immune System. *Seminars in Immunology* vol. 34 52–60 (2017)
- [32] Comenge, J., Sotelo, C., Romero, F., Gallego, O., Barnadas, A., Parada, T. G. C., Domínguez, F., & Puentes, V. F. Detoxifying antitumoral drugs via nanoconjugation: the case of gold nanoparticles and cisplatin. *PloS one* 7, (2012)
- [33] Oberdörster, G., Oberdörster, E., & Oberdörster, J. Nanotoxicology: An emerging discipline evolving from studies of ultrafine particles. *Environmental Health Perspectives* vol. 113 823–839 (2005)
- [34] Talmadge, J. E., Singh, R. K., Fidler, I. J., & Raz, A. Murine models to evaluate novel and conventional therapeutic strategies for cancer. *American Journal of Pathology* vol. 170 793–804 (2007)
- [35] Bastús, N. G., Piella, J., & Puentes, V. Quantifying the Sensitivity of Multipolar (Dipolar, Quadrupolar, and Octapolar) Surface Plasmon Resonances in Silver Nanoparticles: The Effect of Size, Composition, and Surface Coating. *Langmuir* 32, 290–300 (2016)
- [36] Wang, H., Brandl, D. W., Nordlander, P., & Halas, N. J. Plasmonic Nanostructures: Artificial Molecules. *Accounts of Chemical Research* 40, 53–62 (2006)
- [37] Jain, P. K., Lee, K. S., El-Sayed, I. H., & El-Sayed, M. A. Calculated absorption and scattering properties of gold nanoparticles of different size, shape, and composition: Applications in biological imaging and biomedicine. *Journal of Physical Chemistry B* 110, 7238–7248 (2006)
- [38] Englebienne, P., Van Hoonacker, A., & Verhas, M. Surface plasmon resonance: Principles, methods and applications in biomedical sciences. *Spectroscopy* 17, 255–273 (2003)
- [39] Sun, Y. & Xia, Y. Gold and silver nanoparticles: A class of chromophores with colors tunable in the range from 400 to 750 nm. *Analyst* 128, 686–691 (2003)
- [40] Mie, G. Beiträge zur Optik trüber Medien, speziell kolloidaler Metallösungen. *Annalen der Physik* 330, 377–445 (1908)
- [41] Bohren, C. F. & Huffman, D. R. *Absorption and Scattering of Light by Small Particles*. *Absorption and Scattering of Light by Small Particles* (Wiley, 1998).
- [42] Piella, J., Bastús, N. G., & Puentes, V. Modeling the Optical Responses of Noble Metal Nanoparticles Subjected to Physicochemical Transformations in Physiological Environments: Aggregation, Dissolution and Oxidation. *Zeitschrift für Physikalische Chemie* 231, 33–50 (2017)
- [43] Farooq, S., Araujo, R. E. de, Farooq, S., & Araujo, R. E. de. Engineering a Localized Surface Plasmon Resonance Platform for Molecular Biosensing. *Open Journal of Applied Sciences* 8, 126–139 (2018)
- [44] Tejerina, B., Takeshita, T., Ausman, L., & Schatz, G. C. Nanosphere Optics Lab Field Simulator. (2007)

- [45] Juluri, B. K., Huang, J., & Jensen, L. Extinction, Scattering and Absorption efficiencies of single and multilayer nanoparticles. (2010)
- [46] Link, S. & El-Sayed, M. A. Spectral Properties and Relaxation Dynamics of Surface Plasmon Electronic Oscillations in Gold and Silver Nanodots and Nanorods. *Journal of Physical Chemistry B* 103, 8410–8426 (1999)
- [47] Kreibig, U. & Genzel, L. Optical absorption of small metallic particles. *Surface Science* 156, 678–700 (1985)
- [48] Link, S. & El-Sayed, M. A. Shape and size dependence of radiative, non-radiative and photothermal properties of gold nanocrystals. *International Reviews in Physical Chemistry* vol. 19 409–453 (2000)
- [49] Jans, H. & Huo, Q. Gold nanoparticle-enabled biological and chemical detection and analysis. *Chemical Society Reviews* 41, 2849–2866 (2012)
- [50] Lu, X., Rycenga, M., Skrabalak, S. E., Wiley, B., & Xia, Y. Chemical synthesis of novel plasmonic nanoparticles. *Annual Review of Physical Chemistry* vol. 60 167–192 (2009)
- [51] Jain, P. K., Huang, X., El-Sayed, I. H., & El-Sayed, M. A. Noble metals on the nanoscale: Optical and photothermal properties and some applications in imaging, sensing, biology, and medicine. *Accounts of Chemical Research* 41, 1578–1586 (2008)
- [52] Wiley, B., Sun, Y., Mayers, B., & Xia, Y. Shape-Controlled Synthesis of Metal Nanostructures: The Case of Silver. *Chemistry – A European Journal* 11, 454–463 (2005)
- [53] Chanana, M. & Liz-Marzán, L. M. Coating matters: The influence of coating materials on the optical properties of gold nanoparticles. *Nanophotonics* 1, 199–220 (2012)
- [54] Editors, G., Hartland, G. V, Wu, X., Sun, Y., Pelton, M., Wang, H., Zou, S., Chem Phys, P., Imura, K., Chae Kim, Y., Kim, S., Hong Jeong, D., Okamoto, H., Crut, A., Maioli, P., Del Fatti, N., Staleva, H., Skrabalak, S. E., Carey, C. R., Kosel, T., Xia, Y., Hartland, G. V, Kealley, C. S., Cortie, M. B., Maarroof, A. I., Xu, X., Rycenga, M., Hou, K. K., Cobley, C. M., Schwartz, A. G., C Camargo, P. H., Rodríguez-Fernández, J., Funston, A. M., Pérez-Juste, J., Álvarez-Puebla, R. A., Liz-Marzán, L. M., Mulvaney, P., Zijlstra, P., M Chon, J. W., Gu, M., & Chem, P. The effect of surface roughness on the plasmonic response of individual sub-micron gold spheres. *Physical Chemistry Chemical Physics* 11, 5909–5914 (2009)
- [55] Kreibig, U. & Vollmer, M. Optical Properties of Metal Clusters. 25, (1995)
- [56] Evanoff, D. D. & Chumanov, G. Synthesis and Optical Properties of Silver Nanoparticles and Arrays. *ChemPhysChem* 6, 1221–1231 (2005)
- [57] Nowack, B., Krug, H. F., & Height, M. 120 years of nanosilver history: Implications for policy makers. *Environmental Science and Technology* 45, 1177–1183 (2011)
- [58] Garside, J. & Jančić, S. J. Growth and dissolution of potash alum crystals in the subsieve size range. *AIChE Journal* 22, 887–894 (1976)
- [59] Beck, G. R., Ha, S. W., Camalier, C. E., Yamaguchi, M., Li, Y., Lee, J. K., &

- Weitzmann, M. N. Bioactive silica-based nanoparticles stimulate bone-forming osteoblasts, suppress bone-resorbing osteoclasts, and enhance bone mineral density in vivo. *Nanomedicine : nanotechnology, biology, and medicine* 8, 793–803 (2012)
- [60] Price, C. T., Koval, K. J., & Langford, J. R. Silicon: A review of its potential role in the prevention and treatment of postmenopausal osteoporosis. *International Journal of Endocrinology* 2013, (2013)
- [61] GRAS Notice (GRN) No. 996 y Re: GRAS Notice for Synthetic Amorphous Silica as a Carrier in White Sugar.
- [62] Reimer, P. & Balzer, T. Ferucarbotran (Resovist): a new clinically approved RES-specific contrast agent for contrast-enhanced MRI of the liver: properties, clinical development, and applications. *European Radiology* 13, 1266–1276 (2003)
- [63] Maier-Hauff, K., Ulrich, F., Nestler, D., Niehoff, H., Wust, P., Thiesen, B., Orawa, H., Budach, V., & Jordan, A. Efficacy and safety of intratumoral thermotherapy using magnetic iron-oxide nanoparticles combined with external beam radiotherapy on patients with recurrent glioblastoma multiforme. *Journal of Neuro-Oncology* 103, 317 (2011)
- [64] Schwenk, M. H. Ferumoxytol: a new intravenous iron preparation for the treatment of iron deficiency anemia in patients with chronic kidney disease. *Pharmacotherapy* 30, 70–79 (2010)
- [65] Science, N. & Council, T. 2016 National Nanotechnology Initiative Strategic Plan.
- [66] Trio wins Nobel chemistry prize for ‘world’s smallest machines’ | Reuters. <https://www.reuters.com/article/us-nobel-prize-chemistry/trio-wins-nobel-chemistry-prize-for-worlds-smallest-machines-idUSKCN1250WA>
- [67] Xia, Y., Li, W., Cobley, C. M., Chen, J., Xia, X., Zhang, Q., Yang, M., Cho, E. C., & Brown, P. K. Gold nanocages: from synthesis to theranostic applications. *Accounts of chemical research* 44, 914–924 (2011)
- [68] Victor & Comenge, J. The Role of PEG Conformation in Mixed Layers: From Protein Corona Substrate to Steric Stabilization Avoiding Protein Adsorption. *ScienceOpen Research* (2015)
- [69] Mi, Y., Guo, Y., & Feng, S. S. Nanomedicine for multimodality treatment of cancer. *Nanomedicine* 7, 1791–1794 (2012)
- [70] Casals, E., Gusta, M. F., Cobaleda-Siles, M., Garcia-Sanz, A., & Puentes, V. F. Cancer resistance to treatment and antiresistance tools offered by multimodal multifunctional nanoparticles. *Cancer Nanotechnology* 8, 7 (2017)
- [71] Pelaz, B., Alexiou, C., Alvarez-Puebla, R. A., Alves, F., Andrews, A. M., Ashraf, S., Balogh, L. P., Parak, W. J., *et al.* Diverse Applications of Nanomedicine. *ACS Nano* 11, 2313–2381 (2017)
- [72] Vargason, A. M., Anselmo, A. C., & Mitragotri, S. The evolution of commercial drug delivery technologies. *Nature Biomedical Engineering* 5, 951–967 (2021)
- [73] García-Fernández, L., Garcia-Pardo, J., Tort, O., Prior, I., Brust, M., Casals, E., Lorenzo, J., & Puentes, V. F. Conserved effects and altered trafficking of Cetuximab antibodies conjugated to gold nanoparticles with precise control of their number and

- orientation. *Nanoscale* 9, 6111–6121 (2017)
- [74] Meng, H., Liong, M., Xia, T., Li, Z., Ji, Z., Zink, J. I., & Nel, A. E. Engineered design of mesoporous silica nanoparticles to deliver doxorubicin and p-glycoprotein siRNA to overcome drug resistance in a cancer cell line. *ACS Nano* 4, 4539–4550 (2010)
- [75] MacDiarmid, J. A., Amaro-Mugridge, N. B., Madrid-Weiss, J., Sedliarou, I., Wetzel, S., Kochar, K., Brahmbhatt, V. N., Phillips, L., Pattison, S. T., Petti, C., Stillman, B., Graham, R. M., & Brahmbhatt, H. Sequential treatment of drug-resistant tumors with targeted minicells containing siRNA or a cytotoxic drug. *Nature Biotechnology* 27, 643–651 (2009)
- [76] Fan, Y. & Moon, J. J. Nanoparticle Drug Delivery Systems Designed to Improve Cancer Vaccines and Immunotherapy. *Vaccines* 2015, 3, 662–685 (2015)
- [77] Morgan, R. A., Dudley, M. E., Wunderlich, J. R., Hughes, M. S., Yang, J. C., Sherry, R. M., Royal, R. E., Topalian, S. L., Kammula, U. S., Restifo, N. P., Zheng, Z., Nahvi, A., De Vries, C. R., Rogers-Freezer, L. J., Mavroukakis, S. A., & Rosenberg, S. A. Cancer regression in patients after transfer of genetically engineered lymphocytes. *Science* 314, 126–129 (2006)
- [78] Reddy, S. T., Swartz, M. A., & Hubbell, J. A. Targeting dendritic cells with biomaterials: developing the next generation of vaccines. *Trends in Immunology* 27, 573–579 (2006)
- [79] Järvinen, R., Kaasinen, E., Sankila, A., & Rintala, E. Long-term Efficacy of Maintenance Bacillus Calmette-Guérin versus Maintenance Mitomycin C Instillation Therapy in Frequently Recurrent TaT1 Tumours without Carcinoma In Situ: A Subgroup Analysis of the Prospective, Randomised FinnBladder I Study with a 20-Year Follow-up. *European Urology* 56, 260–265 (2009)
- [80] Bachmann, M. F., Rohrer, U. H., Kündig, T. M., Bürki, K., Hengartner, H., & Zinkernagel, R. M. The Influence of Antigen Organization on B Cell Responsiveness. *Science* 262, 1448–1451 (1993)
- [81] Karapetis, C. S., Khambata-Ford, S., Jonker, D. J., O’Callaghan, C. J., Tu, D., Tebbutt, N. C., Simes, R. J., Chalchal, H., Shapiro, J. D., Robitaille, S., Price, T. J., Shepherd, L., Au, H.-J., Langer, C., Moore, M. J., & Zalcberg, J. R. K-ras Mutations and Benefit from Cetuximab in Advanced Colorectal Cancer. *New England Journal of Medicine* 359, 1757–1765 (2008)
- [82] Bhattacharyya, S., Bhattacharya, R., Curley, S., McNiven, M. A., & Mukherjee, P. Nanoconjugation modulates the trafficking and mechanism of antibody induced receptor endocytosis. *Proceedings of the National Academy of Sciences of the United States of America* 107, 14541–14546 (2010)
- [83] Prego, C., Paolicelli, P., Díaz, B., Vicente, S., Sánchez, A., González-Fernández, Á., & Alonso, M. J. Chitosan-based nanoparticles for improving immunization against hepatitis B infection. *Vaccine* 28, 2607–2614 (2010)
- [84] Comenge, J., Sotelo, C., Romero, F., Gallego, O., Barnadas, A., Parada, T. G.-C., Domínguez, F., & Puentes, V. F. Detoxifying Antitumoral Drugs via Nanoconjugation: The Case of Gold Nanoparticles and Cisplatin. *PLoS ONE* 7, e47562 (2012)

- [85] Li, J. & Loh, X. J. Cyclodextrin-based supramolecular architectures: Syntheses, structures, and applications for drug and gene delivery. *Advanced Drug Delivery Reviews* 60, 1000–1017 (2008)
- [86] Dobson, J. Gene therapy progress and prospects: magnetic nanoparticle-based gene delivery. *Gene Therapy* 13, 283–287 (2006)
- [87] Ghosh, P., Han, G., De, M., Kim, C. K., & Rotello, V. M. Gold nanoparticles in delivery applications. *Advanced Drug Delivery Reviews* 60, 1307–1315 (2008)
- [88] Loh, X. J., Lee, T. C., Dou, Q., & Deen, G. R. Utilising inorganic nanocarriers for gene delivery. *Biomaterials Science* 4, 70–86 (2015)
- [89] Rosi, N. L., Giljohann, D. A., Thaxton, C. S., Lytton-Jean, A. K. R., Han, M. S., & Mirkin, C. A. Oligonucleotide-Modified Gold Nanoparticles for Intracellular Gene Regulation. *Science* 312, (2006)
- [90] Guo, X. & Huang, L. Recent advances in nonviral vectors for gene delivery. *Accounts of Chemical Research* 45, 971–979 (2012)
- [91] Yamashita, S., Fukushima, H., Akiyama, Y., Niidome, Y., Mori, T., Katayama, Y., & Niidome, T. Controlled-release system of single-stranded DNA triggered by the photothermal effect of gold nanorods and its in vivo application. *Bioorganic & Medicinal Chemistry* 19, 2130–2135 (2011)
- [92] Heckman, K. L., Decoteau, W., Estevez, A., Reed, K. J., Costanzo, W., Sanford, D., Leiter, J. C., Clauss, J., Knapp, K., Gomez, C., Mullen, P., Rathbun, E., Prime, K., Marini, J., Patchefsky, J., Patchefsky, A. S., Hailstone, R. K., & Erlichman, J. S. Custom cerium oxide nanoparticles protect against a free radical mediated autoimmune degenerative disease in the brain. *ACS Nano* 7, 10582–10596 (2013)
- [93] Hirst, S. M., Karakoti, A. S., Tyler, R. D., Sriranganathan, N., Seal, S., & Reilly, C. M. Anti-inflammatory Properties of Cerium Oxide Nanoparticles. *Small* 5, 2848–2856 (2009)
- [94] Oró, D., Yudina, T., Fernández-Varo, G., Casals, E., Reichenbach, V., Casals, G., De La Presa, B. G., Sandalinas, S., Carvajal, S., Puntès, V., & Jiménez, W. Cerium oxide nanoparticles reduce steatosis, portal hypertension and display anti-inflammatory properties in rats with liver fibrosis. *Journal of Hepatology* 64, 691–698 (2016)
- [95] Liu, P.-F., Lo, C.-W., Chen, C.-H., Hsieh, M.-F., & Huang, C.-M. Use of nanoparticles as therapy for methicillin-resistant *Staphylococcus aureus* infections. *Current drug metabolism* 10, 875–84 (2009)
- [96] Dowding, J. M., Dosani, T., Kumar, A., Seal, S., & Self, W. T. Cerium oxide nanoparticles scavenge nitric oxide radical ($\cdot\text{NO}$). *Chemical Communications* 48, 4896–4898 (2012)
- [97] Estevez, A. Y., Pritchard, S., Harper, K., Aston, J. W., Lynch, A., Lucky, J. J., Ludington, J. S., Chatani, P., Mosenthal, W. P., Leiter, J. C., Andreescu, S., & Erlichman, J. S. Neuroprotective mechanisms of cerium oxide nanoparticles in a mouse hippocampal brain slice model of ischemia. *Free Radical Biology and Medicine* 51, 1155–1163 (2011)
- [98] Selvaraj, V., Nepal, N., Rogers, S., Manne, N. D. P. K., Arvapalli, R., Rice, K. M.,

- Asano, S., Fankhanel, E., Ma, J. J., Shokuhfar, T., Maheshwari, M., & Blough, E. R. Inhibition of MAP kinase/NF- κ B mediated signaling and attenuation of lipopolysaccharide induced severe sepsis by cerium oxide nanoparticles. *Biomaterials* 59, 160–171 (2015)
- [99] Xu, C. & Qu, X. Cerium oxide nanoparticle: a remarkably versatile rare earth nanomaterial for biological applications. *NPG Asia Materials* 6, e90–e90 (2014)
- [100] Niu, J., Azfer, A., Rogers, L. M., Wang, X., & Kolattukudy, P. E. Cardioprotective effects of cerium oxide nanoparticles in a transgenic murine model of cardiomyopathy. *Cardiovascular Research* 73, 549–559 (2007)
- [101] Asati, A., Santra, S., Kaittanis, C., & Perez, J. M. Surface-charge-dependent cell localization and cytotoxicity of cerium oxide nanoparticles. *ACS Nano* 4, 5321–5331 (2010)
- [102] Carvajal, S., Oró, D., Fernández-Varo, G., Yudina, T., Perramón, M., Oller, L., Casals, G., de la Presa, B. G., Puentes, V., & Jiménez, W. Therapeutic effect of cerium oxide nanoparticles (CeO₂NPs) in rats with diet-induced non-alcoholic steatohepatitis. *Journal of Hepatology* 66, S608 (2017)
- [103] Pimblott, S. M. & LaVerne, J. A. Production of low-energy electrons by ionizing radiation. *Radiation Physics and Chemistry* 76, 1244–1247 (2007)
- [104] Sanche, L. Low energy electron-driven damage in biomolecules. *The European Physical Journal D - Atomic, Molecular, Optical and Plasma Physics* 35, 367–390 (2005)
- [105] von Sonntag, C. Free-Radical-Induced DNA Damage and Its Repair. *Free-Radical-Induced DNA Damage and Its Repair* (2006)
- [106] Boudaïffa, B., Cloutier, P., Hunting, D., Huels, M. A., & Sanche, L. Resonant formation of DNA strand breaks by low-energy (3 to 20 eV) electrons. *Science* 287, 1658–1660 (2000)
- [107] Chithrani, D. B., Jelveh, S., Jalali, F., Van Prooijen, M., Allen, C., Bristow, R. G., Hill, R. P., & Jaffray, D. A. Gold nanoparticles as radiation sensitizers in cancer therapy. *Radiation Research* 173, 719–728 (2010)
- [108] Rahman, W. N., Corde, S., Yagi, N., Abdul Aziz, S. A., Annabell, N., & Geso, M. Optimal energy for cell radiosensitivity enhancement by gold nanoparticles using synchrotron-based monoenergetic photon beams. *International Journal of Nanomedicine* 9, 2459–2467 (2014)
- [109] Bobyk, L., Edouard, M., Deman, P., Vautrin, M., Pernet-Gallay, K., Delaroche, J., Adam, J. F., Estève, F., Ravanat, J. L., & Elleaume, H. Photoactivation of gold nanoparticles for glioma treatment. *Nanomedicine: Nanotechnology, Biology and Medicine* 9, 1089–1097 (2013)
- [110] Hainfeld, J. F., Dilmanian, F. A., Slatkin, D. N., & Smilowitz, H. M. Radiotherapy enhancement with gold nanoparticles. *Journal of Pharmacy and Pharmacology* 60, 977–985 (2008)
- [111] Huang, X., El-Sayed, I. H., Wei, Q., & El-Sayed, M. A. Cancer Cell Imaging and Photothermal Therapy in the Near-Infrared Region by Using Gold Nanorods. *Journal*

- of the American Chemical Society 128, 2115–2120 (2006)
- [112] Jana, N. R., Gearheart, L., & Murphy, C. J. Seed-Mediated Growth Approach for Shape-Controlled Synthesis of Spheroidal and Rod-like Gold Nanoparticles Using a Surfactant Template. *Advanced Materials* 13, 1389–1393 (2001)
 - [113] Nikoobakht, B. & El-Sayed, M. A. Preparation and growth mechanism of gold nanorods (NRs) using seed-mediated growth method. *Chemistry of Materials* 15, 1957–1962 (2003)
 - [114] González, E., Arbiol, J., & Puntès, V. F. Carving at the Nanoscale: Sequential Galvanic Exchange and Kirkendall Growth at Room Temperature. *Science* 334, (2011)
 - [115] Giustini, A. J., Petryk, A. A., Cassim, S. M., Tate, J. A., Baker, I., & Hoopes, P. J. Magnetic nanoparticle hyperthermia in cancer treatment. *Nano LIFE* 01, 17–32 (2010)
 - [116] McCarthy, J. R., Kelly, K. A., Sun, E. Y., & Weissleder, R. Targeted delivery of multifunctional magnetic nanoparticles. *Nanomedicine* vol. 2 153–167 (2007)
 - [117] Pankhurst, Q. A., Thanh, N. K. T., Jones, S. K., & Dobson, J. Progress in applications of magnetic nanoparticles in biomedicine. *Journal of Physics D: Applied Physics* 42, 224001 (2009)
 - [118] Pu, P. Y., Zhang, Y. Z., & Jiang, D. H. Apoptosis induced by hyperthermia in human glioblastoma cell line and murine glioblastoma. *Chinese Journal of Cancer Research* 12, 257–262 (2000)
 - [119] Wust, P., Hildebrandt, B., Sreenivasa, G., Rau, B., Gellermann, J., Riess, H., Felix, R., & Schlag, P. Hyperthermia in combined treatment of cancer. *Lancet Oncology* 3, 487–497 (2002)
 - [120] Shinkai, M. Functional magnetic particles for medical application. *Journal of Bioscience and Bioengineering* 94, 606–613 (2002)
 - [121] Jiang, Q. L., Zheng, S. W., Hong, R. Y., Deng, S. M., Guo, L., Hu, R. L., Gao, B., Huang, M., Cheng, L. F., Liu, G. H., & Wang, Y. Q. Folic acid-conjugated Fe₃O₄ magnetic nanoparticles for hyperthermia and MRI in vitro and in vivo. *Applied Surface Science* 307, 224–233 (2014)
 - [122] Yguerabide, J. & Yguerabide, E. E. Light-Scattering Submicroscopic Particles as Highly Fluorescent Analogs and Their Use as Tracer Labels in Clinical and Biological Applications: I. Theory. *Analytical Biochemistry* 262, 137–156 (1998)
 - [123] Ding, Y., Jiang, Z., Saha, K., Kim, C. S., Kim, S. T., Landis, R. F., Rotello, V. M., Irudayaraj, J., *et al.* Gold Nanoparticles for Nucleic Acid Delivery. *Molecular Therapy* 22, 1075–1083 (2014)
 - [124] Halas, N. J., Lal, S., Chang, W. S., Link, S., & Nordlander, P. Plasmons in strongly coupled metallic nanostructures. *Chemical Reviews* 111, 3913–3961 (2011)
 - [125] Sepúlveda, B., Angelomé, P. C., Lechuga, L. M., & Liz-Marzán, L. M. LSPR-based nanobiosensors. *Nano Today* 4, 244–251 (2009)
 - [126] Ghosh, S. K. & Pal, T. Interparticle coupling effect on the surface plasmon resonance of gold nanoparticles: From theory to applications. *Chemical Reviews* 107, 4797–

4862 (2007)

- [127] Lee, T. M. H. Over-the-Counter Biosensors: Past, Present, and Future. *Sensors* 8, 5535–5559 (2008)
- [128] Whitney, A. V., Elam, J. W., Zou, S., Zinovev, A. V., Stair, P. C., Schatz, G. C., & Van Duyne, R. P. Localized surface plasmon resonance nanosensor: A high-resolution distance-dependence study using atomic layer deposition. *Journal of Physical Chemistry B* 109, 20522–20528 (2005)
- [129] Russo, L., Sánchez-Purrà, M., Rodríguez-Quijada, C., Leonardo, B. M., Puentes, V., & Hamad-Schifferli, K. Detection of resistance protein A (MxA) in paper-based immunoassays with surface enhanced Raman spectroscopy with AuAg nanoshells. *Nanoscale* 11, 10819–10827 (2019)
- [130] Russo, L., Puentes, V., & Merkoçi, A. Tunable electrochemistry of gold-silver alloy nanoshells. *Nano Research* 11, 6336–6345 (2018)
- [131] Russo, L., Leva Bueno, J., Bergua, J. F., Costantini, M., Giannetto, M., Puentes, V., De La Escosura-Muñiz, A., & Merkoçi, A. Low-Cost Strategy for the Development of a Rapid Electrochemical Assay for Bacteria Detection Based on AuAg Nanoshells. *ACS Omega* 3, 18849–18856 (2018)
- [132] Ye, J., Bonroy, K., Nelis, D., Frederix, F., D’Haen, J., Maes, G., & Borghs, G. Enhanced localized surface plasmon resonance sensing on three-dimensional gold nanoparticles assemblies. *Colloids and Surfaces A: Physicochemical and Engineering Aspects* 321, 313–317 (2008)
- [133] Verellen, N., Van Dorpe, P., Huang, C., Lodewijks, K., Vandenbosch, G. A. E., Lagae, L., & Moshchalkov, V. V. Plasmon line shaping using nanocrosses for high sensitivity localized surface plasmon resonance sensing. *Nano Letters* 11, 391–397 (2011)
- [134] Wang, Z., Zhao, J., Xu, X., Guo, L., Xu, L., Sun, M., Hu, S., Kuang, H., Xu, C., & Li, A. An Overview for the Nanoparticles-Based Quantitative Lateral Flow Assay. *Small methods* 6, (2022)
- [135] Huang, C., Wen, T., Shi, F. J., Zeng, X. Y., & Jiao, Y. J. Rapid Detection of IgM Antibodies against the SARS-CoV-2 Virus via Colloidal Gold Nanoparticle-Based Lateral-Flow Assay. *ACS Omega* 5, 12550–12556 (2020)
- [136] Nasrollahzadeh, M., Sajadi, S. M., Sajjadi, M., & Issaabadi, Z. An Introduction to Nanotechnology. *Interface Science and Technology* 28, 1–27 (2019)
- [137] Bastus, N. G., Casals, E., Ojea, I., Varon, M., & Puentes, V. The Reactivity of Colloidal Inorganic Nanoparticles. *The Delivery of Nanoparticles* (2012)
- [138] Casals, E., Gonzalez, E., & Puentes, V. F. Reactivity of inorganic nanoparticles in biological environments: Insights into nanotoxicity mechanisms. *Journal of Physics D: Applied Physics* vol. 45 443001 (2012)
- [139] Casals, E., Gusta, M. F., Montana, L., Mendoza, M., Maiz, N., Carreras, E., & Puentes, V. Nanotechnology for Maternal Foetal Medicine. *Int J Ped & Neo Heal* 2, 55–64 (2018)
- [140] Geranio, L., Heuberger, M., & Nowack, B. The behavior of silver nanotextiles during

- washing. *Environmental Science and Technology* 43, 8113–8118 (2009)
- [141] Elzey, S. & Grassian, V. H. Agglomeration, isolation and dissolution of commercially manufactured silver nanoparticles in aqueous environments. *Journal of Nanoparticle Research* 12, 1945–1958 (2009)
- [142] Li, X., Lenhart, J. J., & Walker, H. W. Aggregation kinetics and dissolution of coated silver nanoparticles. *Langmuir* 28, 1095–1104 (2012)
- [143] Li, X., Lenhart, J. J., & Walker, H. W. Dissolution-accompanied aggregation kinetics of silver nanoparticles. *Langmuir* 26, 16690–16698 (2010)
- [144] Liu, J. & Hurt, R. H. Ion release kinetics and particle persistence in aqueous nano-silver colloids. *Environmental Science and Technology* 44, 2169–2175 (2010)
- [145] M. Elimelech, J. Gregory, X. Jia, R. A. W. Particle deposition and aggregation: measurement, modelling and simulation. 441 (1995)
- [146] Hiemenz, P. C. & Rajagopalan, R. Principles of Colloid and Surface Chemistry, Revised and Expanded. (1997)
- [147] Israelachvili, J. Intermolecular and Surface Forces. (2011)
- [148] Casals, E., Pfaller, T., Duschl, A., Oostingh, G. J., & Puentes, V. Time Evolution of the Nanoparticle Protein Corona. *ACS Nano* 4, 3623–3632 (2010)
- [149] Oostingh, G. J., Casals, E., Italiani, P., Colognato, R., Stritzinger, R., Ponti, J., Pfaller, T., Kohl, Y., Ooms, D., Favilli, F., Leppens, H., Lucchesi, D., Rossi, F., Nelissen, I., Thielecke, H., Puentes, V. F., Duschl, A., & Boraschi, D. Problems and challenges in the development and validation of human cell-based assays to determine nanoparticle-induced immunomodulatory effects. *Particle and Fibre Toxicology* 8, 1–21 (2011)
- [150] Jiang, J., Oberdörster, G., & Biswas, P. Characterization of size, surface charge, and agglomeration state of nanoparticle dispersions for toxicological studies. *Journal of Nanoparticle Research* 11, 77–89 (2008)
- [151] Cedervall, T., Lynch, I., Lindman, S., Berggård, T., Thulin, E., Nilsson, H., Dawson, K. A., & Linse, S. Understanding the nanoparticle-protein corona using methods to quantify exchange rates and affinities of proteins for nanoparticles. *Proceedings of the National Academy of Sciences of the United States of America* 104, 2050–2055 (2007)
- [152] Walkey, C. D., Olsen, J. B., Song, F., Liu, R., Guo, H., Olsen, D. W. H., Cohen, Y., Emili, A., & Chan, W. C. W. Protein corona fingerprinting predicts the cellular interaction of gold and silver nanoparticles. *ACS Nano* 8, 2439–2455 (2014)
- [153] Hamad-Schifferli, K. Exploiting the novel properties of protein coronas: Emerging applications in nanomedicine. *Nanomedicine* vol. 10 1663–1674 (2015)
- [154] Casals, E. & Puentes, V. F. Inorganic nanoparticle biomolecular corona: Formation, evolution and biological impact. *Nanomedicine* vol. 7 1917–1930 (2012)
- [155] Mahmoudi, M., Lynch, I., Ejtehadi, M. R., Monopoli, M. P., Bombelli, F. B., & Laurent, S. Protein-nanoparticle interactions: Opportunities and challenges. *Chemical Reviews* 111, 5610–5637 (2011)

- [156] Monopoli, M. P., Aberg, C., Salvati, A., & Dawson, K. A. Biomolecular coronas provide the biological identity of nanosized materials. *Nature nanotechnology* 7, 779–86 (2012)
- [157] Walczyk, D., Bombelli, F. B., Monopoli, M. P., Lynch, I., & Dawson, K. A. What the cell ‘sees’ in bionanoscience. *Journal of the American Chemical Society* 132, 5761–5768 (2010)
- [158] Maiorano, G., Sabella, S., Sorce, B., Brunetti, V., Malvindi, M. A., Cingolani, R., & Pompa, P. P. Effects of cell culture media on the dynamic formation of protein-nanoparticle complexes and influence on the cellular response. *ACS Nano* 4, 7481–7491 (2010)
- [159] Saha, K., Rahimi, M., Yazdani, M., Kim, S. T., Moyano, D. F., Hou, S., Das, R., Mout, R., Rezaee, F., Mahmoudi, M., & Rotello, V. M. Regulation of Macrophage Recognition through the Interplay of Nanoparticle Surface Functionality and Protein Corona. *ACS Nano* 10, 4421–4430 (2016)
- [160] Monopoli, M. P., Walczyk, D., Campbell, A., Elia, G., Lynch, I., Baldelli Bombelli, F., & Dawson, K. A. Physical-Chemical aspects of protein corona: Relevance to in vitro and in vivo biological impacts of nanoparticles. *Journal of the American Chemical Society* 133, 2525–2534 (2011)
- [161] Casals, E., Pfaller, T., Duschl, A., Oostingh, G. J., & Puentes, V. F. Hardening of the Nanoparticle–Protein Corona in Metal (Au, Ag) and Oxide (Fe₃O₄, CoO, and CeO₂) Nanoparticles. *Small* 7, 3479–3486 (2011)
- [162] Tenzer, S., Docter, D., Rosfa, S., Wlodarski, A., Kuharev, J., Rekik, A., Knauer, S. K., Bantz, C., Nawroth, T., Bier, C., Sirirattanapan, J., Mann, W., Treuel, L., Zellner, R., Maskos, M., Schild, H., & Stauber, R. H. Nanoparticle size is a critical physicochemical determinant of the human blood plasma corona: A comprehensive quantitative proteomic analysis. *ACS Nano* 5, 7155–7167 (2011)
- [163] Walkey, C. D., Olsen, J. B., Guo, H., Emili, A., & Chan, W. C. W. Nanoparticle size and surface chemistry determine serum protein adsorption and macrophage uptake. *Journal of the American Chemical Society* 134, 2139–2147 (2012)
- [164] Gessner, A., Waicz, R., Lieske, A., Paulke, B. R., Mäder, K., & Müller, R. H. Nanoparticles with decreasing surface hydrophobicities: influence on plasma protein adsorption. *International Journal of Pharmaceutics* 196, 245–249 (2000)
- [165] Slack, S. M. & Horbett, T. A. The Vroman Effect. 112–128 (1995)
- [166] Piella, J., Bastús, N. G., & Puentes, V. Size-dependent protein-nanoparticle interactions in citrate-stabilized gold nanoparticles: The emergence of the protein corona. *Bioconjugate Chemistry* 28, 88–97 (2017)
- [167] Shemetov, A. A., Nabiev, I., & Sukhanova, A. Molecular interaction of proteins and peptides with nanoparticles. *ACS Nano* 6, 4585–4602 (2012)
- [168] Goy-López, S., Juárez, J., Alatorre-Meda, M., Casals, E., Puentes, V. F., Taboada, P., & Mosquera, V. Physicochemical characteristics of protein-NP bioconjugates: The role of particle curvature and solution conditions on human serum albumin conformation and fibrillogenesis inhibition. *Langmuir* 28, 9113–9126 (2012)

- [169] Prime, K. L. & Whitesides, G. M. Self-Assembled Organic Monolayers: Model Systems for Studying Adsorption of Proteins at Surfaces. *Science* 252, 1164–1167 (1991)
- [170] Wang, D., Nap, R. J., Lagzi, I., Kowalczyk, B., Han, S., Grzybowski, B. A., & Szleifer, I. How and why nanoparticle's curvature regulates the apparent pK_a of the coating ligands. *Journal of the American Chemical Society* 133, 2192–2197 (2011)
- [171] Lynch, I., Dawson, K. A., & Linse, S. Detecting Cryptic Epitopes Created by Nanoparticles. *Science's STKE* 2006, (2006)
- [172] Zhang, D., Neumann, O., Wang, H., Yuwono, V. M., Barhoumi, A., Perham, M., Hartgerink, J. D., Wittung-Stafshede, P., & Halas, N. J. Gold Nanoparticles Can Induce the Formation of Protein-based Aggregates at Physiological pH. *Nano Letters* 9, 666–671 (2009)
- [173] Bharti, B., Meissner, J., & Findenegg, G. H. Aggregation of silica nanoparticles directed by adsorption of lysozyme. *Langmuir* 27, 9823–9833 (2011)
- [174] Bakalova, R., Zhelev, Z., Kokuryo, D., Spasov, L., Aoki, I., & Saga, T. Chemical nature and structure of organic coating of quantum dots is crucial for their application in imaging diagnostics. *International Journal of Nanomedicine* 6, 1719–1732 (2011)
- [175] Dutta, D., Sundaram, S. K., Teeguarden, J. G., Riley, B. J., Fifield, L. S., Jacobs, J. M., Addleman, S. R., Kaysen, G. A., Moudgil, B. M., & Weber, T. J. Adsorbed Proteins Influence the Biological Activity and Molecular Targeting of Nanomaterials. *Toxicological Sciences* 100, 303–315 (2007)
- [176] Shen, X. C., Liou, X. Y., Ye, L. P., Liang, H., & Wang, Z. Y. Spectroscopic studies on the interaction between human hemoglobin and CdS quantum dots. *Journal of Colloid and Interface Science* 311, 400–406 (2007)
- [177] Röcker, C., Pötzl, M., Zhang, F., Parak, W. J., & Nienhaus, G. U. A quantitative fluorescence study of protein monolayer formation on colloidal nanoparticles. *Nature Nanotechnology* 4, 577–580 (2009)
- [178] Moghimi, S. M., Hunter, A. C., & Murray, J. C. Nanomedicine: current status and future prospects. *The FASEB Journal* 19, 311–330 (2005)
- [179] Riehemann, K., Schneider, S. W., Luger, T. A., Godin, B., Ferrari, M., & Fuchs, H. Nanomedicine—Challenge and Perspectives. *Angewandte Chemie International Edition* 48, 872–897 (2009)
- [180] Dreaden, E. C., Alkilany, A. M., Huang, X., Murphy, C. J., & El-Sayed, M. A. The golden age: gold nanoparticles for biomedicine. *Chemical Society Reviews* 41, 2740–2779 (2012)
- [181] Schütz, C. A., Juillerat-Jeanneret, L., Mueller, H., Lynch, I., & Riediker, M. Therapeutic nanoparticles in clinics and under clinical evaluation. *Nanomedicine* vol. 8 449–467 (2013)
- [182] Izak-Nau, E., Voetz, M., Eiden, S., Duschl, A., & Puntès, V. F. Altered characteristics of silica nanoparticles in bovine and human serum: The importance of nanomaterial characterization prior to its toxicological evaluation. *Particle and Fibre Toxicology* 10, 1–12 (2013)

- [183] Padilla, S., Altamirano, L. ;, Toledo, C. ;, Santiago Vispo, J. R. ;, Ramos, T. I., Villacis-Aguirre, C. A., López-Aguilar, K. V, Padilla, L. S., Altamirano, C., Toledo, J. R., Santiago Vispo, N., José, S., & Yachay, P. The Hitchhiker's Guide to Human Therapeutic Nanoparticle Development. *Pharmaceutics* 14, 247 (2022)
- [184] Allan, J., Belz, S., Hoeveler, A., Hugas, M., Okuda, H., Patri, A., Rauscher, H., Silva, P., Slikker, W., Sokull-Kluettgen, B., Tong, W., & Anklam, E. Regulatory landscape of nanotechnology and nanoplastics from a global perspective. *Regulatory Toxicology and Pharmacology* 122, 104885 (2021)
- [185] Accardo, A., Aloj, L., Aurilio, M., Morelli, G., & Tesauro, D. Receptor binding peptides for target-selective delivery of nanoparticles encapsulated drugs. *International Journal of Nanomedicine* 9, 1537–1557 (2014)
- [186] Marques, M. R. C., Choo, Q., Ashtikar, M., Rocha, T. C., Bremer-Hoffmann, S., & Wacker, M. G. Nanomedicines - Tiny particles and big challenges. *Advanced Drug Delivery Reviews* 151–152, 23–43 (2019)
- [187] Kargul, J., Irminger-Finger, I., & Laurent, G. J. Nanomedicine: Application of nanoparticles in clinical therapies and diagnostics. *The International Journal of Biochemistry & Cell Biology* 75, 140 (2016)
- [188] Gioria, S., Caputo, F., Urbán, P., Maguire, C. M., Bremer-Hoffmann, S., Prina-Mello, A., Calzolari, L., & Mehn, D. Are existing standard methods suitable for the evaluation of nanomedicines: Some case studies. *Nanomedicine* 13, 539–554 (2018)
- [189] Human Medicines Development and Evaluation 1 st International Workshop on Nanomedicines 2010 Summary Report. (2010)
- [190] Torqui, A. & Macau, A. M. Regional Differences During the ICH Regulatory Consultation Process Between the EU, US, and Japan. *Therapeutic Innovation & Regulatory Science* 52, 438–441 (2018)
- [191] Paradise, J. Regulating nanomedicine at the food and drug administration. *AMA Journal of Ethics* 21, 347–355 (2019)
- [192] Fda, Cder, Yeaton, & Ayse. *Drug Products, Including Biological Products, that Contain Nanomaterials - Guidance for Industry*. <https://www.fda.gov/Drugs/GuidanceComplianceRegulatoryInformation/Guidances/default.htm>
- [193] de Vlieger, J. S. B., Crommelin, D. J. A., Tyner, K., Drummond, D. C., Jiang, W., McNeil, S. E., Neervannan, S., Crist, R. M., & Shah, V. P. Report of the AAPS Guidance Forum on the FDA Draft Guidance for Industry: “Drug Products, Including Biological Products, that Contain Nanomaterials”. *AAPS Journal* 21, 1–7 (2019)
- [194] Cho, E. J., Holback, H., Liu, K. C., Abouelmagd, S. A., Park, J., & Yeo, Y. Nanoparticle characterization: State of the art, challenges, and emerging technologies. *Molecular Pharmaceutics* 10, 2093–2110 (2013)

CHAPTER 2

CATIONIC GOLD NANOPARTICLES MEDIATED MRNA DELIVERY FOR PRODUCTION OF CAR-T LYMPHOCYTES FOR CHRONIC LYMPHOID LEUKAEMIA IMMUNOTHERAPY

Cationic Gold Nanoparticles Mediated mRNA Delivery for Production of CAR-T lymphocytes for Chronic Lymphoid Leukaemia Immunotherapy

2.1 Introduction

Prognosis is poor for patients with multiply relapsed or refractory Chronic Lymphocytic Leukaemia (CLL). CLL is the most frequent form of leukaemia in Western countries and is characterized by the clonal proliferation and accumulation of neoplastic B lymphocytes in the blood, bone marrow, lymph nodes, and spleen. It shows poor results with current standard treatment but conversely, very promising results with Chimeric Antigen Receptor (CAR) T-cell therapy targeting have been obtained. [1,2] CAR T-cells immunotherapy is based on the ex-vivo genetic engineering of patient T-lymphocytes that express novel receptors which have enhanced tumour specificity. However, the drawbacks and side effects of this promising therapy mostly associated to the use of viral vectors and CAR T-cell persistence – that will be discussed later in more detail – limit its use.

The proposed project combines multidisciplinary approaches aiming at overcoming several limitations regarding the therapy of CLL patients. It aims to provide an efficient carrier for mRNA to be used as a safer CAR T therapy. The carriers selected are gold nanoparticles (Au NPs) modified with cationic polymers. The use of non-biological agents for mRNA delivery into living systems in order to induce heterologous expression of functional

proteins may provide more advantages than the use of DNA and/or biological vectors for delivery, including rational design, easiness of production and safety. The novelty of this approach is a combination of Au NPs and proton sponges to improve the productive transfection of primary T-cells resulting in transient expression of recombinant CD19-specific T-cell receptor (CAR19), which is expressed in (tumoural) B cells.

2.1.1 CAR T-Cell Therapy

The immune system evolved to distinguish non-self from self to protect the organism. As cancer is derived from our own cells, immune responses to dysregulated cell growth present a unique challenge. This is compounded by immune evasion and immunosuppression mechanisms that develop in the tumour microenvironment. The modern genetic toolbox enables the adoptive transfer of engineered T-cells – CAR T-cells immunotherapy – to create enhanced anticancer immune functions where natural cancer-specific immune responses have failed. [3,4]

Unlike classical T-cell receptor-antigen recognition pathway, CARs enable highly specific targeting of surface antigens in a major histocompatibility complex (MHC)-independent manner, so it allows for their targeting against any cell surface receptor. CARs are formed by combining an extracellular antigen-recognition domains and intracellular T-cell receptor (TCR) signalling domains. The antigen-recognition domain most-commonly consists of a single-chain variable fragment (scFv) derived from a B-cell receptor (BCR), which is anchored to the cell with a hinge and/or transmembrane domain, and binds to the target antigen. The intracellular portion consists of signalling domains necessary for the activation of T-cells. It contains a TCR-derived CD3 ζ domain and, one or more intracellular co-stimulatory domains (**Figure 2.1**). [5]

The manufacturing process of CAR T-cells starts with the isolation of the patient's own T-cells (or those from an allogeneic donor) from blood, a procedure named leukapheresis. Then, T-cells are transduced with the CAR gene construct to be expressed, followed by a T-cell activation and clonal expansion. Finally, the engineered T-cells are intravenously infused into the patient where they recognize and destroy target cells. This approach carries a very low risk of graft-versus-host disease and also enables lipid, protein and carbohydrate antigens to be targeted by T-cells in an MHC-unrestricted fashion. Additionally, one CAR design can be used to treat all cancers expressing the same antigen. In addition, current

advances in *ex vivo* cell expansion enable the production of clinically relevant doses of these therapeutic cells. [6,7]

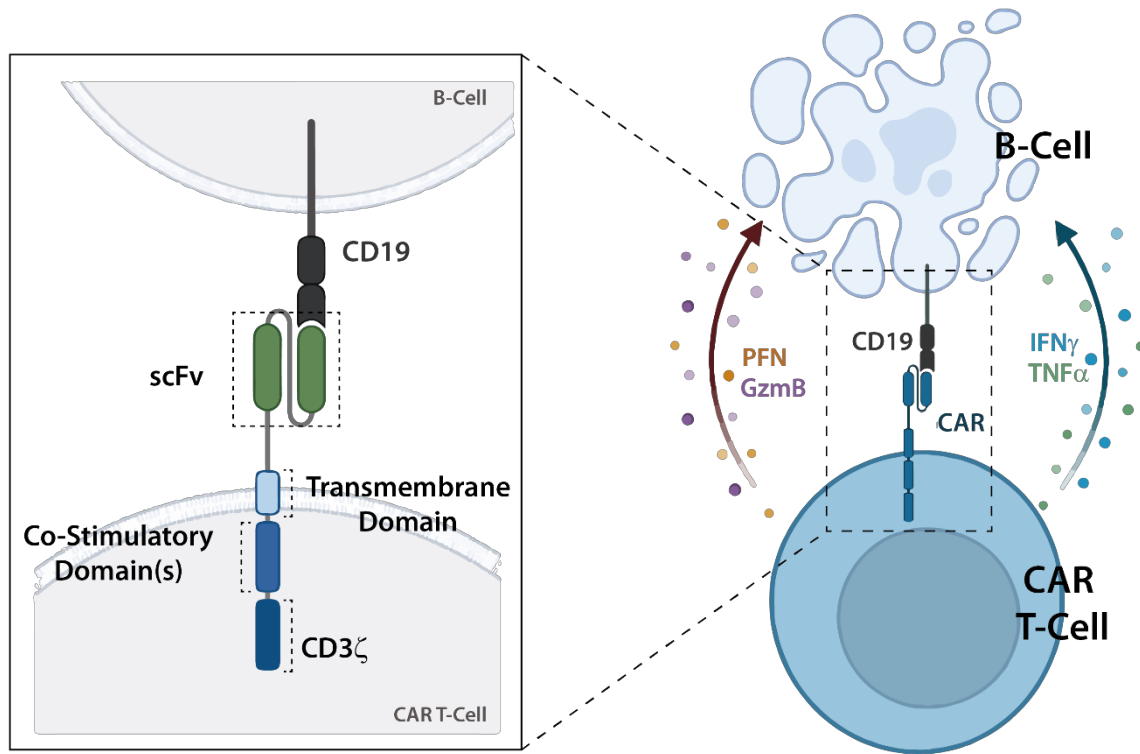


Figure 2.1. CAR T-Cell mechanism and CAR structure (inset). Upon target antigen recognition (CD19), co-stimulatory and intracellular signalling domains of the CAR trigger the activation triggering the T-cell cytolytic mechanism, via the release of perforin (PFN) and granzyme B (GzmB), and the release of interferon- γ (IFN γ) and tumour necrosis factor (TNF- α). On the inset, the structure of the Chimeric Antigen Receptor can be observed.

B-cell malignancies are the most common tumour type to be targeted by engineered T-cells. They are relatively common and express several conserved cell surface markers. Also, circulating B-cell malignancies provide easy access for intravenously infused engineered T-cells, reducing the requirement for therapeutic cells to traffic to the site of a solid tumour. The extracellular glycoprotein CD19 is the most common B-cell target for engineered T-cell therapies. CD19 is expressed on both benign and most malignant B-cells, with minimal non-B-cell expression. In this regard, immunotherapy has provided some of the most spectacular advances in recent years in the treatment of patients with relapsed or refractory haematological malignancies. CD19-directed CAR T-cell therapies (CAR19) have turned around the situation showing impressive results on previously heavily treated refractory patients. Several clinical trials are currently on-going worldwide using CAR19 for the treatment of CLL. [5]

2.1.2 The unmet medical need

CAR T-cell therapy is not free of concerns. Even though they have shown very positive promising results, severe toxicities have been reported and can be life-threatening. The most common severe toxicity is a systemic inflammatory response termed cytokine release syndrome (CRS), characterized by the acute release of inflammatory cytokines from the CAR T-cells and other immune cells. CAR T-cells can also cause neurologic toxicity, a heterogeneous and poorly understood disorder with variable clinical presentation and severity. [8,9] Toxicities secondary to the interaction of CAR T-cells with non-tumour/normal cells expressing the target antigen are termed ‘on-target/off-tumour’ toxicities.

Besides, B-cell aplasia resulting in hypogammaglobulinemia is a side effect of CAR19. Hypogammaglobulinemia should be managed with intravenous immunoglobulin (IVIG) replacement therapy to avoid opportunistic infections. [10] Several approaches have been proposed to overcome this, such as removing CAR T-cells with specific antibodies or selectively eliminating CAR T-cells with suicidal genes.

On the other hand, the production of CAR T-cells for immunotherapy is mainly based on overexpressing the chimeric receptor by using viral vectors. The most common vectors used in CAR T-cell manufacturing are replication-defective vector systems based on two types of retroviruses: γ -retroviruses and lentiviruses. Both γ -retroviruses and lentiviruses deliver RNA, that is reverse-transcribed into DNA in the target cell and integrates into the host genome. [6] These vectors have been engineered to drastically reduce the transcriptional activity of the virus, virtually eliminating the possibility of viral reactivation. However, uncontrolled integration into the genome can potentially lead to insertional mutagenesis, if the integration of vector DNA into host cells is placed near an oncogene.

The use of non-viral vectors is an alternative to overcome these limitations. They allow for a transient expression of the CAR on T-cells, that eventually disappear and so their side-effects. In this regard, the use of mRNA is widely increasing for gene therapy, as well as its use for novel non-viral vaccines. [11–14] The introduction of mRNA into the cells for protein overexpression is an alternative to viral vectors that includes several advantages: no threat of mutagenic insertion, no threat of viral particle reactivation, accessible to dose control, and synthetic animal product-free production, which altogether makes it an attractive approach for clinical use. [15,16] Indeed, the production of CAR T-cell by mRNA electroporation and polymeric vectors has already been reported. Researchers at the

University of Pennsylvania evaluated the mesothelin (MSLN)-specific mRNA CAR-T cells in patients with MSLN-expressing solid tumours and demonstrated the feasibility and safety of this novel strategy. Together with the anti-tumour activity observed, this supported the development of the mRNA CAR-based strategies for solid tumours. [17,18] It is worth noting that multiple infusions may be necessary for mRNA CAR T-cells due to the transient expression of transgene, when the tumour outlast the T cell half-life. [19]

Note that this has an impact on the manufacturing process of CAR T-cells, as displayed in **Figure 2.2A**. Since mRNA is not a self-replicating molecule, the clonal expansion of T-cells must be performed before the transfection step.

2.1.3 The nanotechnology dimension

Genetic material transfer into cells has become a standard procedure in life science research. Various delivery systems for mRNA have been developed and can be classified into two main groups: viral (biological) and non-viral (agent-based) systems. Biological systems utilize mostly viral vectors. Although they exhibit high transduction efficiency, they also trigger immune responses and there's a threat from integration of viral genes into the host genome. Non-viral vectors have gained importance in recent years because of their safety in handling and ease of application compared with viral vectors. In contrast, non-biological systems are, customizable, non-pathogenic and relatively safe, but clinical applications are obstructed by transfection efficiency. [20] Among the non-viral strategies for transfection are: proteamine complexes, polymeric systems, [21] lipid NPs or liposomes and gold NPs. [22] Other strategies not using delivery agents are electroporation and microinjection, but they present high toxicity the former and low efficacy. [23–25]

Current gold standard mRNA transfection mechanisms are based on lipidic-RNA complexes, such as Lipofectamine®, PEI max® or TransIT®. Despite their relative high transfection rate (~50%), they have a high associated toxicity since their cytoplasmic delivery is based on plasma membrane destabilization by its positive charges in order to cross it unspecifically. [27] Also, the expression of the protein encoded in the mRNA transfected is short, with an expression peak at 24-48h that rapidly decreases over time. Nanoparticle-based vectors circumvent these limitations as they enter into the cell via endocytosis uptake. This impacts in minimizing the toxicity since there is no membrane

pore formation, and also allows for a longer protein expression as mRNA is progressively internalized and slowly released into the cytoplasm for its translation.

In this regard, NPs provide an attractive platform for DNA/RNA delivery due to their high surface-to-volume ratio maximizing the payload-to-carrier ratio. Also, the high surface area enables efficient DNA/RNA compaction, an essential parameter for gene delivery.

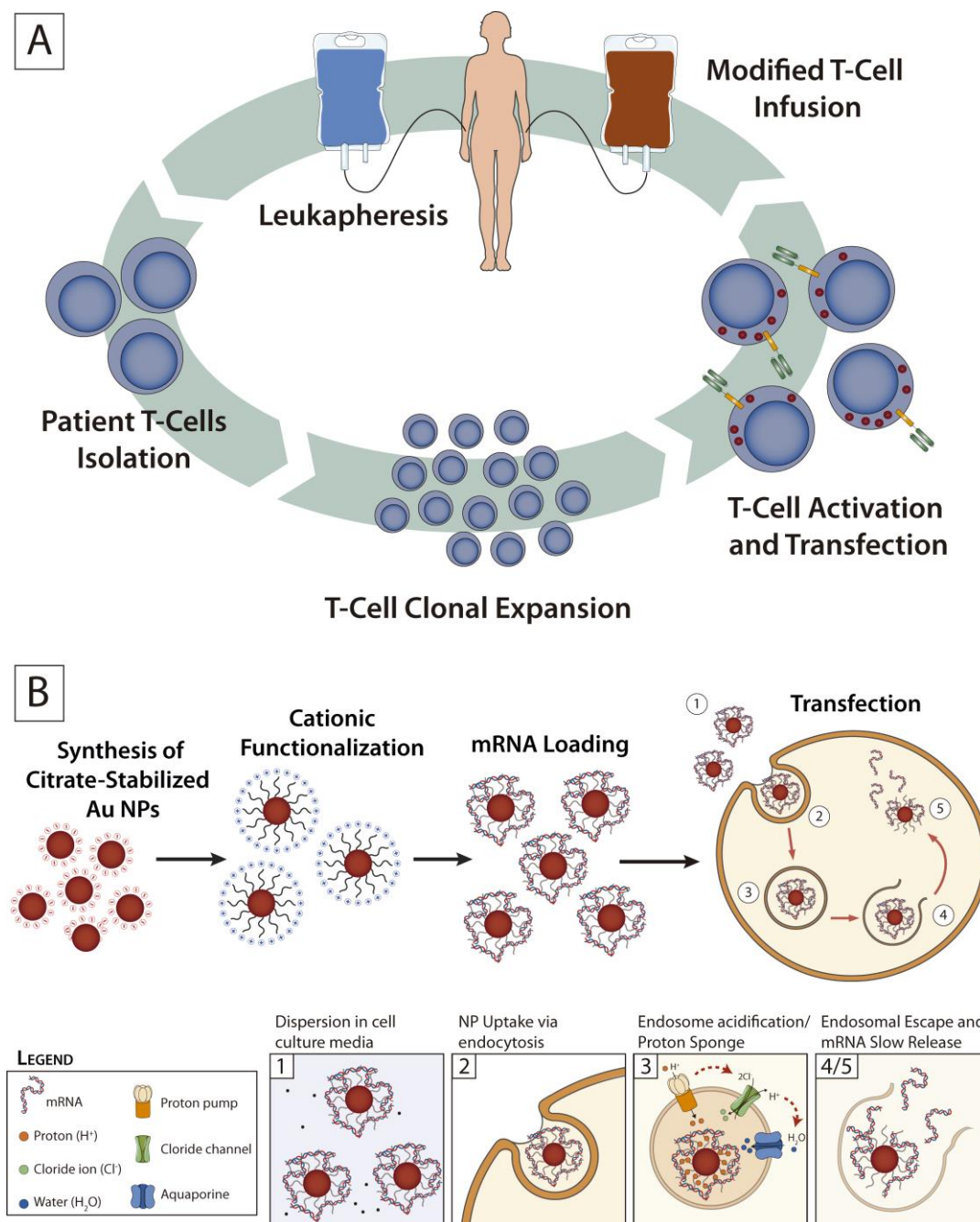


Figure 2.2. (A) CAR T-Cell manufacturing process, based on non-viral nanoparticle mRNA transfection. First, leukocytes are extracted from the patient's blood by a process named leukapheresis, and then T-cell populations are isolated and expanded. Next, T-cells are transfected with mRNA to express the CAR and activated, to finally reintroduce them into the patient. **(B)** Mechanism of the Nanoparticle-based mRNA transfection. To start, nanovectors are produced by the synthesis and cationic coating of Au NPs, and then loaded with mRNA. Next, nanovectors enter the transfecting cells via endocytosis, and deliver the mRNA to the cytosol for its translation after escaping from the endosomes following the proton sponge effect.

Besides, in comparison to DNA, RNA as a drug format has several advantages. First, it does not need to be delivered to the cell nucleus, but only to the cytoplasm, which poses fewer challenges for developing the drug delivery vehicle. Second, it does not integrate into the genome and thus does not pose risks of mutagenesis. Also, it is readily degraded in serum, thus reducing potential safety issues. Low serum stability, however, poses also a hurdle for development of RNA nanomedicines, and vehicles that sufficiently protect the RNA from premature degradation are required. Nanoparticle formulations are attractive as versatile vehicles for RNA delivery, because they may protect the RNA from fast degradation by nucleases and undesired interactions with serum components and biomolecules. Therefore, allowing the endocytosis-mediated uptake of the NP-mRNA complexes. [26,27]

2.1.4 Scientific relevance of the selected materials

To overcome all limitations and enable advanced transient genetic therapy, the binding of mRNA to cationic gold NPs was proposed as a safer way to introduce it in a controlled manner into the selected cells, promoting *in vitro* NP endocytosis and posterior controlled cytoplasmic release (**Figure 2.2B**). More importantly, several formulations of mRNA-NPs were designed (schematically represented in **Figure 2.3**) to control the slow release of the mRNA inside the cell, therefore extending mRNA half-life, and so CD19 expression.

Gold nanoparticles as delivery vehicles

Biomolecules conjugated-gold NPs are becoming promising instruments for addressing challenges faced by the investigation of biological systems. In this context, the use of Au NPs as delivery vehicles keeps exponentially growing. Au NPs have a number of desirable properties that make them excellent candidates for use in delivery applications. First, the gold core is essentially inert, non-toxic, and biocompatible, making it an ideal starting point for carrier construction. [28] Secondly, Au NPs with a wide range of core sizes (1–150 nm) can be fabricated easily with controlled monodispersity. [29] Both, size and monodispersity are key aspects for precise control of drug delivery systems operation. Furthermore, the high surface-to-volume ratio of provides a dense loading of biomolecules with targeting and therapeutic functionalities. [30] Finally, the highly tuneable and versatile surface offers diverse possibilities to incorporate multiple therapeutic drugs or biomacromolecules by covalent or non-covalent conjugation. [31] Thus, thanks to the enhanced biocompatibility

and low toxicity, [32] together with the easy surface functionalization, Au NPs provides a versatile platform for their assembly with, for example, oligonucleotides, [33–35] antibodies, [36,37] and proteins. [38,39]

The inorganic NPs of choice are Au coated by sodium citrate due to its inertness and the well-known strategies for their functionalization/loading. Sizes between 5 and 50 nm of these highly monodisperse citrate-capped Au NPs were selected, as this size regime favours the endocytosis [40–43] and proven stability in physiological media. [44,45]

Cationic Functionalization

The functionalization of the NP's surface allows to control the interaction of NPs with the biological interface. The intrinsic nature of the surfactant layer dictates the colloidal stability of the NPs and their interaction with the surrounding environment. On the other hand, the terminal groups provide the desired functionality and surface charge of the conjugate. This is of particularly important since some of their biological properties such as potential toxicity or cell uptake are dramatically influenced by the surface charge and affinity given by this layer. [46,47]

In our particular case, the Au NPs were functionalized with two different cationic molecules: 11-amino-1-undecanethiol acid (AUT) and polyethyleneimine 2 kDa (PEI). They both contain amine terminal groups providing positive charge to the NP at physiological pH. However, their molecular structure and binding with the gold core are different. AUT consists of a saturated chain of 11 carbons terminated with a thiol group binding to the NP's surface and an amine group exposed, whereas PEI is a branched polymer consisting of ~1800 ethyleneimine monomer repetitions terminated in amine groups. Thus, AUT attaches pseudo-covalently to gold forming a self-assembly monolayer (SAM) on top of it. On the contrary, PEI interacts electrostatically with the negatively charged citrate-stabilized NP by non-covalent bonds, probably in mushroom disposition. [48] It is also worth noting, that the amine density of the PEI coating is much higher due to its branched polymeric nature.

These amine-functionalized nanoconjugates interact electrostatically with nucleic acids, which display a high negative charge. Note that PEI has already been used as transfection agent, but with significant toxicity concerns. However, its absorption to the NP's surface promotes the loss of flexibility and the membrane pore formation ability. Instead, PEI-derived NPs (nanovectors) attach to the cell membrane, not crossing it but inducing endocytosis. Consequently, its toxic aspect is eliminated thanks to the nanoconjugation.

Indeed, detoxification by nanoconjugation has been observed before in different systems, as discussed in the introduction. [49] Thus, the monolayer coverage of Au NPs allows to tune the charge and hydrophobicity to maximize transfection efficiency while reducing associated toxicity.

Successful transfection requires effective complexation and condensation of the genetic materials, protection from nuclease degradation, and cellular uptake through endocytosis coupled with endosomal escape, for its final delivery into the cytoplasm where it will be translated into the coded proteins. Positively charged Au NPs bind to nucleic acids efficiently and densely, and protect them from enzymatic digestion. [50] In previous studies, a series of NPs showed their transfection efficiencies to depend on the number of charged substituents in the monolayer, and the hydrophobic packing surrounding it. [31] Likewise, the efficiency of cellular uptake and/or the subsequent release of DNA/RNA from endosomal vesicles are improved by the cationic functionalization of the NPs. [31]

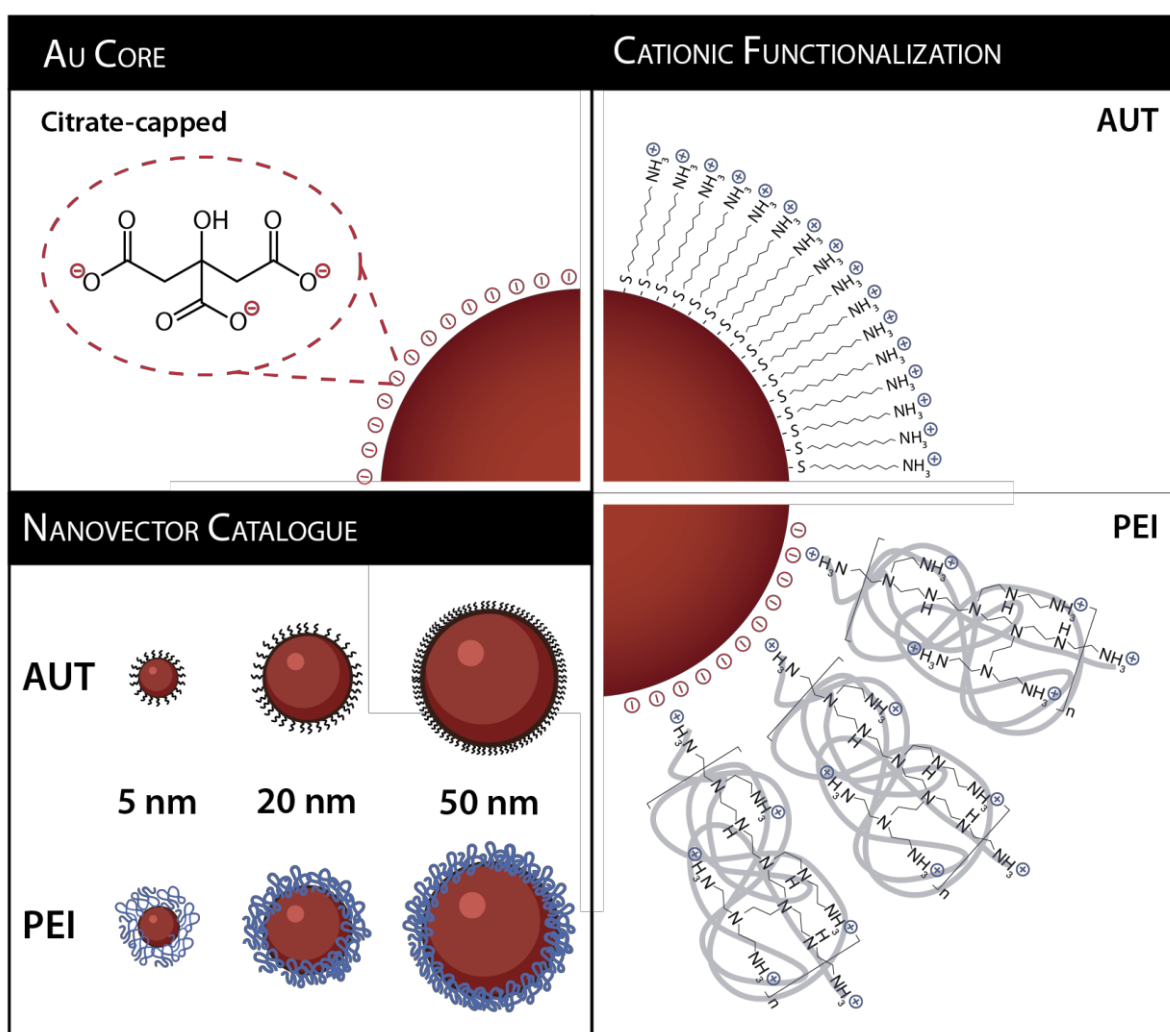


Figure 2.3. Nanovector design. The core of the nanovector consists of citrate-capped Au NPs, of 5 nm, 20 nm or 50 nm. Synthesized NPs are then coated with cationic molecules, AUT or PEI. The full combination of sizes and coatings constitutes the nanovector catalogue, to be tested as mRNA transfection vectors.

Most nanoparticle delivery systems are internalized into cells through the endocytosis pathway. [51] Uptake through endocytosis involves internalization into an endocytic vesicle, fusion into the early endosomal compartment, maturation into a late endosome, and accumulation in the lysosome, where pH decreases to 4.5-4 through an acidification process. Several studies indicated that escape from the endocytic pathway is the rate-determining step in the cargo delivery. Failure to escape may result in entrapment and potential degradation in the lysosome. [52–55] Different mechanisms of endosomal escape have been proposed depending on the nature of the NP, which include: membrane fusion, particle swelling, osmotic rupture by the proton sponge effect, and endosomal membrane destabilization. However, understanding of different endosomal escape mechanisms is still limited and, in many cases, subject to significant debate. Coating of the NPs with ligands having pH buffering capacity (such as PEI) has been reported to provide effective release of the nucleic acid payload through the proton sponge effect. The mechanism proposes that during the acidification of the endosome, polymers with a buffering capacity inhibit the drop in pH, and cause the cell to continue pumping protons into the endosome to reach the desired pH. Proton pumping to the endosome/lysosome is coupled with an influx of chloride counterions and water molecules. Dysregulation in this process causes an abnormal increasing the osmotic pressure, which eventually lyses the endosome by membrane disruption due to the high osmotic pressure and the content is released into the cytosol (**Figure 2.2B**). [56–59] Alternatively, it has also been suggested that polymer and positively charged nanoparticles could escape from the endosome via membrane destabilization. [60]

2.2 Scope of the study

The main objective of the study was to design and develop transfection nanovectors for sustained release of mRNA inside the cell for extended therapeutic levels of CAR expression. This objective involved four different aspects: i) the design of the nanovector: synthesis, functionalization, loading with mRNA, ii) the testing of the nanovector: the study of the molecular mechanisms regulating the interaction cells-nanovector, as well as the characterization of its intrinsic properties and behaviour in biological media, iii) evaluation their efficacy and therapeutic power, and finally iv) the study of its potential hazard and risk assessment.

2.3 Results and Discussion

2.3.1 Development and Characterization of nanovectors

The nanovector consists of a cationic Au NP with adsorbed mRNA for their further delivery into the cytosol. There are two critical points in the development of the nanovector: i) the absorption of enough mRNA and ii) the efficient cytoplasmic release of the mRNA following the “proton sponge” effect. The number of mRNA molecules adsorbed onto the nanovector is expected to depend on the size of the nanovector and the density of amino groups present at their surface, and this density will also determine the efficiency of the cytoplasmic release. Thus, a nanovector catalogue was developed comprising different sizes of gold NP cores, later functionalized with two different cationic molecules – AUT and PEI. Then, their loading with mRNA is studied for their application as non-viral transfection vectors.

2.3.1.1 Synthesis of Nanoparticles

Gold nanoparticles were produced using a well-established seeded growth approach. It is based on synthesising small gold nanoparticles by the citrate reduction of HAuCl_4 , which are then used as seeds to grow them by adding gold precursor up to the desired size. It follows the general principles of the classic Turkevich-Frens Au NP synthesis, [61,62] where citrate is used as both a reducing and stabilizing agent, which can be easily replaced when surface functionalization is required. However, several little adjustments in pH, temperature, citrate: Au precursor ratio, and the sequence of addition, significantly improve the size and morphology control, overcoming the main limitations of the aqueous synthesis of Au NPs. [63] Two well-established variations of this synthetic approach were used depending on the desired NP size. [64,65] For sub-10nm Au NPs, tannic acid is also used as a co-reducing agent leading to smaller gold seeds to be grown, without losing control over size and monodispersity.

In this work three different NPs were prepared and characterized with sizes ranging from 5 nm to 50 nm. Slight variations in the synthetic procedure exist for the large NPs (20 and 50 nm) and the small ones (5 nm).

In the first case (20 and 50 nm), highly monodisperse citrate-stabilized Au NPs were prepared following a well-established kinetically controlled step-by-step seeded-growth method developed by our group. The approach is based on a first burst nucleation by the reduction of HAuCl_4 by sodium citrate at 100 °C. Then, these nuclei are used as seeds for further growth after successive additions of gold precursor. By decreasing the temperature by 10 °C, the nucleation rate is dramatically decreased and the growth of the seeds is kinetically favoured with respect to the formation of new nuclei.

Representative transmission electron microscopy (TEM) images from Au seed particles and those obtained after the growth steps for a typical 20nm-Au NPs and 50nm-Au NPs synthesis are shown in **Figure 2.5** and **Figure 2.6**, respectively. In both cases, Au NPs presented a consistent quasi-spherical morphology and high monodispersity in all growth steps (where “G” stands for growth step). The size distribution of the NPs was calculated from the TEM images acquired.

The evolution of the UV-Vis spectra of the synthesized NPs is represented in **Figure 2.4A** and **Figure 2.7A**. All spectra were normalized to $\lambda_{400\text{nm}}$ for a better comparison. In all cases, the spectra show a LSPR peak that increases in intensity and red-shift as NP size increase. This allows for monitoring NP growth during the synthesis. In the right panel, the LSPR peak position is plotted as a function of the growth step.

Further characterization of the NPs was performed by Dynamic Light Scattering. Size distribution profiles of the growth steps are shown in **Figure 2.4** and **Figure 2.7** by Intensity and Number. Results show monomodal distribution with no aggregates, with increasing diameter as the number of growth steps increases. These results reveal, once more, the high monodispersity of the synthesized nanoparticles. The full characterization of the synthesis of 20 nm and 50 nm-NP is summarized in **Table 2.1** and **Table 2.2**, respectively.

Table 2.1. Summary of sizes and optical properties of the 20 nm Au NPs obtained after different synthesis growth steps.

Growth Step	TEM (nm)	Intensity (nm)	Number (nm)	LSPR peak (nm)
G00	10.5 ± 1.8	18.1 ± 7.3	8.5 ± 2.5	518
G01	14.6 ± 2.3	27.3 ± 14.1	10.3 ± 3.2	520
G02	20.5 ± 3	32.7 ± 11.9	18.6 ± 5.1	522

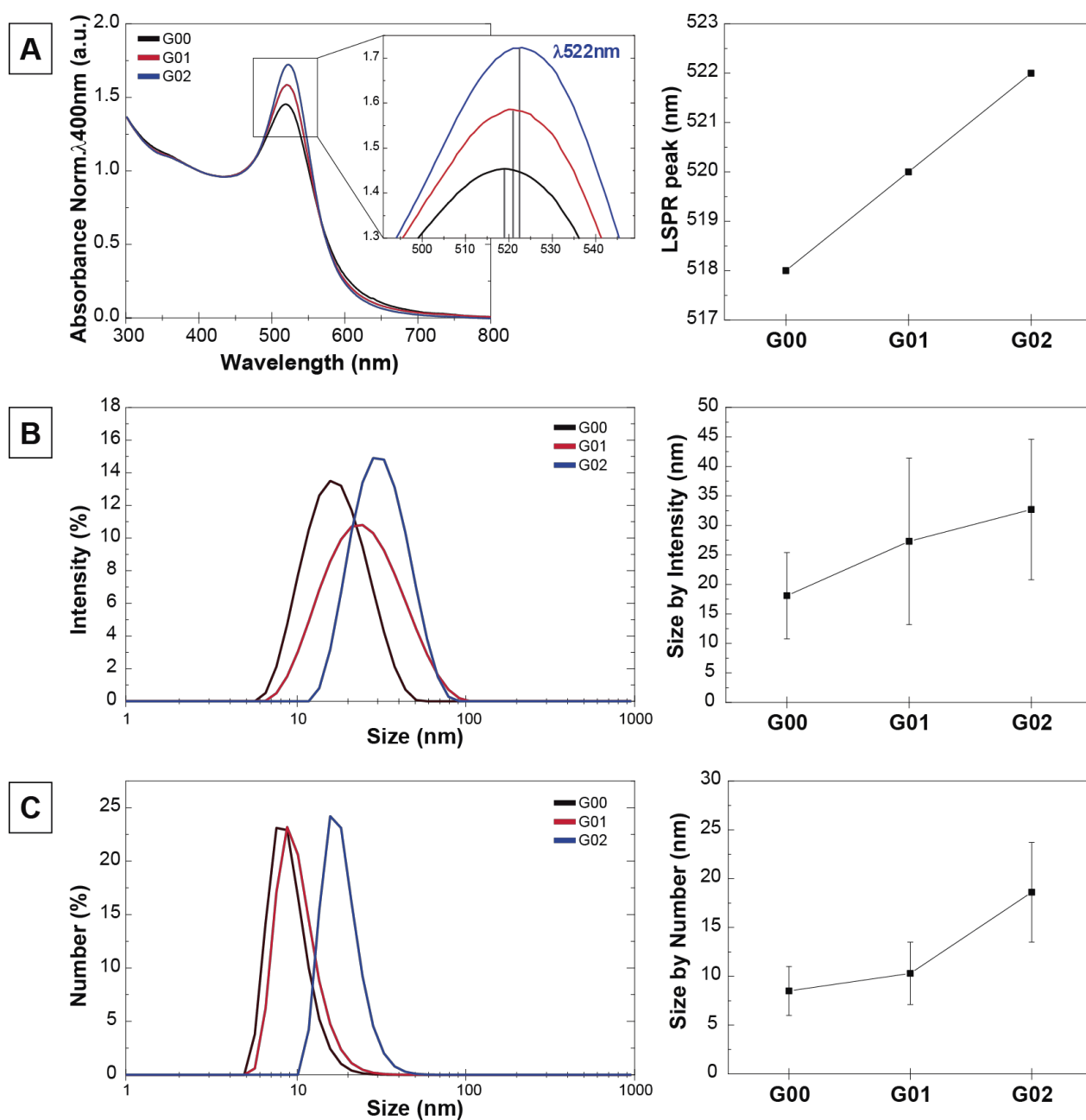


Figure 2.4. Characterization of the Au seed particles and further growth steps up to 20 nm by UV-Vis spectroscopy and DLS. **(A)** UV-Vis spectra of Au NPs growth evolution, and peak position of each growth step (right). Size distribution profiles measured by DLS by Intensity **(B)** and Number **(C)**. On the right, experimental average diameters for each corresponding growth step.

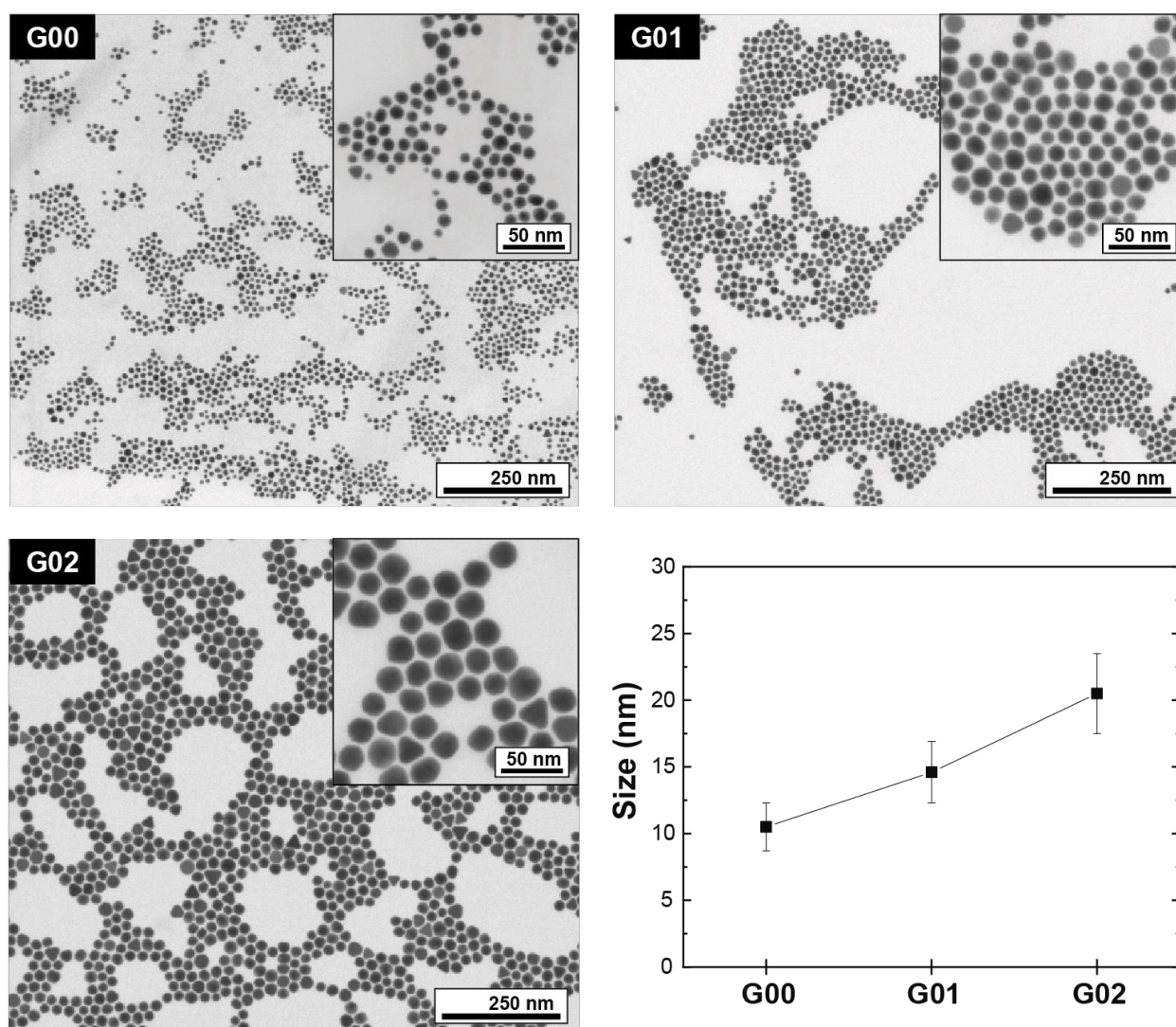


Figure 2.5. Transmission electron microscopy images of Au seed particles and those obtained after different growth steps up to 20 nm. As it can be observed in the summary graph (bottom right), particle size increases from 10.5 ± 1.8 nm to 20.5 ± 3.0 nm.

Table 2.2. Summary of sizes and optical properties of the 50 nm Au NPs obtained after different synthesis growth steps.

Growth Step	TEM (nm)	Intensity (nm)	Number (nm)	LSPR peak (nm)
G00	15.9 ± 2.3	19.3 ± 8.6	10.1 ± 2.7	520
G01	20.6 ± 2.9	25.5 ± 6.2	14.7 ± 3.6	521.5
G02	24.5 ± 2.7	36.4 ± 10.7	24.3 ± 6.1	523.5
G03	29.3 ± 4.1	43.3 ± 13.9	28.2 ± 7.3	525.5
G04	34.5 ± 7.3	48.6 ± 14.2	32.5 ± 8.2	528
G05	40.7 ± 7.8	54.4 ± 15.4	37.3 ± 9.3	531
G06	48.1 ± 6.4	62 ± 19.7	39 ± 10.6	534.5

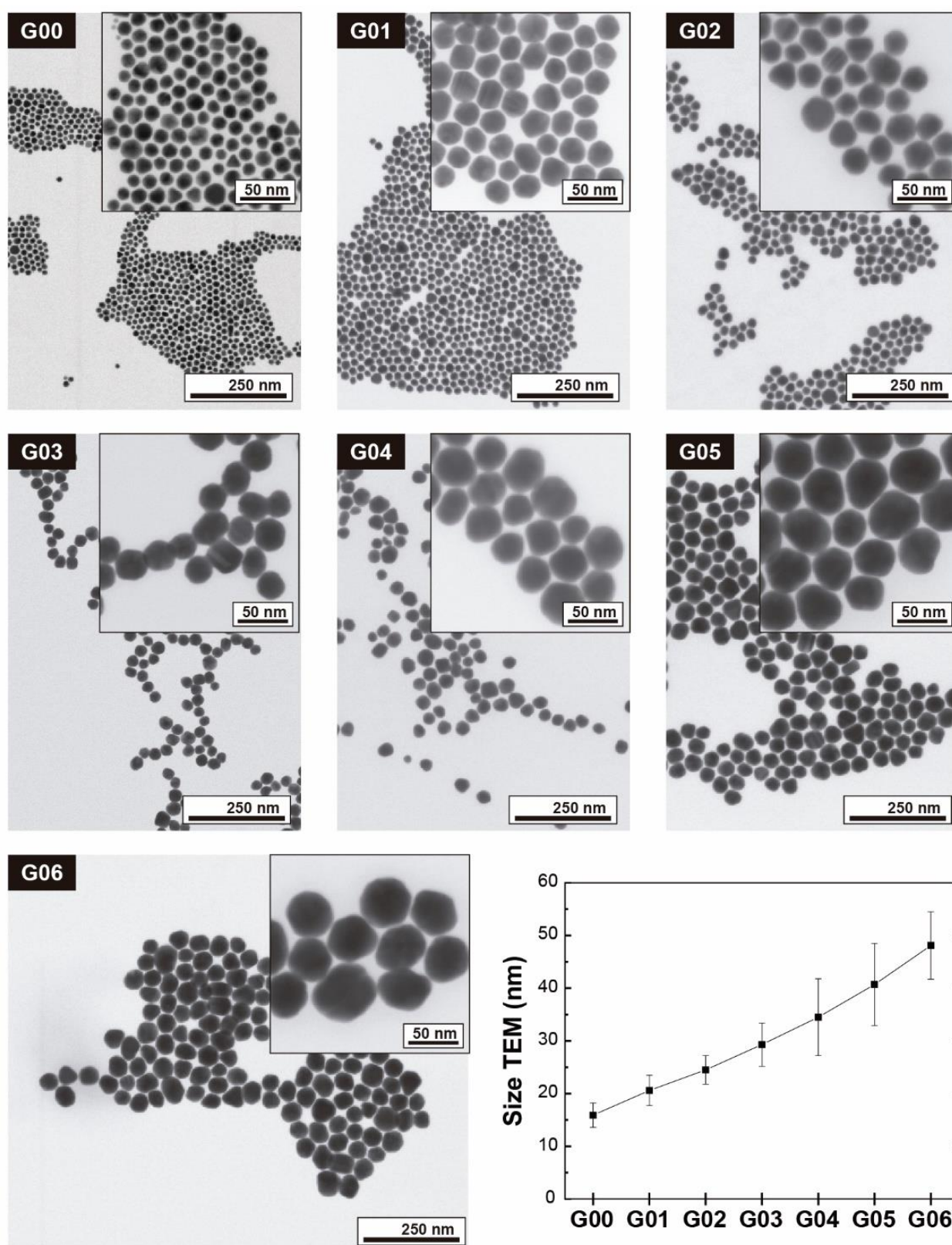


Figure 2.6. Transmission electron microscopy images of Au seed particles and those obtained after different growth steps up to 50 nm. As it can be observed in the summary graph (bottom right), particle size increases from 15.9 ± 2.3 nm to 48.1 ± 6.4 nm.

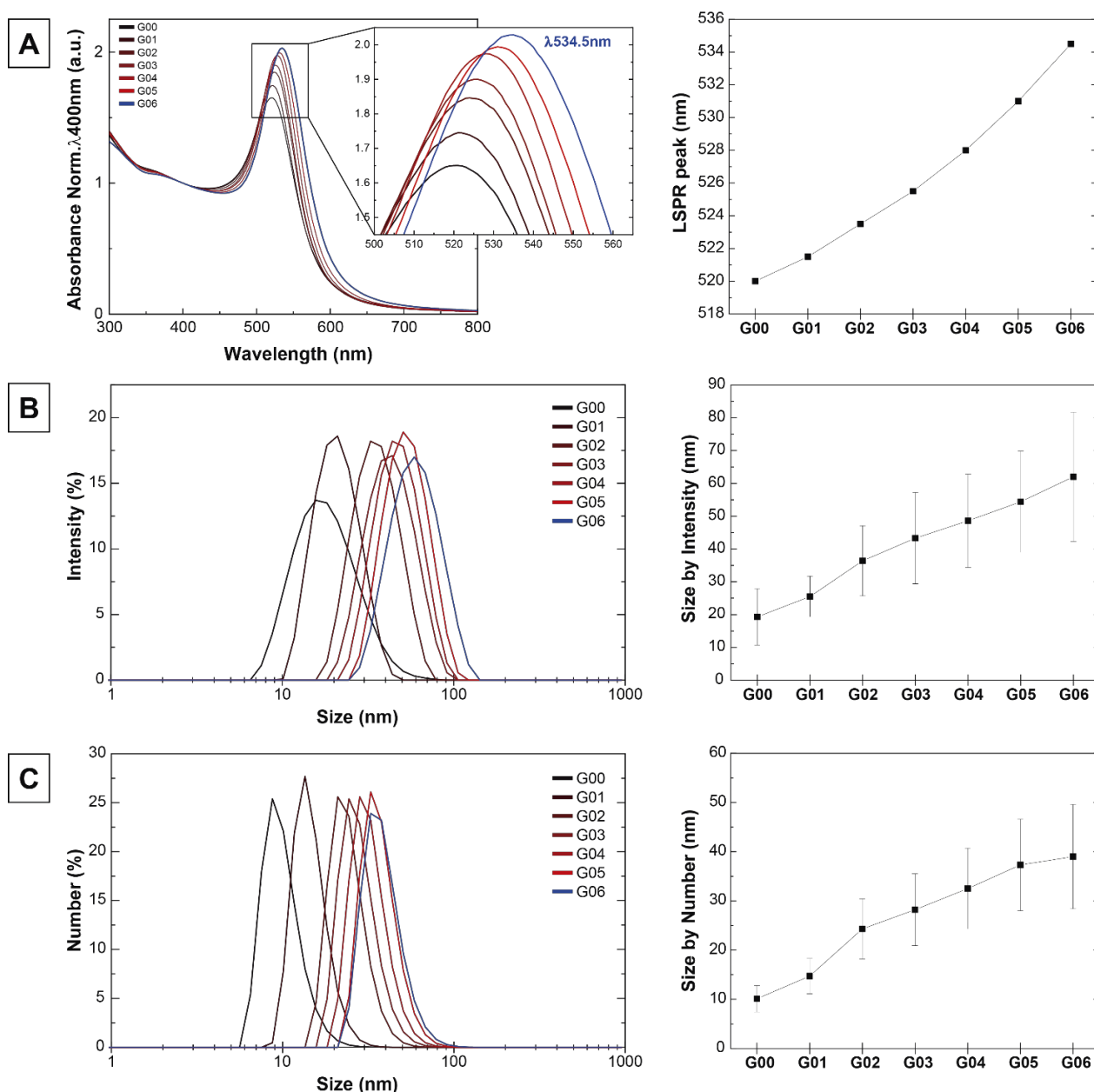


Figure 2.7. Characterization of the Au seed particles and further growth steps up to 50 nm by UV-Vis spectroscopy and DLS. **(A)** UV-Vis spectra of Au NPs growth evolution, and peak position of each growth step (right). Size distribution profiles measured by DLS by Intensity **(B)** and Number **(C)**. On the right, experimental average diameters for each corresponding growth step.

The production and use of sub-10 nm Au NPs are particularly interesting due to their higher surface reactivity and enhanced optical responses. [66–68] Furthermore, in the field of biomedicine their small size also has a huge impact on their interaction with biomolecules as well as their biodistribution and excretion. The synthesis of such NPs requires modifications of the synthetic protocol described above, aimed at particles in the 10-200nm regime. First, the addition of traces of a second (stronger) reducing agent as tannic acid (TA) is critical to decrease nucleation size from 10 to 3.5 nm. Additionally, the presence of potassium carbonate to adjust the pH and the temperature decrease to 72 °C are also crucial

for NPs stability and avoiding undesired secondary nucleation. Up to this point, the synthesis follows the same step-by-step approach for the growth of the seeds. Gold precursor is subsequently added, alternated with dilution steps, until the desired size is reached, in this case 5 nm.

Representative TEM images, clearly show the homogeneity and narrow size distribution of the obtained Au NPs. Several pictures of each sample were taken in order to perform the frequency distribution analysis. The mean average size and standard deviation were measured, which are graphically represented in **Figure 2.8A** and summarized in **Table 2.3**.

Further characterization was also done by UV-vis spectroscopy and DLS. Regarding UV-Vis Spectroscopy (**Figure 2.8B**), Au seeds (G00) present a SPR peaking at 505.5 nm, which red-shifted progressively as the nanoparticle's size increases. In the first growth step (G01), the peak shifts to 508nm, which indicate the increase in size. Likewise, in the second growth step (G02), the peak shifts to 510nm, indicating a further increase in size.

Figure 2.8C shows results from the DLS measurements, also summarized in **Table 2.3**. Au NP show an increasing hydrodynamic diameter with every growth step, measured either by Intensity or Number. No aggregates can be observed. These results reveal high monodispersity of the synthesized gold nanoparticles.

Table 2.3. Summary of sizes and optical properties of the 5 nm Au NPs obtained after different synthesis growth steps

Growth Step	TEM (nm)	Intensity (nm)	Number (nm)	LSPR peak (nm)
G00	4.6 ± 1.1	4.9 ± 0.8	4.3 ± 0.8	505.5
G01	-	-	-	508
G02	5.6 ± 1.4	8.2 ± 2.1	5.9 ± 1.3	510

The presented Au NP synthesis approaches led to the production of spherical highly monodisperse gold nanoparticles. Further, the Au NP synthesis procedures used here are standardized to be performed in aqueous phase, with no need for further modifications of the resulting nanoparticles. This allows to work with Au NPs that are stable in water-based solutions (non-organic dispersants), and don't require the use of extra chemical stabilizers (such as cetyl trimethylammonium bromide – CTAB). This is a critical point for the success of the later use and application of NPs, since the use of any cytotoxic compounds would compromise their use in biological systems.

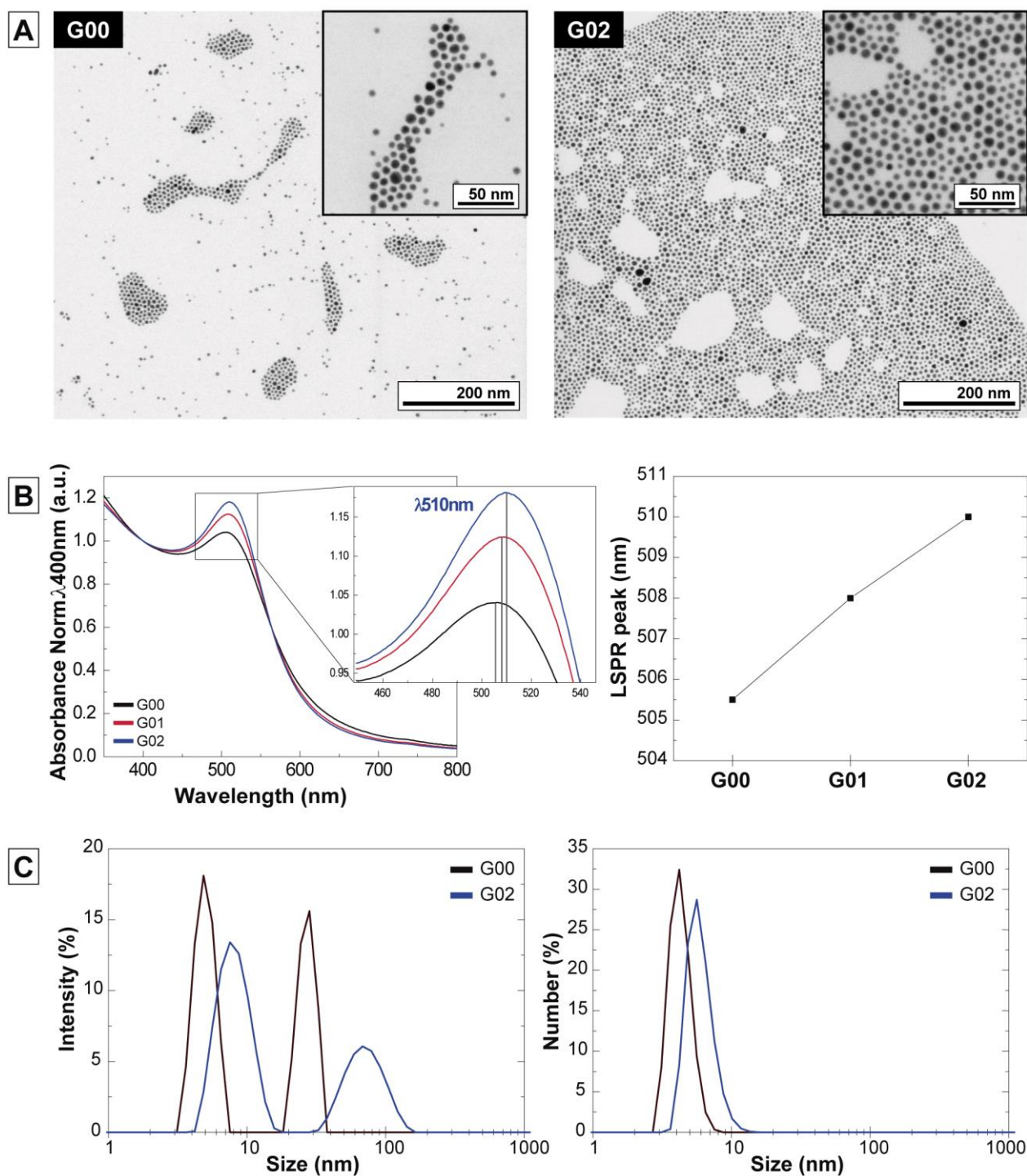


Figure 2.8. (A) Transmission electron microscopy images of Au seed particles and those obtained after different growth steps up to 5 nm. Particle size increases from 4.6 ± 1.1 nm to 5.6 ± 1.4 nm. (B) UV-Vis spectra of Au NPs growth evolution, and peak position of each growth step (right). (C) Size distribution profiles measured by DLS by Intensity (left) and Number (right).

2.3.1.2 Cationic Functionalization

The previously synthesized Au NPs were functionalized with cationic molecules, 11-amino-undecanethiol (AUT) and polyethyleneimine (PEI). The parameters affecting the conjugation – concentration, conjugation time, pH and purification – of NPs to these molecules were studied in order to obtain cationic functionalized Au NPs stable in colloid.

For AUT, the effect of concentration, conjugation time and the purification process was studied. Results are displayed in **Figure 2.9**. As it can be observed, NPs were conjugated to increasing concentrations of AUT from 50 μM to 400 μM . The conjugation process was performed by incubating the NPs at 1.5×10^{12} NP/ml, with an excess of AUT from 3.5 to 30 times of molecules in solution – equivalent to the theoretical footprint area – at pH 2.5.

Citrate-stabilized Au NPs are stable in aqueous media and display the characteristic UV-Vis absorption spectrum with a plasmon band at 522 nm, typical for 20 nm NP. The absorption spectrum is sensitive to the NP environment, and an observable red-shift of the surface plasmon resonance (SPR) band of about 4 nm appears once molecules are conjugated (**Figure 2.9A**). This can be ascribed to the change of the refractive index at the vicinity of the particles, and it is consistent with the binding of AUT via a thiol bond (≈ 45 kcal/mol, pseudo-covalent) to the gold surface. [69] Note that absorbance was normalized to $\lambda 400\text{nm}$ for a better comparison of the spectra.

However, under extremely acidic conditions the stability of citrate-capped Au NPs is compromised due to loss of electrostatic repulsion, and aggregation is only prevented by the effective conjugation of NPs. Therefore, appropriate conjugation conditions are critical to retain NP stability during the coating process. The decrease in absorbance intensity at SPR and the concomitant increase within the range of 600-800 nm suggest that the stability of the conjugates is compromised at lower AUT concentrations tested. These features define the shape of the spectra of the NPs, and allow us to relate it with the degree of NP aggregation state. The aggregation parameter (AP) allows quantifying the degree of aggregation compared to the initial state of the NP solution. It is based on the integrated absorbance between 600 and 700 nm, where higher AP values are related to bigger aggregation. As seen on the inset of **Figure 2.9A**, AP decreases with increasing AUT concentration. It shows a minimum value at 200 μM , where it reaches a plateau. Thus, 200 μM was set as a standard AUT concentration for Au NPs functionalization.

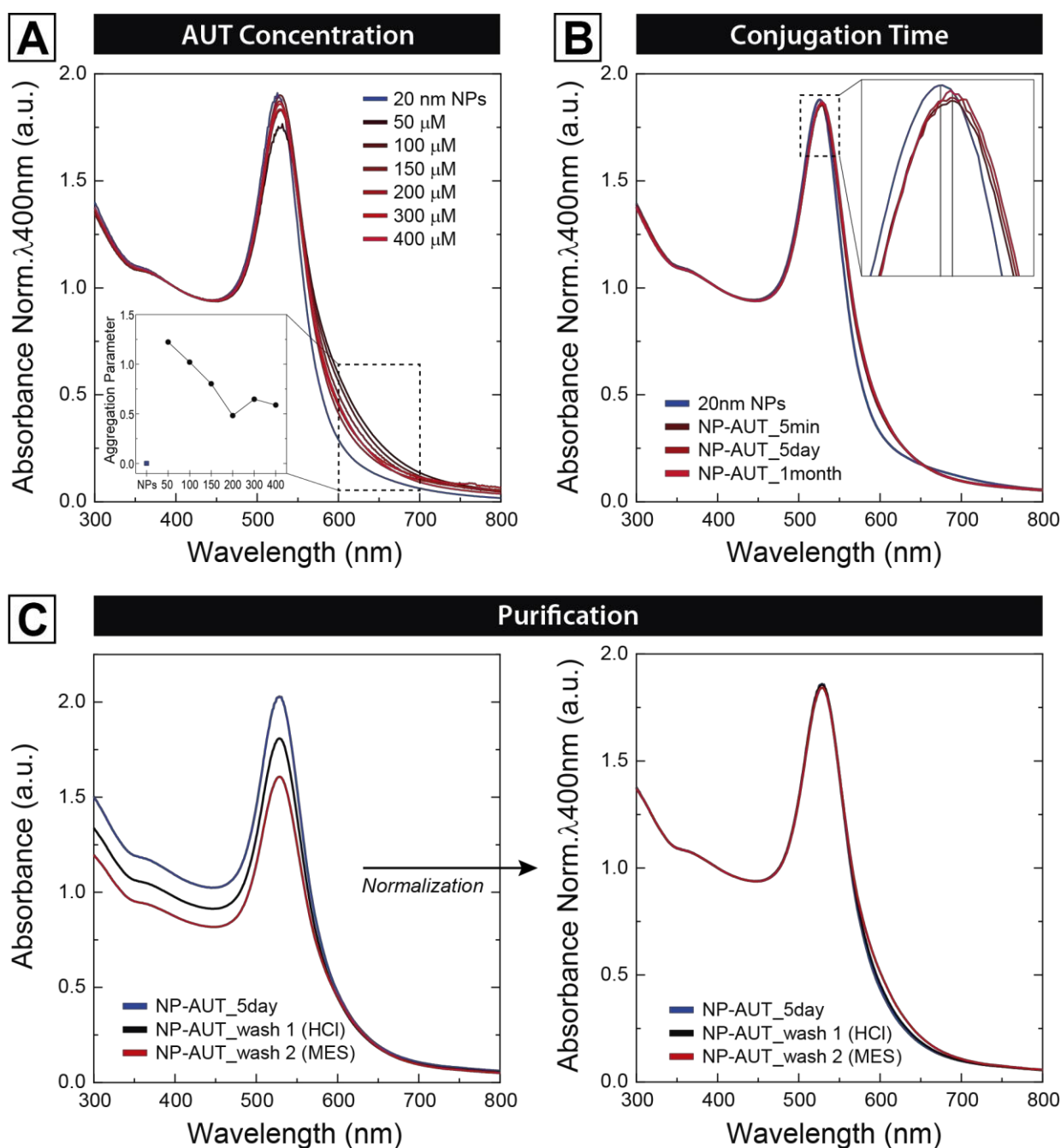


Figure 2.9. Study of the parameters affecting the conjugation of 20 nm Au NP to AUT. (A) AUT Concentration. Au NPs were conjugated to increasing concentrations of AUT (50–400 μM) and characterized by UV-Vis spectroscopy after 24h. On the inset, aggregation parameter was calculated based on the absorbance in the $\lambda 600\text{--}700\text{ nm}$ range related to the initial value. (B) Conjugation time. Au NPs were conjugated to AUT and characterized by UV-Vis spectroscopy after 5 min, 5 days or 1 month. (C) NP Purification. UV-Vis spectra after each purification step, normalized to $\lambda 400\text{ nm}$ (right) for better comparison.

The kinetics of the conjugation process and the long-term stability of the sample were studied by analysing time-dependent measurements of absorbance spectra of AUT-functionalized NPs (NPs-AUT) (**Figure 2.9B**). Representative time points were chosen, 5 min, 5 days and 1 month. AUT conjugation appears quick since the shift occurred within a few minutes. Then, spectra remained unaltered, indicating that the solution is stable for weeks. These results are in agreement with the high affinity of gold towards the SH residue

present in AUT to form a pseudo-covalent thiol-bond on the NP's surface. The indication of an effective NP conjugation with AUT also comes from the fact that NPs would aggregate under these extreme pH conditions without the presence of AUT on its surface. Citrate has 3 pK_a points which are 6.3, 4.7, and 3.1. Therefore, below pH 3 all the hydroxyl residues become protonated, losing their negative charge and, in turn, NPs lose the electrostatic repulsion provided by the citrate capping. The presence of a self-assembled AUT monolayer provides colloidal stability to NPs through the positively charged amine-terminal residue that avoids aggregation by electrostatic repulsion. Nonetheless, 24h was set as a standard conjugation time to allow for complete AUT monolayer formation.

After the conjugation, a purification process is needed to eliminate all the non-conjugated AUT molecules in the solution. For every purification step, NPs-AUT were precipitated by centrifugation and supernatants discarded. A first wash is performed by resuspending the pellets with HCl 2 mM, to maintain the pH in acidic conditions (pH<3) and eliminating citrate traces that might cause NP crosslink and precipitation. Next, a second wash step is performed, resuspending the NPs-AUT in 10 mM 2-(N-morpholino)ethanesulfonic acid buffer (MES) (pH~5). Samples were characterized by UV-Vis spectroscopy on each step of this process, as seen in **Figure 2.9C**. Absorbance spectra (**Figure 2.9C-left**) show a decrease in the intensity by close to 10% in each purification step ascribable to a small fraction of NPs didn't precipitate on the centrifugation (about a 10%). Higher time or speed centrifugation settings, aiming to recover 100% of the mass, could lead to undesired partial NP aggregation due to too aggressive conditions. Normalization of the absorbance spectra are shown in **Figure 2.9C-right**. Despite the decrease in intensity and the change in the dispersion media, no signs of aggregation can be concluded from the obtained spectra. Purification of the functionalized NPs is an essential step in order to avoid non-specific interactions or toxicity. Also it allows to disperse functionalized NPs in MES buffer, for their later loading with oligonucleotides.

Alternatively, branched PEI with a molecular weight ~2000 Da was used for the cationic functionalization of Au NPs (**Figure 2.10**). Note that, its chemical structure differs greatly from AUT. PEI is a large branched polymer with a high density of amine-terminal residues. First, 50 nm Au NPs were conjugated to a range of PEI concentrations from 2 μ M to 200 μ M to explore the optimal conditions to obtain cationic conjugated NP highly stable in colloidal form. Results from the UV-Vis spectroscopy characterization are depicted in **Figure 2.10A**. A significant decrease in the absorbance intensity of the SPR peak can be observed as the concentration of PEI was decreased, compared to the initial citrate-capped

NP solution. It is also correlated with the appearance of a “shoulder”, a localized absorbance increase, in the 600-800nm wavelength region, which is closely related to the aggregation state of the NPs in the form of “stable NP aggregates” (they do not sediment). This shoulder vanishes as coating concentration rise. The normalization of absorbance allows a better visualization of this phenomenon, and the calculation of the AP defines it quantitatively. An evident evolution towards less aggregation is observed with increasing concentrations of PEI, with a minimum AP value at 200 μ M very close to the initial state. Thus, considering the results obtained, 200 μ M was considered a good PEI concentration for NP conjugation since the decrease in absorbance is minimal and there are no signs of aggregation.

At first, the pH conditions for PEI conjugation used were on the range of pH<3, as stated from the previous experience with AUT functionalization. However, the high terminal amine density of branched PEI acts as a proton buffer delaying the media acidification, which is the base of the later exploited proton sponge effect for endosomal escape. This effect, forces the need for higher HCl concentration to reach the desired pH level (~700 mM), which, in turn, is coupled to a huge increase in the ionic strength of the media due to the Cl⁻ counterion. In this regard, highly saline environments cause NP aggregation due to loss of the electrostatic repulsion. In the particular case of PEI conjugation, the combination of different effects happening simultaneously ultimately determines the NP stability. First, at this acidification level, citrate ions become fully protonated and no longer provide electrostatic stability to NPs. As explained, the high ionic strength contributes to NP destabilization. On the other hand, the fast conjugation of PEI onto the NP's surface prevents aggregation by providing electro-steric repulsion, due to its polymeric nature and its high positive charge. If the optimal conditions are not met, as too low PEI concentration, partial aggregation states can be found, with an UV-Vis signature in the 600-800 nm range.

To reduce the risk of NP aggregation during the conjugation process, milder pH conditions were explored. This study was performed in parallel to the previously explained PEI concentration titration. Thus, on **Figure 2.10B**, 50nm Au NPs were conjugated to 200 μ M PEI at different pH values ranging from 2 to 7. Then, NPs were characterized by UV-Vis spectroscopy. Plots from the raw intensity absorbance (left) show a decrease in the SPR peak intensity that correlates with the decrease in pH, suggesting the aggregation of NPs at low pH. This can be seen when comparing normalized spectra at λ 400nm (inset), revealing a slight decrease in the maximum absorbance of the SPR peak that indicates partial NP aggregation. NP aggregation increases as pH drops, evident by the loss of absorbance in the purified conjugates (right). Centrifugation bring NP under a rather stressful conditions,

that might cause irreversible aggregation of the poorly stable colloids. The concentration of HCl needed to titrate the pH at the desired value, and consequently the ionic strength caused by the coupled Cl^- concentration, significantly changes from the most acidic point (700 mM) to the neutral point (34 mM). Therefore, at lower ionic concentrations aggregation is less prone to occur and the efficiency of stable PEI-functionalized NP (NPs-PEI) increases.

These results evidence that the kinetics of PEI critically differ from AUT conjugation. A stable conjugation could be performed at pH 7 (above the 3 pK_a points of citrate, where it is fully deprotonated and negatively charged) because PEI provides steric repulsion that avoids NP crosslink even though citrate interacts electrostatically with amine residues.

In this regard, it is also worth noting that, in this case no red-shift of the SPR peak position was observed suggesting that Au NPs were conjugated to PEI. When the NP's surface interacts with a given molecule, two features define the changes in the SPR peak: the length of the molecule and the nature of the anchoring group. Although PEI is relatively big, it only interacts electrostatically with NP's surface by the positively charged amine residues, not forming covalent bonds. Typically, the interaction with amine residues induce a blue-shift in the spectra, [70] which might be counteracting the red-shift induced by the Au surface functionalization. Yet, as smaller NP exhibit bigger changes in the SPR peak upon surface modification, a red-shift in the peak position is observed after PEI functionalization of 5 nm and 20 nm NPs (**Figure 2.15**). Still, the surface charge measured by Z-Potential of the 50 nm conjugated NPs revealed a high positively charged NPs that confirm the surface coating with PEI (**Figure 2.15**).

The results and understanding acquired from the study of functionalization of Au NPs were used to protocolize the cationic coating for any given Au NP size (see **Table 2.4**). This was implemented by conjugating the full range of Au NP sizes to both selected cationic molecules. Note that a significant increase in the concentration of both, AUT and PEI, needed for the functionalization of the 5 nm Au NPs. It could be that due to their synthetic procedure, the surface of these NPs is not only capped by citrate, but also by traces of tannic acid. Evidence in this direction, suggests that tannic acid interaction with NP's that its interaction with the NP's surface is stronger than citrate. As a consequence, it provides better colloidal stability but reduces the accessibility to the NP's surface when later functionalization is required.

Considering that cationic Au NP functionalization is performed at rather aggressive conditions of salinity and pH, the fact that tannic acid delays the access of the coating to

the surface poses a challenge for its stabilization before aggregation happens under these circumstances. Hence, first attempts to conjugate 5 nm NPs with the established AUT and PEI concentrations for 20 or 50 nm NPs led to the partial aggregation of NPs. Successive experiments where the coating concentration was systematically increased resulted in stable cationic functionalized 5 nm Au NPs. Full characterization of these conjugates is summarized in **Table 2.4**.

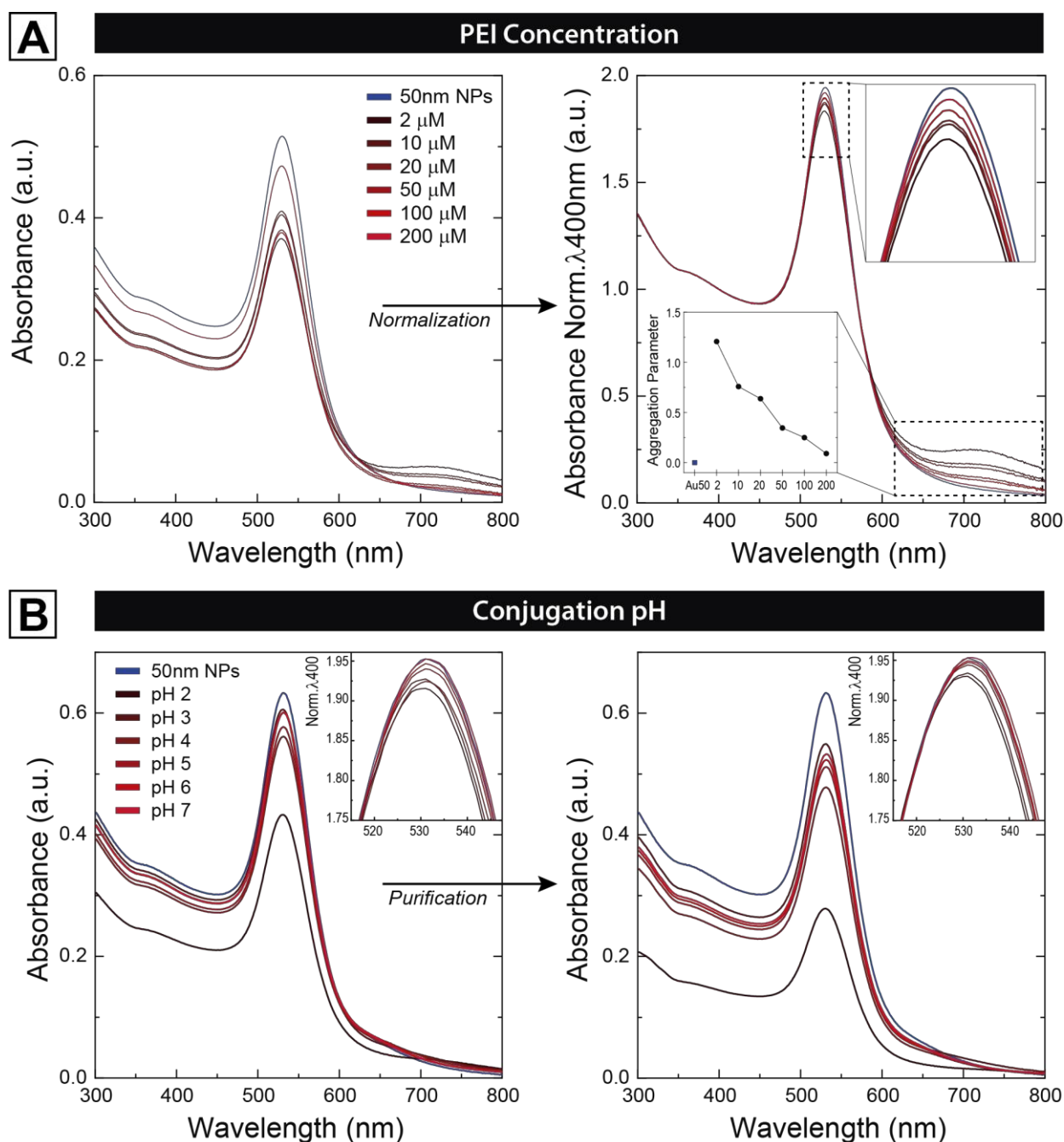


Figure 2.10. Study of the parameters affecting the conjugation of 50 nm Au NP to PEI. (A) PEI Concentration. Au NPs were conjugated to increasing concentrations of PEI (2-200 μM) and characterized by UV-Vis spectroscopy after 24h, and normalized to λ_{400} nm (right) for a better comparison. On the inset, aggregation parameter was calculated based on the absorbance in the $\lambda_{600-800}$ nm range related to the initial value. **(B)** Conjugation pH. Au NPs were conjugated to PEI at different pH values. After 24h, Au NPs were characterized by UV-Vis spectroscopy and after a purification step (right).

2.3.1.3 Loading of Nanoparticles with Oligonucleotides

As a first approach to develop a conjugation protocol, 20 nm and 50 nm NPs-AUT were conjugated to increasing concentrations of single-stranded DNA (ssDNA) as an oligonucleotide model. This experiment was aimed to determine an optimal ratio of ssDNA molecules to NP. It was performed following the basic principles of previous expertise of protein conjugation to Au NP. [45,71,72] The addition sequence was always adding the NPs-AUT onto the oligonucleotide solution, in order to maximize NPs surface coverage while avoiding uncontrolled aggregation during the mixture of both solutions. The incubation was performed at 4 °C, to minimize the risk of nucleic acid degradation and denaturalization, and under mild stirring conditions to avoid NP sedimentation overtime. The conjugation time was set to 24h to ensure surface saturation. Thus, the only changing parameter was the concentration of ssDNA from 0.41 to 53 µg/ml, corresponding to ssDNA:NP ratios of 7.8:1 to 1000:1 in solution.

For the case of 20nm NPs-AUT, the characterization of samples by UV-Vis (**Figure 2.11A-C**) and DLS (**Figure 2.11D**) suggest that the stability of the conjugates increased as the ssDNA:NP ratio increased. The typical UV-Vis spectra of aggregated Au NPs is observed at the lowest ratios tested [7.8-31.2]. This spectra is characterized by a broadening in the LSPR peak (**Figure 2.11A**) and huge shift in the peak position (**Figure 2.11C**). Remarkably, aggregation intensifies after NP's purification. Oppositely, NPs are stable at higher ratios [62.5-1000]. Thus, LSPR peak position red-shifts due to the presence of the ssDNA loading on the NP's surface, but is maintained at the same wavelength. Similarly, spectra show no signs of NP aggregation. Note that, an increase of absorbance intensity is observed at $\lambda_{260\text{nm}}$, corresponding to the presence and increase in ssDNA concentration in solution. Upon purification, the absorbance intensity rises as the ssDNA:NP ratio does. Centrifugation is a rather aggressive stress for NPs, so at higher concentrations, a more stable ssDNA corona is formed that protects NPs from aggregation even after following a purification process. This translates into better NP redispersion, read as a better recovery of absorbance intensity to initial values. The calculated aggregation parameter (**Figure 2.11C**) correlates well with these findings. It stabilizes at the same ratio value as the ΔSPR and ΔDLS size, showing more aggregation on the purified samples. Accordingly, DLS results (**Figure 2.11D**) indicate the formation of aggregates at low ratios, but a $\Delta 5\text{nm}$ size at higher ratios, that escalates after purification. On the other hand, the Z-potential (**Figure 2.11E**) shifts from positive to negative values after purification. This confirms the presence of the ssDNA at the surface of the NPs-AUT since DNA is negatively charged at pH 5.35. [73]

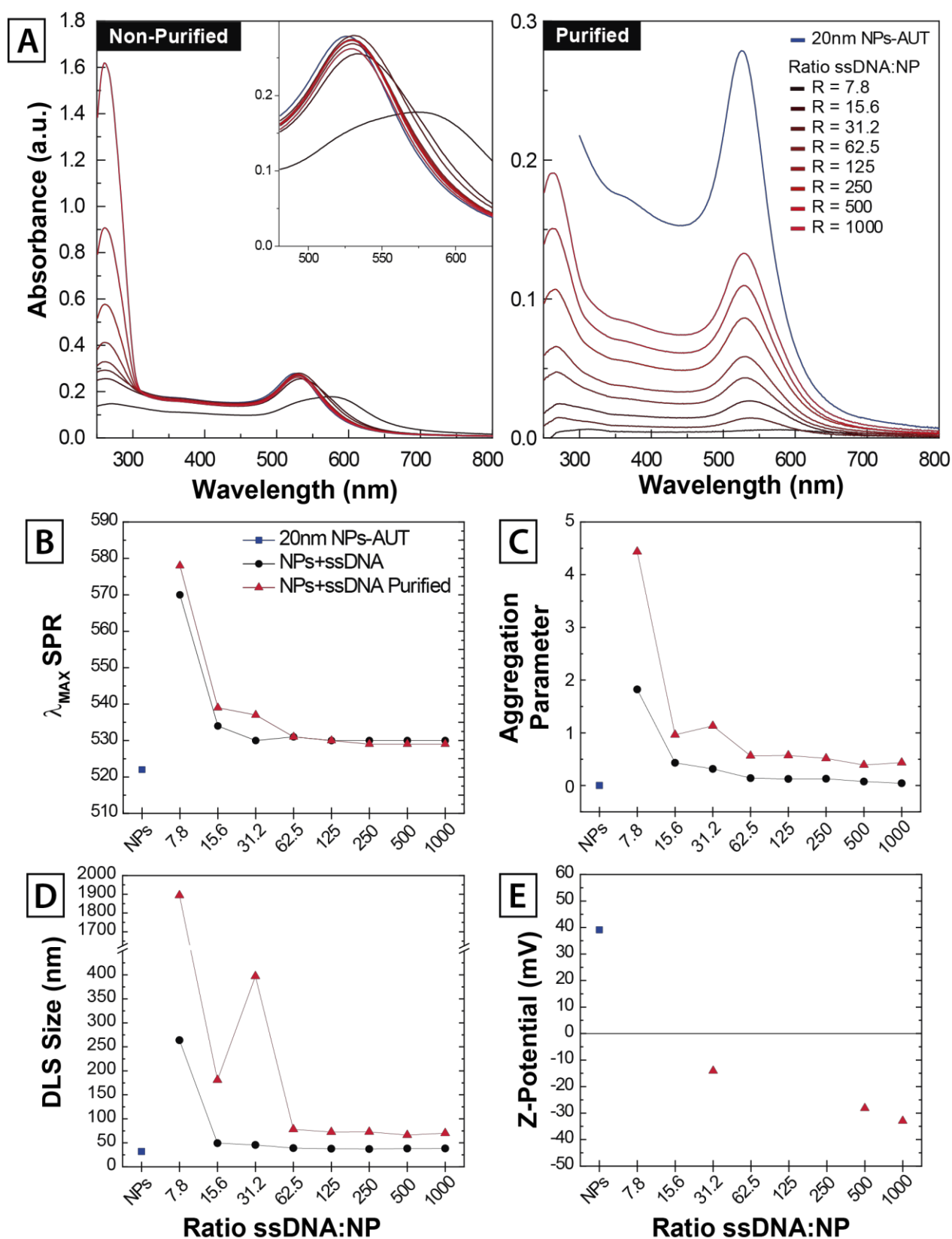


Figure 2.11. Loading of Au 20nm NPs-AUT to ssDNA. (A) UV-Vis spectra of Au NPs after 24h of incubation with increasing ssDNA:NP ratios, before and after NP purification. (B) SPR peak position at each ratio. (C) Calculated aggregation parameter based on the absorbance in the 600-700 nm range of each ratio related to the initial value. (D) Experimental average DLS diameters for each ratio. (E) Zeta-Potential of the purified conjugates after 24h of incubation.

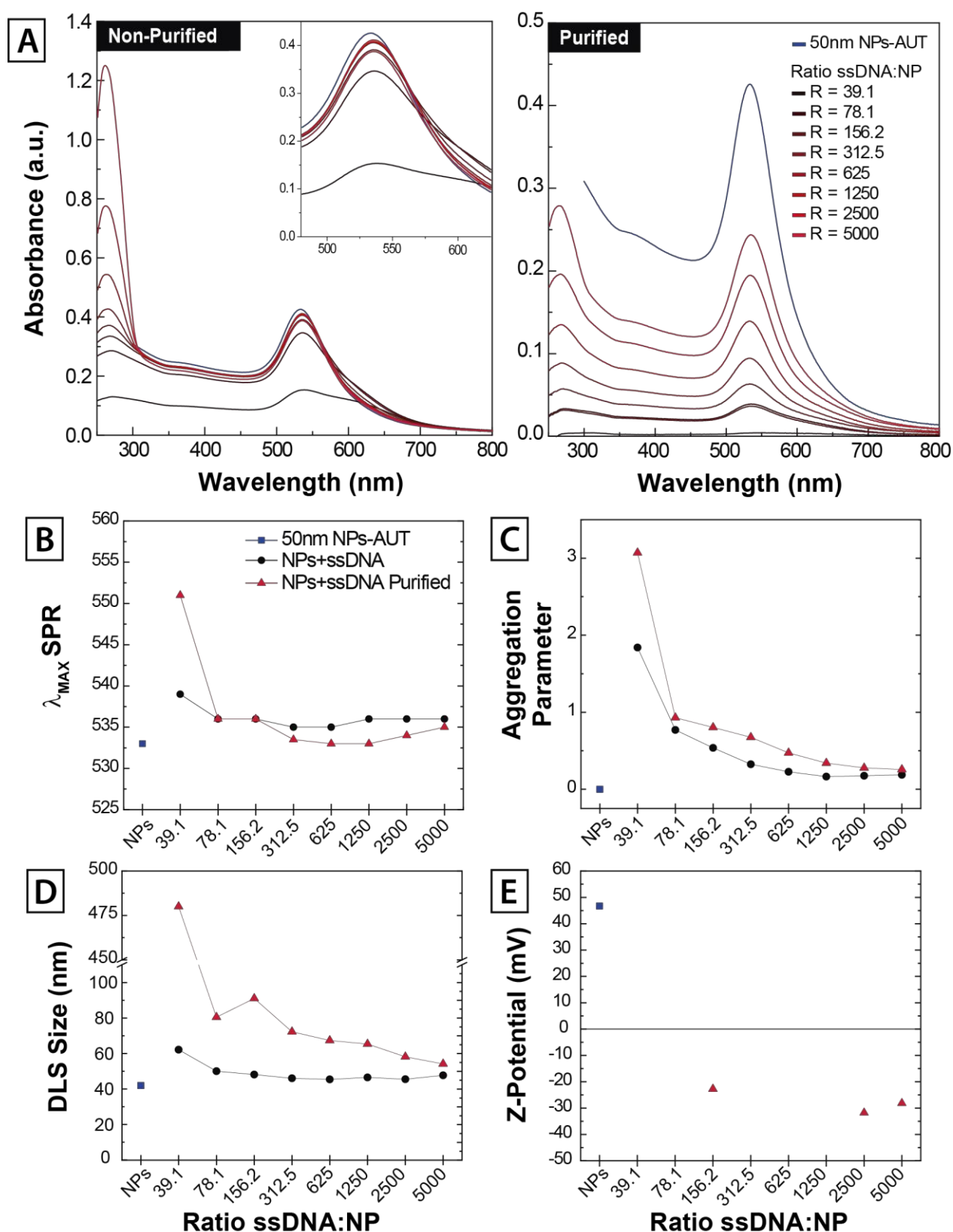


Figure 2.12. Loading of Au 50nm NPs-AUT to ssDNA. (A) UV-Vis spectra of Au NPs after 24h of incubation with increasing ssDNA:NP ratios, before and after NP purification. (B) SPR peak position at each ratio. (C) Calculated aggregation parameter based on the absorbance in the $\lambda_{600-700}$ nm range of each ratio related to the initial value. (D) Experimental average DLS diameters for each ratio. (E) Zeta-Potential of the purified conjugates after 24h of incubation.

Similar results were observed on the ssDNA loading of 50nm Au NPs-AUT, all displayed on **Figure 2.12**. The formation of aggregates at low ssDNA:NP ratios is observed by UV-Vis (**Figure 2.12A-C**) and DLS (**Figure 2.12D**). As the ratio ssDNA:NP increase, there is a trend towards a more stable conjugate. Likewise, Z-Potential measurements (**Figure 2.12E**) confirm the adsorption of ssDNA at the surface of the NPs, at any given ratio.

To set a good ssDNA:NP ratio for a standardization oligonucleotide loading protocol, the main aspect to consider is the concentration of ssDNA that ensures that there is enough excess of molecules to conjugate to the NPs in order to avoid uncontrolled aggregation. Considering that i) stability of NPs increases as the ssDNA:NP ratio increases until reaching a critical concentration in which the NPs remain stable, and ii) stability is assessed by UV-Vis spectroscopy and DLS, we study the critical point is where the Δ SPR and DLS size don't change compared to the following higher ratio, and the AP is low. Therefore, the optimal ssDNA:NP established for NP conjugation was **R=50 for 20nm-NP** and **R=300 for 50nm-NP**. These ratios were also found to correlate for ssDNA/nm² of NP surface.

On the other hand, a standard loading ratio also had to be established for the 5 nm-NPs. In this case, the corresponding ssDNA:NP ratio was extrapolated from the experimental results obtained from the bigger NPs since the purification of 5 nm-NP from the non-conjugated ssDNA was too complex. Thus, the ratio was inferred based on the relative DNA footprint area extrapolated and NP concentration, and set to **R=5 for 5nm-NP**. The relative oligonucleotide:NP ratios were kept as described, regardless of the NP's coating, for all the following experiments where DNA/RNA conjugations were performed, otherwise would be specified. The resultant constructs from the loading of oligonucleotides to cationic Au NPs are named nanovectors.

2.3.1.4 Time evolution of RNA/DNA loading

The kinetics of oligonucleotides loading to cationic NPs was studied over time to better understand of the interaction between both entities, using ssDNA as an RNA model. In this experiment 50 nm Au NPs, coated with AUT and PEI, were used. Cationic NPs were incubated with ssDNA at the previously established ratio of [300:1] for 24h. An aliquot was extracted at different time points for its characterization by UV-Vis spectroscopy, DLS and Z-Potential in order to monitor the evolution of the loading process.

The results from the loading of NPs-AUT are displayed on **Figure 2.13**, where it can be observed how the interaction of ssDNA and cationic NPs is fast. This can be seen by

evaluating changes in SPR peak position (**Figure 2.13C**), DLS size (**Figure 2.13D**) and surface charge measured by Z-Potential (**Figure 2.13E**) at the different time points studied, which after 1h of incubation remained unaltered. The complete UV-Vis spectra of all time points are shown in **Figure 2.13A**. Two main changes stand out compared to the non-loaded NP-AUT spectra used as reference. A red-shift in the SPR peak position is observed and zoomed in the inset for a better visualization, which clearly indicates a loading of ssDNA on the NP's surface as discussed in the previous section. As plotted in **Figure 2.13C**, it corresponds to a $\Delta 1-2$ nm, that stabilizes at 8h. Also, a high intensity peak at $\lambda 260\text{nm}$ appears, corresponding to the presence of oligonucleotides in the solution.

Conversely, after a purification step of the sample changes in the measured UV-Vis spectra over time can be seen. At short times, the absorbance intensity is decreased but progressively increases over time almost to the initial value. As explained, the instant shift of the peak position indicates that the interaction between NP-AUT and ssDNA is fast. Yet, the progression of the spectra after purification points out that the layer of loaded ssDNA might still be under an evolution process, probably a hardening of the corona. Similar results had been observed in previous studies regarding the conjugation of proteins to Au NPs. [44,45,68,72] It is claimed that it stands for a reorganization of the biomolecule layer, which hardens over time by forming non-covalent Van der Waals bonds optimizing its spatial disposition. In turn, this phenomenon contributes to increasing the stability of the resultant conjugates, especially in adverse conditions (as centrifugation or dispersing the NP in highly saline media). Therefore, purification is crucial to study the time evolution of the adsorbed protein/oligo layer. It is indispensable to remove the unbound and loosely bound molecules, and forcing the conjugates out of the dynamic equilibrium.

Similarly, an increase in the DLS measured size is obvious from the first time point (**Figure 2.13D**). DLS size values did not change significantly over time. However, a constant slight decrease in size is observed after purification of the sample. In this case, if we also take the evolution of the protein corona as a reference, the ssDNA layer is not uniform. It would consist by a hard portion, that strongly interacts with the NP's surface, and a softer portion that is in dynamic equilibrium with the free ssDNA dispersed in the media. The purification of the sample displaces such equilibrium since it washes out the excess of all the non-conjugated ssDNA. Thus, reducing the hydrodynamic size of the soft corona caused by the loss of ssDNA molecules with weak electrostatic interactions during purification.

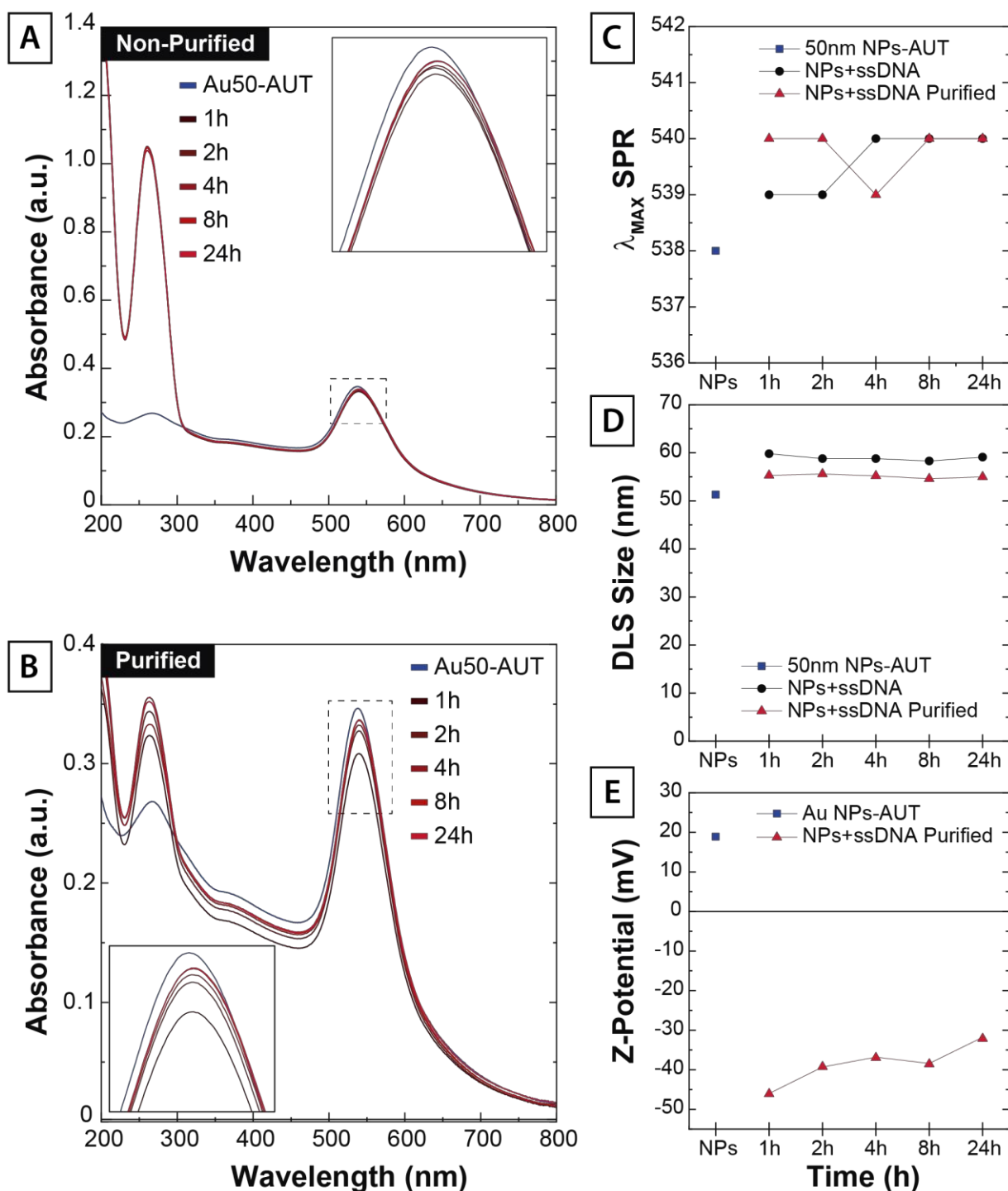


Figure 2.13. Loading kinetics of Au 50nm-AUT NPs to ssDNA. UV-Vis spectra of Au NPs loaded with ssDNA at each time point of incubation, before (A) and after NP purification (B). The presence of ssDNA in solution is revealed by an appearance of a peak at λ_{260} nm. (C) SPR peak position of Au NPs at time point. (D) Experimental average DLS diameters at each time point. (E) Zeta-Potential of the purified conjugates at each time point.

Finally, a clear evidence of the loading of ssDNA is the drop in the surface charge (Figure 2.13E). The measured Z-Potential abruptly changes from +19mV to highly negative values below -30mV. The presence of ssDNA on the surface of the NP-AUT, which is negatively charged at this pH value (~ 5), defined the charge of the overall construct. The purification

step is critical for the Z-Potential analysis, otherwise the free ssDNA in solution would interfere with the measurement.

On the other hand, the ssDNA loading kinetics of the NPs-PEI was also studied over time. The results from sample characterization at each time point are all displayed on **Figure 2.14**. The characterization of the samples by UV-Vis indicates the loading at the NP's surface already at the shortest time point by the displacement of the SPR peak (**Figure 2.14A**). Subtle fluctuations in the absorbance intensity of the SPR peak don't follow any coherent trend and might be owned to slightly deviations in the dilution of the sample. A consistent $\Delta 2$ nm shift in the peak position is observed at all time, even in the purified conjugates (**Figure 2.14C**). Nonetheless, like in the NPs-AUT, an evolution of the absorbance intensity after purification is evident (**Figure 2.14B**). A reorganization of the loaded ssDNA layer towards a harder corona might be happening, which prevents NP aggregation on the purification process and it's translated into decreasing the loss of absorbance intensity of the purified nanovectors.

Likewise, an increase in the hydrodynamic size measured by DLS can be seen from the start of the loading process (**Figure 2.14D**). Also, same small size reduction happens after the purification of the samples, probably due to the removal of the ssDNA soft corona. Yet, the DLS increase in this case is larger than in the AUT-coated NPs. This results, coupled with the fact the surface charge doesn't invert to negative values (**Figure 2.14E**), point out that significant differences in the resultant nanovector constructs could exist. This variability could be attributed to the disposition of the cationic coating at the NP's surface. As previously discussed, AUT forms a self-assembled monolayer whereas PEI, considering the branched polymeric nature and the high molecular weight, is most likely to be in a mushroom disposition. Besides, polymers have certain structure mobility that could be changing triggered by the interaction with ssDNA. Last but not least, the fact that surface charge is maintained at positive values could impact significantly the interaction of the nanovectors with the cell surface, and thus, a critical role in the transfection efficiency.

A general conclusion from the results obtained in the study of the loading process of oligonucleotides on cationic Au NPs is that, although the interaction between both entities seems fast, an underlying evolution is still happening. Therefore, 24h of incubation time of oligonucleotide loading is set for the standard protocol.

Finally, aiming to calculate the loading of ssDNA to cationic Au NPs, a DNA quantification was performed by Nanodrop. For this, at the end on the incubation time (24h) supernatant

from the purification step were collected and the ssDNA concentration measured. Thus, the loaded ssDNA quantification was extrapolated from the free non-loaded ssDNA in the supernatant fraction. Nanodrop results after exposing cationic NPs at 3×10^{11} NP/ml to 19.15 ng/ μ l reveal a loading of 48% (9.3 ng/ μ l) for NPs-AUT and 45% (8.7 ng/ μ l) for NPs-PEI.

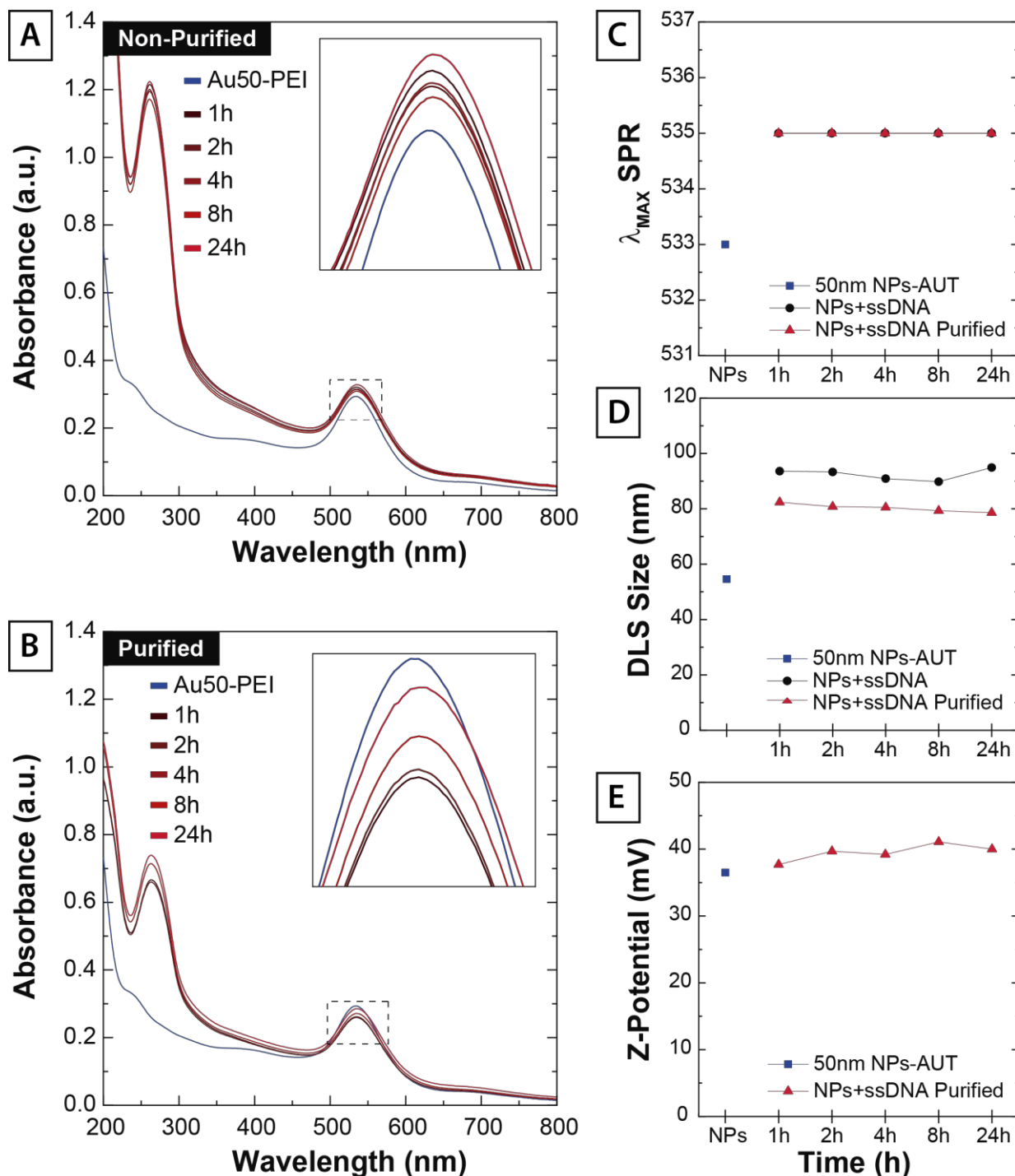


Figure 2.14. Loading kinetics of Au 50nm-PEI NPs to ssDNA. UV-Vis spectra of Au NPs loaded with ssDNA at each time point of incubation, before (A) and after NP purification (B). The presence of ssDNA in solution is revealed by an appearance of a peak at $\lambda_{260\text{nm}}$. (C) SPR peak position of Au NPs at time point. (D) Experimental average DLS diameters at each time point. (E) Zeta-Potential of the purified conjugates at each time point.

2.3.1.5 Nanovector Catalogue Summary

All the previous experiments presented and discussed, on the scope of standardizing a protocol for mRNA loading and studying its interaction with NPs, were performed using ssDNA as an oligonucleotide model and a limited selection of NPs in size and cationic coating. Thus, in order to corroborate these findings, the full range of NP sizes were functionalized with AUT and PEI, and later loaded with mRNA ~1000b. Together, they comprise the full Nanovector Catalogue, that will be later used as transfection vectors.

Characterization by UV-Vis spectroscopy, DLS and Z-Potential was performed at each step and summarized in **Table 2.4**. Additionally, the evolution of the UV-Vis spectra for each size with every functionalization layer is depicted in **Figure 2.15**. All results obtained agree with the expected from the previous experience of the former results discussed. As a general trend, the SPR peak position red-shifts upon cationic functionalization of the NPs and the mRNA loading, except for 20 nm and 50 nm PEI coating. The sensibility of surface modification differs based on NP size, where smaller NPs exhibit bigger SPR-shifts. [68] Similarly, the DLS hydrodynamic size increases at each step due to of the cationic coating and the deposition of mRNA at the NP's surface.

Table 2.4. Characterization of the Nanovector Catalogue. Summary of sizes, optical properties and surface charge of citrate-capped Au NPs of 5, 20 and 50 nm, cationic functionalized Au NPs with AUT of PEI, and loaded with mRNA. Note that, the pH at which Z-Potential of the citrate-capped NPs was measured (pH~8.6) is different than the other measurements, where NPs were dispersed in MES buffer (pH~5). This impacts fundamentally the surface charge of the NP.

	NPs	NPs-AUT	NPs-AUT+RNA	NPs-PEI	NPs-PEI+RNA
Au 5 nm					
SPR (nm)	510	521	533	516	519
DLS (nm)	6.1 ± 1.2	11.6 ± 3.6	62.7 ± 25.5	15.6 ± 4.9	15.1 ± 3.6
Z-Pot (mV)	-59.7	+5.8	-10.3	+26.2	+9.3
Au 20 nm					
SPR (nm)	522	526	531	523	524
DLS (nm)	30.4 ± 10.6	37.0 ± 13.3	54.6 ± 22.9	38.9 ± 15.3	44.9 ± 19.6
Z-Pot (mV)	-44.4	+18.6	-28.6	+34.4	+21.7
Au 50 nm					
SPR (nm)	531	533	540	531	534
DLS (nm)	49.6 ± 14.5	58.8 ± 25.9	75.0 ± 35.7	67.5 ± 30.2	72.8 ± 26.4
Z-Pot (mV)	-41.2	+31.2	-25.7	+44.3	+34.9

Finally, surface charge also gradually changes. Citrate-capped synthesized NPs have a high negative charge, that dramatically changes towards positive values after either AUT or PEI coating. The loading of mRNA causes a charge inversion for the AUT-coated NP but not for the PEI-coated ones, which still present a positive Z-Potential.

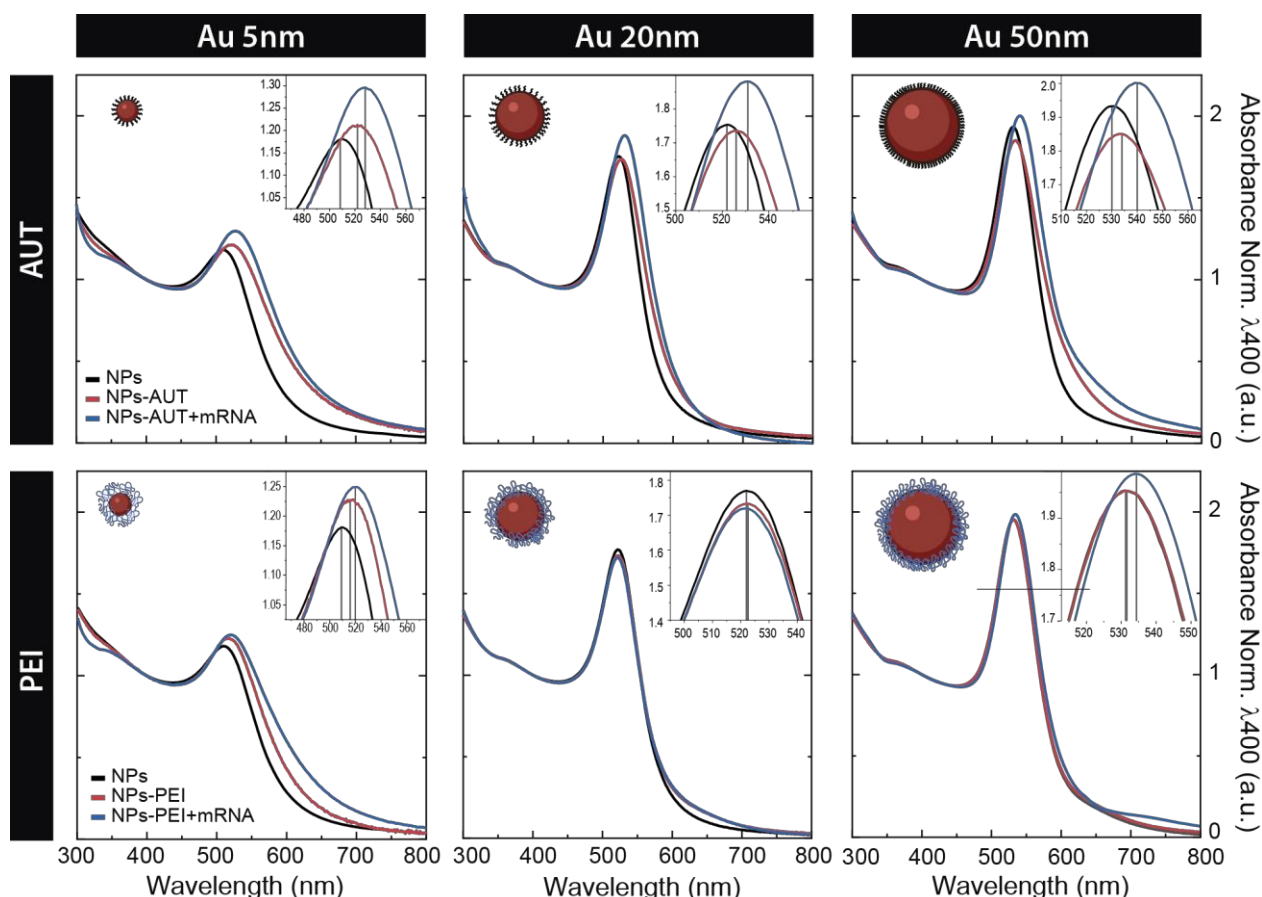


Figure 2.15. Nanovector Catalogue. UV-Vis spectra of citrate-capped Au NPs of 5, 20 and 50 nm, cationic functionalized Au NPs with AUT or PEI, and loaded with mRNA. Absorbance is normalized to λ_{400} nm for a better comparison.

2.3.2 Uptake and Delivery Mechanistic Aspects

The cationic functionalization of the NP and their later loading with ssDNA changed their size, optical, and surface charge properties. Consequently, surface modification of the NPs shields the original surface properties of the NPs, and alters their size and composition providing the NPs with a new biological identity. Surfactants (whatever their nature) are what is ultimately “seen” by cells, and determines the physiological response and

interaction of the NPs with living systems, including cellular uptake, circulation lifetime, signalling, biodistribution, therapeutic effects and toxicity. [74–78]

The study of the nanovectors properties is, consequently, a critical step in understanding their behaviour and efficacy as transfection vehicles. For this, their stability in physiological media, cellular uptake and the release of ssDNA were explored.

2.3.2.1 Stability of Nanovectors

The colloidal stability of the nanovectors was tested in different biological relevant media. This provides a better understanding of their physicochemical properties on transfection cell culture media that will ultimately allow a better understanding of the results when used as transfection vectors. Cationic functionalized 50 nm Au NPs, alone and loaded with ssDNA, were dispersed in phosphate buffer (PB) 10mM and Optimem, and incubated for 24h. Although PB has the same pH as Optimem, the stability in both media was studied first to isolate the effect of ionic strength of the media (as Optimem has a very high saline concentration), and also to avoid the potential interference that the presence of phenol red could cause.

The UV-Vis spectra from the characterization of the samples is illustrated in **Figure 2.16**. Cationic NPs, both AUT and PEI-coated, aggregate when dispersed either in PB or Optimem. The SPR peak critically broadens and it shows a huge increase in the absorbance intensity in the 600-800nm region. Complementary characterization of the samples by DLS and Z-Potential confirm these results, summarized in **Table 2.5**. The measured hydrodynamic size of the NP increases to values bigger than 400nm. This was also corroborated by the visual examination of the sample since aggregates precipitated fast to the bottom of the cuvette. Surface charge of NPs-AUT shifts to low negative values as a response to the pH increase to 7.4, whereas NPs-PEI remain in the positive range but with a value close to neutral. The loss of net surface charge, also coupled to the high salinity of Optimem, is what led to NP aggregation, due to the lack of electrostatic repulsion. Note that Z-Potential cannot be performed to NPs dispersed in Optimem due to its huge ionic strength, thus conductivity, of the media.

Stability of the nanovectors in physiologically buffered media significantly improved when cationic NPs had been previously loaded with ssDNA. For the AUT-coated nanovectors, although there is a drop in the surface charge of the nanovectors, SPR peaks show no signs of aggregation. A slight increase in the DLS size can also be seen after their dispersion in

PB and Optimem as the nanovector loads ssDNA. The formation of a ssDNA corona on the surface of the cationic NPs provides steric repulsion to the conjugates and prevents their aggregation even in the most hostile conditions. However, as for the case of PEI-functionalized nanovectors, some destabilization can be observed when dispersed either in PB and Optimem. Absorbance of the UV-Vis spectra increases in the longer wavelengths, and DLS size also grows.

Note that, here, only 50 nm NP were used as a model to show nanovector stability in biological media. Further experiments performed with the rest of NP sizes displayed similar results regarding the cationic coating and the presence of ssDNA corona.

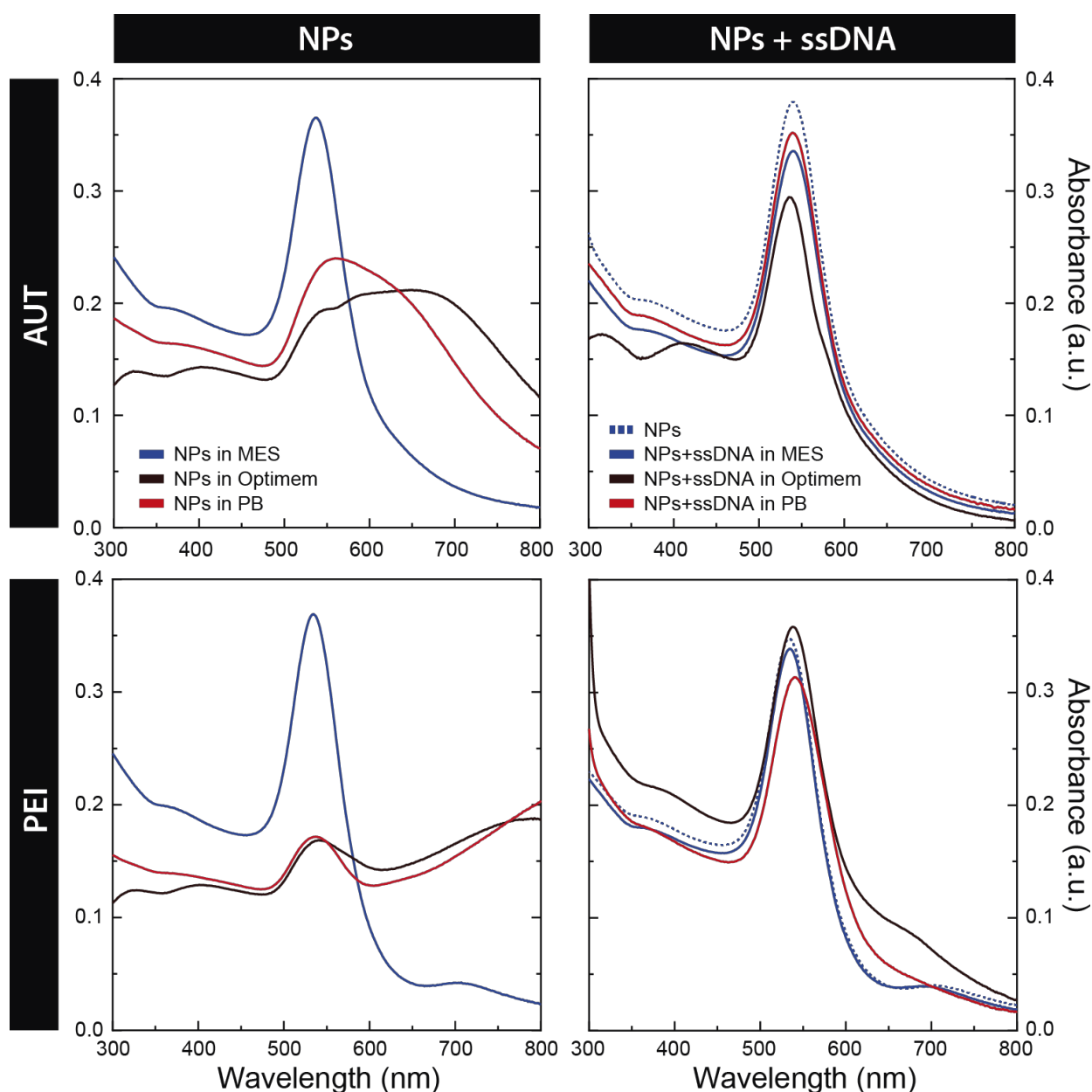


Figure 2.16. Stability in biological media. UV-Vis spectra of the cationic-coated Au NPs, alone or loaded with mRNA after 24h of incubation in Optimem and phosphate buffer (PB) 10 mM. MES buffer 10 mM was used as a reference stability control.

Table 2.5. Stability. Summary of sizes and surface charge of the cationic-coated Au NPs, alone or loaded with mRNA after 24h of incubation in Optimem and phosphate buffer 10 mM.

	NPs		NPs + ssDNA	
	DLS	Z-Pot	DLS	Z-Pot
AUT				
in MES	69,6 ± 29,8	+31,2	78,1 ± 32,0	-28,6
in Optimem	437,1 ± 261,1	-	95,2 ± 42,0	-
in PB	491,5 ± 165,7	-11,1	86,2 ± 35,3	-3,4
PEI				
in MES	69,6 ± 28,4	+24,9	65,8 ± 25,7	+34,9
in Optimem	-	-	97,1 ± 43,0	-
in PB	433,3 ± 197,4	+9,7	103,7 ± 59,4	+3,9

2.3.2.2 Confocal Imaging of Nanovector Uptake

It is important to assess the capacity of the nanovectors to enter in the intracellular space. It has been extensively reported the cellular internalization of Au NPs in the past. [79–81] However, the developed nanovectors are composed of a cationic layer and loaded with oligonucleotides which can critically impact on their cellular uptake after their dispersion in cell culture media. In this regard, nanovector uptake was studied by exposing HEK293 cells to ssDNA loaded cationic Au NPs. All the experimental conditions used were the same as the standard transfection protocol. After 24h, cells were fixed and stained in order to reveal the cellular structure, nuclei and actin. Samples were observed under the Confocal microscope and representative images are depicted in **Figure 2.17**.

Note that the use of confocal laser scanning microscopy (CLSM) allows to image non-labelled Au NPs in reflectance (scattering) mode. The principles and methodology of Au NPs imaging by CLSM will be described and deeply discussed on Chapter 3. Additionally, the multiplex staining allows to discriminate if NPs had been internalized and to locate them on a subcellular level from a certain z-section of the sample.

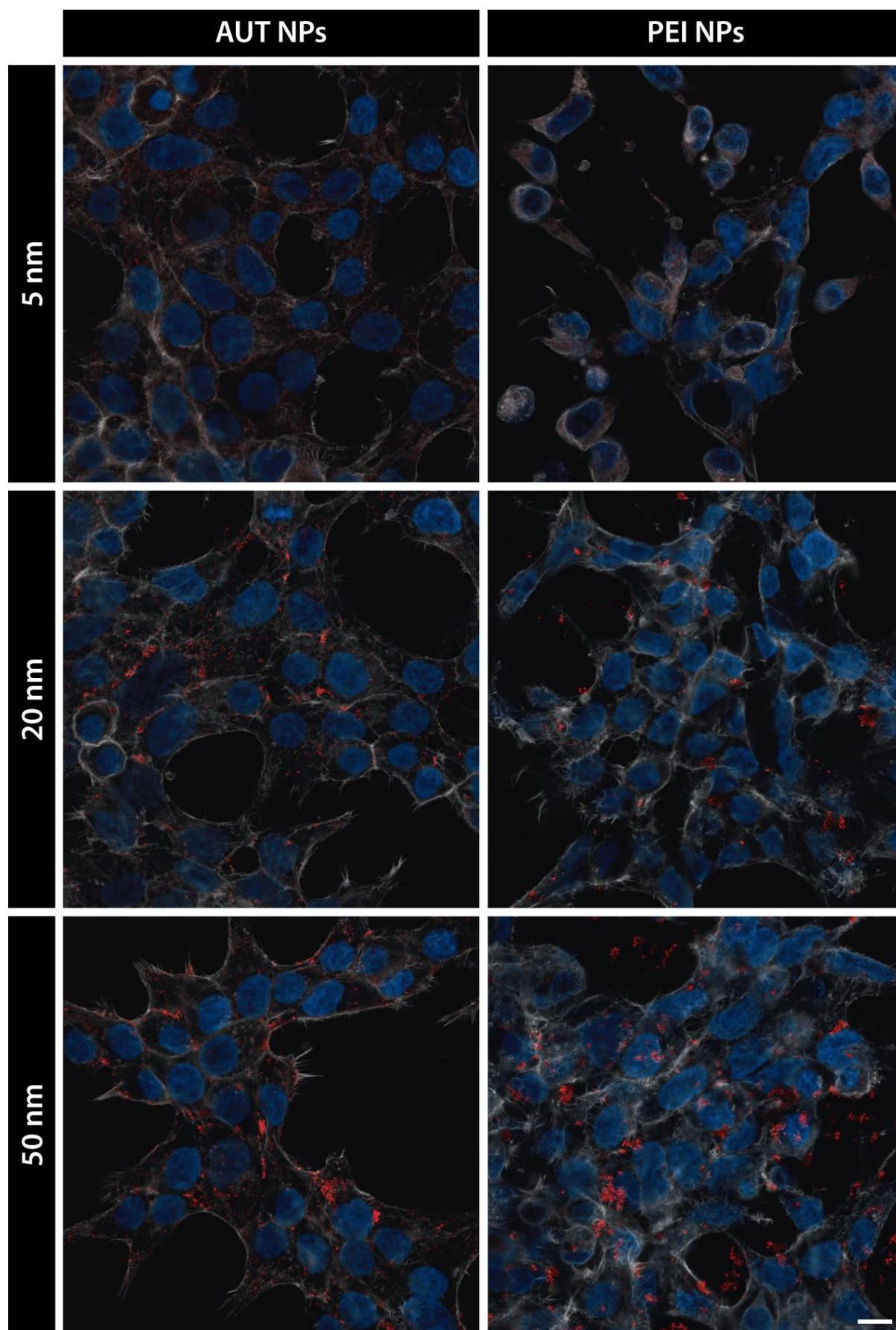


Figure 2.17. Nanovector Uptake. Cationic-coated Au NPs loaded with ssDNA were exposed to HEK293 cultured cells and imaged by confocal microscope at 24h. Actin (white) and nuclei (blue) were stained for subcellular NP localization. Scale bar = 10 μ m.

After exposure, Au NPs, of either size or coating, can be found homogeneously distributed all over the sample but mostly in the intracellular space. Signal intensity is higher for the bigger NPs since their light scattering contribution is larger, whereas small NPs have very low or none. Still, there is some signal for the 5 nm and 20 nm NP that usually correspond to NP located in vesicles where their concentration is higher. The biological aggregation that allow to observe small NPs does not happen in the extracellular space where NPs are colloiddally stable. However, as the scattering contribution is higher for larger NPs, single NP imaging is possible and, consequently, they can also be observed in the extracellular space. Hence, 50 nm NP can also be found in the extracellular space, especially the PEI-coated ones.

On most of the cases, cells show a normal morphology despite their exposure to nanovectors. However, after 24h of incubation with 5 nm Au NP-PEI, HEK293 cells show a round apoptotic-like morphology and cell confluence decreased considerably. These visual findings are in agreement with the cytotoxicity results that will be discussed later in section 2.3.4 . Further, this experiment allowed to study the nanovector behaviour and provided a deeper understanding of its role as a transfection vector by correlating these results with the mRNA transfections.

In a later study, a quantitative analysis of the 50 nm NP uptake by Jurkat cell line was performed as a first step to explore the potential of gold NPs as possible vehicles for mRNA delivery into T-cells. It is important to point out the fact that Jurkat cells grow in suspension. Therefore, their interaction with NPs dispersed in the media is rather different from the studied HEK293 cells, which are adhered to the bottom of the well. In this case, it will be mostly determined by the probability of NP-cell collisions due to Brownian motion, while for adherent cells NP sedimentation caused by gravity could play a major role. Also, the relatively non-phagocytic nature of T cells, compared to the phagocytic immune cell such as macrophages and neutrophils, poses a challenge to the efficient delivery of NPs to T cell's cytoplasm. [82,83]

Aiming to quantify NP uptake, after 24h of incubation with 50 nm Au NP coated with AUT, cells were imaged by CLSM and NPs (green) imaged simultaneously. Citrate-capped Au 50 nm NPs were used as a control. On **Figure 2.18A** a representative image of Jurkat cells exposed to Au NPs-AUT is presented. The picture corresponds to a bright-field image overlaid with the confocal signal acquisition of propidium iodide and NPs. Indeed, the uptake of 50nm Au NP, Au NP-AUT can be observed. However, in order to quantitate the

uptake and compare different conditions and NP surface modifications, we started to develop an algorithm that will evaluate the number and intensity reflecting gold NPs (probably as aggregates) in the cytosol, while eliminating signals attributed to the gold NPs accumulated in dead cells.

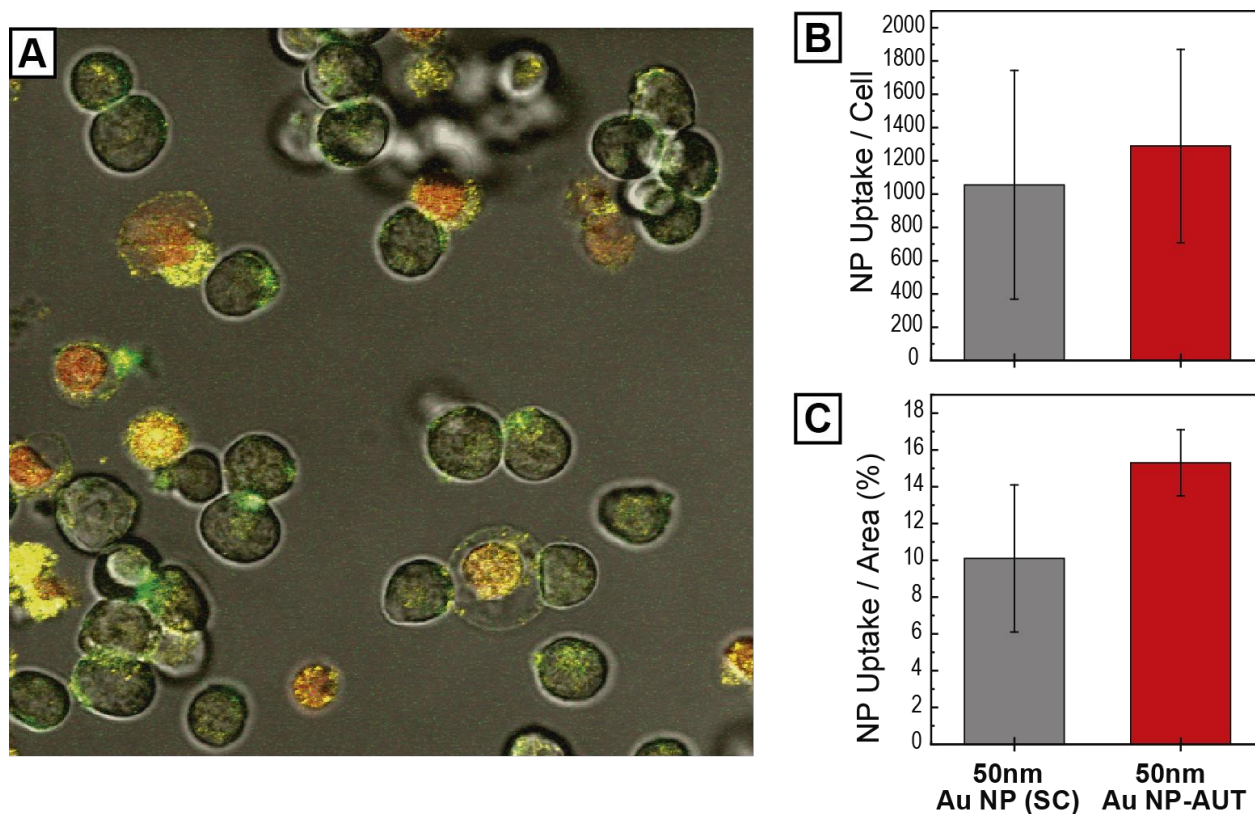


Figure 2.18. Nanoparticle Uptake on Jurkat cells. (A) Bright-field image of Jurkat cells in suspension, overlaid with the imaging of Au NPs by reflectance mode on the Confocal Microscope (green). Propidium iodine staining was used as a viability control (red). Quantification analysis of NP uptake by NP/cell (B) or by area (C). Images provided by Dr. Alex Barbul and Prof. Rafi Korenstein from Tel-Aviv University.

ImageJ analysis software was used in order to calculate the NP uptake (Figure 2.18B-C). Discrete intensity dots were counted as individual NP, whereas single cell contours were defined from the bright-field acquisitions. Results revealed a mean uptake of 1289 NP/cell, compared to 1056 NP/cell from control Au NP (SC). Still, high variability can be observed (SD >45%). Alternatively, NP distribution was calculated based on the NP occupancy area of cells. Likewise, AUT-coated NPs occupy a higher area percentage of Jurkat than control NP, but in this case with bigger significant difference and lower standard deviation.

This results point out that cationic functionalized NPs are more prone to interact with cell surface and ultimately leads to higher internalization rates than citrate-capped Au NPs. Still, further studies are needed to evaluate the ultimate subcellular localization of the internalized Au NPs, in order to assess their ability to reach to cytoplasmic space. Also, the final nanovector – cationic NPs loaded with oligonucleotides – uptake should be studied

to confirm that same internalization rate and behaviour is observed in the Jurkat cell line as in the HEK293, or with the non-loaded NPs as reported in these results.

2.3.2.3 Proton Sponge Efficiency

Nanoparticles with size ranging 5-100 nm enter the intracellular space via endocytosis. However, the subcellular fate of the NPs will depend on their properties. [40,84] Upon vesicle formation, they enter into the endocytic pathway where pH progressively decreases with the vesicle maturation process. The biological purpose of this process is to activate the endolysosomal proteases to digest the cargo into smaller peptides for signal transduction, antigen-presentation for immune surveillance, and cellular and organismal homeostasis. However, NPs with pH buffering capacity can inhibit this process, disrupt the endosomal membrane, and escape from the endosome, by the proton sponge effect. [57,59,60] Reaching the cytoplasmic space is critical for the delivery of mRNA into the cytosol, where the ribosomes that will translate it into the coded protein for its expression are located.

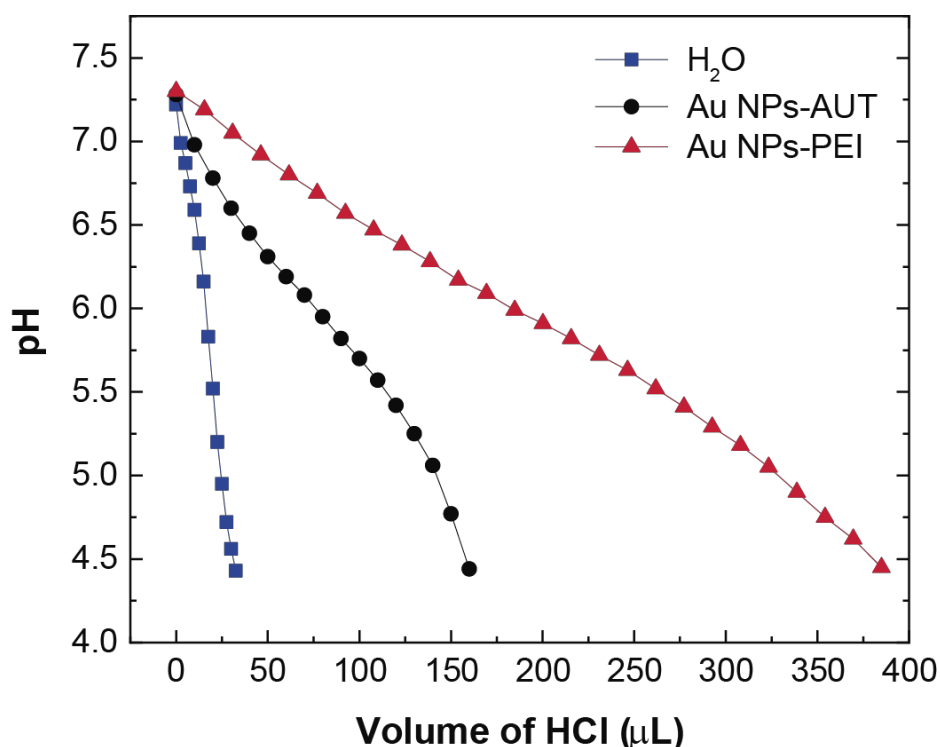


Figure 2.19. Proton Sponge Efficacy. The proton buffer capacity of the cationic-coated Au NPs was analysed by measuring the decrease in pH as a function of HCl volume added to the solution.

The proton sponge efficiency of cationic Au NPs was tested *in vitro* (**Figure 2.19**). First, the pH of the NPs solution was brought to 7.3, as in homeostatic physiological conditions and cell culture media. Then, in order to mimic the lysosome acidification process, HCl was added while the pH was monitored continuously until it dropped to 4.4. The proton

sponge efficiency of the NPs was evaluated as a function of the HCl added, thus H^+ , needed to reach the same pH value. As it can be observed in the graph, PEI and AUT-coated NP solutions present a delay in the pH drop compared to the water solution used as reference. This happens because part of the added protons, instead of entering into the water equilibrium $[H_3O^+ + OH^- \rightleftharpoons H_2O]$ that determines the pH value, they are protonating the amine residues on the AUT and PEI molecules. Further, the Au NPs-PEI show a much greater ability to capture protons, compared to NPs-AUT. This correlates with the fact that the amine concentration of the PEI-coated NPs is higher since PEI ($M_w \sim 2000$) has 7202 amines for each PEI molecule compared to AUT ($M_w = 240$), which only has 1 terminal amine residue.

2.3.2.4 TEM Imaging of Nanoparticles Uptake

The observation of cells exposed to cationic NP and nanovectors by confocal microscopy confirmed their internalization, but lacked to provide their subcellular location. Aiming to study the intracellular trafficking of the nanovector in more detail, exposed cells were observed by electron microscopy to reveal the cellular ultrastructure. For this, HEK293 cells were incubated for 24h with PEI-coated 20 nm Au NPs.

TEM imaging of the samples reveals that NPs follow an internalization pathway via endocytosis. Representative TEM images of the proposed process are shown in **Figure 2.20**. First, NPs-PEI stuck to the cell membrane (**Figure 2.20A**) from where they were internalized in endocytic vesicles (**Figure 2.20B**). On a typical endocytosis process, the maturation of these vesicles has several steps from early and late endosomes to amphisomes, to finally reach the active lysosome stage where the cargo is digested by the proteases. In this case, it could be observed that close to 85% of the internalized NPs-PEI were found either in amphisomes (**Figure 2.20C**) or in lysosomes (**Figure 2.20D**). However, the 15% remaining were located dispersed in the cytoplasmic space (**Figure 2.20E**). This entails the fact that NPs-PEI escaped from the endocytic pathway at some point after their endocytosis. As discussed before, the coating of Au NPs with PEI may confer proton sponge capacity allowing for an endosomal escape, as both results suggest.

Further, this results are of remarkable significance since they confirm that cationic functionalized NPs could reach the cytoplasmic space, which is critical in their later use as mRNA delivery vectors.

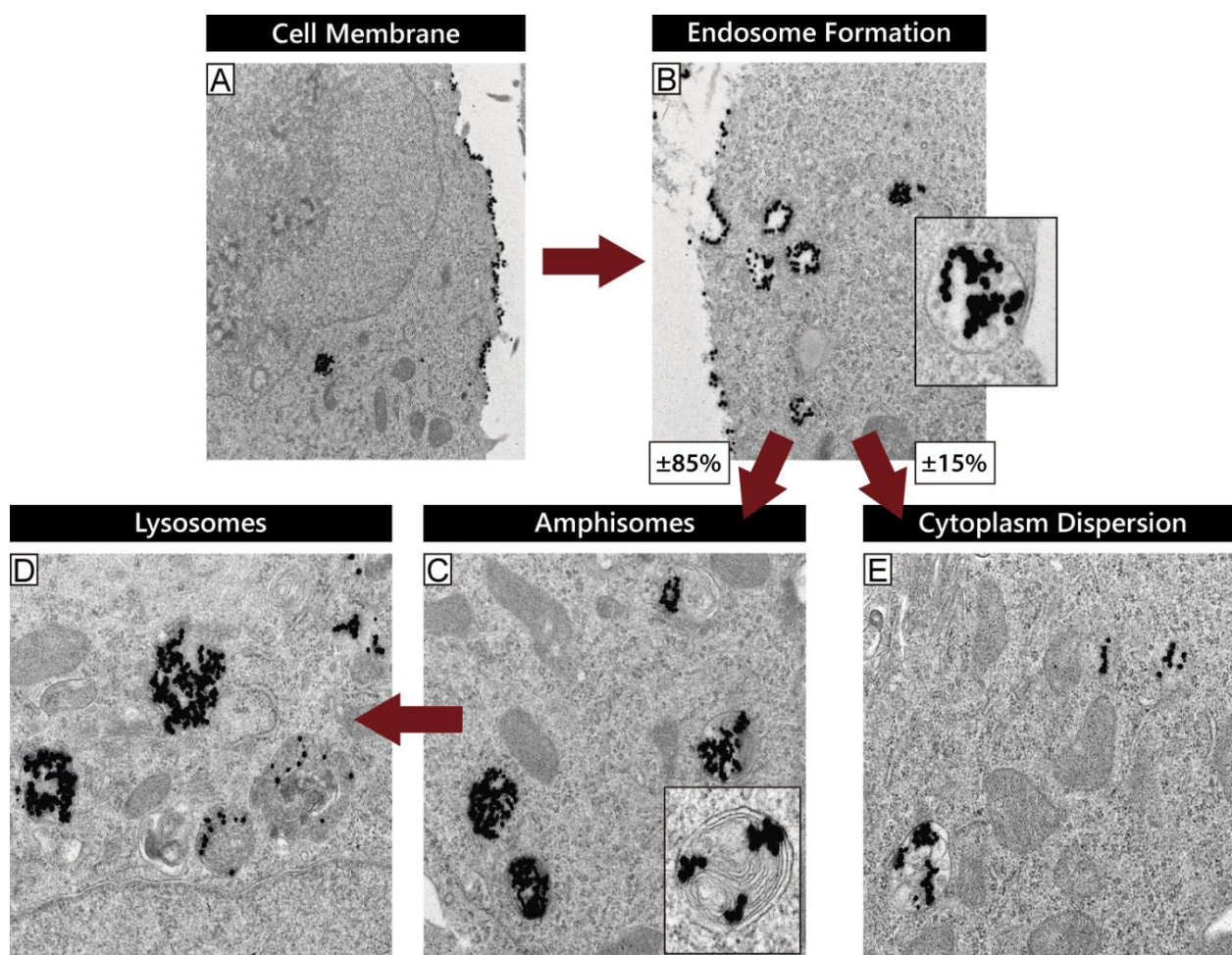


Figure 2.20. Au NP-PEI Intracellular Trafficking on HEK293 cells. Representative transmission electron microscopy images from HEK293 cells exposed to PEI-coated 20 nm Au NPs. The proposed internalization pathway is schematically represented at the different stages: **(A)** membrane attachment, **(B)** internalization in endosomes, maturation to **(C)** amphisomes and later **(D)** lysosomes. **(E)** Shows NPs dispersed in the cytoplasmic space after escaping from the endosomes. Images provided by the Nanobiology Unit at Istituto di Ricerche Farmacologiche Mario Negri.

2.3.2.5 ssDNA Release Kinetics from Nanovectors

Once nanovectors have reached the cytoplasmic space, a critical point for the success and efficiency in protein expression is the release of the adsorbed mRNA from the cationic NP conjugates. Previous results suggest that the interaction between both entities is strong, based on electrostatic forces. The main trigger for the release is the increase in the pH, first from the MES buffer to the culture media (that would correspond to the unintended burst release of nanovectors, the loss of loading before reaching the target) and then from the lysosome to the cytoplasmic space. The pH increase weakens the bond between the NP and the mRNA, which detaches and can be translated by the ribosome. Failing in its release from the NP's surface could critically impact in the protein expression.

The release of ssDNA from the nanovector construct was studied over time. For this, 50 nm Au NPs coated with AUT and PEI were first loaded with ssDNA. After 24h of incubation, nanovectors were dispersed in PB 10mM (pH 7.4) to a final relative volume of 10%. These experimental settings mimic the physiological conditions in transfection experiments, regarding the pH of the culture media and NP dilution within it. These experiments allow to study the nanovector behaviour and provide a deeper understanding of its role as a transfection vector.

As it can be observed in **Figure 2.21A**, there is a sustained increasing release of ssDNA over time for both types of nanovectors. The release is represented as a percentage from the quantified ssDNA load. NPs-PEI show a slightly higher rate of release, more remarkable at 24h. The detachment of ssDNA from the cationic NP is probably triggered by the pH increase, which lowers the net surface charge of the cationic coating as discussed in section 2.3.2.1. The loss of positive charge weakens the electrostatic interaction between the oligonucleotide and the NP, which displaces the dynamic equilibrium towards a ssDNA release in the dispersion media.

The characterization of the nanovectors at different time points of exposure to PB 10 mM also revealed changes in their physicochemical properties. Their evolution was monitored by UV-Vis spectroscopy, DLS and Z-Potential and the results are summarized in **Figure 2.21B** for the AUT-coated NPs and in **Figure 2.21C** for the PEI-coated NPs. In both cases, the SPR peak position blue-shifts progressively in time up to a $\Delta 2\text{nm}$ that indicated a modification of the NP's surface that correlates well with a partial detachment of the ssDNA corona. On the other hand, an increase in the DLS size can be observed, that exacerbates after the purification process. This could be explained as a loss in the colloidal stability of the nanovectors during ssDNA release in the media of study. Finally, inconsistencies are found regarding the Z-Potential measurements. Slight fluctuations in the surface charge of the NPs-AUT upon dispersion in PB 10 mM, but overall the net charge remains in the negative range. This stands in agreement with the fact that only a fraction of ssDNA has detached from the nanovector. However, regarding the NPs-PEI Z-Potential is consistently positive despite the loading of ssDNA, as previously discussed. There is a considerable drop from +53 mV to +40 mV, since the overall surface charge of this construct corresponds to the PEI, that could be explained by a loss of charge due to the pH increase. Yet, no evident conclusions could be drawn from the Z-Potential analysis.

These results point out a slow release of ssDNA (thus probably mRNA) from the nanovector that would contribute to a delayed delivery of the mRNA which could extend the expression of the coded protein. Besides, still a big fraction of the loaded ssDNA is bound on the nanovector. In this regard, endocytosis of NP usually happens at short times, approximately within the first 4h, when the release rate is still rather low. This would ensure that most of the mRNA release on the transfection would happen inside the cell.

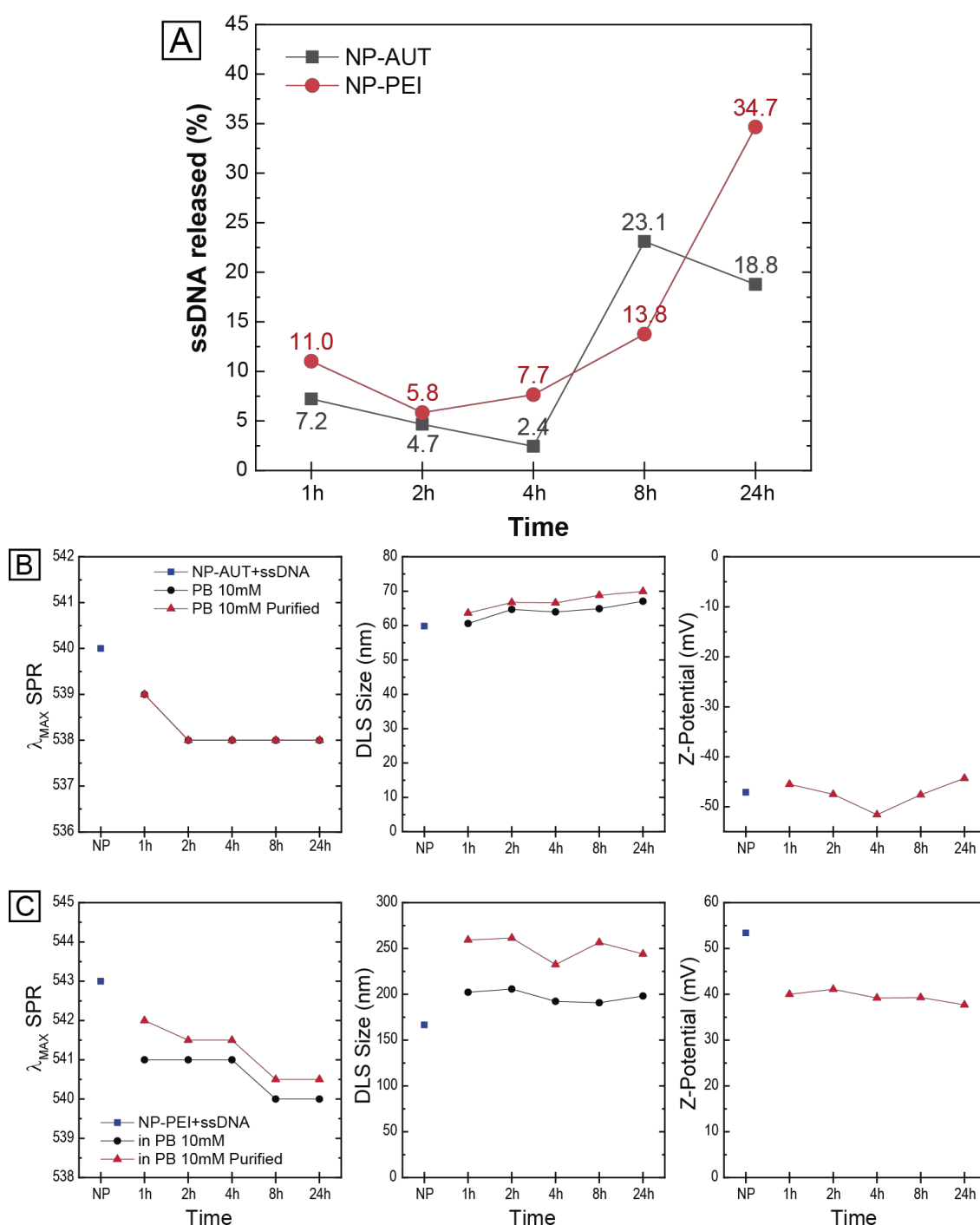


Figure 2.21. ssDNA Release Kinetics. (A) ssDNA released from the cationic nanoparticle over time, respect to the total ssDNA loaded. Release kinetics were studied as a function of time, characterized by UV-Vis spectroscopy, DLS and Z-Potential. SPR peak position, measured average size and surface charge at each time point are plotted, for AUT (B) and PEI (C) coated Au NPs.

2.3.3 Transfection of mRNA with Nanovectors

HEK293 cultured cells were exposed to nanovectors to identify the best formulation regarding cell survival and mRNA stability against degradation and efficacy for protein expression, compared to state-of-the-art TransIT® transfection vehicle. Green fluorescence protein (GFP) coding mRNA was used as a model to study the efficacy of the different nanovectors. Protein expression was analysed by conventional fluorescence and confocal microscopy, and flow cytometry. Special attention was paid at the sustained release and sustained expression, and the safety of the new employed nanovectors.

Additionally, alternative ways for improving mRNA delivery were also explored. Although, transient chemical protonation of the cell surface has been reported to enhance endocytic-like uptake of NPs, [24,25] no improvement was observed in this case. In contrast, the combined use of nanovectors and chloroquine showed promising results in enhancing GFP expression on the transfected cells without compromising safety.

2.3.3.1 Transfection Efficiency of Nanovectors

The effectiveness of Au transfection in HEK293 cells was assayed using 5, 20 and 50 nm Au NP coated with PEI and AUT, loaded with *GFP* mRNA. The GFP expression was analysed in a short (24 and 48 h) and long (7 days) times post-transfection, by flow cytometry (**Figure 2.23**) and fluorescence microscopy (**Figure 2.22**). For this, HEK293 cells at 70% of confluence were transfected with colloiddally stable nanovectors.

The observation of the transfected cells by fluorescence microscopy allowed for a first visual inspection of the samples to evaluate qualitatively cell morphology and transfection efficiency. **Figure 2.22B** shows the transient expression of GFP. As it can be seen, all the Au NP-PEI were capable to transfect the HEK293 cells. However, some morphological and adherence changes were observed, especially after exposition to 5nm NPs-PEI, as reported in the previous section. Interestingly, the expression of the GFP protein was preserved for 7 days. On the contrary, the transfection performed with the AUT-coated nanovectors was unsuccessful since no GFP expression was observed.

Regarding the transfection control, cells showed major changes in morphology and their adherence of the monolayer after the use of the commercial reagent TransIT®, indicating a high toxic effect due to membrane perturbation on the transfection process. Although a peak in GFP expression is observed at 48h, it decreased at 7 days after transfection.

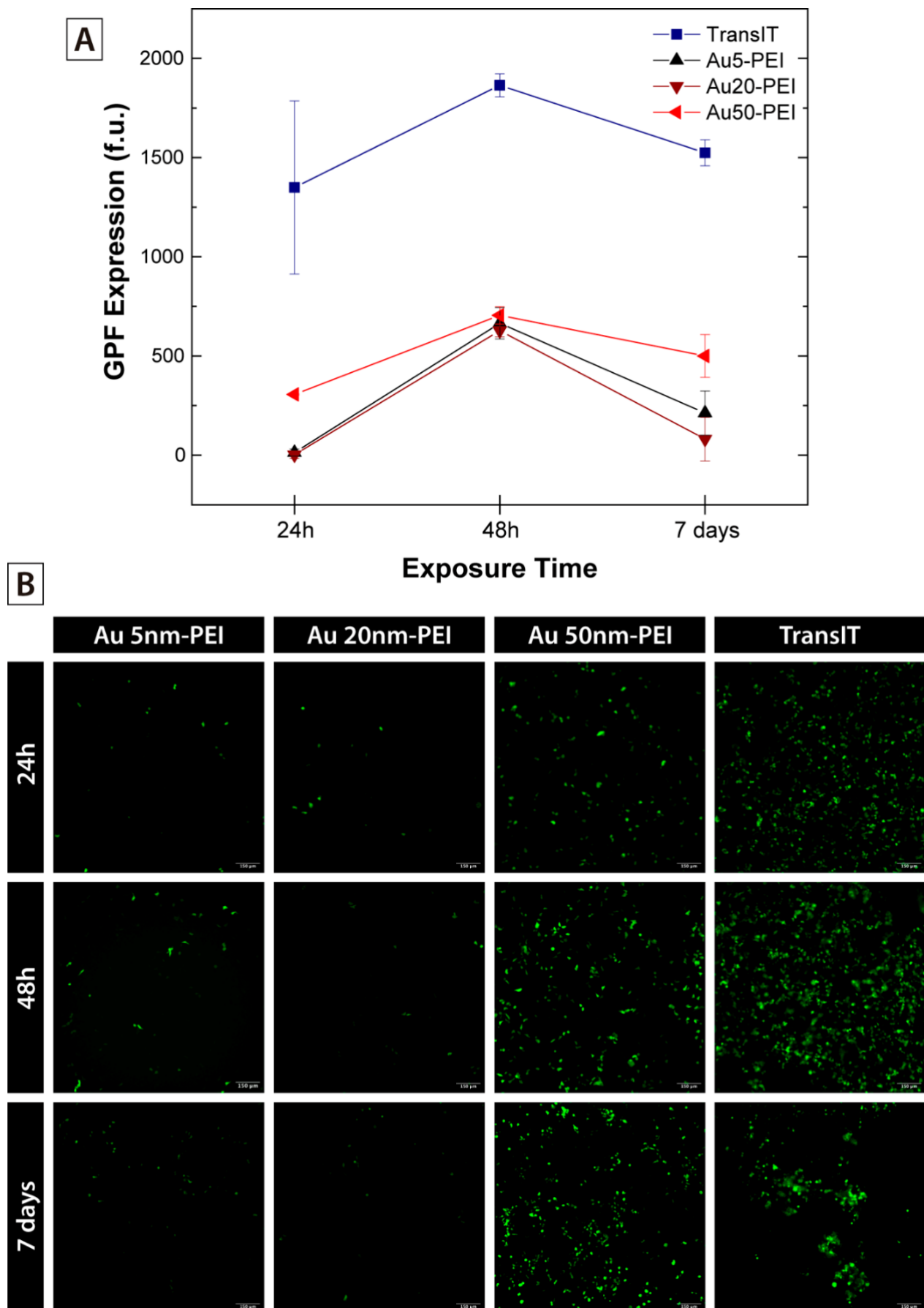


Figure 2.22. GFP Expression by Wide-Field Fluorescence Microscopy. (A) Quantification of the PEI-coated nanovectors transfection efficiency over time based on the mean GFP expression. (B) Wide-Field Fluorescence images of transfected HEK293 cells at 24h, 48h, and 7 days. Scale bar = 150 μm.

Further, the mean fluorescence intensity of GFP was quantified from the acquired images. As observed in **Figure 2.22A**, HEK293 cells transfected with TransIT® show the highest GFP fluorescence signal but with relative high intensity variability within the same population. Regarding the PEI-nanovectors, 50 nm NP show the highest efficiency on all time points, and GFP expressions is maintained to 7 days, while that from TransIT® has started decreasing.

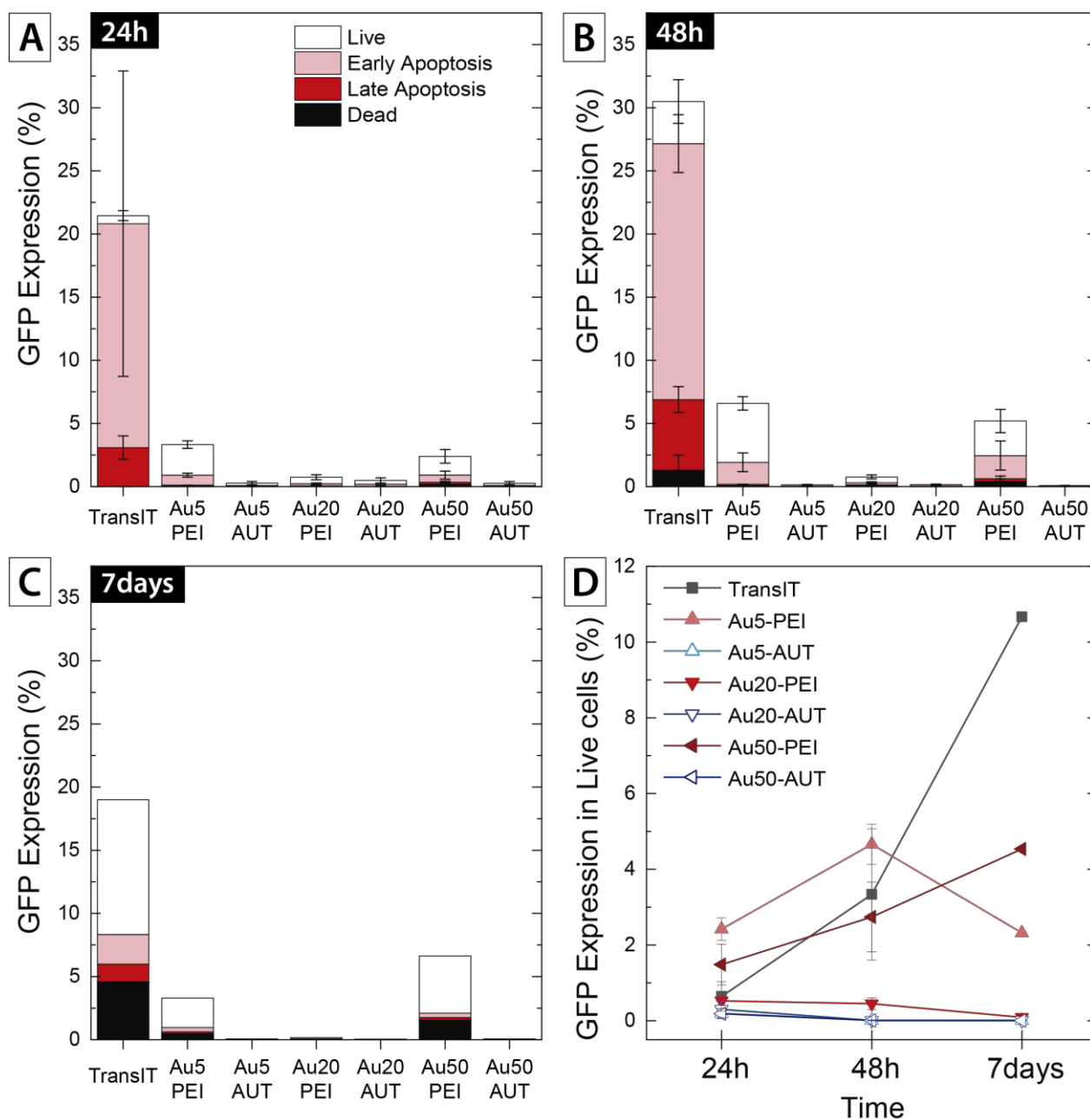


Figure 2.23. GFP Expression by Flow Cytometry. Quantification of the nanovectors transfection based on the mean GFP expression at 24h (A), 48h (B), and 7 days (C). Cell viability was analysed by Annexin V/PI iodine staining and cell state classified as live, in early or late apoptosis, or dead. (D) Summary of the GFP expression after transfection, in live cells population, as a function of time.

In a later experiment, the transfection efficiency from the total cell population was measured by flow cytometry. To gain further insights into the transfection events, cellular viability was evaluated using Annexin/PI in order to also study apoptosis or necrosis phenomena in those expressing GFP. Thus, GFP positive cells were sorted in live, early or late apoptosis, or dead depending on the relative intensity of both viability markers.

Figure 2.23A-C show the expression in live cells at 24h, 48h and 7 days. Similarly, as in the GFP fluorescence intensity quantification, all sizes of PEI-coated nanovectors showed GFP expression to some extent, whereas AUT-nanovectors did not succeed on mRNA delivery. However, it stands out the fact that when GFP expression is normalized to live cells (**Figure 2.23D**), differences between TransIT® and nanovectors dramatically decrease. This results reveal a high and prolonged transfection efficiency of HEK293 cells by PEI-nanovectors, which is coupled with low cytotoxicity, since the apoptosis cell ratio is not enhanced.

There is a need to understand the intracellular pathways to deliver the mRNA into a target cell. Although measuring the intracellular expression of GFP is an excellent way to investigate the transfection efficiency of NPs, it does not clarify the uptake mechanism and the consequent mRNA delivery. So, HEK293 cells were treated with chloroquine, a common compound used to halt endosomal maturation, in order to study its effects in boosting NP endosomal escape.

GFP expression was visualized by wide-field fluorescence microscopy (**Figure 2.24B**). As shown in **Figure 2.24A**, cells incubated with chloroquine for 4 hours prior to transfection exhibited enhanced transfection for PEI-nanovectors. The statistical analysis shows a significant fluorescence signal increase for 5nm and 50nm PEI-nanovectors, and higher but not significant for 20nm. Conversely, no enhancement effect was observed in cells transfected with AUT-coated nanovectors.

As largely reported in the literature, chloroquine enhances endosomal escape by the proton sponge effect. Chloroquine enters the endosome by membrane diffusion and is protonated during endosome maturation resulting in Cl^- and H_2O influx, endosome swelling and rupture, releasing endosomal cargoes into the cytoplasm. [85,86] Accordingly, this results support the hypothesis that Au NPs-PEI reach the cytoplasmic space via endosomal escape by the proton sponge mechanism. Also, this study provides new insights into the characterization of nanovectors that ensure suitable mRNA delivery into the cells without a cytotoxic effect.

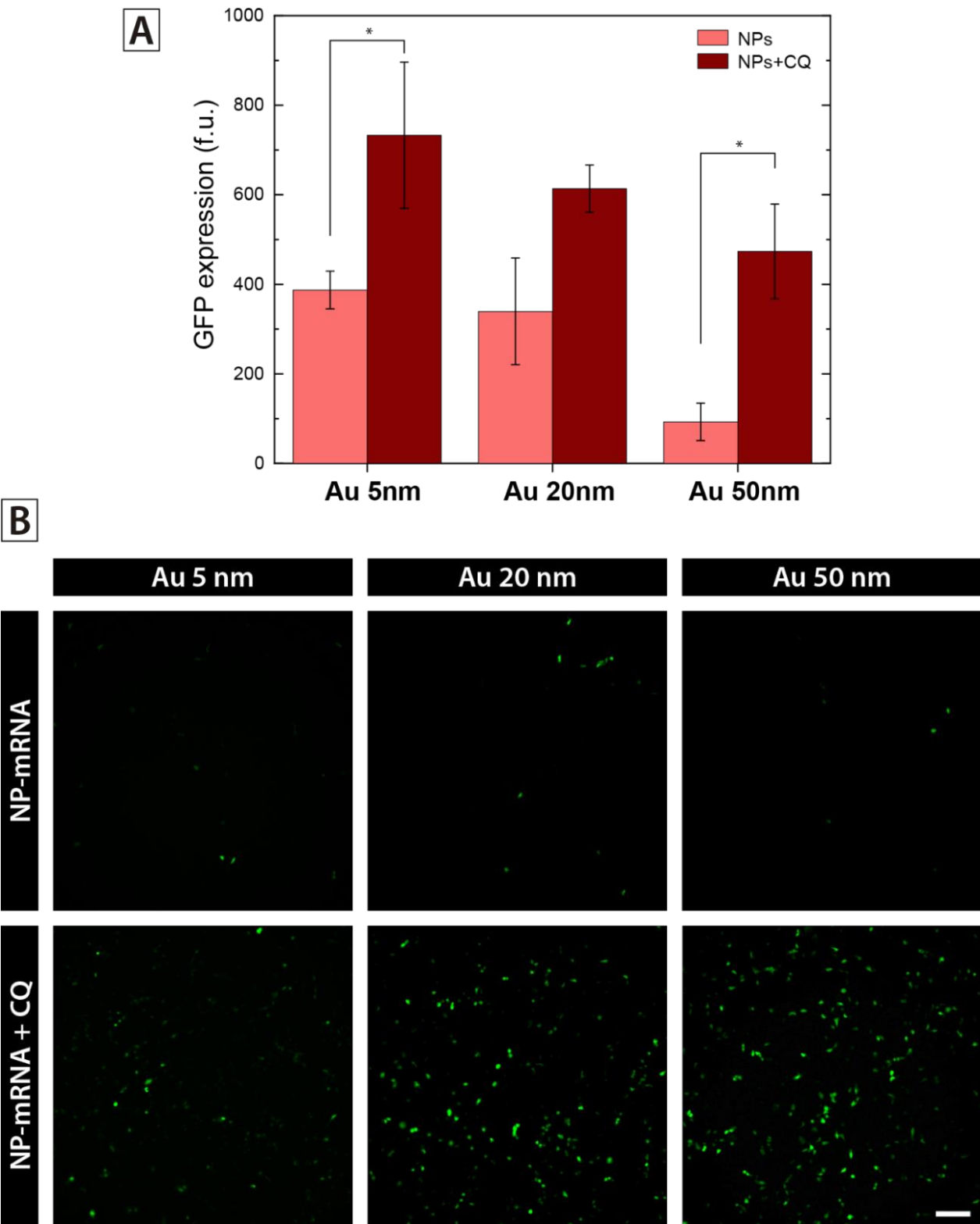


Figure 2.24. Effect of chloroquine in transfection. (A) Transfection efficiency based on the mean GFP expression at 24h. (* $p > 0.05$) **(B)** Wide-field Fluorescence images of HEK293 cells transfected with PEI-coated nanovectors, alone or in combination with chloroquine, at 24h. Scale bar = 150 μm .

2.3.3.2 Confocal Imaging of mRNA-GFP Transfected HEK293 cells

Next, the expression of GFP after the mRNA transfection on HEK293 cells was also visualized by wide-field and confocal microscopy. In this case, 20 nm and 50 nm NPs-PEI were used. Representative images are depicted in **Figure 2.25**. After 24h, cells were fixed and stained in order to reveal the cellular structure, nuclei and actin.

A first visual inspection of the transfection efficiency was performed at the Wide-Field Fluorescence microscope at low magnification (20X). In agreement with the flow cytometry results, a higher number of cells expressing GFP can be observed for the cells transfected with 50 nm NPs. GFP signal intensity is highly variable between the successfully transfected cell population. Also, the spatial distribution of the transfected cells is quite homogeneous, no GFP+ cell clusters or denser areas were found.

Observation of the samples under the CLSM enabled to image the Au NPs simultaneously by reflectance mode. Representative pictures at 40X and 60X magnifications are shown in **Figure 2.25**. Au NPs, either 20 nm or 50 nm, can be found homogeneously distributed all over the sample but mostly in the intracellular space. Conversely, no significant higher NP uptake by GFP+ cells is observed compared to the non-expressing population. These findings, coupled with the TEM observations of the NPs intracellular trafficking, may indicate that, despite most of the cells have internalized nanovectors, they are not located in the cytoplasmic space. Endosomal escape may happen later in time for these nanovectors, delaying the mRNA delivery and expression, which is also in agreement with the sustained GFP expression observed by flow cytometry. Additionally, variability in protein expression could be ascribed to differences in the cell cycle stage between the HEK293 population. [87]

On the other hand, magnification of the samples reveals that, despite the variability in GFP signal intensity between different cells, GFP expression is homogeneously distributed within a single transfected cell.

Differences in NP signal intensity between 20 nm and 50 nm NPs follow the same trend as discussed in section 2.3.2.2, where the nanovector uptake was analysed. Smaller NPs have lower intensity since they have very low or none light scattering contribution. Thus, they are only found in the intracellular space, or in an aggregation state, generally located inside vesicles where NP concentration is high.

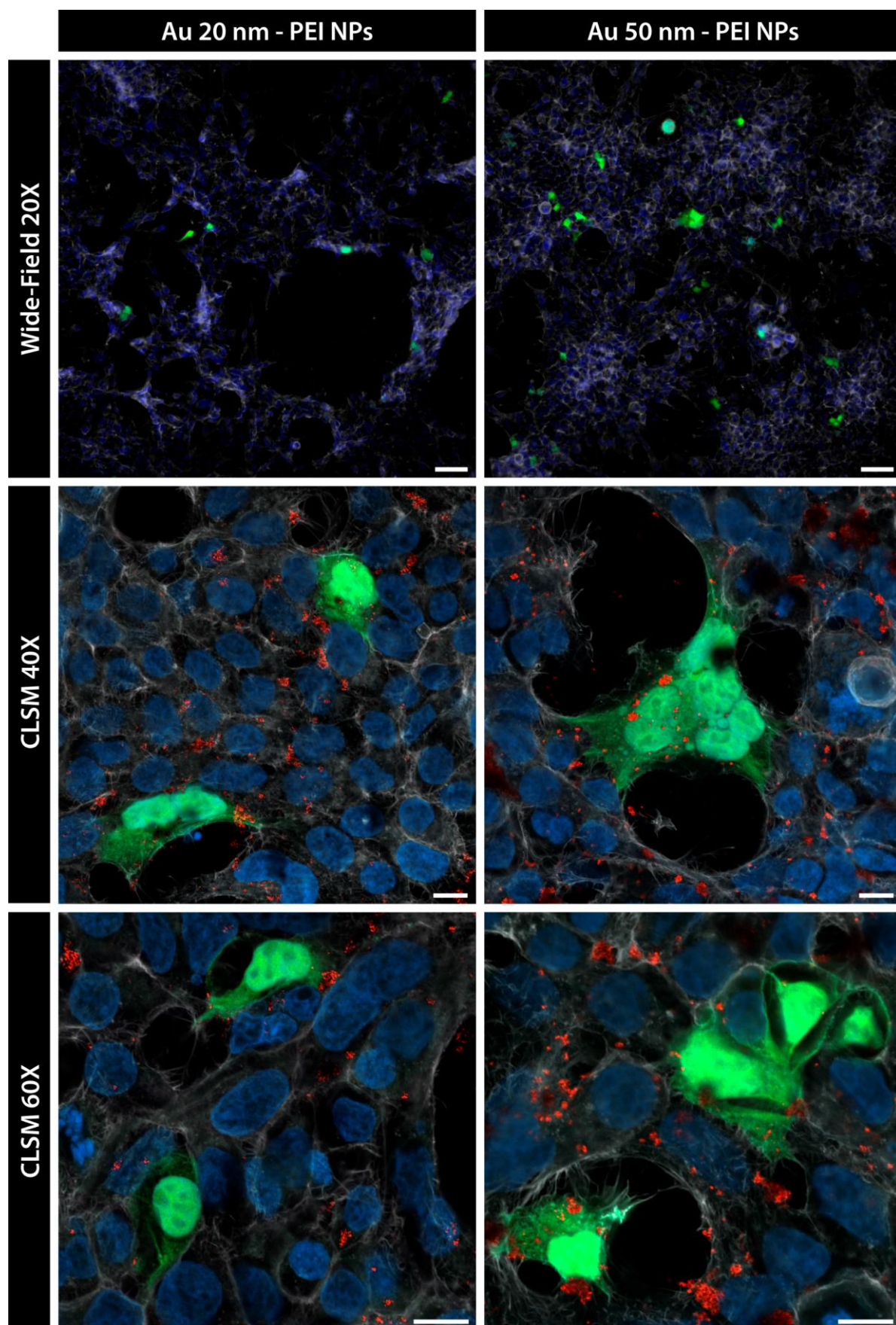


Figure 2.25. Wide-Field Fluorescence and Confocal Imaging of mRNA-GFP Transfected HEK293 cells. GFP (green) expression is observed in transfected cells with 20 nm and 50 nm PEI-coated nanovectors. For cell structure, actin (purple in WF, white in CLSM) and nuclei (blue) were stained. WF Scale Bar = 50 μ m. CLSM Scale Bar = 10 μ m.

2.3.4 Cytotoxicity and Risk Assessment of Nanovectors

A key point in the success of nanovectors as non-viral transfection vehicles must be their low cytotoxicity. Other current standard transfection methods, as TransIT® or Lipofectamine®, show good transfection rates but have very poor cell viability. It is claimed that their internalization pathway is through membrane disruption, which is what ultimately causes their toxicity. [26] In contrast, nanovectors seem to internalize via endocytosis reducing significantly the associated toxicity.

To evaluate the biosafety of Au NPs in HEK293 cells, we measured the cell viability percentage by Resazurin reduction using Prestoblue and the cell membrane integrity test by LDH quantification.

As shown in **Figure 2.26**, a slight decrease of the cell viability in HEK293 cells were determined with an exposition of 5 nm Au NPs coated with PEI and PEI-ssDNA at the maximum concentration of 3.3×10^{13} NP/ml during 24h and 48h. The cell membrane integrity was also compromised at the same NP concentration with a reduction of about 30% in viability. On the contrary, AUT-coated 5nm Au NP do not show any cytotoxic action. Regarding 20 nm and 50 nm Au NPs, non-significant variation in the cell viability between Au-treated and non-treated cells was quantified even when exposing the cells to the highest concentration, corresponding to 2.7×10^{12} NP/ml and 3×10^{11} NP/ml respectively. After seven days of exposure, the percentage of the cell viability only suffered a reduction close to 40% in the case of NPs-PEI. Further, membrane leakage was slightly increased in all the experimental cells groups. However, LDH release to the medium might be due to normal cell regeneration in culture.

Some previous studies reported Au NPs cytotoxicity is mediated by their size, which inhibited the proliferation and triggered cell cycle arrest. [88–90] However, the present results suggest that there is not such toxic effect related to NP size, at last in the studied range. Yet, cationic functionalization of the Au NPs did compromise cell viability and membrane integrity in some cases. Cell integrity could be affected by the interaction with the unbounded PEI in the NP's surface.

To gain further insight in the transfection associated toxicity, HEK293 cells were exposed to nanovectors and sorted based on their viability state. Annexin V/PI staining was used to categorize cell populations as live, in early or late apoptosis, and dead. Viability controls were also included, cells without any treatment for negative control, and H₂O₂ for positive

cell death control. In this experiment, TransIT® was also included to compare its toxicity with the NP-based nanovectors. Selected time points were the same as the ones for the transfections experiments, 24h, 48h and 7 days.

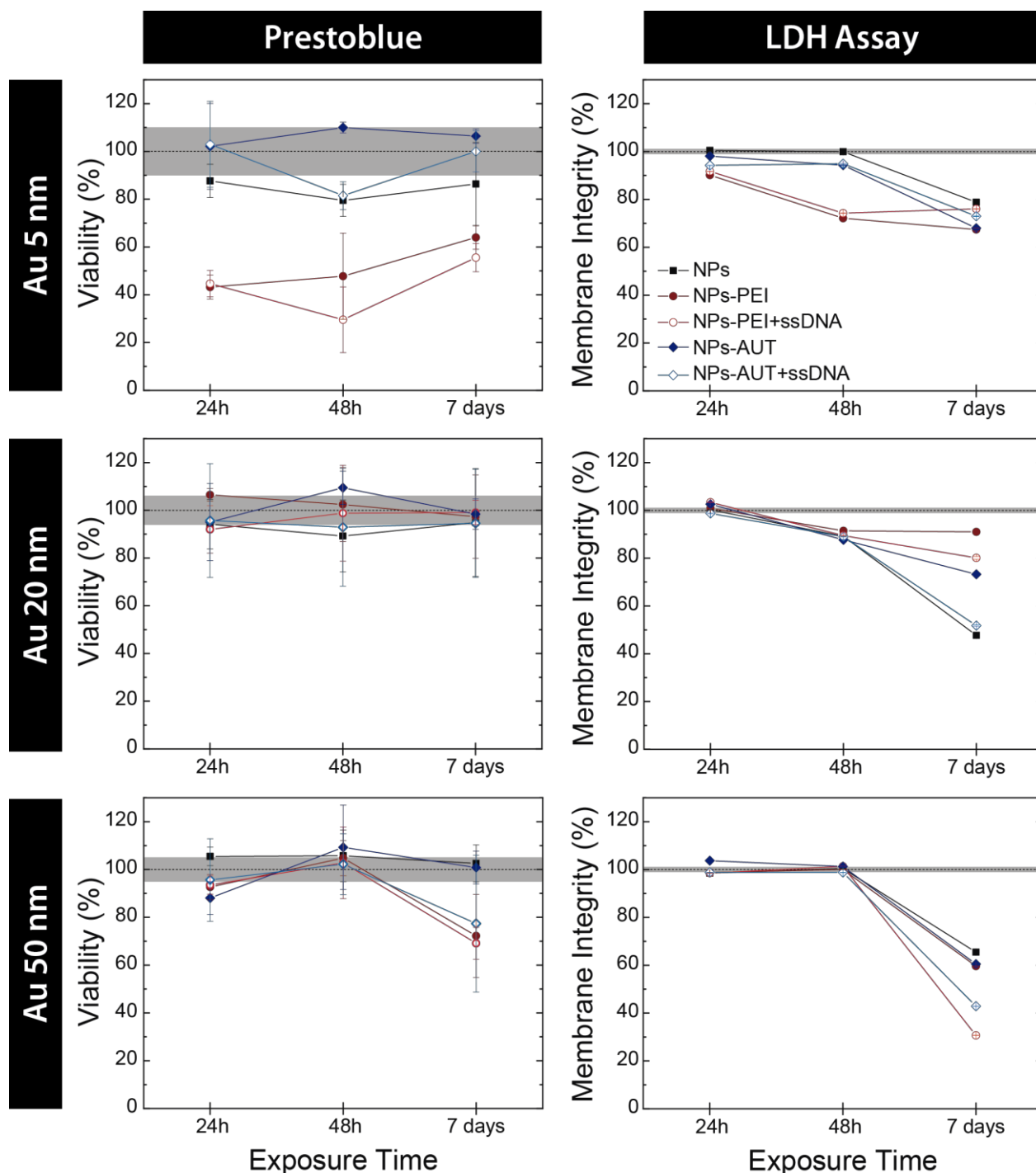


Figure 2.26. Nanovector Cytotoxicity Studies. The action of Au NP coated with PEI and AUT, and loaded ssDNA was tested at different concentrations. The percentage of resazurin reduction (left) and cell membrane integrity (right) are shown at the maximum Au nanoparticles concentration. Dashed line corresponds to control values for reference, and grey area overlaid to its relative standard deviation.

Results displayed in **Figure 2.27** show an evident difference in the viability profile of TransIT® compared to nanovectors at short times. While cationic NPs, either loaded with ssDNA or not, present a cell population distribution similar to the negative control, TransIT® exposed cells do oppositely. The proportion of cells in a pro-apoptotic state is much higher, comparable with the cells treated with H₂O₂. **Figure 2.27** shows how the proportion of phosphatidylserine-exposing HEK293 cells dramatically increases after transfection with TransIT®. The percentage of early and late apoptosis was maintained at 48 h. Accordingly, dead cells proportion increased at each incubation time. In contrast, cells transfected with the nanovectors preserved their viability and the apoptosis entrance was delayed. At 7 days post-exposure, viability values stabilized. Only a non-significant slight increase in the pro-apoptotic populations can be observed for TransIT® and 5 nm Au NPs-PEI. Once again, these results confirm that NP-based formulations are safe platforms for their use as delivery vectors.

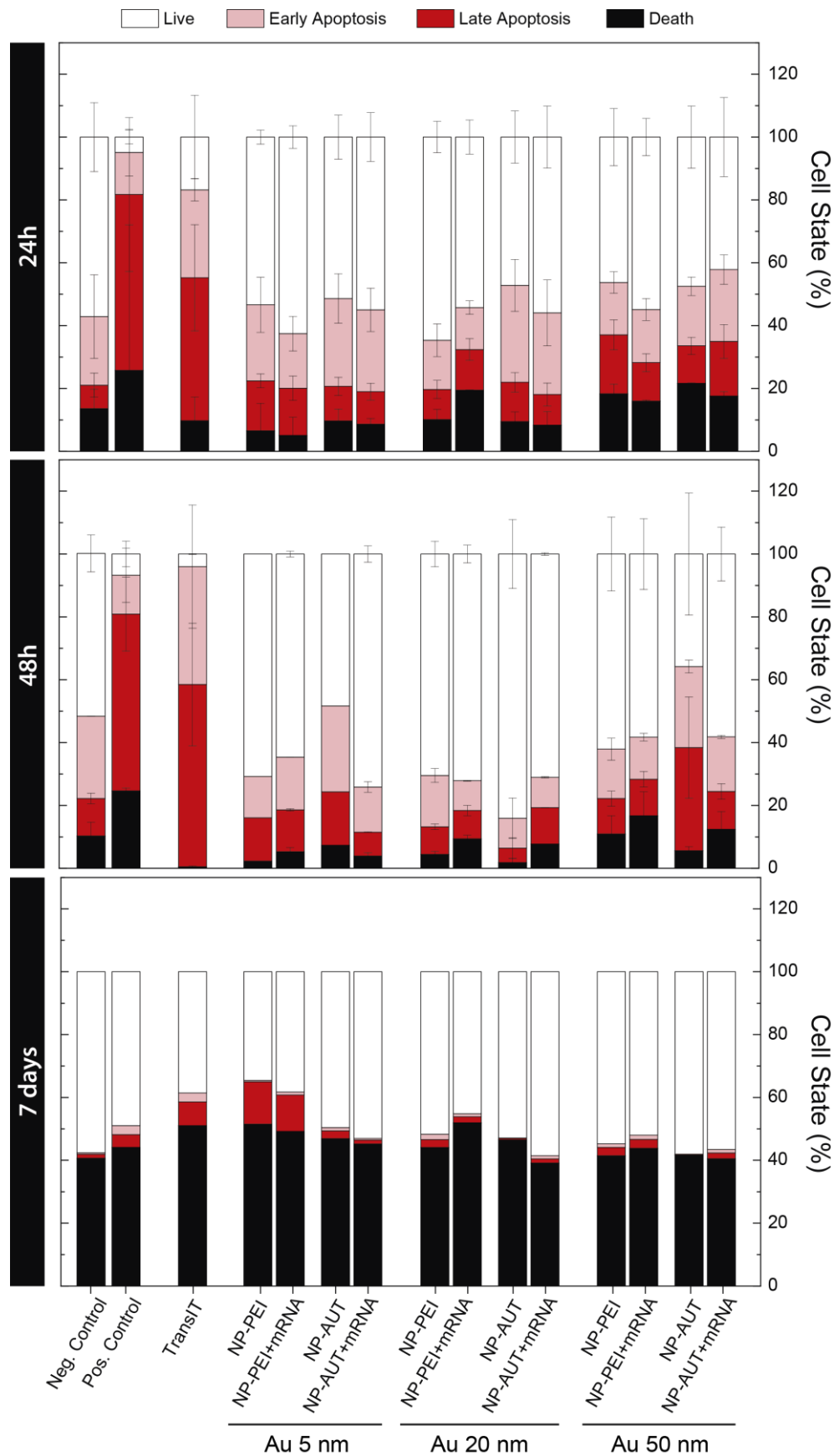


Figure 2.27. Nanovector Cytotoxicity by Annexin V/PI staining. After 24h, 48h, or 7 days of HEK293 cells exposition to cationic NPs, alone or loaded with ssDNA, Annexin V/PI staining was performed to analyse cell viability. Cell state was classified as live, in early or late apoptosis, or dead according to relative intensity of each marker

2.4 References

- [1] Rozman, C. & Montserrat, E. Chronic Lymphocytic Leukemia. *New England Journal of Medicine* 333, 1052–1057 (1995)
- [2] Porter, D. L., Hwang, W. T., Frey, N. V., Lacey, S. F., Shaw, P. A., Loren, A. W., Bagg, A., Marcucci, K. T., Shen, A., Gonzalez, V., Ambrose, D., Grupp, S. A., Chew, A., Zheng, Z., Milone, M. C., Levine, B. L., Melenhorst, J. J., & June, C. H. Chimeric antigen receptor T cells persist and induce sustained remissions in relapsed refractory chronic lymphocytic leukemia. *Science translational medicine* 7, (2015)
- [3] Fesnak, A. D., June, C. H., & Levine, B. L. Engineered T cells: the promise and challenges of cancer immunotherapy. *Nature Reviews Cancer* 16, 566–581 (2016)
- [4] Sermer, D. & Brentjens, R. CAR T-cell therapy: Full speed ahead. *Hematological Oncology* 37, 95–100 (2019)
- [5] Jackson, H. J., Rafiq, S., & Brentjens, R. J. Driving CAR T-cells forward. *Nature Reviews Clinical Oncology* 13, 370–383 (2016)
- [6] Levine, B. L., Miskin, J., Wonnacott, K., & Keir, C. Global Manufacturing of CAR T Cell Therapy. *Molecular Therapy - Methods & Clinical Development* 4, 92–101 (2017)
- [7] Zhao, Y., Moon, E., Carpenito, C., Paulos, C. M., Liu, X., Brennan, A. L., Chew, A., Carroll, R. G., Scholler, J., Levine, B. L., Albelda, S. M., & June, C. H. Multiple injections of electroporated autologous T cells expressing a chimeric antigen receptor mediate regression of human disseminated tumor. *Cancer research* 70, 9053–9061 (2010)
- [8] Brudno, J. N. & Kochenderfer, J. N. Recent advances in CAR T-cell toxicity: Mechanisms, manifestations and management. *Blood Reviews* 34, 45–55 (2019)
- [9] Bonifant, C. L., Jackson, H. J., Brentjens, R. J., & Curran, K. J. Toxicity and management in CAR T-cell therapy. *Molecular Therapy - Oncolytics* 3, 16011 (2016)
- [10] Namuduri, M. & Brentjens, R. J. Medical management of side effects related to CAR T cell therapy in hematologic malignancies. *Expert Review of Hematology* vol. 9 511–513 (2016)
- [11] Shukla, R., Shanmugam, R. K., Ramasamy, V., Arora, U., Batra, G., Acklin, J. A., Krammer, F., Lim, J. K., Swaminathan, S., & Khanna, N. Zika virus envelope nanoparticle antibodies protect mice without risk of disease enhancement. *EBioMedicine* 54, (2020)
- [12] Rong, H., Qi, M., Pan, J., Sun, Y., Gao, J., Zhang, X., Li, W., Zhang, B., Zhang, X.-E., & Cui, Z. Self-Assembling Nanovaccine Confers Complete Protection Against Zika Virus Without Causing Antibody-Dependent Enhancement. *Frontiers in Immunology* 0, 2169 (2022)
- [13] Thi, T. T. H., Suys, E. J. A., Lee, J. S., Nguyen, D. H., Park, K. D., & Truong, N. P. Lipid-Based Nanoparticles in the Clinic and Clinical Trials: From Cancer

- Nanomedicine to COVID-19 Vaccines. *Vaccines* 9, 359 (2021)
- [14] Guerrini, G., Magrì, D., Gioria, S., Medaglini, D., & Calzolari, L. Characterization of nanoparticles-based vaccines for COVID-19. *Nature Nanotechnology* 17, 570–576 (2022)
- [15] McLenachan, S., Zhang, D., Palomo, A. B. A., Edel, M. J., Chen, F. K., Abrous, D., Koehl, M., Li, H., *et al.* mRNA Transfection of Mouse and Human Neural Stem Cell Cultures. *PLoS ONE* 8, e83596 (2013)
- [16] Zhao, Y., Moon, E., Carpenito, C., Paulos, C. M., Liu, X., Brennan, A. L., Chew, A., Carroll, R. G., Scholler, J., Levine, B. L., Albelda, S. M., & June, C. H. Multiple Injections of Electroporated Autologous T Cells Expressing a Chimeric Antigen Receptor Mediate Regression of Human Disseminated Tumor. *Cancer Research* 70, (2010)
- [17] Beatty, G. L., Haas, A. R., Maus, M. V., Torigian, D. A., Soulen, M. C., Plesa, G., Chew, A., Zhao, Y., Levine, B. L., Albelda, S. M., Kalos, M., & June, C. H. Mesothelin-specific chimeric antigen receptor mRNA-engineered T cells induce anti-tumor activity in solid malignancies. *Cancer immunology research* 2, 112–120 (2014)
- [18] Maus, M. V., Haas, A. R., Beatty, G. L., Albelda, S. M., Levine, B. L., Liu, X., Zhao, Y., Kalos, M., & June, C. H. T cells expressing chimeric antigen receptors can cause anaphylaxis in humans. *Cancer immunology research* 1, 26–31 (2013)
- [19] Wang, Z., Wu, Z., Liu, Y., & Han, W. New development in CAR-T cell therapy. *Journal of Hematology and Oncology* 10, 1–11 (2017)
- [20] Yeom, J. H., Ryou, S. M., Won, M., Park, M., Bae, J., & Lee, K. Inhibition of Xenograft Tumor Growth by Gold Nanoparticle-DNA Oligonucleotide Conjugates-Assisted Delivery of BAX mRNA. *PLoS ONE* 8, 75369 (2013)
- [21] Moffett, H. F., Coon, M. E., Radtke, S., Stephan, S. B., McKnight, L., Lambert, A., Stoddard, B. L., Kiem, H. P., & Stephan, M. T. Hit-and-run programming of therapeutic cytoreagents using mRNA nanocarriers. *Nature Communications* 8, 389 (2017)
- [22] Rosi, N. L., Giljohann, D. A., Thaxton, C. S., Lytton-Jean, A. K. R., Han, M. S., & Mirkin, C. A. Oligonucleotide-Modified Gold Nanoparticles for Intracellular Gene Regulation. *Science* 312, (2006)
- [23] Islam, M. A., Reesor, E. K. G., Xu, Y., Zope, H. R., Zetter, B. R., & Shi, J. Biomaterials for mRNA delivery. *Biomaterials Science* 3, 1519–1533 (2015)
- [24] Ben-Dov, N., Korenstein, R., Doherty, G., McMahon, H., Baumgart, T., Capraro, B., Zhu, C., Pozzan, T., *et al.* Enhancement of Cell Membrane Invaginations, Vesiculation and Uptake of Macromolecules by Protonation of the Cell Surface. *PLoS ONE* 7, e35204 (2012)
- [25] Ben-Dov, N., Rozman Grinberg, I., Korenstein, R., Villemejeane, J., Mir, L., Ho, S., Mittal, G., Rols, M., *et al.* Electroendocytosis Is Driven by the Binding of Electrochemically Produced Protons to the Cell's Surface. *PLoS ONE* 7, e50299

(2012)

- [26] Meng, Z., O’Keeffe-Ahern, J., Lyu, J., Pierucci, L., Zhou, D., & Wang, W. A new developing class of gene delivery: messenger RNA-based therapeutics. *Biomaterials Science* 5, 2381–2392 (2017)
- [27] Grabbe, S., Haas, H., Diken, M., Kranz, L. M., Langguth, P., & Sahin, U. Translating nanoparticulate-personalized cancer vaccines into clinical applications: Case study with RNA-lipoplexes for the treatment of melanoma. *Nanomedicine* 11, 2723–2734 (2016)
- [28] Connor, E. E., Mwamuka, J., Gole, A., Murphy, C. J., & Wyatt, M. D. Gold Nanoparticles Are Taken Up by Human Cells but Do Not Cause Acute Cytotoxicity. *Small* 1, 325–327 (2005)
- [29] Daniel, M.-C. & Astruc, D. Gold nanoparticles: assembly, supramolecular chemistry, quantum-size-related properties, and applications toward biology, catalysis, and nanotechnology. *Chemical reviews* 104, 293–346 (2004)
- [30] Love, J. C., Estroff, L. A., Kriebel, J. K., Nuzzo, R. G., & Whitesides, G. M. Self-assembled monolayers of thiolates on metals as a form of nanotechnology. *Chemical Reviews* 105, 1103–1169 (2005)
- [31] Rana, S., Bajaj, A., Mout, R., & Rotello, V. M. Monolayer coated gold nanoparticles for delivery applications. *Advanced Drug Delivery Reviews* 64, 200–216 (2012)
- [32] Khlebtsov, N. & Dykmana, L. Biodistribution and toxicity of engineered gold nanoparticles: a review of in vitro and in vivo studies. *Chemical Society reviews* 40, 1647–1671 (2011)
- [33] Zhang, T., Chen, P., Sun, Y., Xing, Y., Yang, Y., Dong, Y., Xu, L., Yang, Z., & Liu, D. A new strategy improves assembly efficiency of DNA mono-modified gold nanoparticles. *Chemical Communications* 47, 5774–5776 (2011)
- [34] Guo, S., Huang, Y., Jiang, Q., Sun, Y., Deng, L., Liang, Z., Du, Q., Xing, J., Zhao, Y., Wang, P. C., Dong, A., & Liang, X. J. Enhanced gene delivery and siRNA silencing by gold nanoparticles coated with charge-reversal polyelectrolyte. *ACS nano* 4, 5505–5511 (2010)
- [35] Park, S. & Hamad-Schifferli, K. Enhancement of in vitro translation by gold nanoparticle-DNA conjugates. *ACS Nano* 4, 2555–2560 (2010)
- [36] Eck, W., Craig, G., Sigdel, A., Ritter, G., Old, L. J., Tang, L., Brennan, M. F., Allen, P. J., & Mason, M. D. PEGylated gold nanoparticles conjugated to monoclonal F19 antibodies as targeted labeling agents for human pancreatic carcinoma tissue. *ACS nano* 2, 2263–2272 (2008)
- [37] Huang, X., El-Sayed, I. H., Qian, W., & El-Sayed, M. A. Cancer cell imaging and photothermal therapy in the near-infrared region by using gold nanorods. *Journal of the American Chemical Society* 128, 2115–2120 (2006)
- [38] Calzolari, L., Franchini, F., Gilliland, D., & Rossi, F. Protein-nanoparticle interaction: Identification of the ubiquitin-gold nanoparticle interaction site. *Nano Letters* 10, 3101–3105 (2010)

- [39] Aubin-Tam, M. E. & Hamad-Schifferli, K. Gold nanoparticle-cytochrome c complexes: The effect of nanoparticle ligand charge on protein structure. *Langmuir* 21, 12080–12084 (2005)
- [40] Shan, Y., Ma, S., Nie, L., Shang, X., Hao, X., Tang, Z., & Wang, H. Size-dependent endocytosis of single gold nanoparticles. *Chemical Communications* 47, 8091–8093 (2011)
- [41] Lesniak, A., Salvati, A., Santos-Martinez, M. J., Radomski, M. W., Dawson, K. A., & Åberg, C. Nanoparticle adhesion to the cell membrane and its effect on nanoparticle uptake efficiency. *Journal of the American Chemical Society* 135, 1438–1444 (2013)
- [42] Cheng, X., Tian, X., Wu, A., Li, J., Tian, J., Chong, Y., Chai, Z., Zhao, Y., Chen, C., & Ge, C. Protein Corona Influences Cellular Uptake of Gold Nanoparticles by Phagocytic and Nonphagocytic Cells in a Size-Dependent Manner. *ACS Applied Materials and Interfaces* 7, 20568–20575 (2015)
- [43] Liu, X., Huang, N., Li, H., Jin, Q., & Ji, J. Surface and size effects on Cell interaction of gold nanoparticles with both phagocytic and nonphagocytic cells. *Langmuir* 29, 9138–9148 (2013)
- [44] Casals, E., Pfaller, T., Duschl, A., Oostingh, G. J., & Puentes, V. Time evolution of the nanoparticle protein corona. *ACS Nano* 4, 3623–3632 (2010)
- [45] Casals, E., Pfaller, T., Duschl, A., Oostingh, G. J., & Puentes, V. F. Hardening of the Nanoparticle–Protein Corona in Metal (Au, Ag) and Oxide (Fe₃O₄, CoO, and CeO₂) Nanoparticles. *Small* 7, 3479–3486 (2011)
- [46] Casals, E., Gusta, M. F., Montana, L., Mendoza, M., Maiz, N., Carreras, E., & Puentes, V. Nanotechnology for Maternal Foetal Medicine. *Int J Ped & Neo Heal* 2, 57–66 (2018)
- [47] Barbero, F., Russo, L., Vitali, M., Piella, J., Salvo, I., Borrajo, M. L., Busquets-Fité, M., Grandori, R., Bastús, N. G., Casals, E., & Puentes, V. Formation of the Protein Corona: The Interface between Nanoparticles and the Immune System. *Seminars in Immunology* 34, 52–60 (2017)
- [48] Hill, R. J. Hydrodynamics and electrokinetics of spherical liposomes with coatings of terminally anchored poly(ethylene glycol): numerically exact electrokinetics with self-consistent mean-field polymer. *Physical review. E, Statistical, nonlinear, and soft matter physics* 70, 16 (2004)
- [49] Comenge, J., Sotelo, C., Romero, F., Gallego, O., Barnadas, A., Parada, T. G.-C., Domínguez, F., & Puentes, V. F. Detoxifying Antitumoral Drugs via Nanoconjugation: The Case of Gold Nanoparticles and Cisplatin. *PLoS ONE* 7, e47562 (2012)
- [50] Han, H. Y., Ro, K. E., & McPherson, B. A. Stability of Gold Nanoparticle-Bound DNA toward Biological, Physical, and Chemical Agents. *Chemical Biology & Drug Design* 67, 78–82 (2006)
- [51] Canton, I. & Battaglia, G. Endocytosis at the nanoscale. *Chemical Society Reviews*

- 41, 2718–2739 (2012)
- [52] Horn, J. M. & Obermeyer, A. C. Genetic and Covalent Protein Modification Strategies to Facilitate Intracellular Delivery. *Biomacromolecules* 22, 4883–4904 (2021)
 - [53] Wu, D., Zhu, X., Ao, J., Song, E., & Song, Y. Delivery of Ultrasmall Nanoparticles to the Cytosolic Compartment of Pyroptotic J774A.1 Macrophages via GSDMDNtermMembrane Pores. *ACS Applied Materials and Interfaces* 13, 50823–50835 (2021)
 - [54] Iqbal, S., Luo, B., Melamed, J. R., & Day, E. S. Critical Evaluation of Different Lysosomal Labeling Methods Used to Analyze RNA Nanocarrier Trafficking in Cells. *Bioconjugate Chemistry* 32, 2245–2256 (2021)
 - [55] Wahane, A., Malik, S., Shih, K. C., Gaddam, R. R., Chen, C., Liu, Y., Nieh, M. P., Vikram, A., & Bahal, R. Dual-Modality Poly-l-histidine Nanoparticles to Deliver Peptide Nucleic Acids and Paclitaxel for in Vivo Cancer Therapy. *ACS Applied Materials and Interfaces* 13, 45244–45258 (2021)
 - [56] Ding, Y., Jiang, Z., Saha, K., Kim, C. S., Kim, S. T., Landis, R. F., Rotello, V. M., Irudayaraj, J., *et al.* Gold Nanoparticles for Nucleic Acid Delivery. *Molecular Therapy* 22, 1075–1083 (2014)
 - [57] Liang, W. & W. Lam, J. K. Endosomal Escape Pathways for Non-Viral Nucleic Acid Delivery Systems. in *Molecular Regulation of Endocytosis* (InTech, 2012).
 - [58] Ceresa, B. Molecular Regulation of Endocytosis. *Molecular Regulation of Endocytosis* (2012)
 - [59] Behr, J. P. The Proton Sponge: a Trick to Enter Cells the Viruses Did Not Exploit. *CHIMIA* 51, 34 (1997)
 - [60] Smith, S. A., Selby, L. I., Johnston, A. P. R., & Such, G. K. The Endosomal Escape of Nanoparticles: Toward More Efficient Cellular Delivery. *Bioconjugate Chemistry* 30, 263–272 (2019)
 - [61] Turkevich, J., Stevenson, P. C., & Hillier, J. A study of the nucleation and growth processes in the synthesis of colloidal gold. *Discussions of the Faraday Society* vol. 11 55–75 (1951)
 - [62] Frens, G. Controlled Nucleation for the Regulation of the Particle Size in Monodisperse Gold Suspensions. *Nature Physical Science* 241, 20–22 (1973)
 - [63] Schulz, F., Homolka, T., Bastús, N. G., Puentes, V., Weller, H., & Vossmeier, T. Little Adjustments Significantly Improve the Turkevich Synthesis of Gold Nanoparticles. *Langmuir* 30, 10779–10784 (2014)
 - [64] Bastús, N. G., Comenge, J., & Puentes, V. Kinetically controlled seeded growth synthesis of citrate-stabilized gold nanoparticles of up to 200 nm: Size focusing versus ostwald ripening. *Langmuir* 27, 11098–11105 (2011)
 - [65] Piella, J., Bastús, N. G., & Puentes, V. Size-Controlled Synthesis of Sub-10-nanometer Citrate-Stabilized Gold Nanoparticles and Related Optical Properties. *Chemistry of*

- Materials* 28, 1066–1075 (2016)
- [66] Piella, J., Bastús, N. G., & Puntès, V. Size-Controlled Synthesis of Sub-10-nanometer Citrate-Stabilized Gold Nanoparticles and Related Optical Properties. *Chemistry of Materials* 28, 1066–1075 (2016)
- [67] Bastús, N. G., Piella, J., & Puntès, V. Quantifying the Sensitivity of Multipolar (Dipolar, Quadrupolar, and Octapolar) Surface Plasmon Resonances in Silver Nanoparticles: The Effect of Size, Composition, and Surface Coating. *Langmuir* 32, 290–300 (2016)
- [68] Piella, J., Bastús, N. G., & Puntès, V. Size-dependent protein-nanoparticle interactions in citrate-stabilized gold nanoparticles: The emergence of the protein corona. *Bioconjugate Chemistry* 28, 88–97 (2017)
- [69] Bastús, N. G., Sánchez-Tilló, E., Pujals, S., Farrera, C., Kogan, M. J., Giralt, E., Celada, A., Lloberas, J., & Puntès, V. Peptides conjugated to gold nanoparticles induce macrophage activation. *Molecular Immunology* 46, 743–748 (2009)
- [70] Chen, F., Li, X., Hihath, J., Huang, Z., & Tao, N. Effect of anchoring groups on single-molecule conductance: Comparative study of thiol-, amine-, and carboxylic-acid-terminated molecules. *Journal of the American Chemical Society* 128, 15874–15881 (2006)
- [71] Casals, E., Pfaller, T., Duschl, A., Oostingh, G. J., & Puntès, V. Time evolution of the nanoparticle protein corona. *ACS Nano* 4, 3623–3632 (2010)
- [72] Vitali, M., Casals, E., Canals, F., Colomé, N., & Puntès, V. Simple spectroscopic determination of the hard protein corona composition in AuNPs: Albumin at 75%. *Nanoscale* 12, 15832–15844 (2020)
- [73] Sherbet, G. V., Lakshmi, M. S., & Cajone, F. Isoelectric characteristics and the secondary structure of some nucleic acids. *Biophysics of structure and mechanism* 10, 121–128 (1983)
- [74] Tenzer, S., Docter, D., Kuharev, J., Musyanovych, A., Fetz, V., Hecht, R., Schlenk, F., Fischer, D., Kiouptsi, K., Reinhardt, C., Landfester, K., Schild, H., Maskos, M., Knauer, S. K., & Stauber, R. H. Rapid formation of plasma protein corona critically affects nanoparticle pathophysiology. *Nature Nanotechnology* 8, 772–781 (2013)
- [75] Lynch, I., Salvati, A., & Dawson, K. A. What does the cell see? *Nature Nanotechnology* 4, 546–547 (2009)
- [76] Salvati, A., Pitek, A. S., Monopoli, M. P., Prapainop, K., Bombelli, F. B., Hristov, D. R., Kelly, P. M., Åberg, C., Mahon, E., & Dawson, K. A. Transferrin-functionalized nanoparticles lose their targeting capabilities when a biomolecule corona adsorbs on the surface. *Nature Nanotechnology* 8, 137–143 (2013)
- [77] Corbo, C., Molinaro, R., Parodi, A., Toledano Furman, N. E., Salvatore, F., & Tasciotti, E. The impact of nanoparticle protein corona on cytotoxicity, immunotoxicity and target drug delivery. *Nanomedicine* 11, 81–100 (2016)
- [78] Saha, K., Moyano, D. F., & Rotello, V. M. Protein coronas suppress the hemolytic activity of hydrophilic and hydrophobic nanoparticles. *Materials Horizons* 1, 102–

105 (2013)

- [79] Ojea-Jiménez, I., García-Fernández, L., Lorenzo, J., & Puentes, V. F. Facile Preparation of Cationic Gold Nanoparticle-Bioconjugates for Cell Penetration and Nuclear Targeting. *ACS Nano* 6, 7692–7702 (2012)
- [80] Ando, J., Fujita, K., Smith, N. I., & Kawata, S. Dynamic SERS imaging of cellular transport pathways with endocytosed gold nanoparticles. *Nano Letters* 11, 5344–5348 (2011)
- [81] Hao, X., Wu, J., Shan, Y., Cai, M., Shang, X., Jiang, J., & Wang, H. Caveolae-mediated endocytosis of biocompatible gold nanoparticles in living Hela cells *. *Journal of Physics: Condensed Matter* 24, 164207 (2012)
- [82] Li, X., Omonova Tuychi qizi, C., Mohamed Khamis, A., Zhang, C., & Su, Z. Nanotechnology for Enhanced Cytoplasmic and Organelle Delivery of Bioactive Molecules to Immune Cells. *Pharmaceutical Research* 39, 1065–1083 (2022)
- [83] Charpentier, J. C. & King, P. D. Mechanisms and functions of endocytosis in T cells. *Cell communication and signaling* 19, (2021)
- [84] Saha, K., Rahimi, M., Yazdani, M., Kim, S. T., Moyano, D. F., Hou, S., Das, R., Mout, R., Rezaee, F., Mahmoudi, M., & Rotello, V. M. Regulation of Macrophage Recognition through the Interplay of Nanoparticle Surface Functionality and Protein Corona. *ACS Nano* 10, 4421–4430 (2016)
- [85] Fredericksen, B. L., Wei, B. L., Yao, J., Luo, T., & Garcia, J. V. Inhibition of Endosomal/Lysosomal Degradation Increases the Infectivity of Human Immunodeficiency Virus. *Journal of Virology* 76, 11440–11446 (2002)
- [86] Heath, N., Osteikoetxea, X., De Oliveria, T. M., Lázaro-Ibáñez, E., Shatnyeva, O., Schindler, C., Tighe, N., Mayr, L. M., Dekker, N., Overman, R., & Davies, R. Endosomal escape enhancing compounds facilitate functional delivery of extracellular vesicle cargo. *Nanomedicine* 14, 2799–2814 (2019)
- [87] Yu, J. N., Ma, S. F., Miao, D. Q., Tan, X. W., Liu, X. Y., Lu, J. H., & Tan, J. H. Effects of Cell Cycle Status on the Efficiency of Liposome-mediated Gene Transfection in Mouse Fetal Fibroblasts. *Journal of Reproduction and Development* 52, 373–382 (2006)
- [88] Vales, G., Suhonen, S., Siivola, K. M., Savolainen, K. M., Catalán, J., & Norppa, H. Genotoxicity and Cytotoxicity of Gold Nanoparticles In Vitro: Role of Surface Functionalization and Particle Size. *Nanomaterials* 10, 271 (2020)
- [89] Sani, A., Cao, C., & Cui, D. Toxicity of gold nanoparticles (AuNPs): A review. *Biochemistry and Biophysics Reports* 26, 100991 (2021)
- [90] Jawaaid, P., Rehman, M. U., Zhao, Q. L., Misawa, M., Ishikawa, K., Hori, M., Shimizu, T., Saitoh, J. ichi, Noguchi, K., & Kondo, T. Small size gold nanoparticles enhance apoptosis-induced by cold atmospheric plasma via depletion of intracellular GSH and modification of oxidative stress. *Cell Death Discovery* 6, 1–12 (2020)

CHAPTER 3

CONFOCAL IMAGING OF UNLABELLED NANOPARTICLES IN CELLS AND BIOLOGICAL TISSUES

Confocal Imaging of Unlabelled Nanoparticles in Cells and Biological Tissues

3.1 Introduction

The motivation of this work arises from the growing interest in the use of metal NPs in medicine and biology. [1–8] Detailed cellular and *in vivo* studies are required for their application on biological systems for treatment or diagnostic purposes. [9–15] The first problem we encounter is the approach to study NP-cell interactions, in order to evaluate their safety and efficacy. Understanding the interactions between nanoparticles (NPs) and biological systems requires real-time methods to track NPs and biomolecules simultaneously. To our best knowledge, no techniques have been utilized for real-time imaging label-free NPs and fluorescent biomolecules simultaneously.

Biological systems, including tissues and *in vitro* cultures, are most commonly observed using optical-based microscopes. Confocal laser scanning microscopy (CLSM) is an excellent tool for high spatial precision imaging fluorescence-labelled biomolecules in cells and tissues. However, NPs are usually in the size range 1-200nm, which falls below the optical resolution limit. Additionally, they generally lack intrinsic fluorescence. Only quantum dots (QDs), which have intrinsic fluorescence, or NPs labelled with fluorophores attached to their surface or into its core [16–20] can be visualized using CLSM. QDs drawbacks, including cost, toxicity, and a typical window of excitation wavelength (365-405 nm) that results in significant autofluorescence in many biological systems, hinders

their use. In the later, the presence of the fluorophore poses a big challenge since it can alter NP's surface chemistry or detach from it, also it could compromise NP's physicochemical properties, ultimately affecting NP's biological response. [21–25]

NPs can also be visualized inside cells by label-free techniques. Electron microscopy (EM) remains the primary technique for studying biological systems at atomic-level resolution. However, EM is costly, labour-intensive, limited to materials with sufficient electron density contrast, and primarily restricted to fixed specimens. Moreover, it limits the inspection to a small portion of the sample, and it does not allow fluorescence imaging of biomolecules, so identifying sub-cellular entities is based on electron contrast.

Several imaging methods have been developed as an alternative to standard electronic techniques. Alternative real-time techniques are scatter-enhanced phase-contrast microscopy [26], hyperspectral stimulated Raman scattering microscopy [27], optical diffraction tomography [28], or reflected light hyperspectral microscopy [29]. While these methods have the advantage of tracking label-free NPs in real-time, they do not represent standard techniques available for the scientific community.

As an alternative, the light scattered by NPs represents the most direct optical NP detection method because it is label-free and applicable to all types of materials, including noble metal and non-metallic NPs. Nanoparticles have the potential to become versatile biomarkers. For example, in metal NPs, their absorption and scattering cross-sections are several orders of magnitude higher than fluorescing organic dyes. Additionally, NPs do not suffer from photobleaching, and their extinction spectrum can be tuned by adjusting their size and shape. [5,30,31] Therefore, their visualization in biological systems by routine laboratory tools such as light microscopy is crucial. However, the size far below the diffraction limit motivates determining which conditions NPs, either in dispersion or cell-associated, can be reliably detected by standard confocal microscopy.

Conventional dark-field microscopy interfaced with a confocal laser scanning microscope (CLSM) has been used to monitor NPs in living cells. Yet, most studies rely on modifications performed on the confocal microscope to adapt it to collect the light scattered on a dark field approach. [32–35] Because the wavelength of light scattered by the NPs is the same as the wavelength of the illumination laser, part of the light scattered by the NPs can be detected by the detector in a conventional confocal microscope. Wang et al. showed this possibility by visualizing Ag NPs inside the cell using a conventional confocal microscope. [36] In the present work, we perform a systematic study of the possibilities and

limitations of the method, usually restricted to a single material or size of NPs, and the use of biological samples with no multiple staining, far from the standard/regular samples used in the biomedical field.

3.2 Scope of the study

The aim of this study was to provide a deep insight into the optical properties of the NPs and the mechanistic description of NP light scattering based on those. It relies on a commercially available conventional confocal microscope without the need for further hardware modifications. In this study, the size limit of Au NPs for their imaging on confocal microscopy was resolved, and the method was extended to other materials relevant in the biomedical field and other complex hybrid nanoparticles. The process was tested and validated on either fixed or live cells for high-resolution multiplex imaging and tissue sections from *in vivo* studies. Overall, it aims to provide the tools for understanding NP confocal imaging to apply to any particular case of interest.

3.3 Results and Discussion

The aim of this first section is to provide the proof-of-concept of the imaging of Au NPs on the Laser Scanning Confocal Microscope by comparing the theoretical simulated optical properties of the NPs with the experimental data. Later, the single particle imaging and size resolution limits are discussed.

3.3.1 Principles of Au NP Scattering

In this work we prepared and characterized a number of different NPs. These NPs have been observed either dispersed onto a substrate (after drop-casting) or in colloidal suspension.

Highly monodisperse citrate-stabilized Au NPs of 100 nm in diameter were prepared following a well-established kinetically controlled seeded-growth method developed by our group. [37] Representative transmission electron microscopy (TEM) images, clearly show the homogeneity, and narrow size distribution of the obtained Au NPs (**Figure 3.1A**).

The ability of gold NPs to interact resonantly with light is usually expressed in terms of extinction efficiency, usually plot as localized surface plasmon resonance (LSPR). It stands for the loss of light from a transmitted beam, and is the sum of two mechanisms, absorption and scattering. The LSPR is a distinctive and easily measurable signature indicative of morphology (size and shape), composition, surface chemistry, aggregation state and physical environment of NPs. Absorbance spectrum, measured by UV–vis spectroscopy, reveals a strong peak around 571 nm, corresponding to the dipolar plasmon resonance of ~100 nm (**Figure 3.1B**).

Since SPR is a collective oscillation of free electrons in the Au NP, it will cause a strong scattering and absorption of light simultaneously. This is revealed when experimental data was compared with calculations based on the standard Mie theory using Mie Plot software. **Figure 3.1C** shows the calculated extinction (Q_{ext}), scattering (Q_{sca}), and absorption (Q_{abs}) efficiency. As it can be observed, the scattering contribution (blue line) is a significant part of the extinction spectra. Vertical lines correspond to confocal microscope excitation wavelengths (488, 514, 561 and 639 nm). The relative contributions of scattering and absorption to the total extinction are plotted as a function of the wavelength in **Figure 3.1C, inset**. As seen, longer wavelengths have higher albedo (ratio of scattering contribution to total extinction). However, the strongest scattering is induced when Au NPs

are irradiated by a light within the maximum scattering band, which corresponds to 561 nm laser excitation.

The described light scattering of the NPs can be used to image them in Confocal Laser Scanning Microscopy (CLSM), even if the size of the NPs is below the optical resolution limit of 200 nm. For this, the confocal must be used in reflectance mode instead of the commonly used fluorescence mode. Au NPs in colloidal solution were imaged by CLSM using four different single lasers: 488 nm, 514 nm, 561 nm, 639 nm. Independently of the wavelength of choice, the scattered light from Au NPs is monochromatic, and the wavelength is the same as the illuminating laser. Thus, the detection window needs to be set to collect the signal on the same wavelength as the laser used. A filter in the range (± 15 nm) was set to cover the wavelength of the laser only for the detection of the scattered light from Au NPs.

The images of the scattered light of Au NPs at the four different lasers used are shown in **Figure 3.1D**. In all cases, discrete light intensity spots can be clearly seen. A line was drawn from the left bottom corner to the right upper corner, and the measured intensities were plotted. Even though same settings were used for all the lasers, different signal intensities were measured. Analysis of the intensity profile is shown in **Figure 3.1E**. As expected, the highest intensity profile was found at 561 nm. For the other analysed wavelengths, as the band of Au NPs is from 400 to 600 nm, the light scattered can be detected but with a relatively weaker intensity than that of 561 nm laser. This correlates with the wavelength-dependent Au NPs scattering profile previously calculated. Altogether, these results suggest that the choice of the laser is a critical point for the optimal set-up to image the NPs by CLSM in reflectance mode.

3.3.2 Single Particle Imaging

At this point, to make the study quantitative, a critical question is whether a single Au NP can be individually detected. Considering the experimental conditions used following the ideal Nyquist rate of sampling, the lateral resolution of the CLSM at 561 nm is $R_L = 160$ nm, and the diffraction-limited spot size is 210 nm. If the distance of two adjacent spots containing Au NPs is larger than the lateral resolution, they can be distinguished from each other in x - y plane. A scan resolution of 1040×1040 pixels is used to acquire the CLSM images. Therefore, each pixel size is around 82 nm.

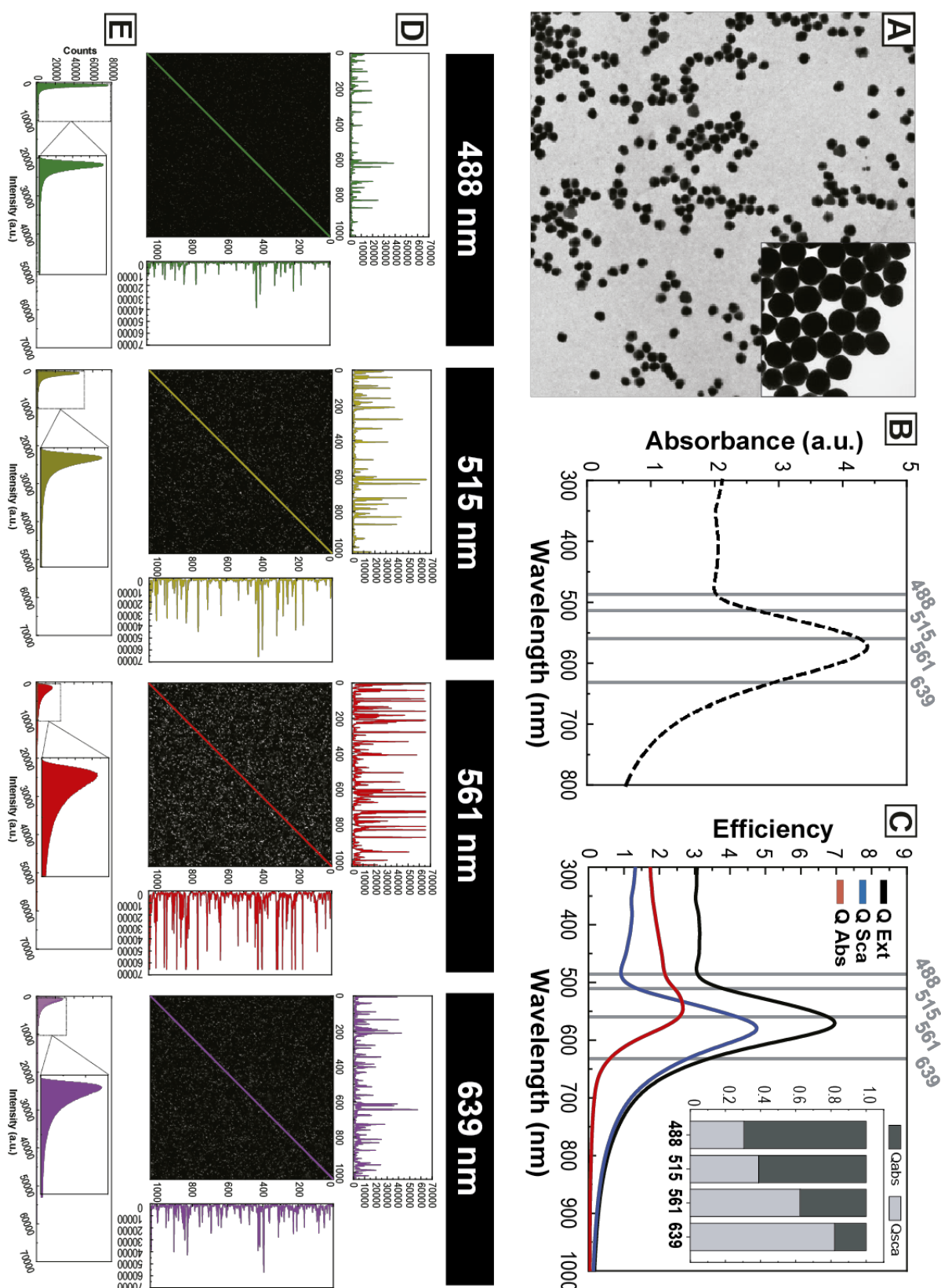


Figure 3.1. (A) Representative transmission electron microscopy (TEM) images of highly monodisperse citrate-stabilized Au NPs of 100 nm. (B) Absorbance spectrum of Au NPs measured by UV-vis spectroscopy. Vertical lines correspond to confocal microscope laser excitation wavelengths (488, 514, 561 and 639 nm). (C) Calculated extinction (Q_{ext}), scattering (Q_{sca}), and absorption (Q_{abs}) efficiency of 100 nm Au NPs. On the inset, the albedo is shown. (D) CLSM images of the scattered light of Au NPs at the four different lasers used are shown, with the respective signal intensity profile at the x-y axis. (E) Analysis of the intensity profile.

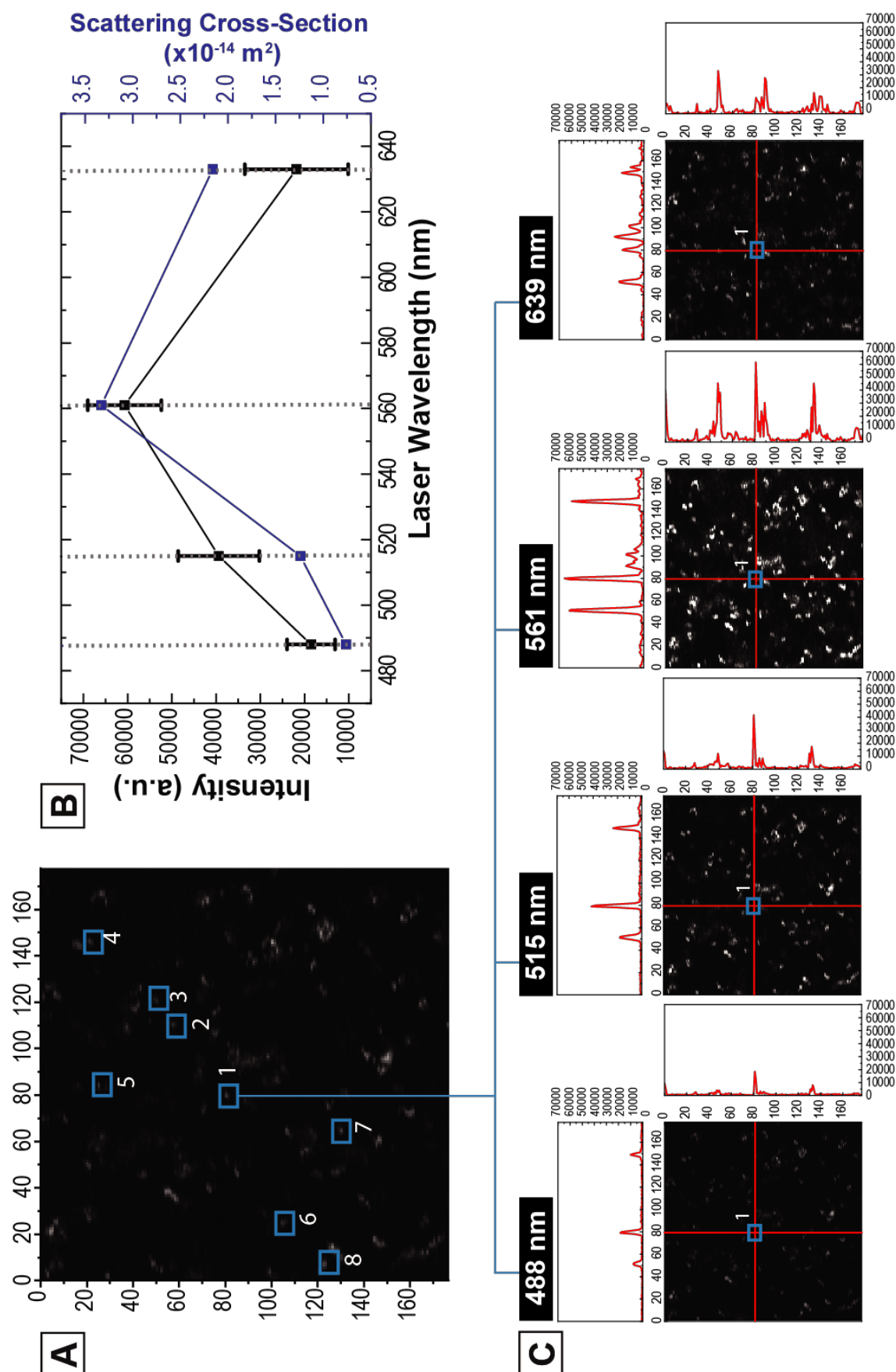


Figure 3.2. Detection of single Au NPs. (A) CLSM image of the scattered light of Au NPs and those selected for the study. (B) CLSM image corresponds to pixels 0-166, 0-166 (x,y) of **Figure 3.1**. Mean intensity values and calculated scattering cross-section values. (C) CLSM images of the scattered light of individual Au NPs (#1) at the four different lasers used.

Having this consideration in mind, we measured the intensity of scattered light of 10 selected individual Au NPs of a region of interest at the four different lasers previously studied (**Figure 3.2A**), and calculated the mean intensity value (**Figure 3.2B**). Measurements show how scattered intensity depends on the laser used. On **Figure 3.2C**, a selected region of interest from **Figure 3.2A** is amplified and the intensity profile and the x and y axis for each wavelength plotted. Remarkably, obtained values correlate well with the theoretical scattering cross-section values previously calculated. Actually, the scattering cross section of a 100 nm Au NPs is wavelength-dependent and larger than its real size, because of the SPR. These results confirm that the intensity profile provides information about a single NP event, suggesting that the CLSM method can distinguish individual Au NPs. For that, monodispersity is crucial, otherwise as scattering is strongly dependent on size, polydispersity results in non-quantifiable scattering.

3.3.3 Au NP Size Resolution Limit

Taking this into account, the size resolution limits of confocal observation of Au NPs is experimentally studied. For this, 15, 50, 100 and 150 nm NPs were synthesized using the previously mentioned seeded-growth method. The synthesized NPs were fully characterized. TEM images are shown in **Figure 3.3**, the corresponding size distribution is summarized in Table 1 along with the DLS results and the LSPR peak position measured by UV-Vis spectroscopy. Unlike conventional dyes, the optical absorption and scattering properties of Au NP can be tuned by changing their size and shape. The LSPR peak position depends on NPs size, composition, and chemical state, so it broadens and red-shifts as NP size increases.

The synthesized NPs were imaged in colloidal suspension, on the CLSM using the reflectance mode. Images acquired are shown in **Figure 3.3** and the corresponding measured intensities are plotted below. No signal was detected from the 15 nm-NPs due to the minimal scattering contribution. However, scattering from larger NPs could be detected, with increasing signal as NP's size increases (see **Table 3.1**). Using the principles of the Mie theory of light scattering, the individual contributions of absorption and scattering, and the total extinction were calculated. Note that in these experiments there is no aggregation, as DLS shows, NPs are colloidally stable and non-aggregated in solution. Au NPs with a diameter of 15 nm show essentially only surface plasmon enhanced absorption with negligible scattering. Consequently, there is no appreciable contrast. When particle diameter increases from 15 nm to 150 nm, the scattering cross-section of the NP and the

relative contribution of scattering to the total extinction increases. Consequently, the NPs appear in the image.

Simulation plots of the optical properties of Au NPs based on the standard Mie theory using Mie Plot software are shown in **Figure 3.4**. Here the intensity of extinction, scattering and absorption are plotted as a function of size and wavelength in a heatmap format. Brightest spots relate to higher intensity values, and darkest to the lowest values. The highest intensity point in extinction corresponds to a 98.2 nm NP at λ 569nm, whereas in scattering corresponds to a 123.6 nm NP at λ 607nm. Results illustrated in this graphs are very interesting. Scattering profile allows to anticipate which laser would be the best option for the Confocal imaging of a given NP size. Nevertheless, it will still depend on the particular properties of the synthesized NPs, especially size polydispersity.

The increase in the ratio of scattering to absorption with NPs volume provides a tool for NPs selection for biological applications. For instance, larger NPs are more suitable for light-scattering-based imaging applications while NPs with a high absorption cross-section in the laser excitation region, facilitates selective photothermal therapy.

Table 3.1. Summary of sizes and optical properties of Au NPs synthesized and used on **Figure 3.3**.

	TEM (nm)	DLS diameter (nm)	LSPR (nm)	Mean Scattering Intensities	Sca Cross-section (cm ² /NP)
15 nm	12.7 ± 1.4	16.5 ± 5.8	519	2.2 ± 0.4	3.0930x10 ⁻¹³
50 nm	53.8 ± 4.7	63.7 ± 12.5	535	21.5 ± 7.2	3.3336 x10 ⁻¹⁰
100 nm	102.5 ± 8.9	114.1 ± 34.3	571	39.7 ± 13.9	1.16278x10 ⁻⁹
150nm	148.4 ± 17.0	176.4 ± 50.9	546 / q653	52.9 ± 18.8	2.3770 x10 ⁻⁹

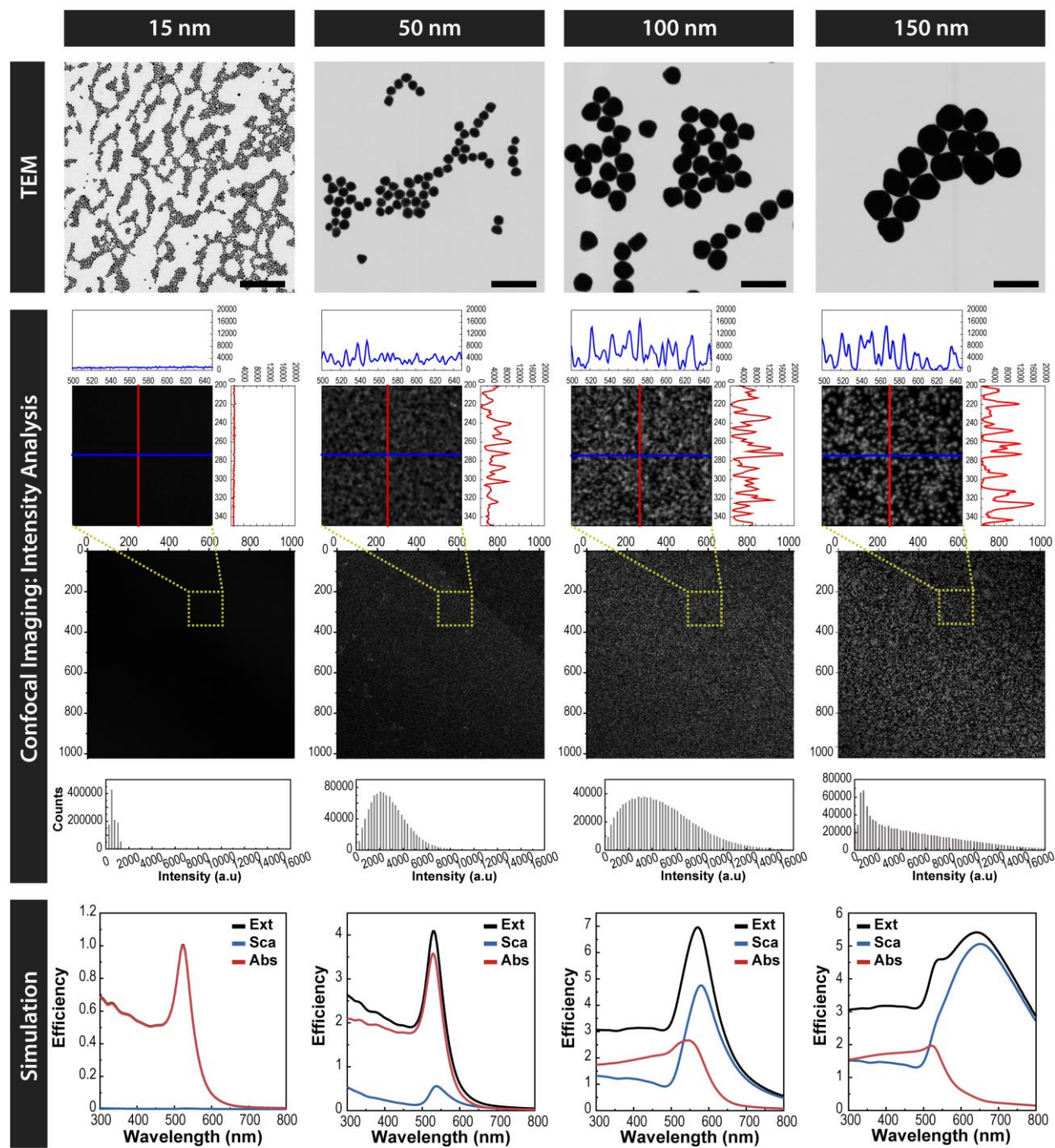


Figure 3.3. Au NP Size Resolution Limit. (Up) Representative transmission electron microscopy images of highly monodisperse citrate-stabilized Au NPs of ~15 nm, ~50 nm, ~100 nm and ~150 nm. Scale bar = 250 nm. **(Middle)** CLSM images and intensity analysis of the scattered light of different sized Au NPs at 561 nm. A selected region of interest is amplified for an analysis of the intensity profile. **(Down)** Calculated extinction (Qext), scattering (Qsca), and absorption (Qabs) efficiency of 15 nm, 50 nm, 100 nm and 150 nm.

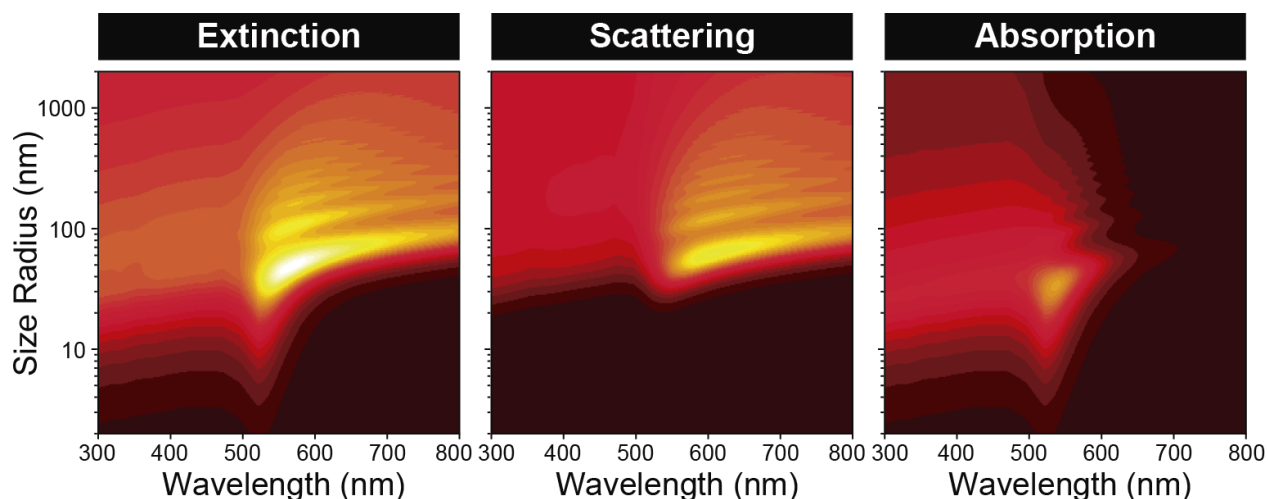


Figure 3.4. Mie Plot of Simulated Gold Nanoparticles Optical Properties. The efficiency of extinction, scattering and absorption is represented as a heatmap, where the size radius (y axis) is plotted against the wavelength (x axis). Dark colors represent low efficiency values, and bright colors high efficiency values.

3.3.4 Confocal Imaging of Au NPs in Biological Systems

3.3.4.1 Fixed Cultured Cells

Since the motivation of this work was to find a good alternative for NP-cell interaction observation, we further applied this to imaging of cultured cells exposed to NPs. In this case, to better localize the NPs we prepared Au@SiO₂-FITC NPs (diameter 245.5 ± 13.6 nm, **Figure 3.5A**). Au@SiO₂-FITC NPs comprises an Au core (~ 60 nm) surrounded by three concentric layers of SiO₂, the inner acting as a spacer, the intermediate containing the Fluorescein isothiocyanate fluorophore (FITC, excitation max. 490 nm, emission max. 525 nm), and the outer acting as a protective layer. The UV-Vis spectra of the synthesized NPs is shown in **Figure 3.5B**. In this form, by controlling the fluorophore location within the SiO₂ shell, the Au core is able to induce an enhancement in the dye signal by plasmon enhanced fluorescence (**Figure 3.5C**), [38] and the fluorophore is protected from the solution. Thus, these NPs present dual-mode image capabilities providing, in a single entity, the fluorescent signal from the FITC fluorophore and the scattering light from the Au NP. As a consequence, the system allows the colocalization of the NPs by scattering and fluorescent imaging, confirming the reliability of the use of CLSM to visualize single Au NP.

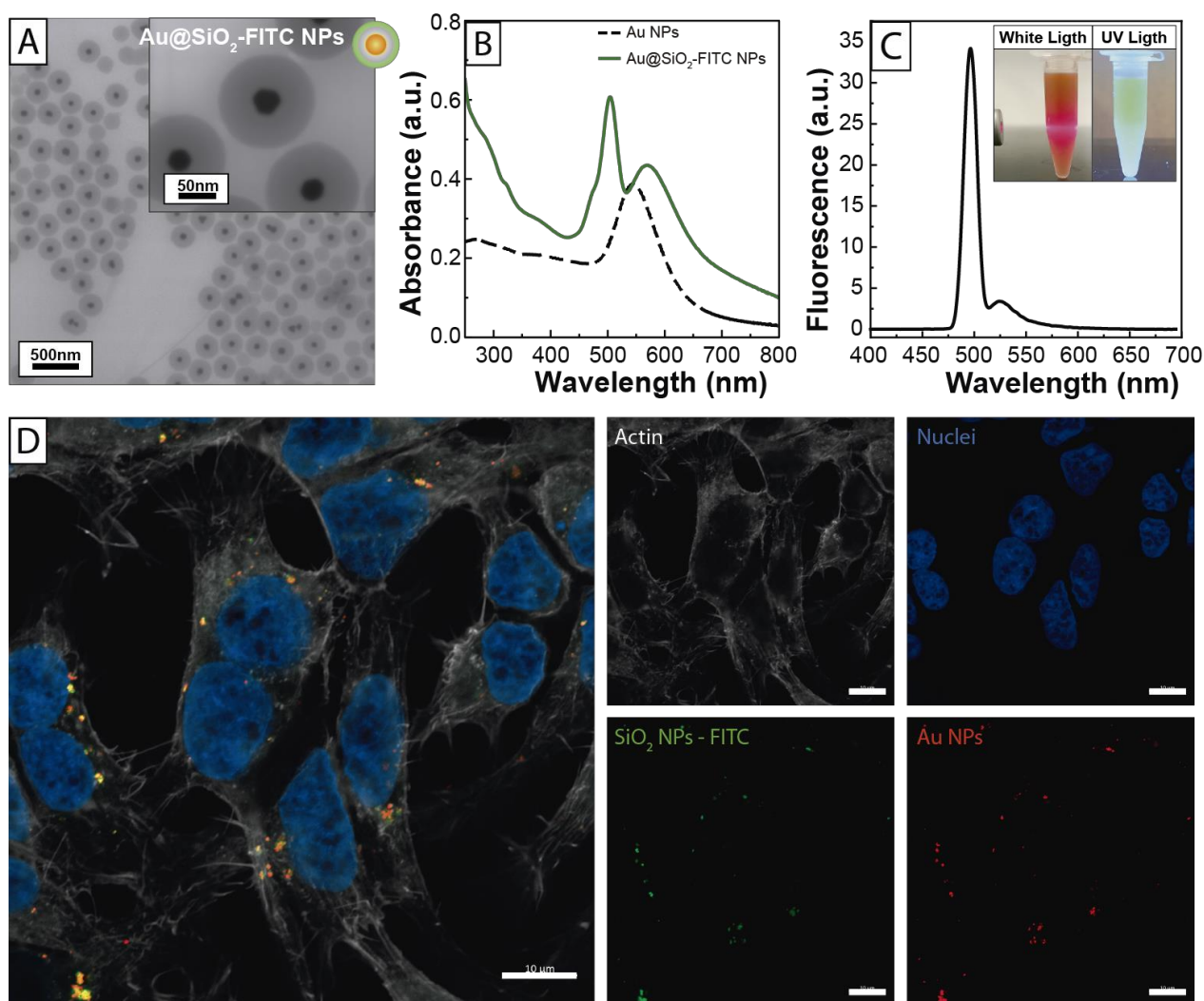


Figure 3.5. Imaging of Au@SiO₂-FITC NPs on HEK293 cells. (A) Representative transmission electron microscopy (TEM) images of Au@SiO₂-FITC NPs. (B) Absorbance spectrum of Au@SiO₂-FITC NPs measured by UV-vis spectroscopy. (C) Fluorescence spectra (emission) of colloidal solution of Au@SiO₂-FITC NPs. The spectra were taken in a 1:10 dilution in pure water at neutral pH and using an excitation wavelength of 495nm. (C, inset) Pictures of the NPs taken upon exposure to white light and under ultra-violet excitation. HEK293 cells exposed to Au@SiO₂-FITC NPs. (D) Composite image of the merged channel on the left, and split channels on the right showing stained actin (white) and nuclei (blue), and signal from NP imaged by fluorescence with FITC (green) and reflectance from the Au core (red). Scale bar = 10 μ m.

In this regard, HEK293 cells were incubated with Au@SiO₂-FITC NPs and imaged using the confocal microscope in reflectance mode (**Figure 3.5D**). Before exposure to cultured cells, NPs were stabilized with BSA in order to avoid NP aggregation. [39] After 24h, samples were fixed and stained for their visualization on the confocal microscope. The scattering produced by the 60nm-Au core of the NPs (red) allowed imaging of the NPs using the reflectance mode as explained above. Additionally, NPs were simultaneously imaged by the FITC (green) present on the SiO₂ shell using the conventional fluorescence mode. For each imaging two tracks were set, each with the respective laser used to irradiate

the sample, and two corresponding bandpass filters were set to separate the scattered light from Au NPs and the fluorescence of FITC. The laser used to image the Au core by light scattering was 561 nm, with an optical window filter set to 555-579 nm while FITC was excited using the 488 nm laser and the emission collected between 499-570 nm. Additionally, Phalloidin used for actin staining (excitation 639nm, emission 650-694nm), and Hoechst 3342 for nuclei staining (excitation 405nm, emission 408-480nm), revealed the subcellular structure. The fluorescent markers available provide subcellular resolution of the samples, while the reflectance mode allow us to image non-modified NPs interacting with biological systems. Thus, the multiplex staining allows us to locate the NPs in the sample, either in the extracellular space, intracellularly or bound to the cell membrane, from a certain z-section of the sample.

A colocalization analysis of the Au and FITC signals was performed (**Table 3.2**). The colocalization coefficient was measured as a function of the pixel intensity (Pearson's Correlation Coefficient) and as function of the spatial overlap (Manders' Correlation Coefficient). In both cases, it shows a positive correlation between the Au and FITC signal. The spatial correlation between both signals proves that the signal collected from the laser reflection comes precisely from the light scattered by the Au core, confirming the reliability of NP scattering imaging.

Table 3.2. Colocalization analysis of Au:FITC signal from Au@SiO₂-FITC NPs exposed to HEK293 cells (Figure 3.5D). Zen Blue 3.0 (Zeiss) software was used to perform the colocalization analysis. Pearson's and Manders' Correlation Coefficients shown a positive correlation for Au:FITC signal. ¹ This value quantifies the degree to which two channels follow a simple linear relationship of intensity. Values can range from -1 (an inverse or "anti-colocalization" relationship), to 0 (a random cloud of no relationship), or +1 (a perfect linear slope). ² This measurement is similar to Pearson's above but ranges from 0 to +1. It does not incorporate a relationship to mean intensity (as with Pearson's), so it largely just looks for spatial overlap alone above the fixed threshold. ³ These values are reported as pairs that range from 0 to 1. The metric simply calculates the fraction of pixels colocalized to the total number of pixels from the specified channel.

Pearson's Correlation Coefficient¹	Manders' Correlation Coefficient²	Colocationization Coefficient: Au signal³	Colocationization Coefficient: FITC signal³
0.64786	0.73811	0.90105	0.6436

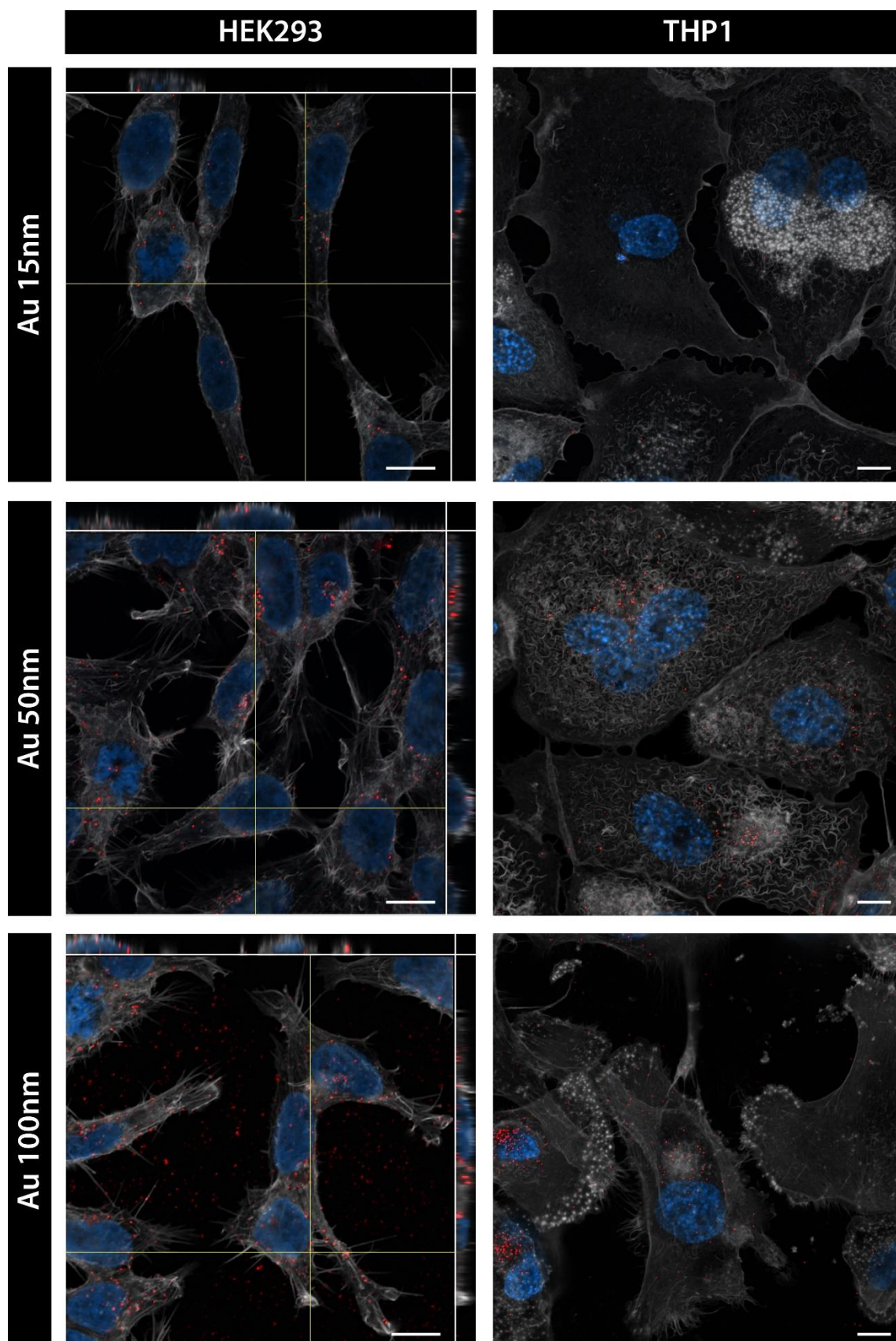


Figure 3.6. Imaging of Au NPs in fixed cultured cells. (Left) HEK293 cells exposed to 15 nm, 50 nm, and 150 nm Au NPs. Yellow lines correspond to the relative position of the x and y-axis from the z-stack, depicted as orthogonal views (right and above). **(Right)** THP1 cells exposed to 15 nm, 50 nm, and 150 nm Au NPs. Actin (white) and nuclei (blue) staining were acquired by conventional fluorescence, and NPs (red) were imaged by reflectance. Scale bar = 10 μ m.

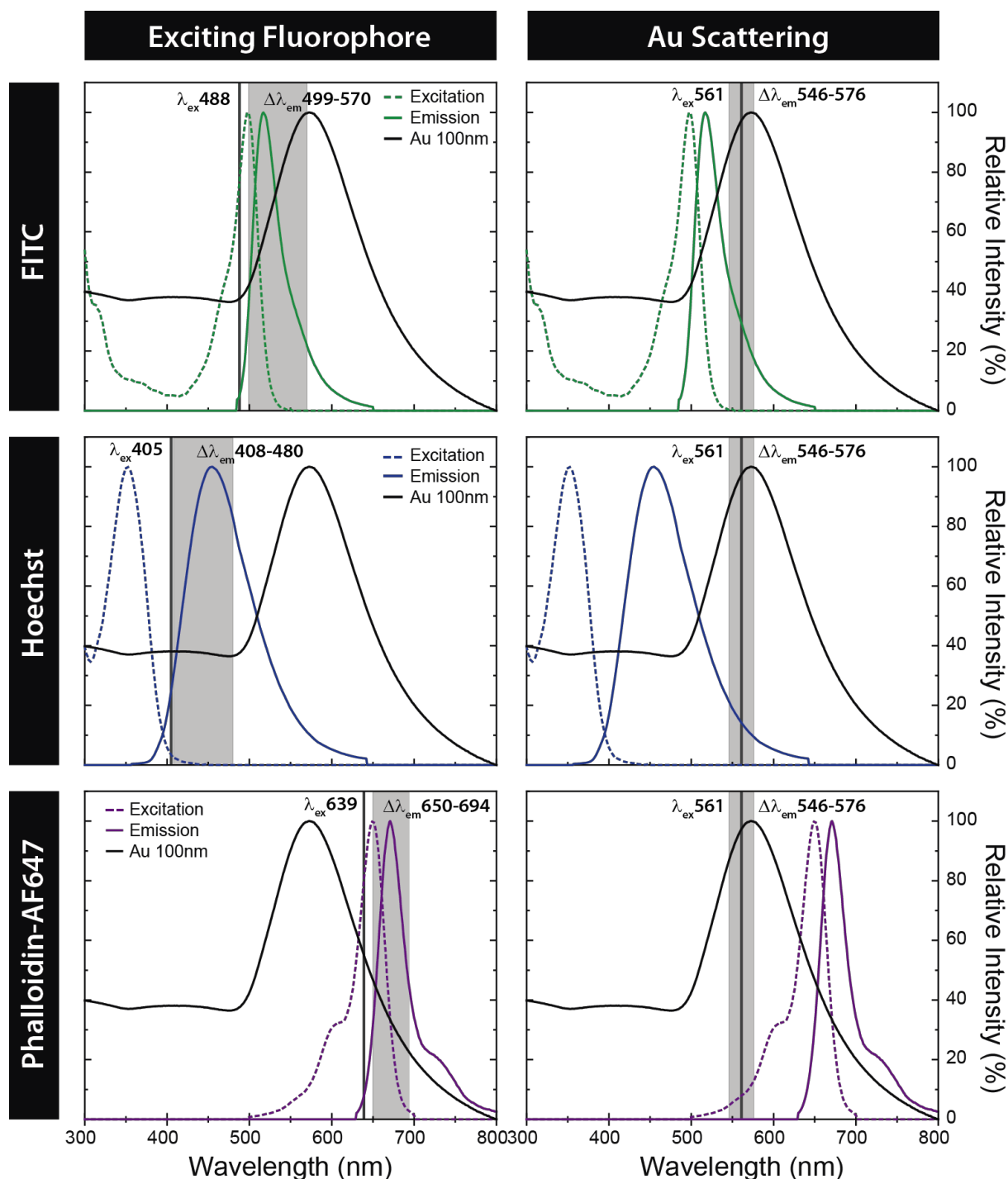


Figure 3.7. Graphical representation of emission/excitation profiles of the fluorophores used in the biological experiments, overlapped with the scattering spectra of the 100nm-Au NPs, all expressed in relative intensity and each normalized to maximum. Vertical black reference lines are drawn at the wavelength of the laser used for each particular case, and the shaded grey area corresponds to the relative emission window. As observed in the confocal images from **Figure 3.5**, there is no signal overlapping nor interference from the light scattering produced by the NP and the signal from the excited fluorophores. When operating in the fluorescence mode, either the wavelengths of emission windows are too far from the source wavelength to collect the scattering from the NPs, or the relative intensity of the NP's scattering is much lower than the dye signal. On the other hand, on the reflectance mode, the settings of the laser and the emission window is not suited to collect the emission of the dye, in case the 561nm laser excites it.

To further investigate the sensitivity and resolution of the method, HEK293 and THP1 cells were exposed to 15 nm, 50 nm and 100 nm NPs. Cellular structure was again stained with Phalloidin for actin and Hoechst for nuclei, and cells fixed 24h after NPs exposure. Z-projections from the samples were performed and depicted as orthogonal views in order to assess the subcellular localization of the NPs.

As seen in **Figure 3.6**, the signal intensity increases as the NP's gets larger which correlates with the scattering contribution. Indeed, scattering of smaller Au NPs (<15 nm) is almost insignificant. Therefore, smaller Au NPs (15nm) were generally observed when they were located in the vesicles due to endosomal concentration of NPs is high and they optically behave as aggregates. On the contrary, the light scattered by 50nm and 100nm, even when they are individually dispersed, is enough to be detected by CLSM.

This is translated into the fact that can be indistinctively imaged at the intra and extracellular space at the four different laser wavelengths, as shown on **Figure 3.8**, where 4 different laser are used to image 100nm Au NPs on HEK293 cultured cells. Control experiments showed that precursors, organic dyes, and subcellular organelle had no effects on the scattered light imaging of NPs.

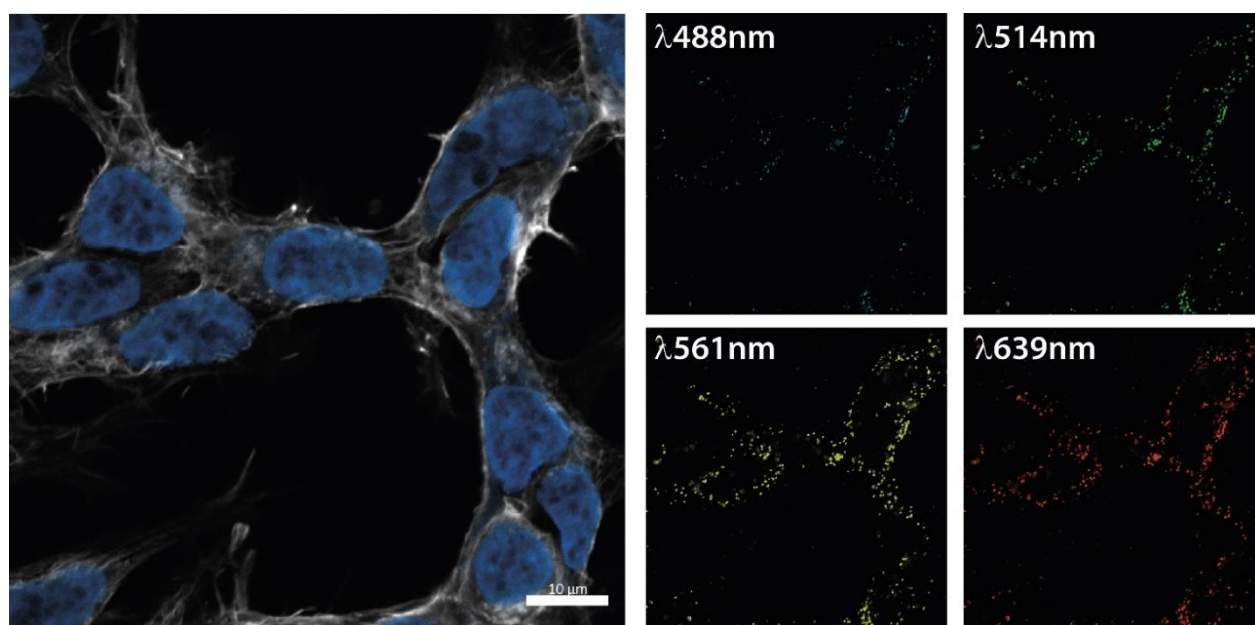


Figure 3.8. Lambda analysis of HEK293 cells exposed to 100nm-Au NPs. The Au NPs can be imaged using any of the lasers (488, 514, 561 or 639nm) using the reflectance mode to collect the light scattering. However, the highest signal intensity corresponds to the 561nm. No interference or signal overlap with the Hoechst or Phalloidin-AF647 is observed on any of the lasers used by reflectance. Scale bar = 10 μ m.

Note that the presence of the NPs, either Au@SiO₂-FITC or any size Au NPs, on the sample did not interfere nor overlap with the signal of the cellular markers, proving the multiplexing capacity of the method. Further, the signal from the scattering of the Au core could be specifically collected without any signal overlap from the other emission tracks (**Figure 3.7**).

Finally, since the scattering of the Au core was acquired in a separated track, it was possible to image all the fluorescent markers in high resolution mode (using the Airyscan detector in the LSM980 confocal microscope), shown in **Figure 3.8**. This enabled a more precise subcellular localization of the NPs in the cells.

3.3.4.2 Tissue Sections

To further expand the possible application of imaging NPs by light scattering, the visualization of NPs in tissue sections after *in vivo* administration of NPs was explored. For this, mice were injected intravenously with Au@SiO₂-FITC@PS NPs and sacrificed at 24h. Tissue sections from the organs collected were stained (actin and nuclei). Images from the reconstructed complete tissue sections acquired in tiles with the wide-field fluorescence microscope are displayed in **Figure 3.9** and **Figure 3.10**. NPs were found to be well dispersed all over the organ samples.

Representative areas from the tissue sections were selected and observed on the Confocal microscope, shown in **Figure 3.11**. As in the cultured cells, NPs were simultaneously imaged through the FITC signal by fluorescence mode and the Au scattering by the reflectance mode.

On the liver samples, NPs are mostly located outside the hepatocytes, in the sinusoidal space inside the stellate cells, as cellular morphology suggests. On the other hand, on the spleen samples NPs are located in the margins of the white pulp.

A region of interest (ROI) of both tissues was amplified for more detail, and signal channels split (**Figure 3.11A** and **E**). Both signals spatially correlate, further proving CLSM as a reliable method for Au NPs imaging on biological entities. Not only that, but this opens to the possibility to perform more detailed studies on NP-cell interactions on *in vivo* experiments, as biodistributions, not limiting to Electron Microscopy.

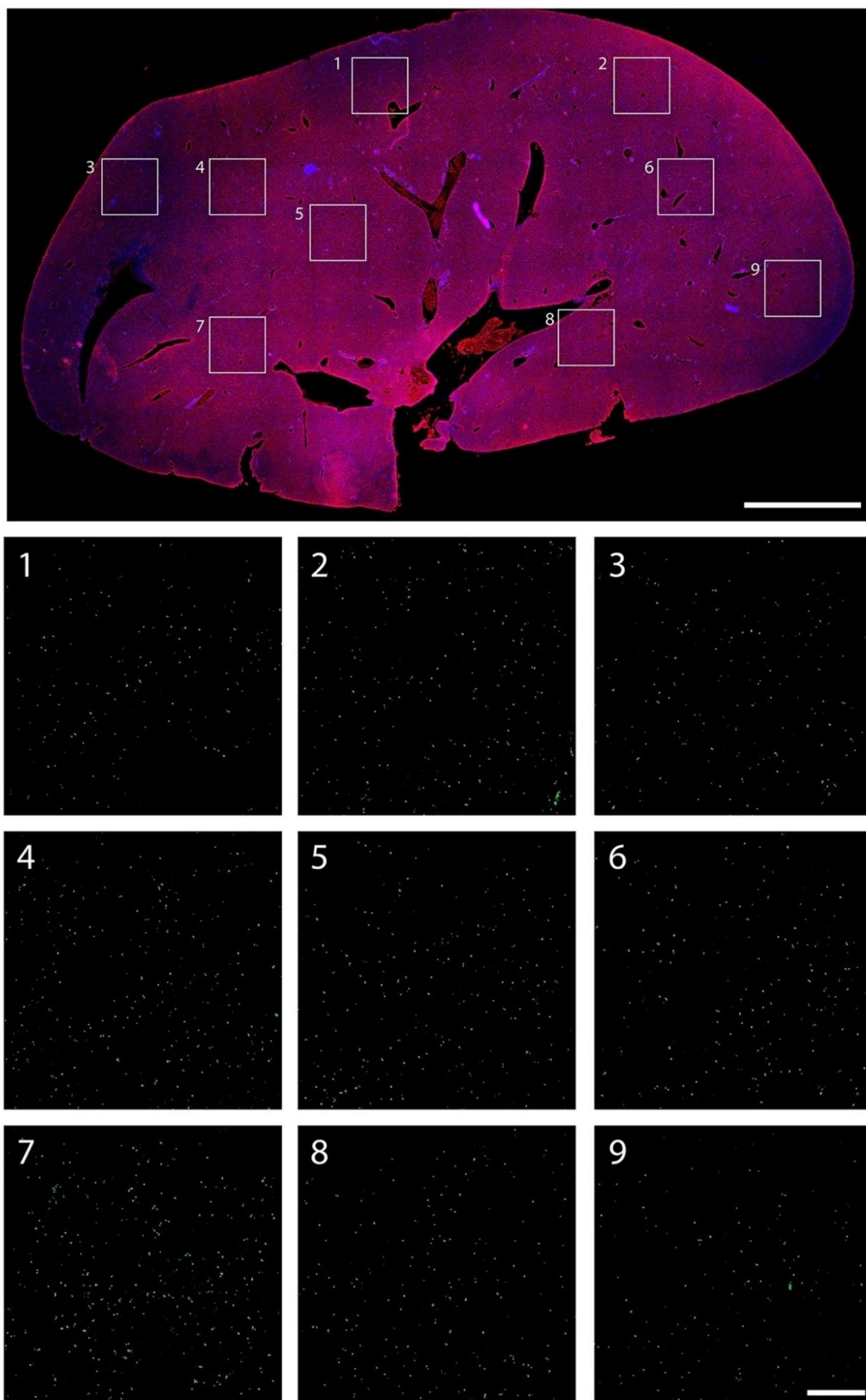


Figure 3.9. Wide-field microscopy of liver section. (Up) Merged tiles from whole liver section, with actin (red) and nuclei (blue) staining. Scale bar = 2 mm. **(Down, 1-9)** Individual tiles from selected regions of interest with FITC signal (green) from Au@SiO₂-FITC@PS NPs. Scale bar = 200 μ m.

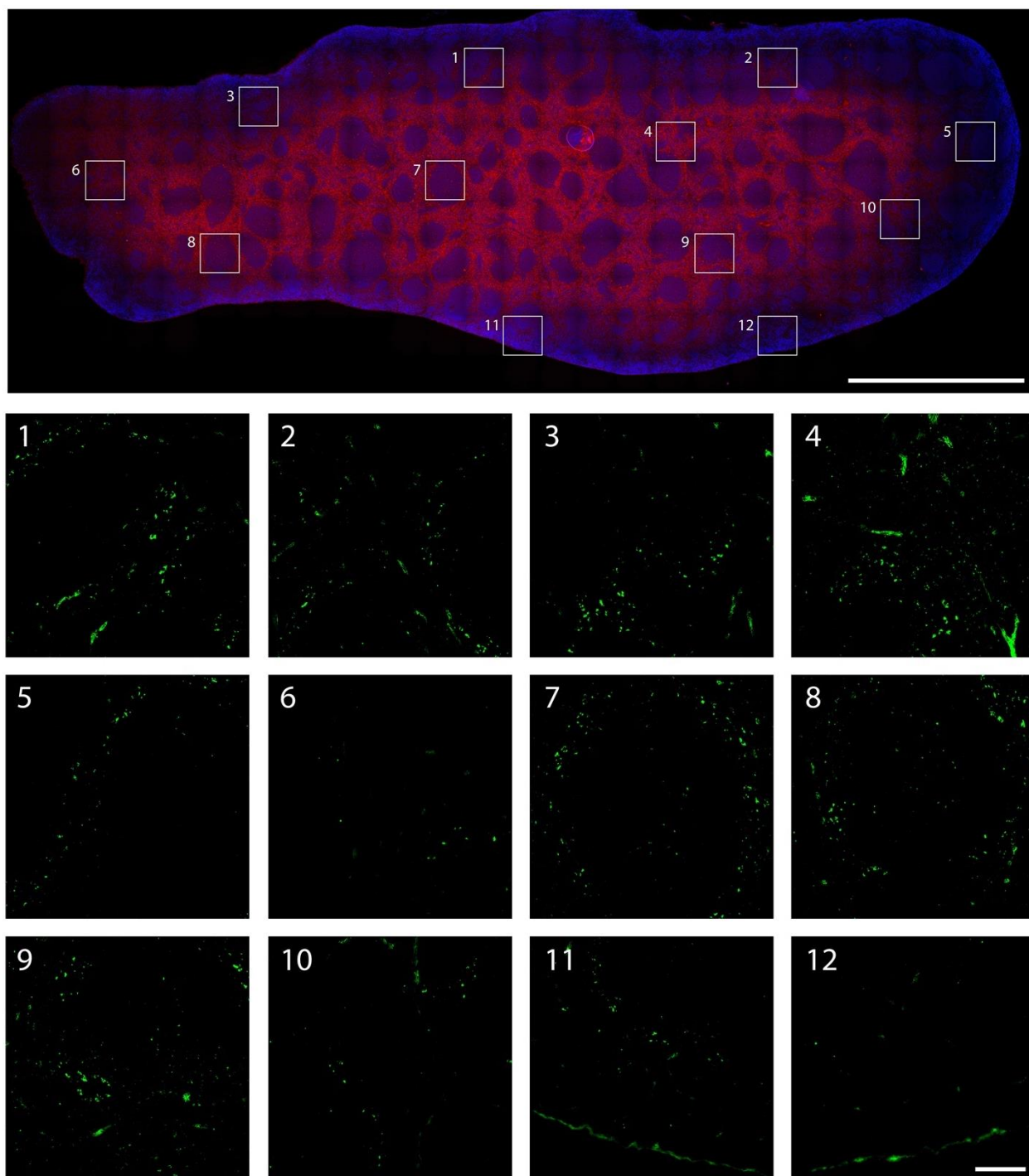


Figure 3.10. Wide-field microscopy of spleen section. (Up) Merged tiles from whole spleen section, with actin (red) and nuclei (blue) staining. Scale bar = 2 mm. **(Down, 1-12)** Individual tiles from selected regions of interest with FITC signal (green) from Au@SiO₂-FITC@PS NPs. Scale bar = 100 μ m.

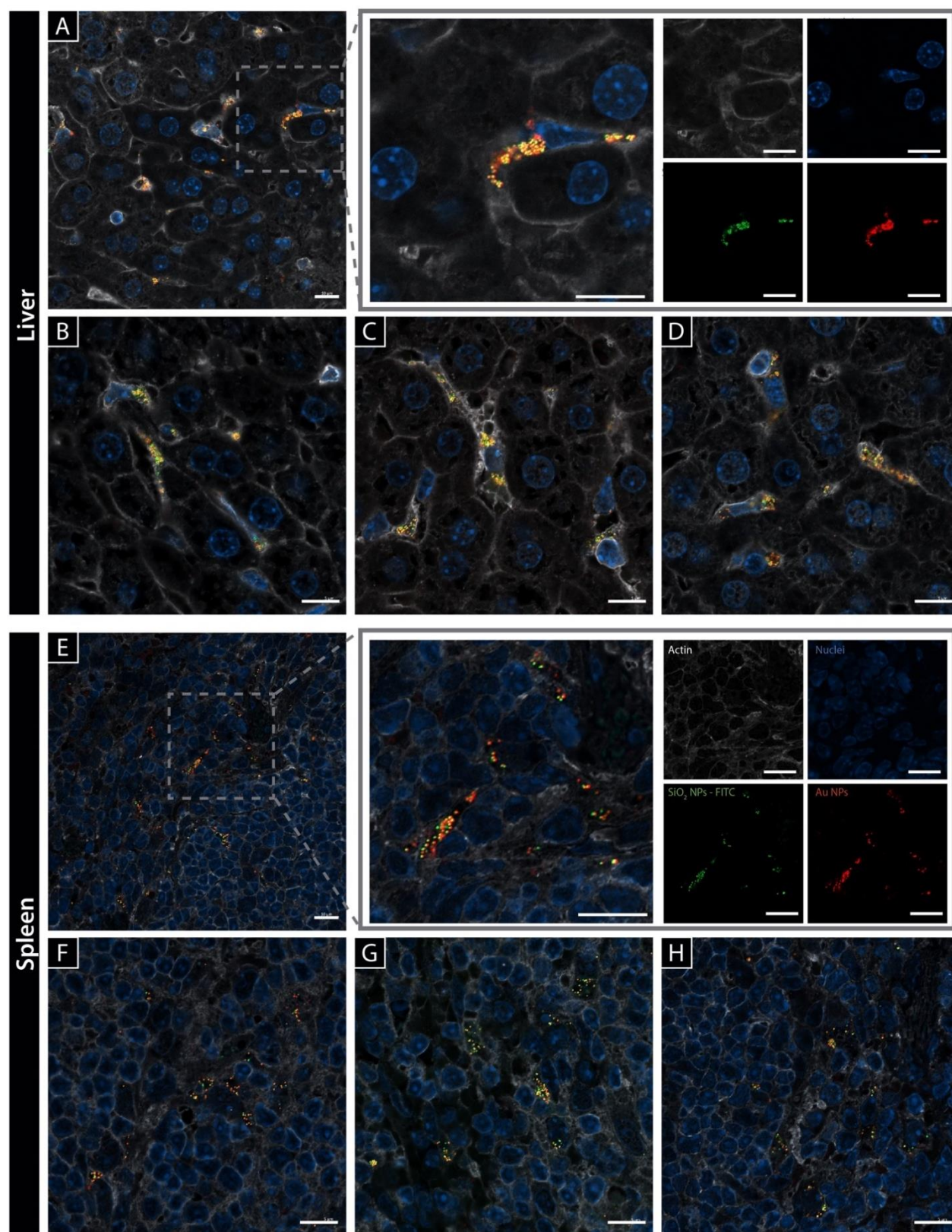


Figure 3.11. Representative CLSM images of NPs in tissue sections. Confocal imaging from the liver (**A-D**) and spleen (**E-H**) sections of the mouse exposed to Au@SiO₂-FITC@PS NPs. A selected area is zoomed from a representative image from a liver (**A**) and spleen (**E**) section at 60X magnification. On the right, the signal from each channel is split. Below, additional images from liver (**B-D**) and spleen (**F-H**) sections at 40X magnification are shown. Scale bar = 10 μ m.

3.3.4.3 *In vivo* Imaging

One of the advantages of confocal microscopy is that it can be performed on living cells. So, in contrast to TEM imaging, in confocal microscopy it is possible to observe real time interaction between NPs and live cells (or tissue). The fluorescent markers available provide subcellular resolution of the samples, while the reflectance mode allow us to image non-modified NPs interacting with biological systems.

On this study, HEK293 cells were cultured on a microslide, and nuclei and cytoplasm were stained before their observation. The aim of this experiment was to study NP-cell interaction *in vitro* by passively monitoring the sample for 24h after NP exposure. Four different ROIs were selected, a video of each one was mounted with all the time frames acquired.

Images were recorded upon their addition on the cell culture. On **Figure 3.12**, captions from the selected ROIs at different time points are shown. Two kinds of shapes can be differentiated of the signal collected from the Au NPs. One would be attributed to ‘static’ NPs, as the other show a drift on the signal which would correlate to a NP in Brownian motion in the media. Mostly, static NP correlate in space with the cytoplasm marker or close to the nucleus, which both indicate that the NP is in the intracellular space or bound to the cell membrane. Note that the fact that the recording was set for 24h did not allow for a better resolution images. Long exposure times can induce cell phototoxicity, which can cause cellular membrane bebbing and even cell death. On the other hand, fluorescent markers can experience photobleaching, where they are chemically altered irreversibly losing its fluorescence, which in turn can also cause phototoxicity. To avoid this, the *in vivo* recording where set at low laser energy and minimal caption time.

On this regard, NPs are ideal candidates since they do not suffer photobleaching as they are imaged by light scattering. As it can be seen on the videos Au signal intensity does not decrease during the recording. Last but not least, the laser energy needed is extremely low compared to that to excite fluorophores, critical when observing living cells. This correlates with the fact that cross-section scattering values of the Au NPs (**Table 3.1**) are several orders of magnitude higher than, for instance, the cross-section of the FITC fluorophore ($5.3 \times 10^{-18} \text{ cm}^2/\text{molecule}$).

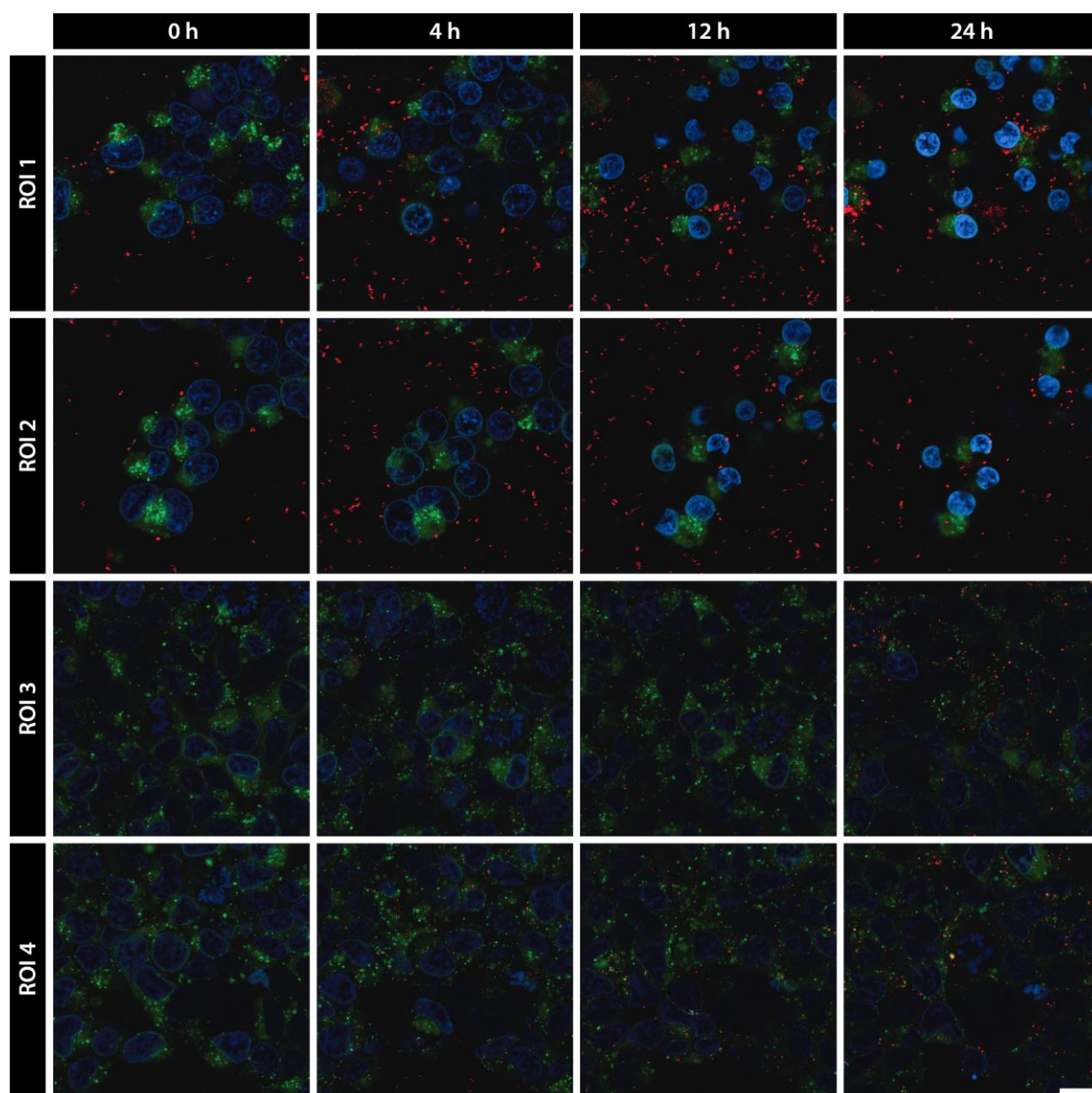


Figure 3.12. Time frames from the real-time imaging of Au NPs on HEK293 cells at time 0h, 4h, 12h and 24h. Cytoplasm (green) and nuclei (blue) staining were acquired by conventional fluorescence, and NPs (red) were imaged by reflectance. Scale bar = 10 μm .

3.3.5 Other Materials

The same principles of light scattering apply to a wide range of other inorganic NPs. Here, some of them relevant in the biomedical field, were also successfully imaged on the confocal microscope using the reflectance mode. For this, silver NPs (Ag NPs), [40] cerium oxide NPs (CeO_2 NPs), [41] iron oxide (Fe_3O_4 NPs), [42] and gold-cerium oxide hybrid core-shell NPs ($\text{Au}@\text{CeO}_2$ NPs) [43] were synthesized. Their characterization by TEM, DLS and UV-Vis spectra is summarized in **Table 3.3**. These NPs were imaged on the CLSM on colloidal suspension (**Figure 3.13A and D**).

Calculated extinction (Q_{ext}), scattering (Q_{sca}), and absorption (Q_{abs}) efficiency are shown in **Figure 3.13C** and **F**, showing that the strongest scattering is induced when NPs are irradiated by a light within the maximum scattering band. Ag NPs exhibit strong surface plasmon resonance, which peak position red-shifts as NP's size increases typically ranging between 400-550nm. Likewise, their scattering contribution to the total extinction increases with size. Ag NPs were imaged using the 514nm laser where the higher the signal collected. The images acquired on reflectance mode showed that bigger NPs scatter more light, while no appreciable signal is collected for the small NPs (15nm). This correlated well with the relative scattering efficiency calculated for each NP size (**Figure 3.13C**).

On the other hand, oxides like CeO_2 and Fe_3O_4 NPs could also be imaged on the confocal microscope using the 639 nm laser. However, it was possible due to their agglomeration state. Typically, the aqueous synthesis of CeO_2 and Fe_3O_4 NPs leads to small NPs (3-7nm), that tend to aggregate into larger stable agglomerates. The light scattering of individual NPs would be too weak to image them on the confocal microscope, but not for the aggregates.

Finally, confocal imaging by reflectance mode was also performed on hybrid core-shell $\text{Au}@\text{CeO}_2$ NPs. For the synthesis, two sizes of Au NPs, 40 and 100nm, were used as templates to grow the CeO_2 shell of 8nm and 18nm respectively. The presence of the CeO_2 coating results in both an increase in the LSPR extinction peak intensity of the Au core and a systematic red-shift of its position. When imaging them on the confocal microscope using the 561nm laser, it translated into higher scattering efficiency, compared to same size Au NPs.

Table 3.3. Summary of sizes and optical properties of NPs synthesized and used on **Figure 3.13**.

		TEM (nm)	DLS diameter (nm)	Peak Position (nm)
Ag	15 nm	14.4 \pm 2.1	17.8 \pm 2.1	402
	50 nm	43.2 \pm 6.8	62.8 \pm 21.7	429
	100 nm	97.6 \pm 9.6	101.7 \pm 29.5	493 / q408
	150nm	140.8 \pm 10.9	142.1 \pm 54.2	544 / q425
CeO_2	3.5 nm	4.2 \pm 1.5	470.0 \pm 203.9	291
$\text{Au}@\text{CeO}_2$	40 nm	Au 37.9 \pm 3.8 Ce shell 8.3 \pm 0.9	34.3 \pm 6.9 / 782.2 \pm 234.1	283 / 546
	100 nm	Au 103.9 \pm 17.1 Ce shell 18.4 \pm 4.3	178.7 \pm 72.1	283 / 628
Fe_3O_4	7 nm	10.7 \pm 2.3	75.5 \pm 13.8 / 375.0 \pm 102.6	-

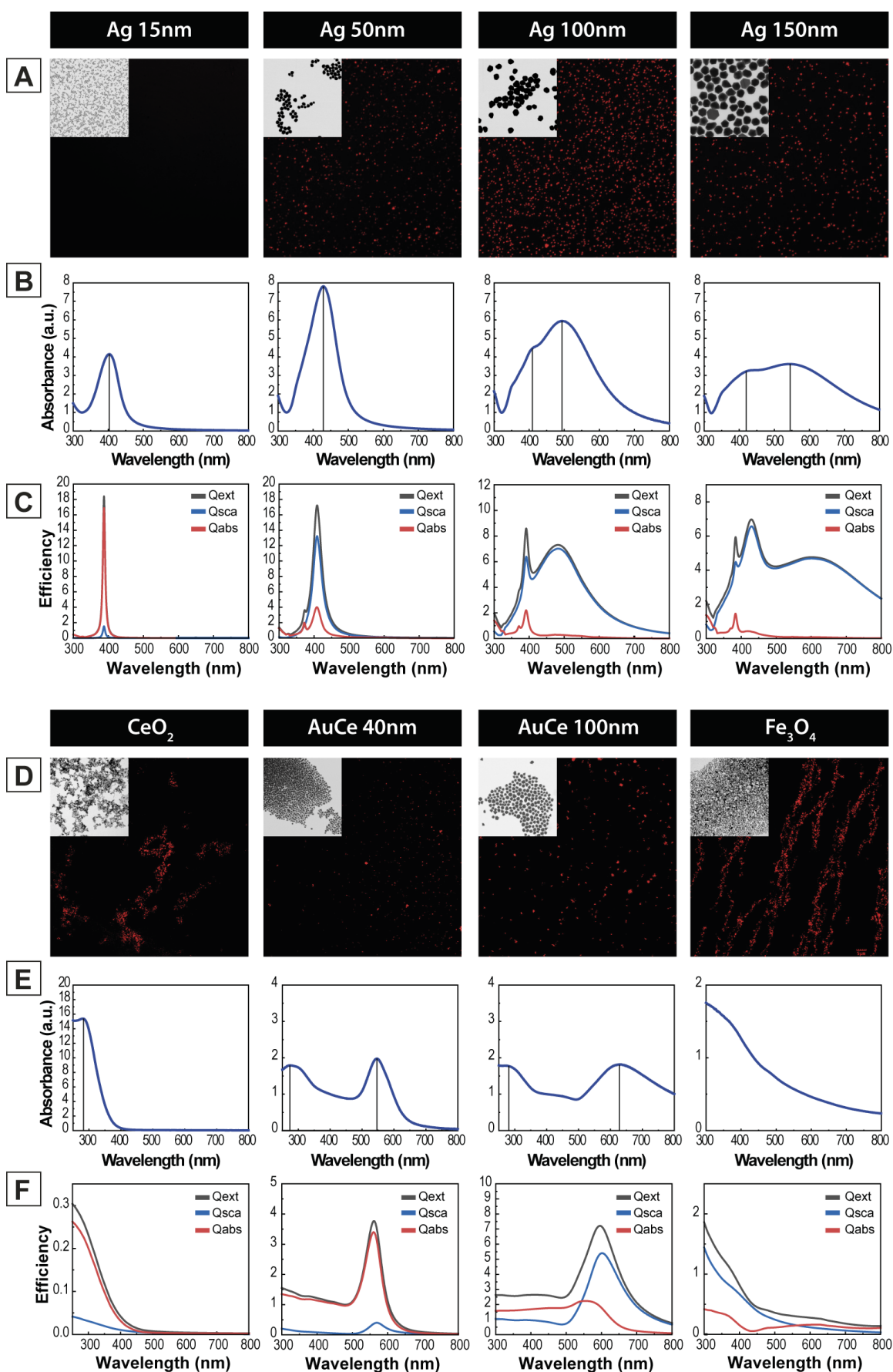


Figure 3.13. Optical properties and CSLM imaging of other materials. (A, D) CSLM images of different sizes and compositions NPs. Ag NPs were imaged with the 515 nm laser, CeO₂ and Fe₃O₄ NPs with the 639 nm laser, and Au@CeO₂ NPs with the 561 nm laser. (Inset) Representative TEM images of the NPs. (B, E) UV-Vis spectra of NPs. (C, F) Calculated extinction (Qext), scattering (Qsca), and absorption (Qabs) efficiency.

3.4 References

- [1] Englebienne, P., Van Hoonacker, A., & Verhas, M. Surface plasmon resonance: Principles, methods and applications in biomedical sciences. *Spectroscopy* 17, 255–273 (2003)
- [2] Sperling, R. A., Gil, P. R., Zhang, F., Zanella, M., & Parak, W. J. Biological applications of gold nanoparticles. *Chemical Society Reviews* 37, 1896–1908 (2008)
- [3] Jain, P. K., Huang, X., El-Sayed, I. H., & El-Sayed, M. A. Noble metals on the nanoscale: Optical and photothermal properties and some applications in imaging, sensing, biology, and medicine. *Accounts of Chemical Research* 41, 1578–1586 (2008)
- [4] Jans, H. & Huo, Q. Gold nanoparticle-enabled biological and chemical detection and analysis. *Chemical Society Reviews* 41, 2849–2866 (2012)
- [5] Jain, P. K., Lee, K. S., El-Sayed, I. H., & El-Sayed, M. A. Calculated absorption and scattering properties of gold nanoparticles of different size, shape, and composition: Applications in biological imaging and biomedicine. *Journal of Physical Chemistry B* 110, 7238–7248 (2006)
- [6] Reimer, P. & Balzer, T. Ferucarbotran (Resovist): a new clinically approved RES-specific contrast agent for contrast-enhanced MRI of the liver: properties, clinical development, and applications. *European Radiology* 13, 1266–1276 (2003)
- [7] Xu, C. & Qu, X. Cerium oxide nanoparticle: a remarkably versatile rare earth nanomaterial for biological applications. *NPG Asia Materials* 6, e90–e90 (2014)
- [8] Pankhurst, Q. A., Thanh, N. K. T., Jones, S. K., & Dobson, J. Progress in applications of magnetic nanoparticles in biomedicine. *Journal of Physics D: Applied Physics* 42, 224001 (2009)
- [9] Talmadge, J. E., Singh, R. K., Fidler, I. J., & Raz, A. Murine models to evaluate novel and conventional therapeutic strategies for cancer. *American Journal of Pathology* vol. 170 793–804 (2007)
- [10] Casals, E. & Puentes, V. F. Inorganic nanoparticle biomolecular corona: Formation, evolution and biological impact. *Nanomedicine* vol. 7 1917–1930 (2012)
- [11] Monopoli, M. P., Walczyk, D., Campbell, A., Elia, G., Lynch, I., Baldelli Bombelli, F., & Dawson, K. A. Physical-Chemical aspects of protein corona: Relevance to *in vitro* and *in vivo* biological impacts of nanoparticles. *Journal of the American Chemical Society* 133, 2525–2534 (2011)
- [12] Monopoli, M. P., Aberg, C., Salvati, A., & Dawson, K. A. Biomolecular coronas provide the biological identity of nanosized materials. *Nature nanotechnology* 7, 779–86 (2012)
- [13] Goy-López, S., Juárez, J., Alatorre-Meda, M., Casals, E., Puentes, V. F., Taboada, P., & Mosquera, V. Physicochemical characteristics of protein-NP bioconjugates: The role of particle curvature and solution conditions on human serum albumin conformation and fibrillogenesis inhibition. *Langmuir* 28, 9113–9126 (2012)

- [14] Izak-Nau, E., Voetz, M., Eiden, S., Duschl, A., & Puentes, V. F. Altered characteristics of silica nanoparticles in bovine and human serum: The importance of nanomaterial characterization prior to its toxicological evaluation. *Particle and Fibre Toxicology* 10, 1–12 (2013)
- [15] Cho, E. J., Holback, H., Liu, K. C., Abouelmagd, S. A., Park, J., & Yeo, Y. Nanoparticle characterization: State of the art, challenges, and emerging technologies. *Molecular Pharmaceutics* 10, 2093–2110 (2013)
- [16] Wegner, K. D. & Hildebrandt, N. Quantum dots: bright and versatile *in vitro* and *in vivo* fluorescence imaging biosensors. *Chemical Society Reviews* 44, 4792–4834 (2015)
- [17] Larson, D. R., Zipfel, W. R., Williams, R. M., Clark, S. W., Bruchez, M. P., Wise, F. W., & Webb, W. W. Water-soluble quantum dots for multiphoton fluorescence imaging *in vivo*. *Science* 300, 1434–1436 (2003)
- [18] Van Schooneveld, M. M., Cormode, D. P., Koole, R., Van Wijngaarden, J. T., Calcagno, C., Skajaa, T., Hilhorst, J., 'T Hart, D. C., Fayad, Z. A., Mulder, W. J. M., & Meijerink, A. A fluorescent, paramagnetic and PEGylated gold/silica nanoparticle for MRI, CT and fluorescence imaging. *Contrast Media & Molecular Imaging* 5, 231–236 (2010)
- [19] Wu, C., Bull, B., Szymanski, C., Christensen, K., & McNeill, J. Multicolor conjugated polymer dots for biological fluorescence imaging. *ACS Nano* 2, 2415–2423 (2008)
- [20] Michalet, X., Pinaud, F., Lacoste, T. D., Dahan, M., Bruchez, M. P., Alivisatos, A. P., & Weiss, S. Properties of fluorescent semiconductor nanocrystals and their application to biological labeling. *Single Molecules* 2, 261–276 (2001)
- [21] Ramirez, M. D. L. A., Martinez-Villacorta, A. M., Gomez-Vallejo, V., Andreozzi, P., Soler-Illia, G., Llop, J., & Moya, S. E. Core vs. surface labelling of mesoporous silica nanoparticles: advancing the understanding of nanoparticle fate and design of labelling strategies. *Nanoscale Advances* 4, 2098–2106 (2022)
- [22] Bindini, E., Ramirez, M. de los A., Rios, X., Cossío, U., Simó, C., Gomez-Vallejo, V., Soler-Illia, G., Llop, J., & Moya, S. E. *In Vivo* Tracking of the Degradation of Mesoporous Silica through ⁸⁹Zr Radio-Labeled Core–Shell Nanoparticles. *Small* 17, 2101519 (2021)
- [23] Wang, W., Gaus, K., Tilley, R. D., & Gooding, J. J. The impact of nanoparticle shape on cellular internalisation and transport: what do the different analysis methods tell us? *Materials Horizons* 6, 1538–1547 (2019)
- [24] Llop, J., Jiang, P., Marradi, M., Gómez-Vallejo, V., Echeverría, M., Yu, S., Puigivila, M., Baz, Z., Szczupak, B., Pérez-Campaña, C., Mao, Z., Gao, C., & Moya, S. E. Visualisation of dual radiolabelled poly(lactide- co -glycolide) nanoparticle degradation *in vivo* using energy-discriminant SPECT. *Journal of Materials Chemistry B* 3, 6293–6300 (2015)
- [25] Sirimuthu, N. M. S., Syme, C. D., & Cooper, J. M. Investigation of the stability of labelled nanoparticles for SE(R)RS measurements in cells. *Chemical Communications* 47, 4099–4101 (2011)

- [26] Tong, L., Liu, Y., Dolash, B. D., Jung, Y., Slipchenko, M. N., Bergstrom, D. E., & Cheng, J. X. Label-free imaging of semiconducting and metallic carbon nanotubes in cells and mice using transient absorption microscopy. *Nature Nanotechnology* 7, 56–61 (2011)
- [27] Huang, B., Yan, S., Xiao, L., Ji, R., Yang, L., Miao, A. J., & Wang, P. Label-Free Imaging of Nanoparticle Uptake Competition in Single Cells by Hyperspectral Stimulated Raman Scattering. *Small* 14, 1703246 (2018)
- [28] Kim, D., Oh, N., Kim, K., Lee, S. Y., Pack, C. G., Park, J. H., & Park, Y. K. Label-free high-resolution 3-D imaging of gold nanoparticles inside live cells using optical diffraction tomography. *Methods* 136, 160–167 (2018)
- [29] Patskovsky, S., Bergeron, E., Rioux, D., & Meunier, M. Wide-field hyperspectral 3D imaging of functionalized gold nanoparticles targeting cancer cells by reflected light microscopy. *Journal of Biophotonics* 8, 401–407 (2015)
- [30] Bastús, N. G., Piella, J., & Puentes, V. Quantifying the Sensitivity of Multipolar (Dipolar, Quadrupolar, and Octapolar) Surface Plasmon Resonances in Silver Nanoparticles: The Effect of Size, Composition, and Surface Coating. *Langmuir* 32, 290–300 (2016)
- [31] Sun, Y. & Xia, Y. Gold and silver nanoparticles: A class of chromophores with colors tunable in the range from 400 to 750 nm. *Analyst* 128, 686–691 (2003)
- [32] Zamora-Perez, P., Tsoutsi, D., Xu, R., & Rivera-Gil, P. Hyperspectral-Enhanced Dark Field Microscopy for Single and Collective Nanoparticle Characterization in Biological Environments. *Materials* 11, 243 (2018)
- [33] Gibbs-Flournoy, E. A., Bromberg, P. A., Hofer, T. P. J., Samet, J. M., & Zucker, R. M. Darkfield-Confocal Microscopy detection of nanoscale particle internalization by human lung cells. *Particle and Fibre Toxicology* 8, 1–11 (2011)
- [34] Lindfors, K., Kalkbrenner, T., Stoller, P., & Sandoghdar, V. Detection and spectroscopy of gold nanoparticles using supercontinuum white light confocal microscopy. *Physical Review Letters* 93, 037401 (2004)
- [35] Guggenheim, E. J., Khan, A., Pike, J., Chang, L., Lynch, I., & Rappoport, J. Z. Comparison of Confocal and Super-Resolution Reflectance Imaging of Metal Oxide Nanoparticles. *PLOS ONE* 11, e0159980 (2016)
- [36] Wang, F., Chen, B., Yan, B., Yin, Y., Hu, L., Liang, Y., Song, M., & Jiang, G. Scattered Light Imaging Enables Real-Time Monitoring of Label-Free Nanoparticles and Fluorescent Biomolecules in Live Cells. *Journal of the American Chemical Society* 141, 14043–14047 (2019)
- [37] Bastús, N. G., Comenge, J., & Puentes, V. Kinetically controlled seeded growth synthesis of citrate-stabilized gold nanoparticles of up to 200 nm: Size focusing versus ostwald ripening. *Langmuir* 27, 11098–11105 (2011)
- [38] Li, J. F., Li, C. Y., & Aroca, R. F. Plasmon-enhanced fluorescence spectroscopy. *Chemical Society Reviews* 46, 3962–3979 (2017)
- [39] Barbero, F., Russo, L., Vitali, M., Piella, J., Salvo, I., Borrajo, M. L., Busquets-Fité, M., Grandori, R., Bastús, N. G., Casals, E., & Puentes, V. Formation of the Protein

- Corona: The Interface between Nanoparticles and the Immune System. *Seminars in Immunology* 34, 52–60 (2017)
- [40] Bastús, N. G., Merkoçi, F., Piella, J., & Puentes, V. Synthesis of highly monodisperse citrate-stabilized silver nanoparticles of up to 200 nm: Kinetic control and catalytic properties. *Chemistry of Materials* 26, 2836–2846 (2014)
- [41] Oró, D., Yudina, T., Fernández-Varo, G., Casals, E., Reichenbach, V., Casals, G., De La Presa, B. G., Sandalinas, S., Carvajal, S., Puentes, V., & Jiménez, W. Cerium oxide nanoparticles reduce steatosis, portal hypertension and display anti-inflammatory properties in rats with liver fibrosis. *Journal of Hepatology* 64, 691–698 (2016)
- [42] Casals, E., Barrena, R., García, A., González, E., Delgado, L., Busquets-Fité, M., Font, X., Arbiol, J., Glatzel, P., Kvashnina, K., Sánchez, A., & Puentes, V. Programmed Iron Oxide Nanoparticles Disintegration in Anaerobic Digesters Boosts Biogas Production. *Small* 10, 2801–2808 (2014)
- [43] Piella, J., González-Febles, A., Patarroyo, J., Arbiol, J., Bastús, N. G., & Puentes, V. Seeded-Growth Aqueous Synthesis of Colloidal-Stable Citrate-Stabilized Au/CeO₂ Hybrid Nanocrystals: Heterodimers, Core@Shell, and Clover- And Star-Like Structures. *Chemistry of Materials* 31, 7922–7932 (2019)

CHAPTER 4

SIZE EFFECTS ON AG NP - ANTIBIOTIC SYNERGY

Size Effects on Ag NP-Antibiotic Synergy

4.1 Introduction

Antibiotic resistance of pathogens is a concerning issue, with rising incidence worldwide, and a major cause of treatment failure. Antimicrobial resistance (AMR) is defined “as the ability of a microorganism (bacteria, fungi or virus) to resist the action of one or more antimicrobial agents (antibiotics, antifungal or antivirals)”. Accordingly, multi-drug resistant strains show non-susceptibility to more than one antibiotic class of agents. Once bacteria has contact with an antibiotic but is not killed, it responds by adapting and acquiring resistance to it. Mechanisms underlying antibiotic resistance can be (i) intrinsic, (ii) adaptive via transitory changes of gene expression, or (iii) acquired due to a spontaneous mutation or the gain of genetic material. Then, this resistance can be transmitted vertically (to its descendants) or horizontally (sharing of genetic material between different bacteria).

The resistance of bacterial strains to antibiotics has been rapidly growing globally in recent years (Fair and Tor, 2014). [1] Seventy years after antibiotics discovery, and despite decades of successful treatment, our antimicrobial substances are becoming obsolete and untreatable infections in the clinic are part of the new normal. [2] The reasons are overuse of antibiotics, not only by improper medical use, but also from animal farms and the food industry. Rapid spreading of bacteria worldwide due to globalization, absence of rapid diagnostic tests for identifying infections caused by multiresistant bacteria, and appearance of new antibiotics is decreasing and the pharmaceutical companies that develop new antibiotics are disappearing. Today Healthcare Associated Infections represent a major clinical threat worldwide, in particular with the recent emergence of pathogens resistant to most or all available antimicrobial drugs, imposing an enormous burden in terms of

morbidity, mortality and healthcare-associated costs. [3] Not only that, but now we have entered in a period where no more antibiotic molecules are being discovered or developed, but bacterial resistance is dramatically increasing while we are running out of available drugs. Thus, multimodality and other antimicrobial agents such as silver nanoparticles (Ag NPs) are considered to manage and prevent infections. [4] Still, we need to come up with long-term solutions and nanotechnology offers a promising platform to overcome this problem: the combination of biological methods and nanotechnology tools.

In recent years, and fueled by this rising threat of antibiotic resistance, numerous studies have been carried out on the subject of antibacterial efficacy of silver ions and nanoparticles - antibiotic combinations. [5–7] Silver has been employed in the medical field for many centuries due to its antimicrobial properties and the NP form was FDA approved over 130 years ago. [8] It has been applied to treat open wounds, burns, *ophthalmia neonatorum*, surgical instruments, or bone prostheses. Further, it is also present in house-hold products as room sprays, detergents, or water purification treatments. [9,10] Yet, the exact mechanisms of its antimicrobial activity are not fully understood.

Silver has been reported to be a broad-spectrum antibiotic, effective against gram-positive and gram-negative bacteria, MDR bacteria, fungi, virus, and protozoa. [11] Specifically, in bacteria it is hypothesized that triggers membrane damage, reactive oxygen species (ROS) production and silver ions (Ag^+) uptake that finally leads to ATP depletion and inhibition of DNA replication. Klueh et al. (2000) proposed that silver inhibits bacterial growth by inactivating the proteins. This study states that silver ions bind to thiol groups (-SH), altering the functions of enzymes and compounds of the cell membrane important in energy generation and ion transport, all essential for bacteria survival. Moreover, it also elucidated the ability of silver ions to intercalate between the purine and pyrimidine bases of DNA, causing the denaturalization of DNA, which impairs the replication of DNA and cell division, leading to cell death. [12,13] Another study assessing the antibacterial activity of silver was carried out by Yamanaka et al. (2005), who found that Ag^+ affects the expression of 30S ribosomal subunit that causes the denaturalization of the ribosome structure and its protein and enzyme-synthesizing function is impaired. Consequently, expression of proteins and enzymes implicated in the production of ATP was suppressed, indispensable in maintaining cell life. [14] Finally, one of the most accepted antibacterial mechanisms of silver is the production of ROS, which leads to cell death due to damage of different internal cell structures.

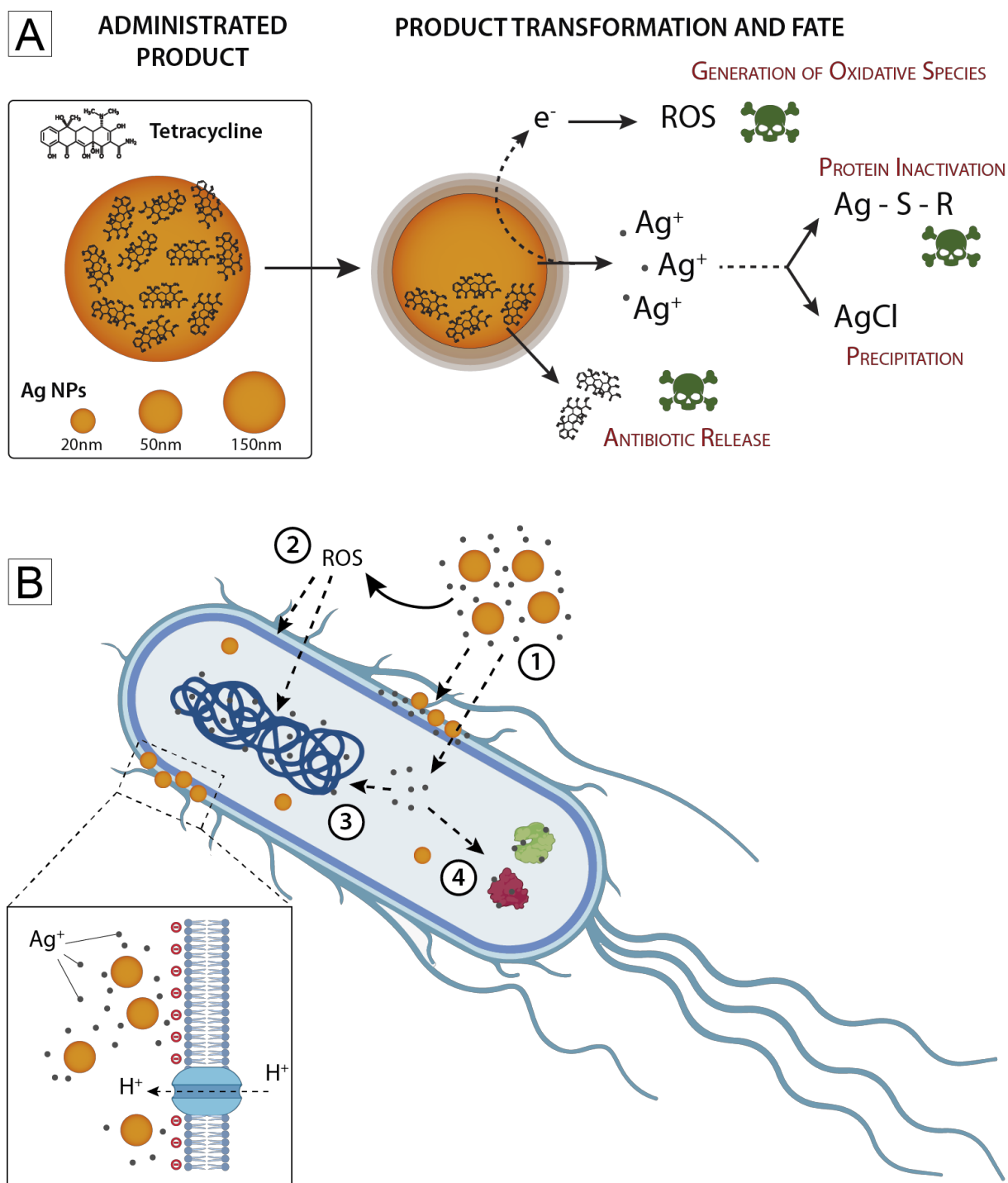


Figure 4.1. Antibacterial mechanisms of action. (A) Schematic representation of the project strategy. The administrated product is based on the combination of 20, 50 and 150 nm Ag NPs with conventional antibiotics. The chemical transformations upon exposure to culture media allow the active principles to act, by antibiotic release from NP and by Ag NPs dissolution. **(B)** Proposed mechanisms of Ag NPs related bacterial damage. (1) Silver ions release is promoted by acidic and aerobic environment (2) Formation of ROS, which then damage both the membrane lipids and DNA. (3-4) Ag⁺ uptake can be promoted by membrane damage (although they might enter also through membrane channels). Ag⁺ ions may bind intracellular proteins and the bacterial chromosome, upon entering the cytosol, thus influencing the metabolic activity and replication. (Inset) positively charged Ag NPs may be attracted by negatively charged bacterial membrane leading to higher local dose of NPs. Here, the proton motive force takes place, causing a local decrease of pH. This can further promote the dissolution of Ag NPs, resulting in a local higher Ag⁺ concentration. In this picture, a gram-negative bacterium has been taken as model microorganism. Adapted from ref: Rizzello 2014

A large and constantly increasing amount of literature evidences the potential role of silver nanoparticles as optimal candidates to treat infectious diseases (reviewed by Rizzello et al.). [11] The antimicrobial properties of silver have been known for a long time, but now bottom-up approaches in nanotechnology enable the design of Ag NP with custom-tailored unique physicochemical properties. The key point is that nanoparticles exhibit different chemical and physical properties as the ionic or bulk material. They have a high surface-to-volume ratio, which provides enlarged contact area with the environment and thus enhances their chemical and biological surface activity. [15] Likewise, working with the particulate form with dimensions at the nanoscale offers a size-dependent body biodistribution and may allow the active principle to be delivered preferentially at the site of infection.

Although the broad-spectrum antimicrobial properties of Ag NPs have been extensively reported, a clear and definitive knowledge of the effects of Ag NPs on microorganisms is still lacking. Many authors claim that Ag NPs are far more efficient than Ag^+ , and properties as size, shape and surface charge have a great influence on their bactericidal potential, being the smallest and positive charged the most effective. [13,16–18] Those factors could influence on the affinity of the nanoparticles to the bacterial membrane, and its disruption, and the ROS generation capacity. However, the discrepancies found in other conducted studies highlight the lack of standardized methods and that those results strongly depend on the method/technique used to carry out the biological assays. [16,19] Regarding this, Xiu and collaborators performed an extensive study on whether Ag NPs have antibacterial activity themselves or it is purely due to Ag^+ release. [19] They found out that the physicochemical properties of Ag NP (size, shape and charge) affect the toxicity only indirectly, by affecting the rate, location and amount of Ag^+ released from the nanoparticle surface. This can only happen under aerobic conditions, since the oxidation of silver is the main cause of Ag^+ ions release, through interaction with H^+ ions; thus, acidic conditions induce an enhanced rate of Ag^+ release than neutral pH conditions (**Figure 4.1**). Additionally, the presence of bacteria also affects the ion release rate due to the acidification of the environment as a result of their metabolism, which in turn is medium and strain-dependent; consequently, the same Ag NPs might display different antibacterial efficacy against different strains. Note that the release of Ag^+ is via a corrosion process that increases ROS production in biological environments. [20,21]

One of the main concerns regarding the use of silver (whatever the type) as an antimicrobial agent is the development of resistance against it. Antibiotic resistance mechanisms are

mainly based on efflux pumps, enzymatic modification or degradation of the antibiotic molecule, and alteration of the target. So, the strategies in order to overcome this phenomenon are focused on (i) inhibiting the resistance enzymes, (ii) block the efflux pumps, (iii) apply synergistic activity between antibiotics and non-antibiotics, and (iv) enhance the entry and the sensitivity to them. Despite the likelihood of developing resistance due to the increasing use of silver, as happens for other antimicrobial compounds, in this case there is a reduced probability of resistance as it targets different bacterial structures and has a complex action mechanism. [15] However, several resistance mechanisms to metals have been described. They are mostly based on ion efflux pumps aimed to avoid/expel Ag^+ from inside the cell, since direct damage caused by Ag NP/ Ag^+ can't be prevented or repaired. In particular, a specific gene cluster named *sil* has been reported to codify for several proteins responsible for silver resistance, which have different functions as membrane efflux pumps (silABC and silP), periplasmic binding proteins (silE), and signal transduction proteins (silRS). [11,22] Considering this, the resistance and sensitivity of bacteria to silver depend on the overall Ag^+ bioavailability. Therefore, if Ag NPs act as a continuous source of Ag^+ ions with the potential ability to saturate the resistance mechanisms, they could be a promising approach for overcome bacterial resistance. In addition, AgNP surfaces can be loaded with antibiotics for multimodal therapy, to which is extremely difficult to become resistant.

The use of nanotechnology in the field of medicine, more specifically drug delivery is a promising approach for targeted and controlled release of drugs. [23] The use of nanocarriers for drug delivery allow to protect the drug, alter (control) its biodistribution, alter its dosage profile (Pharmacokinetics) and deliver a large amount of drug to the cell. Ideally, an antimicrobial compound should only be selective to structures or functions exclusive of bacteria, otherwise it will display side effects related to their mechanism of action and biodistribution. The delivery of antibiotics using nanocarriers to the site of infection could be a promising therapy in order to achieve localized and controlled release, which in turn would help in reducing the dosage and side effects. [24,25] Though, Ag NPs for antibiotic delivery would not only be nanocarriers, but also an active principle themselves due to their antimicrobial characteristics, hereby the multimodal therapy.

Although NPs are a promising platform for the development of novel therapies they also possess serious challenges. The main limitation regarding the use of silver nanoparticles in biomedical applications is their associated toxicity. [9,26–28] The release of Ag^+ ions and the strong oxidative activity associated with Ag NPs corrosion trigger elevated oxidative

stress, which is the main source of their cytotoxic and biocide effects. The increase in oxidative stress is caused by a decrease of the levels of glutathione (GHS) and superoxide dismutase (SOD), and an increase in lipid peroxidation, that finally leads to up-regulation of caspase-3 activity and DNA fragmentation, and ultimately apoptosis. [9,28] Moreover, the cytotoxicity of Ag NPs depends on time, dose, temperature and other factors such as size and surface chemistry. NP size mediates particular cell responses, including uptake, cytotoxicity, ability to penetrate biological barriers, and immunological responses. On the other hand, surface coating can affect shape, aggregation and dissolution ratio, which also have a critical impact on their fate. [26,28–31]

In recent years, numerous studies have been carried out on the subject of antibacterial efficacy of NP-antibiotic combinations. Several conducted studies have proved that while Ag NPs or antibiotic alone may have low bacteriostatic activity, a significant reduction in bacterial growth is observed when they are combined. This is clearly revealed by the decrease in the bacterial minimum inhibitory concentration (MIC), the parameter that defines the amount of antibiotic needed to inhibit bacterial growth. [32,33] Even further, in some cases the resistance has been reverted, and bacteria became again sensitive to previously effective antibiotics. Hence, combined use of NPs and antibiotics makes it possible to reduce the toxicity of both agents towards human cells due to decreased dosage while synergistically enhancing their antimicrobial activities. [15] In this regard, different hypothesis trying to explain the underlying mechanisms of synergy have been proposed: (i) Ag NP and the antibiotic have different mechanisms of action that target different cellular structures, (ii) an increase of the concentration at the site of action because Ag NP are acting as a nanocarriers, (iii) a higher antibiotic uptake/internalization due to membrane disruption as a consequence of silver action, or because (iv) silver impairs the function of resistance proteins against the antibiotic drug. [25,32–37]

There are many reports which revealed that combined use of antibiotics, such as ampicillin, kanamycin, chloramphenicol, enoxacin, neomycin, tetracycline and silver nanoparticles enhanced antimicrobial activity of both compounds. [34,38–41] In a comprehensive study, the combined action of Ag NPs with 14 antibiotics from different groups was examined against gram-positive and gram-negative bacteria, *Staphylococcus aureus* and *Escherichia coli*, respectively. The results of the study showed enhancement of antibacterial activity of penicillin G, amoxicillin, erythromycin, clindamycin and vancomycin in the presence of Ag NPs against both tested strains. [33] In another study enoxacin, kanamycin, neomycin, and tetracycline showed synergistic effect against a resistant *Salmonella typhimurium* DT

104 strain when combined with Ag NPs, while ampicillin and penicillin did not. [39] UV–vis and Raman spectroscopy studies reveal that all these four antibiotics with a synergistic effect can form complexes with Ag NPs, while ampicillin and penicillin do not. The presence of tetracycline enhanced the binding of Ag to *Salmonella* spp. by 21% and Ag^+ release by 26% in comparison to Ag alone, while the presence of penicillin did not. The tetracycline–Ag NPs conjugates interacted more strongly with the bacterial cells, creating a temporal high concentration of Ag^+ near the bacteria cell wall. The observed synergy was attributed to the ability of the targeting properties of the antibiotic to lock the Ag NP at the bacterial cell surface from where Ag^+ will be released. Recently, Ag NPs conjugated to amphotericin B (AmB) were successfully tested against fungal infections, and it was observed that the conjugate retained both the bactericidal effect of silver and the cytotoxic and antifungal effect of AmB. [42]

The proposed project was carried out as a response to the significance of combining the use of Ag NPs with another antibiotic drug and their role in overcoming multi-drug resistant bacteria. The aim of our work was to synthesize Ag NPs with high monodispersity and well-defined size to estimate their antimicrobial activity against selected gram-positive and gram-negative bacteria in combination with representative antibiotics. The selected antibiotics were colistin (polymyxin E), vancomycin, amikacin and tetracycline. These four antibiotics were selected as model of currently employed antibiotic families in the clinic, and represent the major two way of antibiotics action. The first two (colistin and vancomycin) interact with the bacterial cell membrane, colistin is a large cationic heterocyclic compound which interact and interferes with the bacterial cell membrane while vancomycin is a similar cationic heterocycle but with a significant smaller size what helps to permeate the cell membrane, both therefore contributing to attach and shuttle Ag NPs to and into the bacteria. The two other, amikacin and tetracycline interfere with bacterial metabolism targeting synthesis of proteins in the ribosome.

4.2 Scope of the study

This work addresses two questions, (i) the synergistic effect between Ag and antibiotics against multidrug resistant bacteria, and (ii) the determination of the Ag^+ release profile by NP morphology and surface state.

4.3 Results and Discussion

4.3.1 Synthesis of Silver Nanoparticles

Once Ag^+ , provided by Ag NPs, has been identified as the main active principle, a variety of competing chemical approaches are demonstrated for controlling the ion release. Release can be systematically slowed by thiol and citrate ligand binding to the NP surface, formation of sulfidic coatings, or the scavenging of peroxy-intermediates. Release can be accelerated by peroxidation or particle size reduction, while polymer coatings with complexation sites alter the release profile by storing and releasing inventories of surface-bound silver. [43] However, in all these studies NP size has been often ignored or performed with polydisperse and poly-aggregate Ag NPs what strongly interferes with dissolution and introduces high result variability.

Thus, aiming for a precise control over NP size distribution, Ag NPs were produced using a well-established seeded growth approach developed by our group that leads to highly monodisperse citrate-stabilized Ag NPs. [44] It is based on the synthesis of small silver nanoparticles by the reduction of AgNO_3 at 100 °C, which are then used as templates to grow them by adding silver precursor up to the desired size. Ag seeds were obtained after addition of AgNO_3 into a boiling water solution containing sodium citrate (SC) and tannic acid (TA) as reducing agents. Then, these nuclei were used as templates for further growth after successive additions of silver precursor. The growth of the seed particles was kinetically controlled by adjusting the temperature of the reaction, the pH, the seed to precursor ratio, and the balance between both reducing agents. By decreasing the temperature 10 °C, the nucleation rate was dramatically decreased and the growth of the seeds is favoured with respect to the formation of new nuclei. The citrate ion is not only involved in silver reduction, but also plays a critical role in the electrostatic stabilization of the nanoparticles. On the other hand, the incorporation of small amounts of tannic acid on the reaction is critical for the size control of the seeds. It is a stronger reducer than citrate, and the relative concentration of Ag:TA allows to tune the nucleation size of the NPs.

The evolution of the UV-Vis spectra of the NPs is represented in **Figure 4.2** for a typical 140 nm Ag NP seeded-growth synthesis. All spectra are normalized to $\lambda_{325\text{nm}}$ for a better comparison (**A**). In all cases, the spectra show a symmetric LSPR peak that red-shift as NP size increase (**B**). This allows to monitor NP growth during the synthesis. On **Figure 4.2C**,

the LSPR peak position is plotted as a function of the growth step (where “G” stands for growth step). Above ~ 70 nm NP size, the appearance of a new peak can be observed at smaller wavelengths (~ 400 nm), characteristic of quadrupole component of the plasmon resonance, which also red-shifts as NP grow.

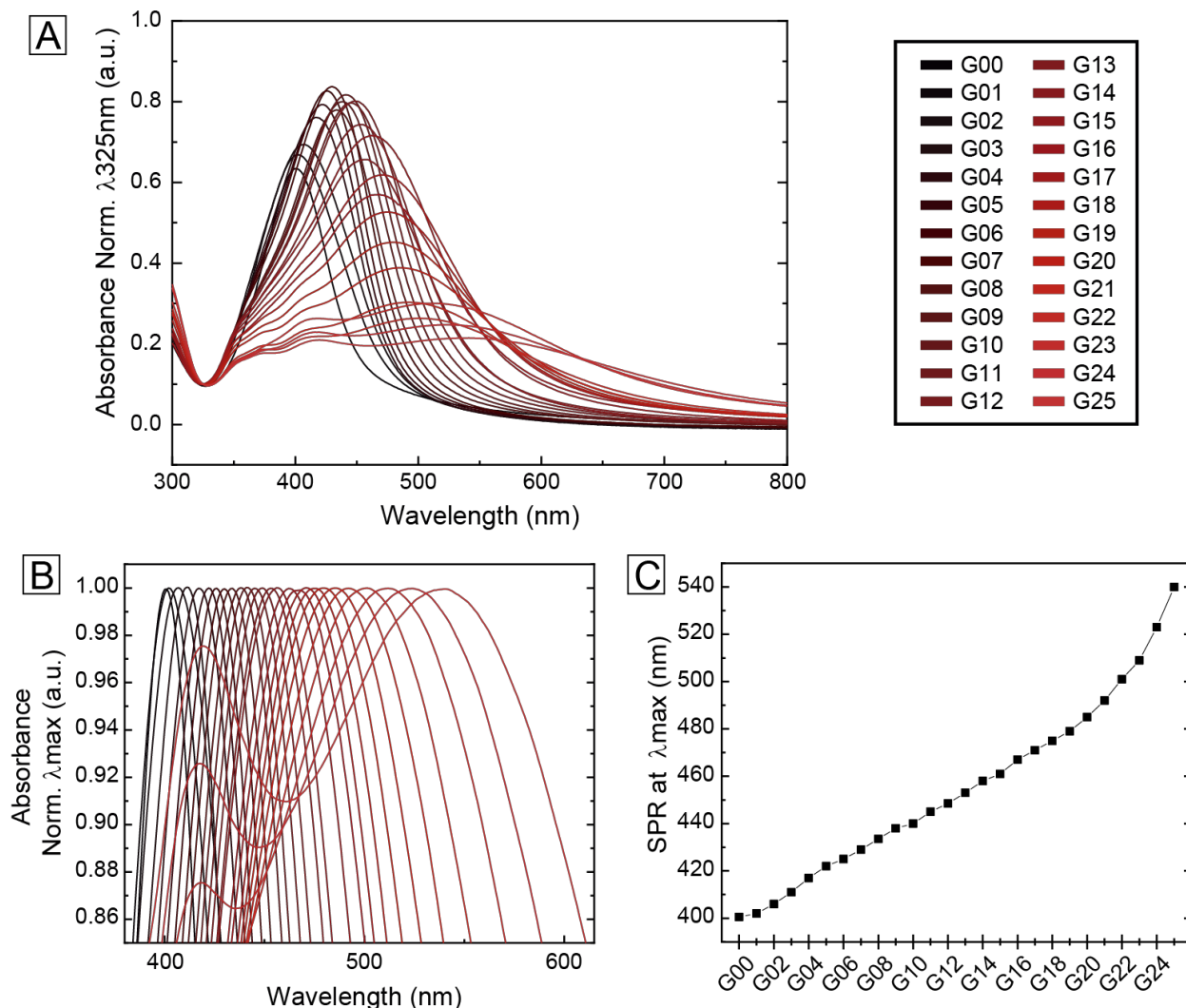


Figure 4.2. Characterization of the Ag seed particles and further growth steps by UV-Vis spectroscopy. (A) UV-Vis spectra of Ag NPs growth evolution. Absorbance is normalized at $\lambda_{325\text{nm}}$ for a better comparison. (B) Absorbance is normalized to the λ_{max} of the SPR dipolar peak for each growth step. (C) Evolution of the dipolar SPR peak position of Ag NPs growth evolution.

For these studies, highly monodisperse citrate-stabilized Ag NPs of three different sizes have been synthesized (~ 20 , 50 , 140 nm). NPs were characterized by the combined use of Scanning Transmission Electron Microscope (STEM), UV-Vis spectroscopy (UV-Vis), Dynamic Light Scattering (DLS) and Zeta potential analysis (Z-pot). Representative TEM images from Ag particles synthesized are shown in **Figure 4.3**. Size distribution of the NPs is calculated from the acquired TEM images. Ag NPs present high monodispersity in all growth steps.

To increase Ag NP stability once exposed to the bacterial growing media, that present high salinity, Ag NP were further conjugated with the bio-compatible polymer polyvinylpyrrolidone (PVP, 55 kDa). PVP is able to interact with the silver surface by the sum of each weak monomer bond, and due to its polymeric nature, it confers steric stabilization to the particles. Thus, after purification NPs were resuspended in a PVP solution to avoid aggregation and provide robust NP colloidal stability in highly saline (physiological) media.

UV-Vis spectra and DLS measurements are presented in **Figure 4.3** of Ag NP before and after PVP conjugation. Narrow particle size distribution was observed before and after stabilization with PVP. Single UV-vis absorption sharp peaks were observed for sizes of 21.0 and 45.9 nm, while for nanoparticles of 139.8 nm the quadrupolar peak appears on the left of a broadened dipolar peak, indicating the large size and small polydispersity of the nanoparticles. As expected, the peaks of PVP stabilized silver nanoparticles were right shifted (few nm towards a longer wavelength) compared to citrate-capped NP. After the conjugation with the polymer a decrease in the Z-Potential value is observed (**Table 4.1**), consistent with the PVP functionalization of the Ag NPs.

Table 4.1. Summary of sizes, optical properties and surface charge of the Ag NPs obtained after synthesis and PVP coating.

	TEM (nm)	LSPR peak (nm)	DLS (nm)	Z-Potential (mV)
Ag 20 nm				
NP	21.0 ± 2.9	402	28.3 ± 6.4	-20.2
NP + PVP	-	404	40.2 ± 13.2	-9.5
Ag 50 nm				
NP	45.9 ± 4.3	433	67.2 ± 21.9	-38.9
NP + PVP	-	435	82.1 ± 27.2	-26.4
Ag 150 nm				
NP	139.8 ± 13.4	594 / q441	125.7 ± 49.3	-29.6
NP + PVP	-	594 / q443	150.6 ± 44.8	-23.0

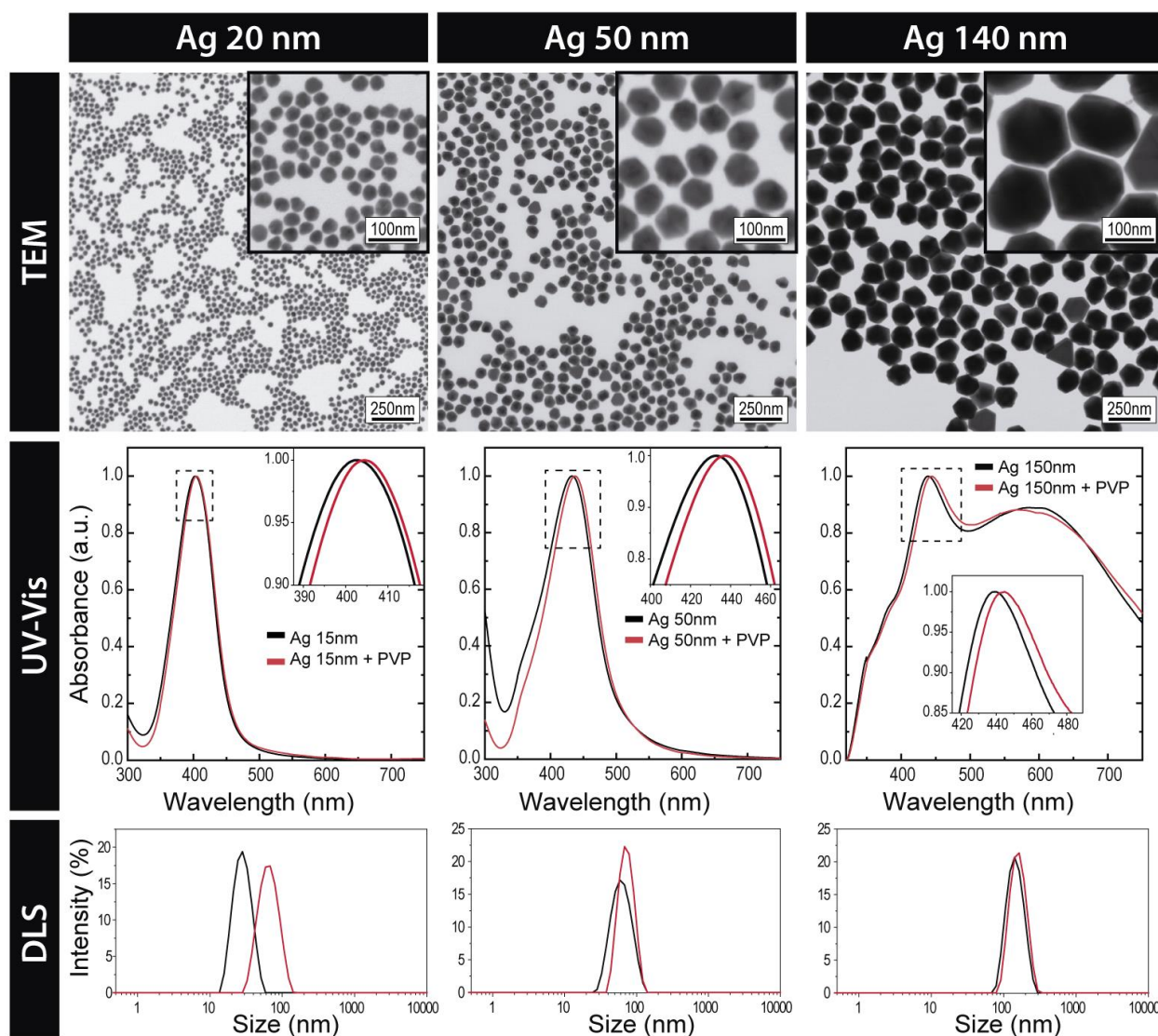


Figure 4.3. Characterization of synthesized Ag NP and coating with PVP. (Up) Transmission electron microscopy images of Ag NPs obtained, with particle size distributions of 21.0 ± 2.9 nm, 45.9 ± 4.3 nm, 139.8 ± 13.4 nm. (Middle) UV-Vis spectra of the citrate-capped Ag NPs, and after PVP coating. Absorbance is normalized to maximum for a better comparison. (Down) Size distribution profiles measured by DLS in Intensity.

4.3.2 Size-dependent corrosion of Silver Nanoparticles in biological media

Ag is a noble metal, but it becomes very reactive at the nanoscale due to the high surface to volume ratio. NP size and surface state critically determine their fate upon exposure to biological environment. Hence, the redox potential of the Ag NPs, which is directly related to its size, determines the Ag^+ ions provision rate and NP dissolution.

In general, due to NP high reactivity, changing the NPs chemical environment triggers chemical transformations towards a more stable thermodynamic states as aggregation, dissolution (corrosion), or interaction with media molecules. [45] This is of especial

importance for the use of NP in biological systems, since their physicochemical properties will determine their fate and consequently, it will strongly condition their performance. Thus, it is important to understand the behavior of NPs in the working media in order to better understand which is the final characteristics of the NP responsible for the observed bio-effects.

In this regard, the corrosion profiles and stability of different sizes of Ag NPs were followed by UV-Vis spectroscopy in Dulbecco's Modified Eagle Medium (DMEM – medium to grow eukaryote cells), and Tryptic Soy Broth (TSB – medium to grow prokaryote cells). In order to understand the behaviour of Ag NPs upon exposure to the media of study, some considerations have to be taken into account. Modelled dissolution processes suggest that the main feature of the spectra evolution is a blue-shift in the LSPR and a decrease in the absorbance intensity. However, dissolution of Ag NP is typically preceded by oxidation, which in turn is characterized by a broadening and significant red-shift of the LSPR. Thus, both processes are usually optically very closely related. Consequently, it challenges the differentiation of NP aggregation and dissolution processes only by optical means, as there is no specific feature that allows to differentiate each one. [46] Besides, dissolution can also trigger aggregation due to the increase in the ionic strength of the solution that could cause loss of NP electrostatic repulsion. In order to indisputably state the NP evolution, UV-Vis characterization has to be complemented with other techniques such as DLS, sensitive to changes in size, and specially aggregation.

4.3.2.1 Size dependent corrosion in DMEM

The size dependent corrosion was studied by dispersing Ag NPs from 10 nm to 100 nm in DMEM supplemented with 10% FBS (cCCM). NP dissolution was monitored by UV-VIS spectroscopy. Note that, Ag NPs were previously conjugated with Human Serum Albumin (HSA) for 24 or 48h in order to form a stable hard protein corona on the nanoparticle surface. The conjugation of the NPs to albumin in a controlled environment allowed to stabilize the NPs before their exposure to a highly saline environment. The conjugation of NP, indistinctively to albumin or PVP, provides steric repulsion, avoiding NP aggregation. [47] Therefore, changes in the optical signatures of the Ag NPs could be unambiguously ascribed to dissolution or oxidation processes, and not aggregation.

The decrease in absorbance of the NPs is plotted against time for the different sizes of NPs exposed to cCCM in **Figure 4.4**. For this, the maximum value of absorbance from the LSPR

dipolar peak of NPs at each time point is normalized to the maximum value of the NPs at the initial state. The individual UV-Vis corrosion profiles from each size are depicted in **Figure 4.4B**. As observed, the smaller the NPs the faster corrosion rate they present. Insets of each NP size profile allow a better visualization of the LSPR evolution. A fast red-shift is observed towards higher wavelengths upon their dispersion in DMEM, while the intensity progressively decreases and the width of the band broadens. These results are in agreement with the oxidative dissolution modelled and previously described. [48]

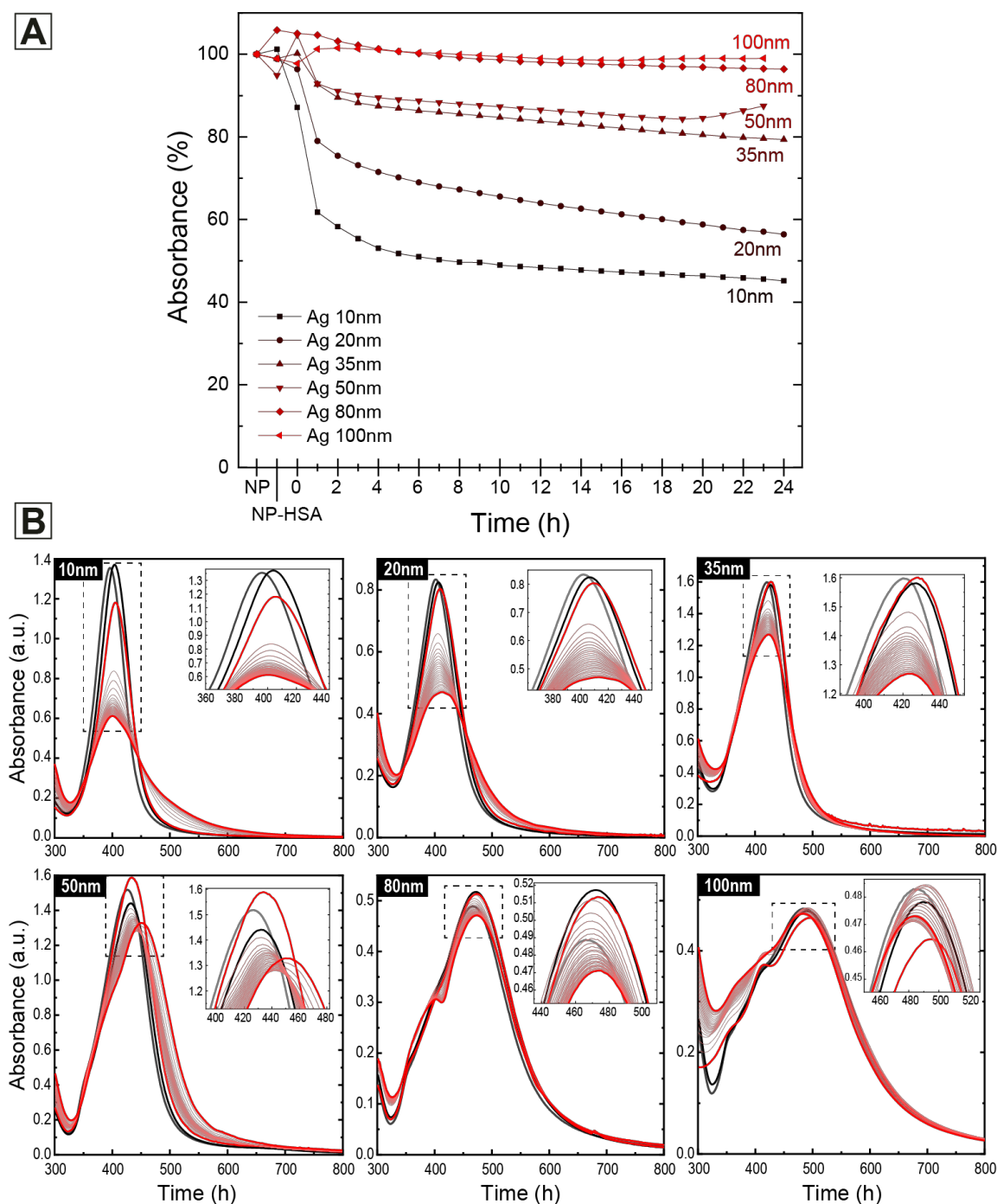


Figure 4.4. Size-dependent corrosion in DMEM. (A) Summary of the absorbance decrease of Ag NPs in DMEM as a function of time. **(B)** UV-Vis spectra evolution of the different size Ag NPs over time in DMEM.

This phenomenon provides both, Ag^+ ions and the corresponding electrons, which results in an increase of ROS –via Fenton-like reactions. [20,21] Indeed, adding H_2O_2 reproduces some of the Ag NPs observed effects. [49] The size of the NP is correlated with its surface reactivity, where the smaller NP are the most reactive. This, in turn is translated in a faster corrosion rate which would be linked to a stronger effect (at short times). However, the life of silver ions in physiological media is short due to the high concentration of free Cl^- that precipitates Ag^+ in the form of AgCl . In turn, AgCl can be solubilized as AgCl_2^- and SH residues that irreversibly precipitate in the form of Ag_2S . Therefore, Ag^+ short half-life makes the permanent provision of ions necessary to maintain its biocidal effect.

4.3.2.2 Stability in bacterial culture media

To understand the behaviour and the fate of Ag NP stabilized with PVP (Ag NP-PVP) in the working media, time dependent physicochemical characterization of NP exposed to TSB has been performed. For this study the TSB was used as bacteria growing media, it is a liquid medium used in isolation and culture of a wide variety of microorganisms. TSB is composed of casein peptone, soya peptone, glucose, dipotassium hydrogen phosphate, sodium chloride, with a pH of 7.3. NaCl (5 g/L) was used as a control to isolate the effect of the electrolytes. All the measurements were performed at 37 °C. The final NP concentration of 7.5 mg/L has been used in the experiments, as this concentration has been reported as MIC of several bacterial strain. [50,51]

Time evolution of the UV-Vis spectra and DLS of 20 nm Ag NP and Ag NP-PVP exposed to TSB and NaCl were followed (**Figure 4.5**). UV-Vis profile and the DLS measurement of Ag NP-PVP are not significantly affected once particles were exposed to NaCl indicating that the colloidal stability of the particle is not compromised by the salt presence. A small decrease in the UV-Vis absorbance was observed after 24h probably due to some corrosion of the sample.

On the other hand, the overall intensity of the UV-Vis spectra of 20 nm Ag NP-PVP when exposed to TSB correlates with a NP aggregation pattern. Generally, indicative evidences of aggregation of Ag NPs are a sharp decrease in the particle absorbance intensity at the initial states, followed by a broadening and red-shift of the LSPR peak and the appearance of a secondary peak (shoulder-like) towards higher wavelength as the extent of the aggregation increases. [46] In this case, absorbance intensity rapidly decreased, and finally disappeared at 24h. Also, the appearance of a second LSPR peak at around 500-700nm can

be observed. The proportion of this second peak to the main LSPR peak at $\sim 402\text{nm}$ increases over time, and its relative position red-shifts progressively.

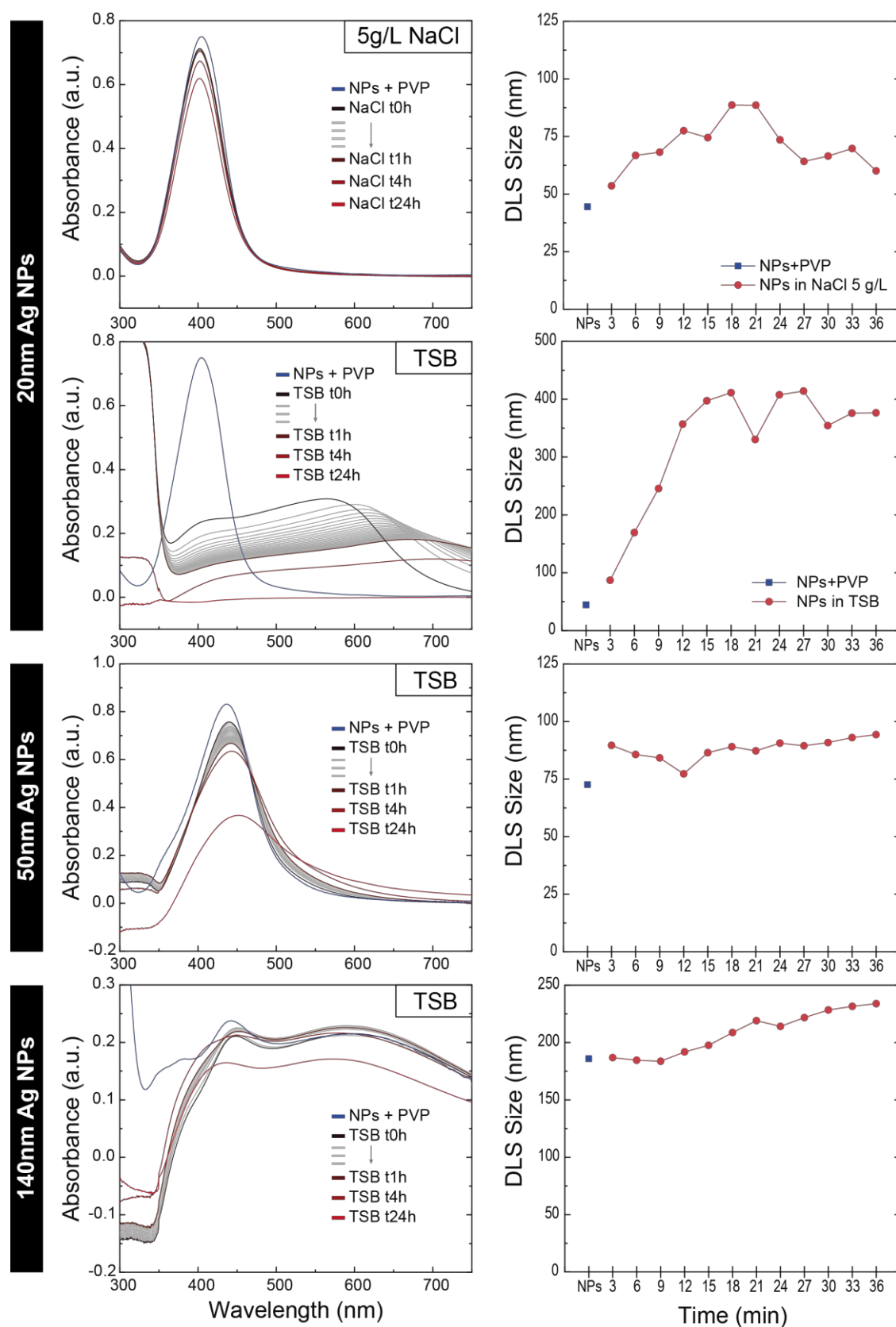


Figure 4.5. Stability in TSB. (Left) UV-Vis spectra evolution of Ag NPs exposed to NaCl (5 g/L) or TSB culture media for 24h. (Right) Evolution of experimental average diameters measured by DLS of the Ag NPs dispersed in the media of study for 36 min.

Looking at the composition of the working media is possible to notice that it is mostly composed by organic matter. We could hypothesize that one or more components of the TSB is able to produce at least a partial ligand exchange with the PVP and interacting with 20 nm Ag NP in an uncontrolled manner that leads to destabilization/aggregation. We could then speculate that the observed profiles in TSB are due to the formation of large NP aggregates, which is in agreement with the appearance of the second peak that could be associated to the inter-particle plasmon coupling during Ag NPs aggregation.

Accordingly, DLS measurement show a rapid increase of the diameter size of the samples. These result clearly show that Ag NP-PVP do not remain colloidally stable for long once exposed to the working media.

In **Figure 4.5** are also reported the time evolutions of the UV-Vis spectra and DLS of 50 and 140 nm Ag NP-PVP exposed to TSB, which greatly differ from the smaller size NP. Regarding the 50 nm NP, there is a 50% decrease in the absorbance intensity at 24h. Also, a 3nm red-shift was observed, which could be due to a change in the dielectric environment surrounding the NP surface. DLS present a size increase around 15 nm after the exposition to TSB but is maintained at least in the first 36 minutes. Both results suggest that in this case NP are not undergoing an aggregation process, but rather a corrosion of the particle overtime. The small increase in the size and the observed red-shift could suggest that also 50 nm Ag NP-PVP were at least partially coated with organic macromolecule present in the TSB, but in this case the organic layer did not lead to aggregation. Similar results were observed for the 140 nm Ag NP-PVP where no evidence of aggregation were observed and a decrease in the absorbance (loss of 25% at 24h) of the NP was observed.

It could be speculated that the differences in stability observed between the 20nm Ag NP-PVP and the 50 and 140 nm Ag NP-PVP could be caused by several factors. The studies were done at the same mass concentration (7.5mg/L), consequently the final NP/ml concentration varies for each size. The 20 nm Ag NP were exposed at a concentration of 1.5×10^{11} NPs/ml (2×10^{14} nm²/ml); the 50 nm at 1.4×10^{10} NPs/ml (9×10^{13} nm²/ml); and the 140 nm at 0.5×10^9 NPs/ml (3×10^{13} nm²/ml). The differences in number and in total surface could be one factor that influenced the colloidal stability of the NP. The faster corrosion rate of smaller Ag NP in a corrosive medium, as the TSB for Ag NP, could also critically influence their fates. Furthermore, the higher reactivity of the smaller NP could influence the type of interaction with media molecules and its kinetics.

From these studies it is possible to conclude that Ag NP-PVP were subject to at least a partial coating by macromolecules present in TSB culture media. PVP coating seems to be able to avoid the aggregation in larger particle but not in smaller. Aggregation of 20 nm Ag NP in TSB environment can significantly impact their antimicrobial effect. The formation of large aggregates could influence the interaction with the bacteria surface. Moreover, the aggregation could probably change the silver corrosion rate, that is suggested as the main cause for Ag NP antimicrobial activity. The decrease in the absorbance after 24h of exposition to TSB of just the 50% for 50 nm Ag NP-PVP and 25% for 140nm Ag NP-PVP suggest that a small amount of silver is released in the first hour of dispersion in TSB, where the bacteria present the latent phase and where it may be possible at least to inhibit or slow down their growth.

4.3.3 Biocidal Effects of Silver Nanoparticles

4.3.3.1 Determination of minimum inhibitory concentration (MIC) and minimum bactericidal concentration (MBC) of silver nanoparticles, silver nitrate and antibiotics against selected bacteria

The biocidal effects of silver in the ionic and nanoparticulated form were explored. For this, selected bacterial strains were exposed to AgNO₃ and Ag NP-PVP were exposed in a dose varying manner to determine the minimum inhibitory concentration (MIC) and the minimum biocidal concentration (MBC). The first one, indicates the concentration of antibiotic when bacteria stop proliferating, thus where the first antibiotic effects are observed, while the MBC corresponds to the concentration needed to kill bacteria. The tested strains belong to both Gram-positive and Gram-negative bacteria, selected for comparative studies of the observed effects. These strains are commonly used in antibacterial assays as standards. Moreover, *P. aeruginosa* has great intrinsic antimicrobial resistance that limits the number of effective antibiotics. On the other hand, *E. coli* and *S. aureus* were also tested in regard of their clinical relevance related to their antibiotic resistance mechanisms. Finally, Ag NP-PVP were chosen for the antimicrobial activity experiments for their increased colloidal stability.

When exposed to bacteria for 24 h, Ag NPs of size 50 and 140 nm did not show any inhibitory activity against selected bacteria. However, 20 nm Ag NPs showed a clear

antimicrobial activity (Table 1). The strongest effect was observed against *E. coli* (MIC=58 µg/ml) while *S. aureus* and *P. aeruginosa* were less sensitive and found to be both MIC 178 µg/ml. Accordingly, the minimum biocidal concentration of Ag NPs for *E. coli* was equal to 256 µg/ml, while for *S. aureus*, and *P. aeruginosa* was higher than 256 µg/ml. When compared by AgNO₃ sensibility, ionic silver exhibited the highest antibacterial activity against *P. aeruginosa*, followed by *S. aureus* and *E. coli*. The MICs of silver nitrate were 12, 16 and 48 µg/ml, respectively. The MBC values of AgNO₃ were found to be 16, 64 and 64 µg/ml for *S. aureus*, *E. coli* and *P. aeruginosa*, respectively. Thus, in all cases the MIC and MBC values of AgNO₃ are lower than 20 nm Ag NPs, in some cases 10-times lower. This results are in agreement with the previous studies presented supporting the hypothesis that the antimicrobial activity of Ag NPs is based on its corrosion, and its rate based on NP's size.

Besides, all test bacteria were sensitive to amikacin and tetracycline, and in exception of *E. coli*, to colistin. Susceptibility of bacterial strains to vancomycin was low (MIC > 256 µg/ml for *S. aureus* and *E. coli*, equal to 256 µg/ml for *P. aeruginosa*) (Table 4.2).

Table 4.2. Determination of Minimal Inhibitory Concentration and Minimal Biocidal Concentration. MIC and MBC values of AgNO₃, Ag NPs and conventional antibiotics values against bacteria by CLSI method. Col: colistin; Van: vancomycin; Ami: amikacin; Te: tetracycline.

Tested strain	MIC AgNO ₃ (µg/ml)	MBC AgNO ₃ (µg/ml)	MIC of Ag NPs (µg/ml)	MBC of Ag NPs (µg/ml)	MIC of antibiotics (µg/ml)				MBC of antibiotics (µg/ml)			
					Col	Van	Ami	Te	Col	Van	Ami	Te
<i>E. coli</i>	48	64	58	256	>256	>256	12	64	>256	>256	16	256
<i>S. aureus</i>	16	16	178	>256	0.250	>256	8	4	0.380	>256	12	256
<i>P. aeruginosa</i>	12	64	178	>256	0.250	256	12	32	0.380	>256	12	96

This results indicate that silver nitrate is more aggressive than Ag NPs, even the more reactive ones, therefore, Ag NPs should be employed for longer actions like in the case of prosthesis and transplants, or permanent disinfection, rather than an antibiotic for immediate use since at short times, the ionic form is more effective than the NP form. Therefore, it is when the short half-life of Ag⁺ is a limitation and longer treatments want to be designed avoiding the continuous introduction of Ag⁺ in the target area that NPs present a significant advantage.

4.3.3.2 Determination of synergistic effect of antibiotics and silver nanoparticles or silver nitrate

Among several *in vitro* methodologies developed to assess *in vitro* pharmacodynamic interactions, microdilution broth checkerboard techniques are commonly used to study antibiotic combinations. Checkerboard data can be analyzed with different pharmacological mathematical models developed to detect deviations from no-interaction theories and to determine synergistic and antagonistic interactions. [52] *In vitro* antibiotic combinations are usually assessed on the basis of the fractional inhibitory concentration (FIC) index, which represents the sum of the FICs of each drug tested, where the FIC is determined for each drug by dividing the MIC of each drug when used in combination by the MIC of each drug when used alone. The FIC index is based on the Loewe additivity zero-interaction theory. [53] This theory is based on the hypothesis that a drug cannot interact with itself and therefore the effect of a self-drug combination will always be additive. The FIC range of 0.5 to 4 is commonly used to define additivity or antagonism results in combination studies, where lower values for the 1 cut-off determine additive effect between the tested compounds. A FIC index lower than 0.5 indicates synergy, because more drug would be required in order to produce the same effect as the drugs alone. Higher values in the range of 1-2 indicate indifferent effect, and above 2 indicate antagonism. In the present study, FIC index was investigated as a predictor of synergy using tetracycline, colistin, amikacin and vancomycin, combined with Ag NPs and AgNO₃ prepared by checkerboard titration method. As seen in **Table 4.3**, synergistic, non-synergistic and indifferent effects were observed when antibiotics were combined with AgNO₃ or Ag NPs.

Generally, combination of antibiotics with AgNO₃ exhibited higher antibacterial activity than their combination with Ag NPs. Synergistic effect of AgNO₃ and all test antibiotics was noticed against *E. coli* (FIC 0.125 - 0.5). Combined action of AgNO₃ with amikacin, colistin or tetracycline enhanced antibacterial activity against *P. aeruginosa* (FIC 0.125 – 0.5), while only combination with colistin and tetracycline enhanced the activity against *S. aureus* (FIC 0.25 - 0.5).

In contrast, combined use of antibiotics with Ag NPs against test bacteria revealed that antibacterial activity was significantly enhanced when NPs were used with tetracycline (FIC 0.125 - 0.25). Also, synergism of Ag NPs and amikacin was recorded for *P. aeruginosa* (FIC = 0.5). However, no other synergetic or anti-cooperative values were observed. In

the rest of combinations, both effects just added up. Yet, this still would allow for dose reduction of both antimicrobials. [54]

Table 4.3. Fractional inhibitory concentration (FIC) index determined for Ag NPs or AgNO₃ in combination with antibiotics against bacteria. Ami; amikacin, Col; colistin, Te; Tetracycline, Van; vancomycin. ≤0.5 synergism (dark green); > 0.5 – 1.0 non-synergistic or additive effect (light green); ≥ 1.0 – 2.0 indifferent effect; ≥2 antagonism effect. *As the MIC was not determined in the wide concentration range of antibiotic (see **Table 4.2**), the highest tested concentration (256 µg/ml) of antibiotic was used.

Tested strain	Gram	FIC of Ag NO ₃ combined with				FIC of Ag NPs combined with			
		Col	Van	Ami	Te	Col	Van	Ami	Te
<i>E. coli</i>	-	0.5	0.5	0.25	0.125	2.0	2.0	2.0	0.125
<i>P. aeruginosa</i>	-	0.5	1.0	0.125	0.25	2.0	2.0	0.5	0.25
<i>S. aureus</i>	+	0.25	1.0	1.0	0.5	1.0	1.0	1.0	0.25

Therefore, these results point out that gram-negative bacteria are more sensitive to the combined use of antibiotic and silver. Similar observations were reported by Kim and his colleagues (2007). [55] Authors suggested that different sensitivity of those two groups of bacteria to Ag NPs results from different cell wall structure. Gram-positive bacteria have a several layers of peptidoglycans and molecules of teichoic or lipoteichoic acids in their cell wall. This generates strong negative charge, and may contribute to sequestration of free silver ions. In this regard, the cell wall of gram-positive bacteria may allow less amount of silver ions to reach the cytoplasmic membrane than in gram-negative bacteria. [56]

There is more than the ion dosing of the NP (**Figure 4.1**). Delivery of antibiotics by nanoparticles to the site of infection is a promising therapy particularly for controlled release of drugs, which in turn decreases the dose required to achieve a beneficial effect. [21] By conjugating the antibiotic to the NP their pharmacokinetic profiles get entangled. Thus, one can use the delivery properties of NPs, such as their loading capacity, their altered biodistribution with accumulation at the site of infection and their ability to protect the carried drug to transport and lock the antibiotic drug at the site of action while the Ag NP will corrode providing the Ag⁺. [57,58]

Finally, there is a concern on the rising resistance against Ag. Some resistance mechanisms may include over production of halides, mineralization of the Ag⁺ or overexpression of copper-related efflux pumps. However, since antibacterial combined therapy targets

multiple cellular sites, and the doses of Ag as adjuvant are low, the emergence of resistance is delayed. [22,59]

4.3.4 Nanoparticle-Bacteria Interaction

In order to further study NP fate and NP-bacteria interaction, samples were imaged by, both, electron microscopy and confocal laser scanning microscopy (CLSM) (**Figure 4.6**). The observation of the exposed bacteria to Ag NPs allows to get a deeper insight into their interaction and provides a better understanding regarding mechanistic aspects of the Ag NP biocidal effects.

After 24h of incubation, electron microscopy, either Scanning or Transmission, reveals the presence of 20 nm Ag NPs attached to the wall of *E. coli*. TEM allowed a clear visualization of the NPs but bacteria could only be observed as shadows. Even though some NPs can also be seen in the same area as bacteria, it is not possible to state if they are internalized or merely outside the cell wall. On the other hand, SEM enabled a better resolution of the bacterial morphology. Some bacteria are seen to be intact, while some others show a shrunk (close to dead) shape. Further, the imaging of the sample by Dark-Field mode provides confirmation of the presence of Ag NPs, unequivocally distinguished from the organic matter present in the media.

Regarding the Ag NPs, they appear to be individually dispersed all over the grid, which indicates that Ag NP were stable and didn't aggregate in the culture media during the incubation process. On the other hand, the size frequency distribution analysis was performed on the Ag NP observed. The average mean size of the Ag NPs size distribution had decreased ~3nm from the characterization performed prior to the biological experiment. The reduction of NP size could be explained by its corrosion and Ag⁺ release.

Finally, *P. aeruginosa* and *E. coli* inoculums exposed to 50 nm Ag NPs for 24h were fixed in Glycerol Jelly mounting medium for their observation on the confocal microscope. The Live/Dead viability kit staining reveals a higher proportion of dead bacteria, or at least indicating membrane damage revealed by propidium iodide staining. The imaging of the Ag NPs by reflectance mode reveals once more, the fact that NPs are colloiddally stable in solution, dispersed on the sample. Also, in some cases colocalizing with the bacteria signal. In the *E. coli* sample, some bacteria displaying abnormal morphology were observed to colocalize with significantly higher signal of NPs. Both features, correlate with the similar findings witnessed by SEM.

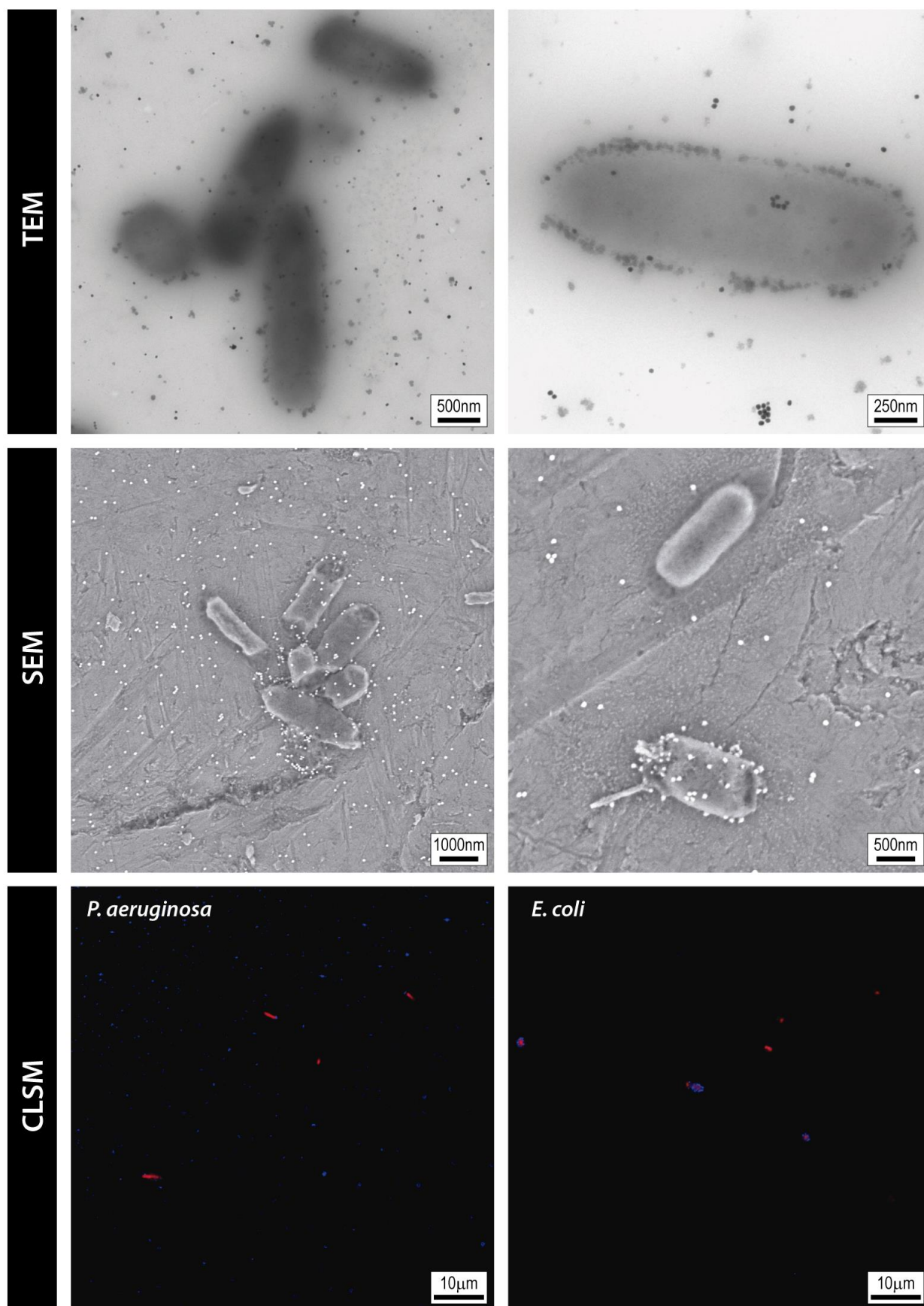


Figure 4.6. Ag-Bacteria interaction. (Up) Transmission and (Middle) Scanning electron microscopy images of *E. coli* inoculums incubated overnight with 20 nm Ag NPs. (Down) Confocal Laser Scanning microscopy images of *E. coli* and *P. aeruginosa* inoculums incubated overnight with 50 nm Ag NPs. Bacteria were stained with Live-Dead Staining solution (red) and Ag NPs were imaged by reflectance mode (blue).

4.3.5 Modelled Ag NPs Dissolution and Ag⁺ Consumption

The MIC and FIC determinations provided an understanding of the bactericidal effect of Ag NPs and the effective Ag⁺ concentrations. The determined effective Ag⁺ concentrations were decreased by two-fold when combined with antibiotics. This suggests that those concentrations of Ag⁺ are necessary to trigger enough membrane permeability and/or ROS production to synergize with the antibiotics. Therefore, at the site of action, is this steady concentration that should be sustained in time provided by the corroding Ag NP.

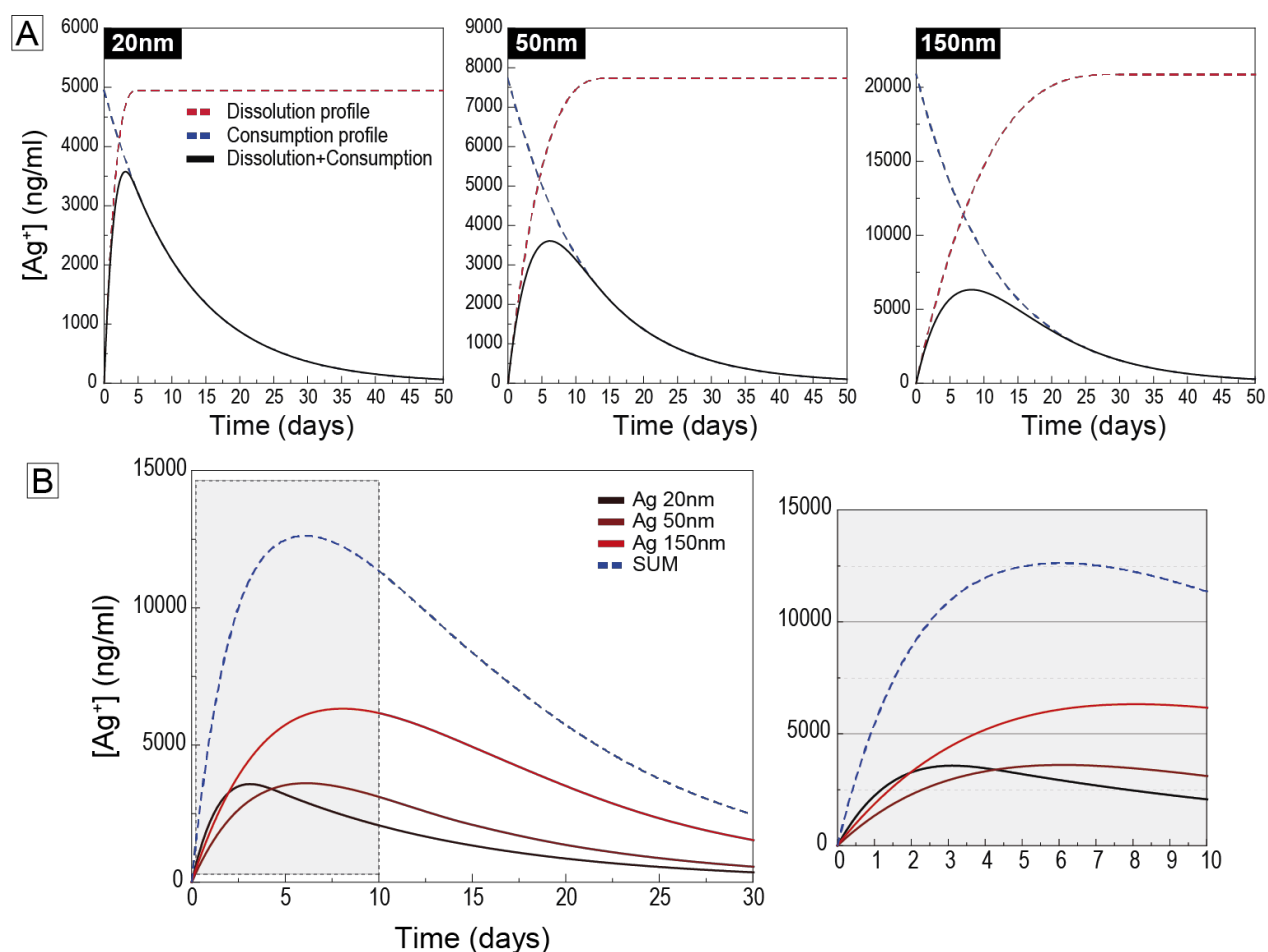


Figure 4.7. Simulation models for Ag NP dissolution and Ag⁺ consumption. (A) Simulation models for single size Ag NPs of 20, 50 and 150 nm. At short times, the curve follows dissolution while large times are dominated by consumption. **(B)** Consumption of Ag⁺ ions coupled to dissolution. Results plotted for 20 nm, 50 nm and 150 nm Ag NPs and the sum of the individual contributions (dotted line). The left plot is a zoom of the grey region in the graph of the left.

Interestingly, the corrosion rate can be easily controlled with the NP diameter, the smaller the NP the faster the corrosion, as observed in cCCM. However, half-life of Ag⁺ in physiological media is rather short due to their precipitation in the form of insoluble species (as AgCl), interaction with small organic molecules or bacterial uptake. Thus, their

consumption should also be taken into account in order to maintain a constant $[\text{Ag}^+]$ in solution.

For this, the dissolution process and the further Ag^+ consumption was modelled and integrated for different sizes of Ag NP upon their dispersion in bacterial culture media.

Figure 4.7A shows the individual simulations for each NP size. Note that in the particular conditions studied, the consumption is slower than the generation of Ag^+ . Thus, at short times the curve follows a dissolution profile while large times are dominated by consumption. Complete dissolution times was assumed and extrapolated from the experimental data on section 4.3.2.1

This allows to program different Ag^+ dosing over time. The graph in **Figure 4.7B** includes the three Ag^+ evolution profiles, and the dashed line corresponds to the sum of the three contributions. Left plot is a zoom of the grey area. Instead of using a single NP size, these results suggest the possibility to adjust the concentration of Ag^+ in solution by adjusting the type and relative concentration of Ag NPs.

Thus, precise control over the synthesis, characterization, surface modification and functionalization of NPs is critical in order to achieve a new generation of bactericidal materials. [6,7] The presented results point out that the development of such nanoparticle formulations either increases the efficacy of established classes of antibiotics or enables dose reduction. [6,40] Thus, nanoparticle platforms present a potential response to anti-microbial resistance, which could stimulate innovation and create a new generation of antibiotic treatments for future medicines.

4.4 References

- [1] Fair, R. J. & Tor, Y. Antibiotics and bacterial resistance in the 21st century. *Perspectives in Medicinal Chemistry* 25–64 (2014)
- [2] A route out of resistance. *Nature Microbiology* 1, 1–2 (2016)
- [3] Brusin, S., Ciancio, B., Diaz Högberg, L., Weist, K., Suetens, C., Griskeviciene, J., Monnet, D., & Heuer, O. Annual epidemiological report.
- [4] Salomoni, R., Léo, P., Montemor, A. F., Rinaldi, B. G., & Rodrigues, M. F. A. Antibacterial effect of silver nanoparticles in *Pseudomonas aeruginosa*. *Nanotechnology, science and applications* 10, 115–121 (2017)
- [5] Subbenaik, S. C. Physical and chemical nature of nanoparticles. *Plant Nanotechnology: Principles and Practices* 15–27 (2016)
- [6] Kumar, M., Curtis, A., & Hoskins, C. Application of Nanoparticle Technologies in the Combat against Anti-Microbial Resistance. *Pharmaceutics* 10, 11 (2018)
- [7] Zhang, X. F., Liu, Z. G., Shen, W., & Gurunathan, S. Silver nanoparticles: Synthesis, characterization, properties, applications, and therapeutic approaches. *International Journal of Molecular Sciences* 17, (2016)
- [8] Fda, Cder, Yeaton, & Ayse. *Drug Products, Including Biological Products, that Contain Nanomaterials - Guidance for Industry*. <https://www.fda.gov/Drugs/GuidanceComplianceRegulatoryInformation/Guidances/default.htm>
- [9] Chen, X. & Schluesener, H. J. Nanosilver: a nanoproduct in medical application. *Toxicology letters* 176, 1–12 (2008)
- [10] García, A., Delgado, L., Torà, J. A., Casals, E., González, E., Puentes, V., Font, X., Carrera, J., & Sánchez, A. Effect of cerium dioxide, titanium dioxide, silver, and gold nanoparticles on the activity of microbial communities intended in wastewater treatment. *Journal of hazardous materials* 199–200, 64–72 (2012)
- [11] Rizzello, L. & Pompa, P. P. Nanosilver-based antibacterial drugs and devices: mechanisms, methodological drawbacks, and guidelines. *Chemical Society reviews* 43, 1501–18 (2014)
- [12] Klueh, U., Wagner, V., Kelly, S., Johnson, A., & Bryers, J. D. Efficacy of silver-coated fabric to prevent bacterial colonization and subsequent device-based biofilm formation. *Journal of biomedical materials research* 53, 621–31 (2000)
- [13] Morones, J. R., Elechiguerra, J. L., Camacho, A., Holt, K., Kouri, J. B., Ramírez, J. T., & Yacaman, M. J. The bactericidal effect of silver nanoparticles. *Nanotechnology* 16, 2346–53 (2005)
- [14] Yamanaka, M., Hara, K., & Kudo, J. Bactericidal actions of a silver ion solution on *Escherichia coli*, studied by energy-filtering transmission electron microscopy and proteomic analysis. *Applied and environmental microbiology* 71, 7589–93 (2005)
- [15] Allahverdiyev, A. M., Kon, K. V., Abamor, E. S., Bagirova, M., & Rafailovich, M. Coping with antibiotic resistance: combining nanoparticles with antibiotics and other antimicrobial agents. *Expert review of anti-infective therapy* 9, 1035–52 (2011)
- [16] Choi, O., Deng, K. K., Kim, N.-J., Ross, L., Surampalli, R. Y., & Hu, Z. The inhibitory effects of silver nanoparticles, silver ions, and silver chloride colloids on microbial growth. *Water research* 42, 3066–74 (2008)
- [17] El Badawy, A. M., Silva, R. G., Morris, B., Scheckel, K. G., Suidan, M. T., & Tolaymat, T. M. Surface charge-dependent toxicity of silver nanoparticles. *Environmental science & technology* 45, 283–7 (2011)
- [18] Pal, S., Tak, Y. K., & Song, J. M. Does the antibacterial activity of silver nanoparticles depend on

- the shape of the nanoparticle? A study of the Gram-negative bacterium *Escherichia coli*. *Applied and environmental microbiology* 73, 1712–20 (2007)
- [19] Xiu, Z., Zhang, Q., Puppala, H. L., Colvin, V. L., & Alvarez, P. J. J. Negligible particle-specific antibacterial activity of silver nanoparticles. *Nano letters* 12, 4271–5 (2012)
- [20] Liochev, S. I. The mechanism of ‘Fenton-like’ reactions and their importance for biological systems. A biologist’s view. *Metal ions in biological systems* 36, 1–39 (1999)
- [21] Nuran Ercal, B. S. P., Hande Gurer-Orhan, B. S. P., & Nukhet Aykin-Burns, B. S. P. Toxic Metals and Oxidative Stress Part I: Mechanisms Involved in Metal induced Oxidative Damage. *Current Topics in Medicinal Chemistry* 1, 529–539 (2005)
- [22] Silver, S. Bacterial silver resistance: molecular biology and uses and misuses of silver compounds. *FEMS Microbiology Reviews* 27, 341–353 (2003)
- [23] Yamada, M., Foote, M., & Prow, T. W. Therapeutic gold, silver, and platinum nanoparticles. *Wiley interdisciplinary reviews. Nanomedicine and nanobiotechnology* 7, 428–45
- [24] De Jong, W. H. & Borm, P. J. A. Drug delivery and nanoparticles: applications and hazards. *International journal of nanomedicine* 3, 133–49 (2008)
- [25] Liu, P.-F., Lo, C.-W., Chen, C.-H., Hsieh, M.-F., & Huang, C.-M. Use of nanoparticles as therapy for methicillin-resistant *Staphylococcus aureus* infections. *Current drug metabolism* 10, 875–84 (2009)
- [26] Rivera Gil, P., Oberdörster, G., Elder, A., Puentes, V., & Parak, W. J. Correlating physico-chemical with toxicological properties of nanoparticles: the present and the future. *ACS nano* 4, 5527–31 (2010)
- [27] Barrena, R., Casals, E., Colón, J., Font, X., Sánchez, A., & Puentes, V. Evaluation of the ecotoxicity of model nanoparticles. *Chemosphere* 75, 850–7 (2009)
- [28] Zhang, T., Wang, L., Chen, Q., & Chen, C. Cytotoxic potential of silver nanoparticles. *Yonsei medical journal* 55, 283–91 (2014)
- [29] Luther, E. M., Koehler, Y., Diendorf, J., Eppler, M., & Dringen, R. Accumulation of silver nanoparticles by cultured primary brain astrocytes. *Nanotechnology* 22, 375101 (2011)
- [30] Park, J., Lim, D.-H., Lim, H.-J., Kwon, T., Choi, J., Jeong, S., Choi, I.-H., & Cheon, J. Size dependent macrophage responses and toxicological effects of Ag nanoparticles. *Chemical communications (Cambridge, England)* 47, 4382–4 (2011)
- [31] Lu, W., Senapati, D., Wang, S., Tovmachenko, O., Singh, A. K., Yu, H., & Ray, P. C. Effect of Surface Coating on the Toxicity of Silver Nanomaterials on Human Skin Keratinocytes. *Chemical physics letters* 487, (2010)
- [32] Li, P., Li, J., Wu, C., Wu, Q., & Li, J. Synergistic antibacterial effects of β -lactam antibiotic combined with silver nanoparticles. *Nanotechnology* 16, 1912–1917 (2005)
- [33] Shahverdi, A. R., Fakhimi, A., Shahverdi, H. R., & Minaian, S. Synthesis and effect of silver nanoparticles on the antibacterial activity of different antibiotics against *Staphylococcus aureus* and *Escherichia coli*. *Nanomedicine : nanotechnology, biology, and medicine* 3, 168–71 (2007)
- [34] Fayaz, A. M., Balaji, K., Girilal, M., Yadav, R., Kalaichelvan, P. T., & Venkatesan, R. Biogenic synthesis of silver nanoparticles and their synergistic effect with antibiotics: a study against gram-positive and gram-negative bacteria. *Nanomedicine : nanotechnology, biology, and medicine* 6, 103–9 (2010)
- [35] Birla, S. S., Tiwari, V. V., Gade, A. K., Ingle, A. P., Yadav, A. P., & Rai, M. K. Fabrication of silver nanoparticles by *Phoma glomerata* and its combined effect against *Escherichia coli*, *Pseudomonas aeruginosa* and *Staphylococcus aureus*. *Letters in applied microbiology* 48, 173–9 (2009)
- [36] Gu, H., Ho, P. L., Tong, E., Wang, L., & Xu, B. Presenting Vancomycin on Nanoparticles to Enhance Antimicrobial Activities. *Nano Letters* 3, 1261–1263 (2003)

- [37] Durán, N., Marcato, P. D., Conti, R. De, Alves, O. L., Costa, F. T. M., & Brocchi, M. Potential use of silver nanoparticles on pathogenic bacteria, their toxicity and possible mechanisms of action. *Journal of the Brazilian Chemical Society* 21, 949–959 (2010)
- [38] Hwang, I. sok, Hwang, J. H., Choi, H., Kim, K. J., & Lee, D. G. Synergistic effects between silver nanoparticles and antibiotics and the mechanisms involved. *Journal of Medical Microbiology* 61, 1719–1726 (2012)
- [39] Deng, H., McShan, D., Zhang, Y., Sinha, S. S., Arslan, Z., Ray, P. C., & Yu, H. Mechanistic Study of the Synergistic Antibacterial Activity of Combined Silver Nanoparticles and Common Antibiotics. *Environmental Science and Technology* 50, 8840–8848 (2016)
- [40] Wypij, M., Świecimska, M., Czarnecka, J., Dahm, H., Rai, M., & Golinska, P. Antimicrobial and cytotoxic activity of silver nanoparticles synthesized from two haloalkaliphilic actinobacterial strains alone and in combination with antibiotics. *Journal of Applied Microbiology* 124, 1411–1424 (2018)
- [41] Wypij, M., Czarnecka, J., Świecimska, M., Dahm, H., Rai, M., & Golinska, P. Synthesis, characterization and evaluation of antimicrobial and cytotoxic activities of biogenic silver nanoparticles synthesized from *Streptomyces xinghaiensis* OF1 strain. *World Journal of Microbiology and Biotechnology* 34, 1–13 (2018)
- [42] Leonhard, V., Alasino, R. V., Munoz, A., & Beltramo, D. M. Silver Nanoparticles with High Loading Capacity of Amphotericin B: Characterization, Bactericidal and Antifungal Effects. *Current Drug Delivery* 15, 850–859 (2018)
- [43] Liu, J., Sonshine, D. A., Shervani, S., & Hurt, R. H. Controlled release of biologically active silver from nanosilver surfaces. *ACS Nano* 4, 6903–6913 (2010)
- [44] Bastús, N. G., Merkoçi, F., Piella, J., & Puentes, V. Synthesis of Highly Monodisperse Citrate-Stabilized Silver Nanoparticles of up to 200 nm: Kinetic Control and Catalytic Properties. *Chemistry of Materials* 26, 2836–2846 (2014)
- [45] Piella, J., Bastús, N. G., & Puentes, V. Size-dependent protein-nanoparticle interactions in citrate-stabilized gold nanoparticles: The emergence of the protein corona. *Bioconjugate Chemistry* 28, 88–97 (2017)
- [46] Piella, J., Bastús, N. G., & Puentes, V. Modeling the Optical Responses of Noble Metal Nanoparticles Subjected to Physicochemical Transformations in Physiological Environments: Aggregation, Dissolution and Oxidation. *Zeitschrift für Physikalische Chemie* 231, 33–50 (2017)
- [47] Barbero, F., Russo, L., Vitali, M., Piella, J., Salvo, I., Borrajo, M. L., Busquets-Fité, M., Grandori, R., Bastús, N. G., Casals, E., & Puentes, V. Formation of the Protein Corona: The Interface between Nanoparticles and the Immune System. *Seminars in Immunology* 34, 52–60 (2017)
- [48] Piella, J., Bastús, N. G., & Puentes, V. Modeling the Optical Responses of Noble Metal Nanoparticles Subjected to Physicochemical Transformations in Physiological Environments: Aggregation, Dissolution and Oxidation. *Zeitschrift für Physikalische Chemie* 231, 33–50 (2017)
- [49] Jiang, H. S., Yin, L. Y., Ren, N. N., Zhao, S. T., Li, Z., Zhi, Y., Shao, H., Li, W., & Gontero, B. Silver nanoparticles induced reactive oxygen species via photosynthetic energy transport imbalance in an aquatic plant. *Nanotoxicology* 11, 157–167 (2017)
- [50] Panáček, A., Kvítek, L., Pucek, R., Kolář, M., Večeřová, R., Pizúrová, N., Sharma, V. K., Nevěčná, T., & Zbořil, R. Silver colloid nanoparticles: Synthesis, characterization, and their antibacterial activity. *Journal of Physical Chemistry B* 110, 16248–16253 (2006)
- [51] Panáček, A., Smékalová, M., Kilianová, M., Pucek, R., Bogdanová, K., Večeřová, R., Kolář, M., Havrdová, M., Pláza, G. A., Chojniak, J., Zbořil, R., & Kvítek, L. Strong and Nonspecific Synergistic Antibacterial Efficiency of Antibiotics Combined with Silver Nanoparticles at Very Low Concentrations Showing No Cytotoxic Effect. *Molecules* 21, 26 (2015)
- [52] Meletiadis, J., Pournaras, S., Roilides, E., & Walsh, T. J. Defining Fractional Inhibitory Concentration Index Cutoffs for Additive Interactions Based on Self-Drug Additive Combinations, Monte Carlo Simulation Analysis, and *In Vitro-In Vivo* Correlation Data for Antifungal Drug

- Combinations against *Aspergillus fumigatus*. *Antimicrobial Agents and Chemotherapy* 54, 602 (2010)
- [53] Berenbaum, M. C. What is synergy? *Pharmacological Reviews* 41, (1989)
- [54] Casals, E., Gusta, M. F., Cobaleda-Siles, M., Garcia-Sanz, A., & Puentes, V. F. Cancer resistance to treatment and antiresistance tools offered by multimodal multifunctional nanoparticles. *Cancer Nanotechnology* 8, 7 (2017)
- [55] Kim, J. S., Kuk, E., Yu, K. N., Kim, J. H., Park, S. J., Lee, H. J., Kim, S. H., Park, Y. K., Park, Y. H., Hwang, C. Y., Kim, Y. K., Lee, Y. S., Jeong, D. H., & Cho, M. H. Antimicrobial effects of silver nanoparticles. *Nanomedicine: Nanotechnology, Biology and Medicine* 3, 95–101 (2007)
- [56] Haghdel, A., Abiri, H., Reza Eskandari, M., -, al, Panahi, S., Reza Sardarian, A., & Esmaeilzadeh, F. Synthesis and characterization of novel silver nanoparticles using *Chamaemelum nobile* extract for antibacterial application. *Advances in Natural Sciences: Nanoscience and Nanotechnology* 8, 025004 (2017)
- [57] Durán-Lobato, M., Niu, Z., & Alonso, M. J. Oral Delivery of Biologics for Precision Medicine. *Advanced Materials* 32, 1901935 (2020)
- [58] Mitchell, M. J., Billingsley, M. M., Haley, R. M., Wechsler, M. E., Peppas, N. A., & Langer, R. Engineering precision nanoparticles for drug delivery. *Nature Reviews Drug Discovery* 20, 101–124 (2020)
- [59] Randall, C. P., Gupta, A., Jackson, N., Busse, D., & O'Neill, A. J. Silver resistance in Gram-negative bacteria: a dissection of endogenous and exogenous mechanisms. *Journal of Antimicrobial Chemotherapy* 70, 1037–1046 (2015)

CHAPTER 5

EXPERIMENTAL SECTION: CHEMICALS, MATERIALS, METHODS AND TECHNIQUES

Experimental Section: Chemicals, Materials, Methods and Techniques

5.1 Chapter 2. Cationic Gold nanoparticles mediated mRNA delivery for production of CAR-T lymphocytes for Chronic Lymphoid Leukaemia Immunotherapy

5.1.1 Chemicals

Gold(III) chloride trihydrate ($\text{HAuCl}_4 \cdot 3\text{H}_2\text{O}$), trisodium citrate ($\text{Na}_3\text{C}_6\text{H}_5\text{O}_7$), tannic acid ($\text{C}_76\text{H}_{52}\text{O}_{46}$), potassium carbonate (K_2CO_3), amino-undecanethiol (AUT), poly-ethyleneimine branched Mn2000 (PEI), 2-(N-morpholino)ethanesulfonic acid buffer solution (MES), sodium hydroxide (NaOH), hydrogen chloride (HCl), single stranded DNA from Salmon testes (ssDNA, D1626), Sodium Phosphate Dibasic (Na_2HPO_4), Sodium phosphate monobasic (NaH_2PO_4), poly-L-lysine, Paraformaldehyde (PFA), Triton-X, Bovine Serum Albumin (BSA), Sodium Chloride (NaCl), Calcium Chloride (CaCl_2), and Roche Lactate Dehydrogenase Assay (LDH), were purchased from Sigma-Aldrich. Dulbecco's Modified Eagle Medium (DMEM), Foetal Bovine Serum (FBS), Hoechst 3342 (H1399), Prolong antifade mounting medium (11559306), Optimem Medium, Pacific Blue-Annexin V, Propidium iodide (PI), accutase, 4-(2-hydroxyethyl)-1-piperazineethanesulfonic acid buffer (HEPES), CellMask Deep-Red Plasma Membrane Stain (C10046) and Prestoblue were purchased from Thermo Fisher. Phalloidin Alexa Fluor 647 (ab176759) was purchased from Abcam. Clean CAP eGFP mRNA (5moU) was

purchased from Tebu-Bio. TransIT®-LT1 Transfection Reagent was purchased from MirusBio.

All chemicals were used as received without further purification. Distilled water passed through a Millipore system ($\rho = 18.2 \text{ M}\Omega$) was used in all experiments. All glassware was first rinsed with acetone and then with Millipore water before use.

5.1.2 Synthesis of Nanoparticles

5.1.2.1 5nm Gold Nanoparticle Synthesis

Following Piella et al, [1] a 150 mL of freshly prepared reducing solution of sodium citrate (SC, 2.2 mM) containing 0.1 mL of tannic acid (TA, 2.5 mM) and 1 mL of potassium carbonate (K_2CO_3 , 150 mM) was heated with a heating mantle in a 250 mL three-necked round-bottom flask under vigorous stirring. When the temperature reached 70 °C, 1 mL of tetrachloroauric acid (HAuCl_4 , 25mM) was injected. The colour of the solution changed rapidly to black-grey (less than 10 s) and then to orange-red in the following 1–2 min. The solution was kept at 70 °C for 5 min more to ensure complete reaction of the gold precursor. Immediately after the synthesis and in the reaction same vessel, the sample was diluted by extracting 55 mL and adding 55 mL of SC (2.2 mM). When the temperature reached again 70 °C, two injections of 0.5 mL of HAuCl_4 (25 mM) on a time interval of 10 min were done. This growing step comprising sample dilution plus 2 injections of HAuCl_4 was repeated until the particles reached the desired size. **Figure 5.1** summarizes the synthesis strategy.

5.1.2.2 20nm and 50nm Gold Nanoparticle Synthesis

Following Bastus et al, [2] a solution of 2.2mM sodium citrate (SC) in Milli-Q water (150 mL) was heated with a heating mantle in a 250 mL three-necked round-bottomed flask for 15 min under vigorous stirring. A condenser was utilized to prevent the evaporation of the solvent. After boiling had commenced, 1 mL of HAuCl_4 (25 mM) was injected. The colour of the solution changed from yellow to bluish grey and then to soft pink in 10 min. Immediately after the synthesis of the Au seeds and in the same reaction vessel, the reaction was cooled until the temperature of the solution reached 90 °C. Then, 1 mL of a HAuCl_4 solution (25 mM) was injected. After 30 min, the reaction was finished. This process was

repeated twice. After that, the sample was diluted by extracting 55 mL of sample and adding 53 mL of Mili-Q water and 2 mL of 60 mM sodium citrate. This solution was then used as a seed solution, and the process was repeated again until the particles reached the desired size. **Figure 5.2** summarizes the synthesis strategy.

Au Seeds Synthesis

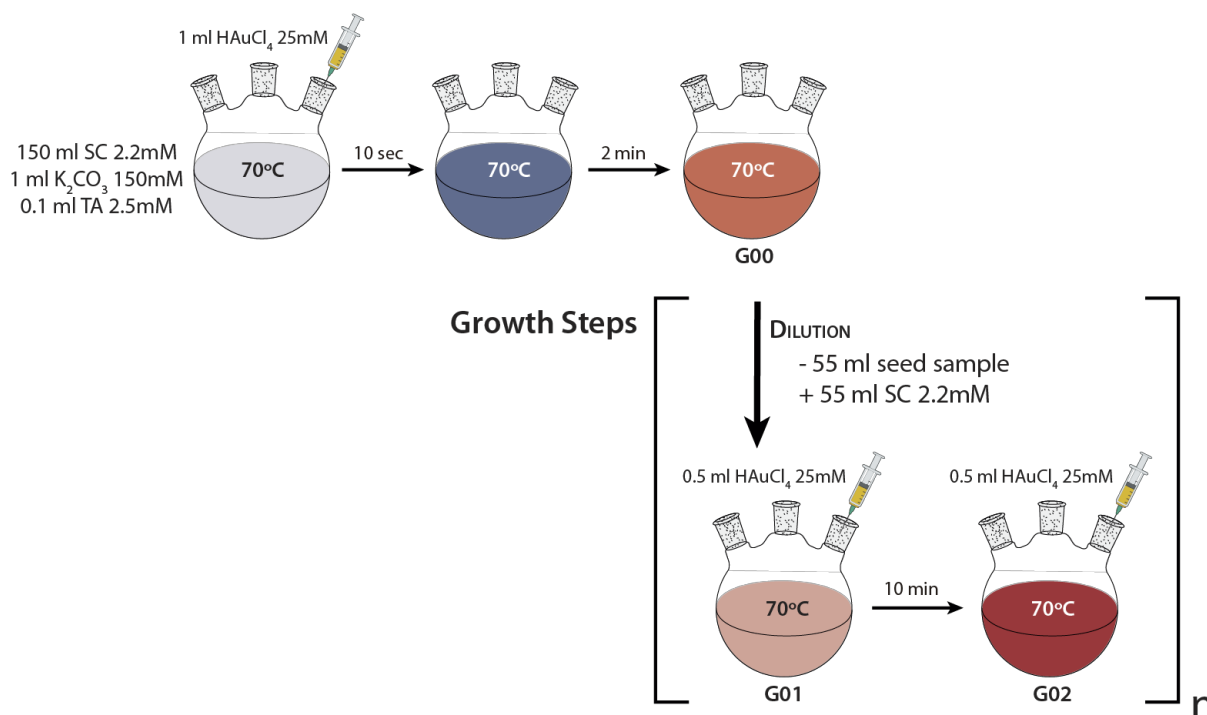


Figure 5.1. Schematic representation of the synthetic procedure for larger Au NPs. Adapted from ref [1].

Au Seeds Synthesis

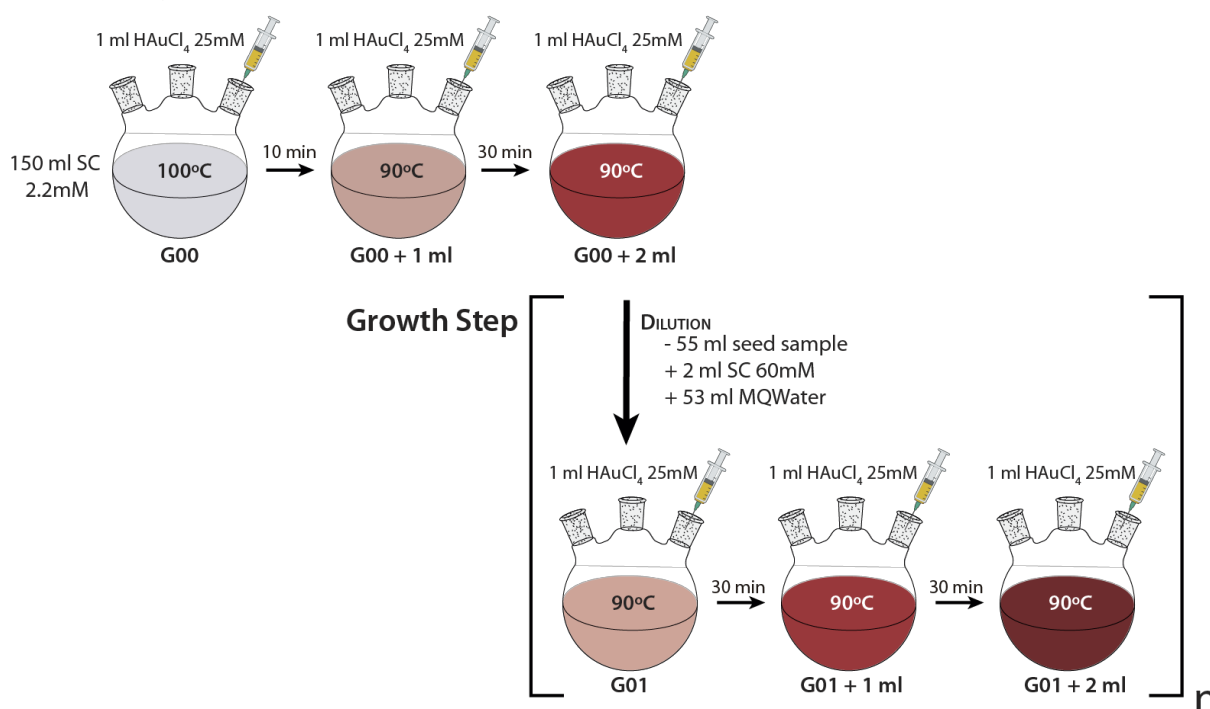


Figure 5.2. Schematic representation of the synthetic procedure for sub-10 Au NPs. Adapted from ref [2].

The produced nanoparticles were fully characterized by Transmission Electron Microscopy, Dynamic Light Scattering, Zeta Potential and UV-Vis Spectroscopy (see section 5.4 for methodologic details).

5.1.3 Functionalization of Nanoparticles

5.1.3.1 Functionalization of Gold Nanoparticles with Cationic molecules: AUT

First parameter explored for a stable functionalization of Au NPs was the concentration of AUT. For this, 20nm Au NPs were concentrated 10-fold relative to the synthesis concentration by centrifugation (conditions were set according the Stokes law for each particle size). Next, AUT solutions with concentrations ranging between 50-400 μ M were prepared in HCl 10mM (pH<3). NPs (10% to final volume) were rapidly added into the AUT solution under vigorous stirring. After 1h, samples were characterized by UV-Vis. Note that at pH values above 3, NPs aggregate and precipitate upon dispersion in the AUT solution. The positive charges of the amine residues of AUT interact with the negatively charged hydroxyl residues of citrate and crosslink triggering NPs aggregation. [3]

The conjugation time was analysed by monitoring the NPs by UV-Vis from 5 min to 1 month. Finally, the purification process of the AUT-coated NPs was studied. The conjugated NPs were precipitated by centrifugation twice, and resuspended to the initial volume, first with HCl 2mM and then with MES 10mM.

5.1.3.2 Functionalization of Gold Nanoparticles with Cationic molecules: PEI

The optimal PEI concentration and pH were studied for Au NPs PEI-coating. On the first case, 50nm Au NPs were concentrated 10-fold relative to the synthesis concentration by centrifugation. Next, PEI solutions with concentrations ranging between 50-200 μ M were prepared in HCl 34mM (pH~7). NPs (10% to final volume) were rapidly added into the PEI solution under vigorous stirring. After 1h, samples were characterized by UV-Vis.

10-fold concentrated 50nm Au NPs were conjugated to PEI (200 μ M) at different pH conditions ranging from 2 to 7. NPs (10% to final volume) were rapidly added into the PEI solution under vigorous stirring. After 24h, samples were characterized by UV-Vis. The conjugated NPs were precipitated by centrifugation, resuspended to the initial volume with water and characterized again by UV-Vis.

5.1.3.3 Functionalization of Gold Nanoparticles with Cationic molecules: Standardized Protocol

Based on the results from the AUT and PEI conjugation studies performed, that will be deeply discussed in section 2.3.1.2, the standardized relative concentrations for each size Au NPs functionalization are the following:

5 nm Au NP	
300 μM AUT 10 mM HCl <i>pH 2.5</i> +10% NPs	400 μM PEI 70 mM HCl <i>pH 7</i> +10% NPs
20 nm and 50 nm Au NP	
200 μM AUT 10 mM HCl <i>pH 2.5</i> +10% NPs	200 μM PEI 34 mM HCl <i>pH 7</i> +10% NPs

Note that there is a significant increase in the concentration of both, AUT and PEI, used for the functionalization of 5 nm Au NPs. This is discussed in section 2.3.1.2

5.1.4 Loading of Nanoparticles with oligonucleotides

Aiming to establish a standard mRNA-NP loading protocol, the optimal ratio mRNA:NP ratio was explored and the conjugation kinetics were studied over time. On this experiments, ssDNA oligomers *ca.* 600-800b were used as a model of mRNA transcript, due to the limitations of stock and price on the later one.

5.1.4.1 Loading of Cationic Gold Nanoparticles with oligonucleotides

20 nm (at 1.5×10^{12} NP/ml) and 50 nm (at 3×10^{11} NP/ml) Au NPs coated with AUT were used, previously purified and dispersed in MES 10mM. For ssDNA loading, first 900 μ l of 2-fold serial dilutions in MES 10mM were prepared, ranging from 53-0.41 μ g/ml. Next, 100 μ l of NPs were rapidly added onto the ssDNA and the mixture was gently homogenized. Thus, the final relative ssDNA:NP ratios ranged from [7.8-1000] for 20nm-NP, and from [39-5000] for 50nm-NP. Samples were incubated for 24h at 4°C under stirring. Next day, samples were characterized by UV-Vis spectroscopy, DLS and Z-Pot before and after

purification. For purification, NPs were precipitated by centrifugation, supernatant was discarded and pellets were resuspended in MES 10 mM to the initial volume.

5.1.4.2 Time evolution of RNA/DNA loading

50 nm Au NPs coated with AUT and PEI were loaded with ssDNA. Briefly, 900 μ l of NPs dispersed in MES 10 mM were added onto 100 μ l of ssDNA to a final ratio DNA:NP=300. Samples were kept at 4°C under stirring. At each time point, 1ml of sample was taken for characterization. For purification, NPs were precipitated by centrifugation, supernatant was stored for ssDNA quantification and pellets were resuspended in MES 10 mM to the initial volume. Conjugates were analysed by UV-Vis spectroscopy, DLS and additionally Z-Potential was measured after purification. The quantification of the ssDNA loaded on the NPs was extrapolated from the measurement of the supernatants at 24h by Nanodrop (Nanodrop 2000 Spectrophotometer, ThermoFisher).

5.1.5 Uptake and Delivery Mechanistic Aspects

5.1.5.1 Stability of nanovectors

To study the stability of nanovectors, 50 nm Au NPs coated with AUT and PEI, alone or loaded with ssDNA, were used. For this, NP solution was diluted 1:10 in the media of study and incubated for 24h at 4 °C. Different biologically relevant media were tested: Optimem (pH 7.4) and Phosphate Buffer (PB) 10mM (pH 7.4). NPs dispersed in MES 10 mM (pH 5) were used as a control. NP stability was studied by UV-Vis and DLS. After 24h samples were characterized. Au NPs were precipitated by centrifugation, the pellets were redispersed in the media of study and Z-Potential was measured.

5.1.5.2 HEK293-cells culture

HEK-293 cell culture was maintained in culture in 75 cm² tissue culture flask using DMEM with heat- inactivated foetal bovine serum (FBS) at 10% at 37°C and humidified 5% CO₂.

5.1.5.3 Confocal imaging of cultured cells exposed to NPs

HEK293 293 cell line (DSMZ) were seeded on an 8-well glass bottom microslide (Sarsted) at 100.000 cell/cm² and incubated overnight. Albuminized Au NPs of 5nm, 20nm and 50nm

NPs coated with AUT or PEI and loaded with ssDNA were added dropwise onto cell cultures and gently homogenized. At 24h cells were fixed with 4% PFA. For immunohistochemistry, samples were first permeabilized with Triton-X 0.2% - BSA 1% for 10min. Samples were incubated with Phalloidin Alexa Fluor 647 ($\lambda_{\text{ex}}650/\lambda_{\text{em}}665$) for 45min for actin staining. Nuclei were stained with Hoechst 3342 ($\lambda_{\text{ex}}350/\lambda_{\text{em}}461$, dilution 1:10000) for 15min. Fading was controlled using the Prolong antifade mounting medium. Samples were observed on the Confocal Laser Scanning Microscopy (CLSM, Zeiss LSM980 Airyscan 2). The principles and methodology of Au NPs imaging by Confocal Microscopy are described and deeply discussed on Chapter 3.

Jurkat cells were washed from growth medium 2 times in PBS by centrifugation (150 g x 10 min at 10 °C). 1.5×10^6 cells/ml were incubated with 6×10^9 per ml of 50 nm Au NPs at 37°C for 30 min, then diluted by cold PBS, washed and resuspended in full growth medium. Detection of the uptake was carried out by Zeiss CLSM 510 Meta confocal microscope with 514 nm laser in reflectance mode. The protocol of simultaneous dead cell labelling by propidium iodide (PI), cell membrane visualization by Wheat Germ Agglutinin-FITC (WGA-FITC) together with Au NP reflection was established. This experiment was performed at Tel-Aviv University, as a collaboration in the ERA-Net “Concord” project.

5.1.5.4 TEM imaging of cultured cells exposed to NPs

HEK293 293 cells were seeded on a 10 cm petri dish at 100.000 cell/cm² and incubated overnight. 20 nm Au NPs coated with PEI were added dropwise onto cell cultures and gently homogenized. At 24h cells were fixed with 2.5% glutaraldehyde in 0.1 M PB. Next, samples were embedded in paraffin following a standard protocol. For observation, paraffin-embedded samples were sectioned using a ultra-microtome and transferred to a carbon coated copper TEM grid.

This experiment was performed at Istituto di Ricerche Farmacologiche Mario Negri, as a collaboration in the ERA-Net “Concord” project.

5.1.5.5 Proton sponge efficiency of Cationic Gold Nanoparticles

First, the pH of a cationic Au NPs solution was adjusted to 7.3 with NaOH. Then, pH was monitored continuously as a known volume of HCl (10 mM) was added dropwise on the Au NPs solution under stirring, until pH 4 was reached. A solution of miliQ water was used

as a control. The proton sponge efficiency of the cationic NPs was calculated based on the HCl volume added, normalized to Au surface (nm²).

5.1.5.6 Release DNA/RNA kinetics of nanovectors

First, 50 nm Au NPs coated with AUT and PEI were loaded with ssDNA. Briefly, 100 μ l of NPs concentrated 10-fold and dispersed in MES 10 mM were added onto the corresponding volume of ssDNA to a final ratio DNA:NP [300:1]. Samples were incubated overnight at 4°C under stirring. Next day, samples were diluted 1:10 in Phosphate Buffer (PB) 10 mM (pH 7.4). At each time point, an aliquot of sample was taken for characterization. For purification, NPs were precipitated by centrifugation, supernatant was stored for ssDNA quantification and pellets were resuspended in PB 2 mM to the initial volume. Conjugates were analysed by UV-Vis spectroscopy, DLS and additionally Z-Potential was measured after purification. The quantification of the ssDNA released from the NPs was extrapolated from the measurement of the supernatants by Nanodrop, and normalized to the previously calculated ssDNA loaded.

5.1.6 Transfection of mRNA with nanovectors

5.1.6.1 Transfection of mRNA with nanovectors

To evaluate the transfection capacity of gold nanoparticles coated with PEI and AUT, HEK-293 cells were cultured in DMEM with FBS 10% in 24-well plate at 50.000 cells/ml. The transfection was performed with 60-70 % confluence and final mRNA concentration of 1000 ng. After 24h of the incubation at 37°C the DMEM medium was removed and replaced for 900 μ L of Optimem medium. Next, specific colloidal ratios [mRNA:NP] were added (100 μ L) for each nanoparticle size for 5 nm Au NPs [5:1], 20 nm [50:1] and 50 nm [300:1]. The next day 100 μ L of FBS were added to each well and left for 48h and 7 days after transfection process. The transfection and cell viability percentages were evaluated by confocal microscopy and flow cytometry.

5.1.6.2 Chloroquine effect

To further inside to the proton sponge mechanism the transfected HEK-cells were treated with chloroquine at 20 μ M for 4 hours before nanovector transfection, performed as

described above. At 24h cells were visualized by Wide-Field fluorescence microscopy and GFP signal intensity quantified. Statistical analysis was performed by the 2-way ANOVA test, using the GraphPad Prism software. For significance, $p > 0.005$ was considered.

5.1.6.3 Flow cytometry

The percentage of Green Fluorescence Protein (GFP) expression after transfection was analysed with BD LSRFortessa™ Cell Analyzer. Forward and side-scatter areas (FSC-A, SSC-A) in a linear scale were used to gate HEK-293 population, and GFP expression was detected by excitation through 480-500nm. To determinate the cell viability, HEK-293 cells were stained with Pacific Blue- Annexin V/ propidium iodide (PI) in accord with the manufacturer's recommendations. Briefly, HEK293 cells were collected by cell detachment using accutase and washed with PBS. After centrifugation cells were resuspended in 100 μ L of Annexin binding buffer (10mM HEPES, 140mM NaCl and 2.5mM CaCl_2). 5 μ L of Annexin V and PI (1mg /mL) were added and incubated at room temperature for 15 minutes. After the incubation period, additional 400 μ L of the binding buffer was added. Acquisition was configured to stop after recording 10,000 events within the HEK-293 cell population.

5.1.6.4 Wide-Field Fluorescence Microscopy

Au nanoparticles transfection efficiency in HEK-293 cells was calculated by GFP expression analysed by Wide-Field microscopy. To this end, HEK-293 cells were visualized in Thunder Wide-Field Fluorescence Microscope (Leica). HEK- 293 cells were labelled with Hoechst 33342 (Thermo Fisher Scientific, 62249) and CellMask Deep-Red Plasma Membrane Stain (Thermo Fisher Scientific, C10046) at 0.5 μ g/mL for 15 min. Fluorophores were excited by 395nm LED (Hoechst 33342) and 635nm LED (Cell Mask Deep Red). For GFP imaging, a 475 nm LED was used for excitation while the emission channel was set to 506-532 nm. For deconvolution of each image, we utilized the algorithm Small Volume Computational Clearing (SVCC). The cytoplasmic expression of GFP was analysed in relation to the nuclear staining detection using the StartDist deep-learning-based method (Fiji) in a total area of 70% of a 24-plate well.

5.1.6.5 Confocal Microscopy

Transfection of mRNA-GFP was performed on an 8-well glass bottom microslide. After 24h, samples were fixed and stained (as detailed in section 2.2.5). Samples were observed on the Thunder Wide-Field Fluorescence Microscope (Leica) and on the Confocal Laser Scanning Microscopy in order to image the GFP ($\lambda_{\text{ex}}488/\lambda_{\text{em}}507$) expression and NP distribution on transfected HEK293 cells.

5.1.7 Cytotoxicity and Risk Assessment of nanovectors

5.1.7.1 Cytotoxicity Assessment of nanovectors

The action of Au NPs in the HEK-293 cells viability was evaluated by PrestoBlue assay and LDH quantification, according to manufacturer's recommendations.

5.1.7.2 Prestoblue

HEK-293 cells were seeded to 1×10^5 cell/mL in 96-well plate during 24 hours before to Au NPs exposition. Serial dilutions of nanoparticles were added at final concentration ranging from 3.3×10^{13} - 1.2×10^{11} for Au 5nm NPs/mL, 2.7×10^{12} - 1.0×10^{10} for Au 20nm NPs/mL and 3×10^{11} - 1.1×10^9 for Au 50nm NPs/mL. To assay the ration DNA:NPs cytotoxicity the PEI/AUT nanoparticles were loaded with ssDNA, as described in section 5.1.4 . After 24, 48h and 7 days cell viability was measured. For this, 10 μ L of PrestoBlue was added to each well, plates were incubated for 2h and fluorescence was measured ($\lambda_{\text{ex}}531\text{nm}$, $\lambda_{\text{em}}572\text{nm}$) by Varioskan LUX (Thermo Fisher Scientific). All experiments were carried out in triplicate, and data was treated and calculated with OriginLab software.

5.1.7.3 LDH Assay

HEK-293 cells were seeded to 1×10^5 cell/mL in 96-well plate during 24 hours before to Au NPs exposition. Serial dilutions of nanoparticles were added at final concentration ranging from 3.3×10^{13} - 1.2×10^{11} for Au 5nm NPs/mL, 2.7×10^{12} - 1.0×10^{10} for Au 20nm NPs/mL and 3×10^{11} - 1.1×10^9 for Au 50nm NPs/mL. To assay the ration DNA:NPs cytotoxicity the PEI/AUT nanoparticles were loaded with ssDNA, as described in section 5.1.4 . After 24, 48h and 7 days cell viability was measured. For LDH quantification once incubation time

was reached, 50 μ L of each cell supernatant was transferred to a new plate, mixed with 50 μ L of reagent, and incubated in the dark for 20 min at room temperature. The absorbance from the released LDH was measured at 490 nm wavelength and 650 nm as reference wavelength. Cells without treatment (DMEM) were the negative control, while cells treated with 0.1% Triton X-100 were the positive control. Percentage cell viability was calculated as follows:

$$Viability (\%) = \frac{(1 - Absorbance \text{ Treated Cells})}{Absorbance \text{ Positive Control}} \times 100$$

5.1.7.4 Annexin V / Propidium Iodide

To determinate the cell viability, HEK-293 cells were stained with Pacific Blue- Annexin V/ propidium iodide (PI) in accord with the manufacturer's recommendations. Briefly, HEK293 cells were collected by cell detachment using accutase and washed with PBS. After centrifugation cells were resuspended in 100 μ L of Annexin binding buffer (10mM HEPES, 140mM NaCl and 2.5mM $CaCl_2$). 5 μ L of Annexin V and PI (1mg /mL) were added and incubated at room temperature for 15 minutes. After the incubation period, additional 400 μ L of the binding buffer was added. Acquisition was configured to stop after recording 10,000 events within the HEK-293 cell population.

5.2 Chapter 3. Confocal Imaging of Unlabelled Nanoparticles in Cells and Biological Tissues

5.2.1 Chemicals

Gold (III) chloride trihydrate ($\text{HAuCl}_4 \cdot 3\text{H}_2\text{O}$), silver nitrate (AgNO_3), trisodium citrate ($\text{Na}_3\text{C}_6\text{H}_5\text{O}_7$), tannic acid ($\text{C}_{76}\text{H}_{52}\text{O}_{46}$), Cerium (III) nitrate hexahydrate (99%), $\text{Ce}(\text{NO}_3)_3 \cdot 6\text{H}_2\text{O}$, iron (II) chloride (FeCl_2), iron (III) chloride (FeCl_3), tetramethylammonium hydroxide (TMAOH), tetraethyl orthosilicate (TEOS), fluorescein-5-isothiocyanate (FITC), (3-aminopropyl)triethoxysilane (APTES), and methacryloxypropyltrimethoxysilane (MPS), foetal bovine serum (FBS), bovine serum albumin (BSA), Sodium Phosphate Dibasic (Na_2HPO_4), Sodium phosphate monobasic (NaH_2PO_4), poly-L-lysine, phorbol 12-myristate 13-acetate (PMA), paraformaldehyde (PFA), Triton-X, and xylene were purchased from Sigma-Aldrich. Dulbecco's Modified Eagle Medium (DMEM), Hoechst 3342 (H1399), Prolong antifade mounting medium (11559306), goat anti-mouse Alexa Fluor568 (A110199), formalin and paraffin were purchased from ThermoFisher. Phalloidin Alexa Fluor 647 (ab176759), and Cell Tracking Red Dye Kit (ab269446) were purchased from Abcam. Anti- β -actin mouse monoclonal antibody (MAB8929) was purchased from R&D Systems.

All chemicals were used as received without further purification. Distilled water passed through a Millipore system ($\rho = 18.2 \text{ M}\Omega$) was used in all experiments. All glassware was first rinsed with Millipore water before use.

5.2.2 Synthesis of Nanoparticles

The produced nanoparticles were fully characterized by Transmission Electron Microscopy, Dynamic Light Scattering, and UV-Vis Spectroscopy (see section 5.4 for methodologic details).

5.2.2.1 Gold Nanoparticles

For this, 15, 50, 100, 150 nm Au NPs were synthesized using a well established seeded-growth method. It is based on the synthesis of small gold nanoparticles by citrate reduction of HAuCl_4 , which are then used as templates to grow them by adding gold precursor up to the desired size. [4] This synthesis is explained and discussed with more detail on Chapter 2 (section 2.3.1.1).

5.2.2.2 Silver Nanoparticles

For this, 15, 50, 100, 150 nm Ag NPs were synthesized using a well established seeded-growth method. It is based on the synthesis of small silver nanoparticles by citrate and tannic acid reduction of AgNO_3 , which are then used as seeds to grow them by adding gold precursor to the desired size. [5] This synthesis is explained and discussed with more detail on Chapter 4 (section 4.3.1).

5.2.2.3 Cerium Oxide Nanoparticles

CeO_2 NPs were synthesized by the chemical precipitation of cerium (III) nitrate hexahydrated in a basic aqueous solution, as reported previously by our group. [6] Controlling the pH of synthesis, small-sized nanoceria can be obtained. Resulting CeO_2 NPs were then stabilized with SC or TMAOH.

5.2.2.4 Gold-Cerium Oxide Hybrid Core-Shell Nanoparticles

Citrate-stabilized Au NPs of 40 nm and 100 nm were synthesized, following the method described above. The Au NPs were used without further purification as seeds for the CeO_2 coating, according to methods previously developed by our group. [7]

5.2.2.5 Iron Oxide Nanoparticles

7 nm Fe_3O_4 NPs were synthesized based on Massart's method. [8] Amounts of FeCl_2 and FeCl_3 were dissolved in deoxygenated water to a molar ratio 1:2 and then added dropwise to a solution of deoxygenated TMAOH. After 30 min of vigorous stirring under a N_2 stream, the Fe_3O_4 precipitate was washed by soft magnetic decantation, redissolved in TMAOH at the desired concentration.

5.2.2.6 Gold@Silica-FITC Nanoparticles

First, citrate-stabilized 60nm Au NPs were synthesized, following the method described above. Later, the Au NPs were coated with a silica shell, used as a spacer, following the well reported the Stöber method by the hydrolysis and subsequent condensation of TEOS in ethanol under basic conditions. Then, the NPs were doped with the dye fluorescein-5-isothiocyanate within the silica matrix, adapting the method from Van Blaaderen. Finally, a subsequent third silica shell for protecting the doped dye from the environmental interactions, were done by another Stöber process. After this, the NPs were purified and dispersed in anhydride ethanol.

5.2.2.7 Gold@Silica-FITC@PS Nanoparticles

Starting from the previous multilayer core-shell NPs dispersed in ethanol, first the NPs were surface-modified with the MPS. Later, the polystyrene shell was grown on top of the NPs by adapting the emulsion polymerization method⁴, in which radicals were generated by thermal decomposition of potassium persulfate to polymerize the styrene precursor. Finally, pH was adjusted to a neutral, next NPs were purified by centrifugation twice and dialyzed against pure water overnight.

5.2.3 Simulations

Calculations of the extinction efficiency (Q_{ext}) of NPs of different diameters in water at 25°C were obtained using MiePlot software and MultiLayer NP Simulator platform freely available online. [9,10] The dielectric constant and refractive index of the metal were that provided by the programs while for the oxides the data were extracted from the literatures. [11] The Q_{ext} was correlated with the empirical value of extinction, or absorbance, (A) through the Beer-Lambert law using the following equation:

$$A = \varepsilon c l \quad (1)$$

where ε is the extinction coefficient of the solution in units ($M^{-1} cm^{-1}$), c is the molar metal atom concentration and l (cm) is the path length of the beam of light through the solution. For particles of radii r (cm), the extinction coefficient can be expressed by:

$$\varepsilon = \frac{3 V_m Q_{ext}}{4 \ln(10) r} \quad (2)$$

Where V_m (M^{-1}) is the molar volume of the metal and Q_{ext} is the above defined dimensionless extinction efficiency.

$$Q_{ext} = \frac{\text{extinction cross section}}{\text{cross section}} = \frac{\sigma_{ext}}{\pi r^2} \quad (3)$$

5.2.4 Confocal Laser Scanning Microscopy (CSLM)

5.2.4.1 Microscope Settings and Operation

The Confocal Laser Scanning Microscope (Zeiss LSM980 with Airyscan 2) was set to reflectance mode. For this, the dichroic mirror was retracted, only a T80/20 beam splitter was set instead, the reflection mode allowed, and the emission window was set at $\Delta 15\text{nm}$ to the laser source wavelength. Colours from the images acquired are chosen arbitrarily in each case to better discriminate all the signals collected.

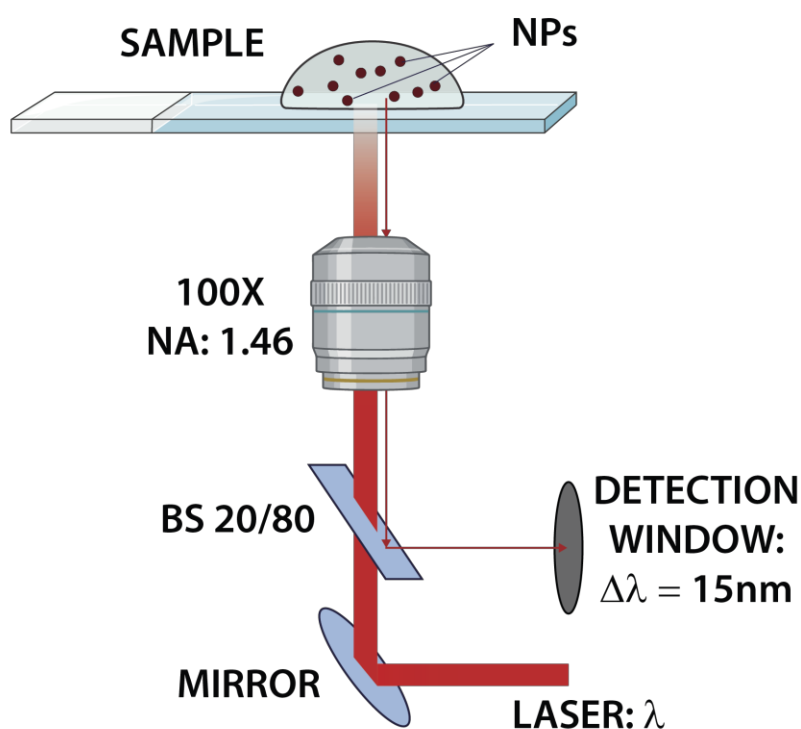


Figure 5.3. Graphical illustration of the Laser Scanning Confocal Microscope reflectance mode set up for NP imaging. The microscope specifications for a typical sample observation at 100X are: Numerical Aperture (NA) = 1.46, refractive index of immerse oil = 1.518, Airy units =1 (adjusted for each laser).

5.2.4.2 Colloidal Nanoparticle Sample Preparation

(i) Nanoparticles in colloidal solution were placed on a 8-well glass bottom microslide.(ii) A 20ul sample of nanoparticles was drop casted on a poly-lysine slide and evaporated on a vacuum chamber. Then, sample was mounted with Prolong antifade mounting medium and a cover slide.

5.2.5 Nanoparticles on Biological Systems

5.2.5.1 HEK293-cells culture

HEK-293 cell culture was maintained in culture in 75 cm² tissue culture flask using DMEM with heat-inactivated foetal bovine serum (FBS) at 10% at 37°C and humidified 5% CO₂.

5.2.5.2 Albuminization of Au NPs

A stock solution of Bovine Serum Albumin (BSA) was prepared at 10mg/ml in Phosphate Buffer (PB) 10mM buffer. Au NPs were added onto the BSA solution to a final relative volume concentration 90-10%, and incubated overnight at 4°C.

5.2.5.3 Confocal Imaging of NPs on fixed cultured cells

HEK293 293 cells (DSMZ) were seeded at 100.000 cell/cm² on a 8-well glass bottom microslide (Sarsted) pre-coated with BSA (1mg/ml) and Poly-L-Lysine (40µg/cm²), and incubated overnight.

THP1 cells (DSMZ) were seeded at 100.000 cell/cm² on a 8-well glass bottom microslide and polarized to M0 phenotype with PMA (20ng/ml). After an overnight incubation, cell culture media was replaced and cells were incubated for 24h more before NP exposure.

Albuminized Au NPs of 15nm, 50nm and 100nm and Au@SiO₂-FITC NPs were added dropwise onto cell cultures and gently homogenized. At 24h cells were fixed with 4% PFA. For immunohistochemistry, samples were first permeabilized with Triton-X 0.2% - BSA 1% for 10min. Samples were incubated with Phalloidin Alexa Fluor 647 for 45min for actin staining. Nuclei were stained with Hoechst 3342 (dilution 1:10000) for 15min. Fading was controlled using the Prolong antifade mounting medium.

5.2.5.4 Confocal Imaging of Gold@Silica-FITC@PS NPs on tissue sections

1.5ug Au/ml of Au@SiO₂-FITC@PS NPs were intravenously injected to each mice. At 24h, mice were sacrificed and liver and spleen were collected. The organs were briefly washed with normal saline, slightly dried with blotting paper and immersed for 4h in 4% formalin for tissue fixation. Next, tissues were embedded in paraffin following a standard protocol. For immunohistochemistry, paraffin-embedded samples were sectioned at 4μm using a microtome and transferred to a poly-lysine coated glass slide. The paraffin was then removed with xylene and the samples rehydrated. Samples were permeabilized with Triton-X 0.2% for 10min. Sections were incubated with anti-β-Actin mouse monoclonal antibody (dilution 1:100) overnight at 4°C, followed by an incubation with a secondary antibody goat anti-mouse Alexa Fluor568 (dilution 1:500). Nuclei were stained with Hoechst 3342 (dilution 1:10000). Fading was controlled using the Prolong antifade mounting medium.

5.2.5.5 Confocal Imaging of Gold NPs on *in vivo* cultured cells

HEK293 293 cell line (DSMZ) were seeded on an 8-well glass bottom microslide (Sarsted) at 100.000 cell/cm² and incubated overnight. Cells were labelled with Cell Tracking Red Dye Kit (dilution 1:20) for 2h, and nuclei were stained with Hoechst 3342 (dilution 1:10000) for 15min. Samples were placed on the Confocal Microscope (37°C, 5% CO₂) and Albuminized 50 nm Au NPs were added dropwise onto cell cultures and gently homogenized. At this point started the sample recording for 24h to monitor the interaction of cell-NP. For the first 4 hours, images were acquired every 15 min, and from that point forward, the acquisition was done every hour.

5.3 Chapter 4. Size Effects on Ag NP - Antibiotic Synergy

5.3.1 Chemicals

Silver nitrate (AgNO_3), trisodium citrate ($\text{Na}_3\text{C}_6\text{H}_5\text{O}_7$), tannic acid ($\text{C}_{76}\text{H}_{52}\text{O}_{46}$), polyvinyl pyrrolidone (PVP, 55KDa), gelatine, glycerol, Tryptic Soy Broth (TSB), Tryptic Soy Agar (TSA), tetracycline, colistin, amikacin and vancomycin were purchased from Sigma-Aldrich. Human Serum Albumin (HSA), Dulbecco's Modified Eagle Medium (DMEM), Foetal Bovine Serum (FBS), Phosphate Buffer Saline (PBS), and Live/Dead BacLight kit were purchased from ThermoFisher.

All chemicals were used as received without purification. Distilled water passed through a Millipore system was used in all experiments.

5.3.2 Synthesis of Silver Nanoparticles

5.3.2.1 Synthesis Method

Following Bastus et al., [5] a 100 mL of aqueous solution containing sodium citrate (5 mM) and tannic acid (0.025 mM) was prepared and heated to reflux with a heating mantle in a three-neck round-bottomed flask for 15 min under vigorous stirring. A condenser was used to prevent the evaporation of the solvent. Next, 1 ml of silver nitrate (25 mM) was then injected. The color of the solution changed rapidly to light yellow. The reaction was left for 30 min.

Immediately after the seed synthesis and in the reaction same vessel, solution was diluted by extracting 20 mL of sample and adding 17 mL of Milli-Q-water. Subsequently, the temperature of the solution was set to 90 °C and 500 μL of sodium citrate (25 mM), 1.5 mL of tannic acid (2.5 mM) and 1 mL of silver nitrate (25 mM) were injected into the vessel. The reaction was left for 30 min. This solution was then used as a seed solution, and the process was repeated again until the particles reached the desired size. **Figure 5.4** summarizes the synthesis strategy.

NPs were purified by centrifugation (from 6000g to 18000g, depending on its size by 10 min.) and further re-suspend in Milli-Q-water prior to sample characterization in order to remove the excess of sodium citrate and tannic acid.

Ag Seeds Synthesis

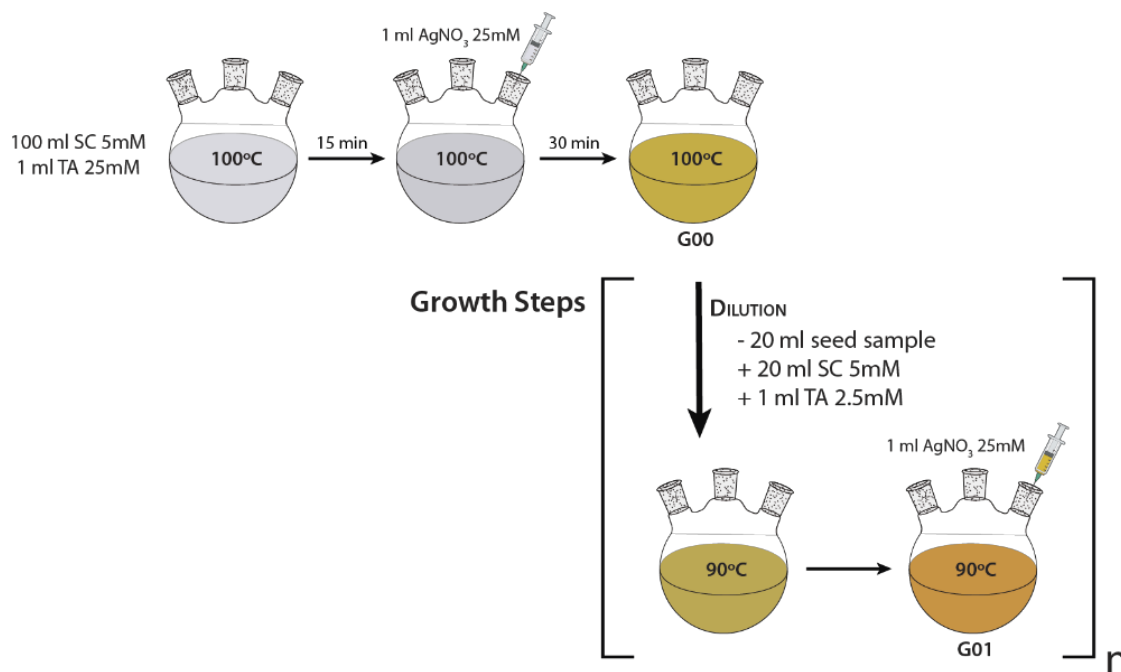


Figure 5.4. Schematic representation of the Ag NPs synthetic procedure. Adapted from ref [5].

5.3.2.2 Nanoparticle Passivation with PVP

Ag NPs were conjugated post synthesis with PVP 55 KDa in order to confer to the particles a steric stabilization. Briefly, a solution of PVP was added to the solution of Ag NPs and leaved under agitation overnight, the final concentrations were 0.05mM of PVP and 7.5 mg/L of Ag NPs. After the conjugation the particle were purified by centrifugation in order to remove the excess of polymer. NP were concentrated 70-fold by resuspending the pellets to the corresponding final volume.

The produced nanoparticles were fully characterized by Transmission Electron Microscopy, Dynamic Light Scattering, Zeta Potential and UV-Vis Spectroscopy (see section 5.4 for methodologic details).

5.3.3 Size-dependent corrosion of Silver Nanoparticles in biological media

5.3.3.1 Size dependent corrosion in DMEM

Different sizes of Ag NPs were synthesized, as described above: 10, 20, 35, 50, 80, 100 nm. Nanoparticles were first incubated with Human Serum Albumin at 1mg/ml final concentration for 24h (10, 20, 35 nm) or 48h (50, 80, 100 nm) at 4°C. After the HSA corona formation, the Ag NPs were dispersed to a final relative volume of 10% in Dulbecco's Modified Eagle Medium (DMEM) complemented with 10% of Foetal Bovine Serum (FBS).

NP evolution was monitored by UV-Vis spectroscopy for 24h. A cuvette stirrer was used in order to avoid NPs sedimentation. The decrease in absorbance was used as a mean to extrapolate the corrosion rate of the Ag NPs.

5.3.3.2 Stability in bacteria culture media

To study the stability of NPs, 20, 50 and 140 nm Ag NPs coated with PVP were used. For this, NP solution was diluted to 7.5 mg/L in the media of study and incubated for 24h at 37 °C. Stability of NPs in Tryptic Soy Broth was explored, and a solution of NaCl (5 g/L) was used as a control. NP evolution was monitored by UV-Vis and DLS.

5.3.4 Biocidal effects of Silver

5.3.4.1 Determination of minimum inhibitory concentration (MIC) and minimum bactericidal concentration (MBC) of silver nanoparticles, silver nitrate and antibiotics against selected bacteria

MIC of Ag NPs, AgNO₃ and antibiotics (tetracycline, colistin, amikacin and vancomycin) were determined against selected bacteria such as *Escherichia coli* (ATCC 8739), *Staphylococcus aureus* (ATCC 6538) and *Pseudomonas aeruginosa* (ATCC 10145) by the microdilution method recommended by Clinical Laboratory Standards Institute. [12] Tests were performed in 96-well microtiter plates, in triplicate. The Tryptic Soy Broth (TSB) were used for bacterial growth. The final concentration 5×10⁵ cfu/ml of bacteria was maintained in each well of microtitre plate. The different concentrations (from 0.016 to 256 µg/ml) of Ag NPs, AgNO₃ and antibiotics were tested. A positive control (broth mixed with

bacterial inoculum) and negative control (sterile non-inoculated broth) were also prepared. Inoculated plates were incubated at 37 °C for 24 h. The MIC values were then estimated visually.

The minimum biocidal (bactericidal) concentrations (MBCs) of Ag NPs, AgNO₃ and antibiotics against bacteria were also determined. After 24-hour incubation, 100 µl of each test sample was aseptically spread onto antimicrobial agent free Tryptic Soy Agar (TSA) plates. Inoculated plates were incubated at 37 °C for 24 h and observed for growth. Inhibition >99.9% of bacterial cells growth was determined as MBC value of antimicrobial agent.

5.3.4.2 Determination of synergistic effect of Antibiotics and Silver (FIC index)

The value of the Fractional Inhibitory Concentration (FIC) index as a predictor of synergy has been investigated using tetracycline, colistin, amikacin and vancomycin, combined with Ag NPs and AgNO₃ was prepared by checkerboard titration method in microtitre plates (in triplicate). [13] The final concentration of bacteria in each well was 5×10⁵ cfu/ml. The trypticase soy broth (TSB) was used as diluents for bacterial strains. The positive and negative controls were maintained. The microtitre plates were incubated at 37 °C for 24 h. Concentrations of Ag NPs, antibiotics and AgNO₃ used for determination of FIC index were as follows: 2× MICs, 1× MICs, 1/2 × MICs, 1/4 × MICs, 1/8 × MICs, 1/16 × MICs. The FIC index was calculated by comparing the value of the MIC of each agent alone with the combination-derived MIC according to formula represented in equation 5.

$$FIC = \frac{MIC_{AgNP} \text{ (combined with Ab)}}{MIC_{AgNP}} + \frac{MIC_{Ab} \text{ (combined with AgNP)}}{MIC_{Ab}} \quad (5)$$

The combination of antimicrobial agents that resulted in at least four-fold reduction in the MIC (1/4 MIC) compared with the MICs of agents alone demonstrated synergistic efficacy (FIC ≤ 0.5). FICs in the > 0.5–1.0 range are considered to be non-synergistic or additive. FICs from 1 to 4 are defined as indifferent, while those of > 4 are antagonistic. [14]

5.3.5 Nanoparticle-Bacteria interaction

Bacterial inoculums were prepared in PBS at 1.5×10⁸ cfu/ml and exposed to 20 nm or 50 nm Ag NPs at 7.5 mg/ml. Samples were incubated overnight at 37 °C and then processed for their imaging.

5.3.5.1 Electron Microscopy

Samples were visualized using 20keV STEM (FEI Magellan 400L XHR STEM). Grids were prepared as follows: 10 μL of sample were drop cast onto a copper TEM grid and left to dry in air.

5.3.5.2 Confocal Microscopy

Samples were first centrifuged at 2500rpm for 5min, and resuspended in Live-Dead Staining solution. After 30 min of incubation, samples were mounted with Glycerol Jelly mounting medium on an 8-well glass bottom microslide. Imaging was performed at the Confocal Laser Scanning Microscopy (CLSM, Zeiss LSM980 Airyscan 2). The principles and methodology of NPs imaging by Confocal Microscopy is described and deeply discussed on Chapter 3.

5.3.6 Simulations

5.3.6.1 Model of Dissolution

Once dispersed in TSB medium, Ag NPs begin to dissolve. The dissolution of the NPs over the time course can be theoretically fitted to a first-order rate process assuming the rate of dissolution is linearly related to the surface area of the NP:

$$\frac{d[\text{Ag}^+]}{dt} = k_{diss} 4\pi r^2 \quad (1)$$

This first-order equation may be integrated analytically to give the $[\text{Ag}^+]$ as a function of time:

$$[\text{Ag}^+](t) = -\frac{4}{3}\pi\rho N_p r_0^3 \left[\left(1 - \frac{t}{t_{diss}}\right)^3 - 1 \right] \quad (2)$$

Where:

- ρ is the bulk density of silver 10.5 g/cm – assumed to be the same throughout the complete dissolution process.
- r_0 is the initial radius of the particle (in nm)
- N_p is the particle concentration in NPs/mL

- t_{diss} is the time to complete the dissolution of the particle. $t_{\text{diss}} = r_0/k$, where k is the first-order rate constant.

5.3.6.2 Model of Consumption

Once generated, the consumption of the $[Ag^+]$ can be fitted to an exponential decay curve:

$$(Ag^+)(t) = e^{-k_c t} \quad (3)$$

Where k_c is the consumption rate constant.

We consider that after 8 hours, the concentration of $[Ag^+]$ is half of the initial $[Ag^+]$ concentration.

$$(Ag^+)(0) = e^{-k_c 0} = 1$$

$$(Ag^+)(8\text{hours}) = \frac{1}{2} (Ag^+)(0) = e^{-8k_c}$$

Solving both equations, we obtain a value for $k_c=0.0866$. Therefore, the consumption of the $[Ag^+]$ can be fitted as follows:

$$(Ag^+)(t) = e^{-0.0866t} \quad (4)$$

With this equation we can model the depletion of Ag^+ from solution. This equation is independent of NPs size and only depends on the amount on $[Ag^+]$ present in solution and the time.

5.4 Nanoparticle's Characterization Techniques

5.4.1 Transmission Electron Microscopy (TEM)

NPs were visualized using 80 keV TEM (Jeol 1010, Japan) and 20keV STEM (FEI Magellan 400L XHR SEM). TEM grids were prepared as follows: 10 μ L of sample were drop cast onto a copper TEM grid and left to dry in air. The TEM images acquired were used for the size distribution analysis. For each sample, the size of at least 500 particles was measured and the average size and standard deviation obtained.

TEM is a microscopy technique in which a beam of electrons is transmitted through a specimen to form an image. An image is formed from the interaction of the electrons with the sample as the beam is transmitted through the specimen. Because the wavelength of electrons is much smaller than that of light, the optimal resolution attainable for TEM images is many orders of magnitude better than that from a light microscope. TEM allows us to image the nanoparticles directly and assess their size distribution (polydispersity) and morphology.

5.4.2 Dynamic Light Scattering (DLS)

A Malvern ZetaSizer Nano ZS instrument (Malvern Instruments) was used to measure NP size. An aliquot of the NP solution was placed in a cell and DLS analyses were performed. Measurements were conducted in a 1 cm optical path cell with precise control of temperature (25 °C).

Dynamic light scattering (DLS) is a non-invasive technique for measuring the size distribution profile of small particles or polymers in solution, typically in the submicron region. A monochromatic light source, usually a laser, is shot through a polarizer and into a sample. The Brownian motion of particles or molecules in suspension causes the incident laser light to be scattered at different intensities. Analysis of these intensity fluctuations yields the velocity of the Brownian motion and hence the particle size using the Stokes-Einstein relationship. Note that the diameter that is measured in DLS is a value that refers to how a particle diffuses within a fluid so it is referred to as a hydrodynamic diameter. The diameter that is obtained by this technique is the diameter of a sphere that has the same

translational diffusion coefficient as the particle. The translational diffusion coefficient will depend not only on the size of the particle core, but also on any surface structure, as well as the concentration and type of ions in the medium. The value of the hydrodynamic diameter is also determined by factors extrinsic to NP's properties, as temperature and the viscosity of the medium. All in all, the DLS measured value gives us information about the size of the NPs in colloid suspension, the polydispersity of the sample and its aggregation state. [15]

5.4.3 Zeta-Potential (Z-Pot; ζ)

A Malvern ZetaSizer Nano ZS instrument (Malvern Instruments) was used to measure NP's surface charge. An aliquot of NP solution was placed in a folded capillary cell and zeta potential analysis were performed under a controlled temperature (25°C).

Zeta potential measurement is a technique for determining the surface charge of nanoparticles in a colloidal solution. The zeta potential of particles is typically measured by Electrophoretic Light Scattering (ELS), an electric field is applied and the electrophoretic mobility of particles is used to calculate the zeta potential. Due to the electric field particles will move at different speeds: highly charged particles will move faster than less charged particles. [16] The magnitude of the zeta potential gives an indication of the potential stability of the colloidal system, correlated to the electrostatic repulsion of the particles in the sample. The general dividing line between stable and unstable suspensions is generally taken at either +30 or -30 mV. [17] A zeta potential value on its own without defining the solution conditions is a virtually meaningless number. Measurements are useful only when the measurement conditions are known. These include factors such as pH, buffer concentration, temperature and ionic strength.

5.4.4 UV-Vis Spectroscopy

The spectrum of each sample was recorded using Agilent Cary 60 UV-Vis Spectrophotometer (Agilent Technologies). An aliquot of the NP solution was placed in a cell and the analysis was performed in the 300–800 nm range at room temperature.

UV-Vis spectroscopy measures the extinction of light (that comprises the scattering and the absorption contributions to the loss of light), in part of the ultraviolet and the full visible regions of the electromagnetic spectrum, that passes through a sample. Regarding metallic NPs, especially the ones that exhibit surface plasmon resonance, the UV-Vis spectra can give us information about their size, shape or concentration. Changes in the spectra can be used to monitor aggregation state or interactions with their surrounding media.

In order to evaluate stability in distinct conditions, Levy et al. [18] defined an empirical measurement of the aggregation process, which measures the variation of the integrated absorbance between 600 and 700 nm. The Aggregation Parameter (AP) is defined as follows:

$$AP = \frac{A - A_0}{A_0}$$

where A is the integrated absorbance between 600 and 700 nm of the sample at a given moment and A_0 is the integrated absorbance between 600 and 700 nm of the initial, fully dispersed solution of NPs. This allows to monitor changes in the stability of a given NP solution after surface modification or dispersion in a different media of study.

5.5 References

- [1] Piella, J., Bastús, N. G., & Puentes, V. Size-Controlled Synthesis of Sub-10-nanometer Citrate-Stabilized Gold Nanoparticles and Related Optical Properties. *Chemistry of Materials* 28, 1066–1075 (2016)
- [2] Bastús, N. G., Comenge, J., & Puentes, V. Kinetically controlled seeded growth synthesis of citrate-stabilized gold nanoparticles of up to 200 nm: Size focusing versus ostwald ripening. *Langmuir* 27, 11098–11105 (2011)
- [3] Ojea-Jiménez, I. & Puentes, V. Instability of Cationic Gold Nanoparticle Bioconjugates: The Role of Citrate Ions. *Journal of the American Chemical Society* 131, 13320–13327 (2009)
- [4] Bastús, N. G., Comenge, J., & Puentes, V. Kinetically Controlled Seeded Growth Synthesis of Citrate-Stabilized Gold Nanoparticles of up to 200 nm: Size Focusing versus Ostwald Ripening. *Langmuir* 27, 11098–11105 (2011)
- [5] Bastús, N. G., Merkoçi, F., Piella, J., & Puentes, V. Synthesis of Highly Monodisperse Citrate-Stabilized Silver Nanoparticles of up to 200 nm: Kinetic Control and Catalytic Properties. *Chemistry of Materials* 26, 2836–2846 (2014)
- [6] Oró, D., Yudina, T., Fernández-Varo, G., Casals, E., Reichenbach, V., Casals, G., De La Presa, B. G., Sandalinas, S., Carvajal, S., Puentes, V., & Jiménez, W. Cerium oxide nanoparticles reduce steatosis, portal hypertension and display anti-inflammatory properties in rats with liver fibrosis. *Journal of Hepatology* 64, 691–698 (2016)
- [7] Piella, J., González-Febles, A., Patarroyo, J., Arbiol, J., Bastús, N. G., & Puentes, V. Seeded-Growth Aqueous Synthesis of Colloidal-Stable Citrate-Stabilized Au/CeO₂ Hybrid Nanocrystals: Heterodimers, Core@Shell, and Clover- And Star-Like Structures. *Chemistry of Materials* 31, 7922–7932 (2019)
- [8] Casals, E., Barrena, R., García, A., González, E., Delgado, L., Busquets-Fité, M., Font, X., Arbiol, J., Glatzel, P., Kvashnina, K., Sánchez, A., & Puentes, V. Programmed Iron Oxide Nanoparticles Disintegration in Anaerobic Digesters Boosts Biogas Production. *Small* 10, 2801–2808 (2014)
- [9] Tejerina, B., Takeshita, T., Ausman, L., & Schatz, G. C. Nanosphere Optics Lab Field Simulator. (2007)
- [10] Juluri, B. K., Huang, J., & Jensen, L. Extinction, Scattering and Absorption efficiencies of single and multilayer nanoparticles. (2010)
- [11] Yin, Y., Li, Z. Y., Zhong, Z., Gates, B., Xia, Y., & Venkateswaran, S. Synthesis and characterization of stable aqueous dispersions of silver nanoparticles through the Tollens process. *Journal of Materials Chemistry* 12, 522–527 (2002)
- [12] M11-A8 Methods for Antimicrobial Susceptibility Testing of Anaerobic Bacteria; Approved Standard-Eighth Edition. (2012)
- [13] Saiman, L. Clinical utility of synergy testing for multidrug-resistant *Pseudomonas aeruginosa* isolated from patients with cystic fibrosis: ‘the motion for’. *Paediatric respiratory reviews* 8, 249–255 (2007)

- [14] Doern, C. D. When does 2 plus 2 equal 5? A review of antimicrobial synergy testing. *Journal of Clinical Microbiology* 52, 4124–4128 (2014)
- [15] Dynamic Light Scattering DLS | Malvern Panalytical. <https://www.malvernpanalytical.com/en/products/technology/light-scattering/dynamic-light-scattering>
- [16] Zeta potential :: Anton Paar Wiki. <https://wiki.anton-paar.com/es-es/potencial-zeta/>
- [17] Zeta Potential | Malvern Panalytical. <https://www.malvernpanalytical.com/en/products/measurement-type/zeta-potential>
- [18] Lévy, R., Thanh, N. T. K., Christopher Doty, R., Hussain, I., Nichols, R. J., Schiffrin, D. J., Brust, M., & Fernig, D. G. Rational and combinatorial design of peptide capping ligands for gold nanoparticles. *Journal of the American Chemical Society* 126, 10076–10084 (2004)

CHAPTER 6

GENERAL CONCLUSIONS

General Conclusions

In this thesis a number of different sizes of noble metal nanoparticles were synthesized and presented. The extensive characterization revealed high monodispersity of the prepared NPs and allowed to study their stability and physicochemical transformations. The outstanding optical properties of these NPs were used to monitor their conjugation to different molecules, their evolution in biological environments, and were also used to develop a method to study NP-cell interactions by optical microscopy.

Synthesized gold and silver nanoparticles were successfully conjugated to several molecules with good control over NP stability. Cationic gold nanoparticles were produced by replacing the citrate cap, and further loaded with oligonucleotides. Similarly, a stable albumin protein corona was achieved on gold and silver nanoparticles to control their dispersion in biological environments. In this regard, passivated nanoparticles were exposed to different biological systems and their interaction was studied, showing very high biocompatibility with low or none toxicity.

As discussed, the nanotechnology field is exponentially growing, and so is the interest in its translation into the clinic. Here, three potential applications of gold and silver nanoparticles were presented: from the use of Au NPs as gene delivery vectors, or the use of Ag NP against multidrug resistant bacteria, to their visualization by confocal microscopy.

In detail:

6.1 Cationic Gold nanoparticles mediated mRNA delivery for production of CAR-T lymphocytes for Chronic Lymphoid Leukaemia Immunotherapy

In this chapter the role of cationic functionalized gold nanoparticles as transfection vectors was explored, with the main objective to use them for the production of CAR T-cells for the treatment of Chronic Lymphocytic Leukaemia. The main conclusions can be summarized as follows:

1. A full nanovector catalogue was designed and developed, consisting of Au NPs functionalized with cationic coatings and loaded with mRNA. For this, Au NPs of 5nm, 20 nm and 50 nm were synthesized with high monodispersity following a previously reported seeded-growth method. NPs were successfully coated with either AUT or PEI to provide cationic surface charge, and then loaded with mRNA, which constitutes the nanovector construct.
2. Mechanistic studies of the nanovector confirm stability in biological media, and the ability to release the previously loaded mRNA over time. Nanovectors also displayed proton sponge capacity, and further microscopy studies suggested their delivery into the cytosol via endosomal escape.
3. The use of PEI-coated Au NPs as mRNA delivery vectors showed low transfection efficiency but sustained GFP protein expression over 7 days, where 50 nm Au NPs displayed the highest transfection rates. Protein expression was increased when nanovector-mRNA transfection was performed combined with chloroquine. The mRNA transfection with NPs induced less cellular damage and mortality due to their internalization and delivery via endocytosis than the polymeric strategy.
4. Cytotoxicity and risk assessment performed by Prestoblue, LDH and Annexin V/PI assays demonstrated they are safe and that didn't induce significant cell damage, except for 5 nm Au-PEI NPs that showed higher toxicity, similar to TransIT® transfection control.
5. Cationic Au NPs were proven to be, low but safe, non-viral vectors for mRNA delivery into cells, with still a wide margin for improvement. Current and future perspectives are to use them as CAR19-mRNA transfection vectors for the production of transient CAR T-cells.

6.2 Confocal Imaging of Unlabelled Nanoparticles in Cells and Biological Tissues

In this section unlabelled inorganic nanoparticles were successfully observed on the Confocal Laser Scanning Microscope (CLSM). The main conclusions can be summarized as follows:

1. Optical properties of Au NPs were used to image them by reflectance mode on the CLSM. The laser with highest intensity signal from the experimental observation is correlated with the wavelength range of the highest scattering efficiency extracted from the optical simulations. Similarly, correlating the theoretical scattering cross-section values with the individual signal measurements, confirms that this method allows single particle imaging. The study of the size resolution limit of this method for Au NPs confirms that a minimum particle diameter of ~ 50 nm is needed, also in agreement with the theoretical scattering simulations.
2. The dual-mode observation and later colocalization analysis of Au@SiO₂-FITC NPs – by conventional fluorescence and reflectance mode – in cultured cells and tissue sections further proves the possibility and reliability of imaging Au NPs by scattering. Not only that, but subcellular structures of biological samples were stained and simultaneously imaged at high resolution demonstrating the multiplexing capacity of this method.
3. The *in vivo* imaging of cultured cells exposed to Au NPs for 24h evidences, once more, that reflectance mode is a good approach for studying NP-cell interactions, due to the high scattering cross-section, with no fluctuations nor degradation (photobleaching), of NPs.
4. Following the same principles, Ag, CeO₂, Fe₃O₄, Au@CeO₂ NPs were also successfully imaged by reflectance mode on the LSCM, which shows the versatility of this methodology.
5. All in all, the Confocal imaging of unlabelled inorganic NPs proves to be a great tool to study NP-cell interactions, inexpensive, and that doesn't require high technical expertise.

6.3 Size Effects on Ag NP - Antibiotic Synergy

In this work the antibacterial properties of silver nanoparticles were studied as a function of NP's size, and their synergistic effect when combined with antibiotics. The main conclusions can be summarized as follows:

1. Citrate-stabilized Ag NPs of sizes from 15 nm to 150 nm were synthesized with high monodispersity following a previously reported seeded-growth method. These NPs were then successfully conjugated with PVP or HSA to provide steric repulsion for their application in highly saline biological media.
2. Corrosion and stability studies in DMEM and TSB culture mediums confirm a higher surface reactivity of smaller size NPs. Thus, Ag NPs show a size-dependent dissolution rate, where smaller NPs corrode faster.
3. Biocidal effects of silver in the ionic and NP form tested by MIC and MBC at 24h against *Pseudomonas aeruginosa*, *Staphylococcus aureus* and *Escherichia coli*, showed a higher antibacterial activity of AgNO₃ than 15 nm Ag NPs, and no effect for 50 nm nor 150 nm NPs, at the concentrations tested.
4. Synergistic effect was observed when 15 nm Ag NPs were combined with tetracycline on all bacterial strains, determined by the FIC index. Also, synergistic effect was observed in the combination of AgNO₃ with all antibiotics in *E. coli*, with colistin and tetracycline in *S. aureus*, and with colistin, amikacin and tetracycline in *P. aeruginosa*.
5. Ag NPs act as a Ag⁺ reservoir, providing ions as they dissolve. Thus, material quality is crucial, including NP monodispersity, stability and controlled chemical transformations. Future perspectives may consider the use of a combination of Ag NPs size, rather than a single one, for the continuous provision of Ag⁺ ions in a controlled rational manner for sustained periods of time.